Modelling sea-ice and oceanic dimethylsulfide production and emissions in the Arctic

by

Hakase Hayashida
B.Sc., Memorial University of Newfoundland, 2011
M.Sc., Memorial University of Newfoundland, 2013

A Dissertation Submitted in Partial Fulfillment of the
Requirements for the Degree of

DOCTOR OF PHILOSOPHY

in the School of Earth and Ocean Sciences

Modelling sea-ice and oceanic dimethylsulfide production and emissions in the Arctic

by

Hakase Hayashida
B.Sc., Memorial University of Newfoundland, 2011
M.Sc., Memorial University of Newfoundland, 2013

Supervisory Committee

Dr. Nadja S. Steiner, Co-Supervisor
(School of Earth and Ocean Sciences)

Dr. Adam H. Monahan, Co-Supervisor
(School of Earth and Ocean Sciences)

Dr. James R. Christian, Departmental Member
(School of Earth and Ocean Sciences)

Dr. Ann-Lise Norman, Additional Member
(University of Calgary)

ABSTRACT

Recent field observations suggest that the radiative forcing of aerosol and clouds in the Arctic may be seasonally regulated by the oceanic emissions of the climatically-important biogenic trace gas dimethylsulfide (DMS). However, the validity of the proposed argument is challenged by the limited spatio-temporal coverage of these earlier studies in this difficult-to-access region. In particular, little is known about the pan-Arctic distribution of the oceanic DMS emissions, its temporal variability, and the impacts of sea-ice biogeochemistry on these emissions. In this dissertation, I investigated these unexplored subjects through numerical modelling. Using a one-dimensional (1-D) column modelling framework, I developed a coupled sea ice-ocean biogeochemical model and assessed the impacts of bottom-ice algae ecosystems on the underlying pelagic ecosystems and the associated production and emissions of DMS. The model was calibrated by time-series measurements of snow and melt-pond depth, ice thickness, bottom-ice and under-ice concentrations of chlorophyll-a and dimethylsulfoniopropionate (DMSP), and under-ice irradiance obtained on the first-year landfast sea ice in Resolute Passage during May-June of 2010. Many of the model parameters for the DMSP and DMS production and removal processes were derived from recent field measurements in the Arctic, which is advantageous over the previous Arctic-focused DMS model studies as their model parameters were based on the measurements in extra-polar regions. The impacts of sea-ice biogeochemistry on the DMS production in the underlying water column and its potential emissions into the overlying atmosphere were quantified through sensitivity experiments. To extend the study domain to the pan-Arctic, I implemented the sea-ice ecosystem and the coupled sea ice-pelagic DMS cycling components of the 1-D column model into a three-dimensional (3-D) regional modelling framework. A multi-decadal model simulation was performed over the period 1969-2015 using realistic atmospheric forcing and lateral boundary conditions. The results of the simulation were evaluated by direct comparisons with available data products and reported values based on field and satellite measurements and other model simulations. The decline of Arctic sea ice was successfully simulated by the model. The magnitude of the pan-Arctic sea-ice and pelagic annual primary production and their general spatial patterns were comparable to other model studies. The mean seasonal cycle and the spatial distribution of the model-based surface seawater DMS climatology within the pan-Arctic showed some similarities with *in situ* measurement- and satellite-based climatologies.

However, at the same time, the comparison of the DMS climatologies was challenged by the bias in the measurement-based climatology, emphasizing the need to update this data product, which was created almost a decade ago, by incorporating data acquired during the recent field campaigns. The analysis of the modelled fluxes of DMS at the ice-sea and sea-air interfaces revealed different responses to the accelerated decline of sea ice over the recent decades (1996-2015). There was no trend in the pan-Arctic ice-to-sea DMS flux due to the counteracting effect of vertical thinning and horizontal shrinking of sea ice that drove ice algal production. In contrast, the pan-Arctic sea-to-air DMS flux showed a consistent increase (about 40 % over the last two decades) driven by the reduction of sea ice cover that promoted outgassing and biological productivity. This finding suggests that the climate warming in the Arctic causes an increase in DMS emissions, and encourages further exploration of the biological climate regulation in the Arctic.

Contents

List of Tables

List of Figures

ACKNOWLEDGEMENTS

I would like to express my sincere gratitude to the following people:

- my supervisors, Nadja Steiner and Adam Monahan, for their continuous support and encouragement throughout the past five years. My enthusiasm for sea-ice biogeochemistry was developed through Nadja and I thank her for providing me the opportunities to pursue research on this topic and network with researchers around the world. My skills in scientific writing and approaches were much improved through constructive feedback from Adam and I also thank him for keeping me on track of the PhD program.

- my committee members, Jim Christian and Ann-Lise Norman. I appreciate Jim for his openness to my irregular visits to his office for discussions on ocean biogeochemistry, and thank Ann-Lise for discussions on atmospheric processes and air-sea interaction during committee meetings and NETCARE workshops.

- my colleagues within/around UVic for both formal and informal meetings and their useful advice: Carsten Abraham, Zelalem Engida, Amber Holdsworth, Warren Lee, Rashed Mahmood, Eric Mortenson, Olivier Riche, Andrew Shao, Tessa Sou, and Neil Swart.

- my collaborators for productive meetings and countless emails: Virginie Galindo, Roya Ghahremaninezhad, Michel Gosselin, Margaux Gourdal, Xianmin Hu, Maurice Levasseur, and Martine Lizotte.

- Mike Berkley, Ed Wiebe, and Belaid Moa for their technical support for computational resources.

- Allison, Kimberly, and Kalisa for their administrative support.

- my former supervisor, Entcho Demirov, for his guidance and introducing me to the wonderful world of numerical modelling and ocean biogeochemistry.

- my parents for pushing me to study abroad which opened up opportunities.

- my sisters for their laughter.

- my wife, Aishah, and my son, Hamza, for their love, patience, joy, and comfort.

I would like to acknowledge the financial support from NETCARE, ArcticNET, the Faculty of Graduate Studies and the Graduate Students' Society at UVic, and CUPE4163. I would also like to acknowledge the computing resource provided by Compute Canada and Westgrid for conducting 3-D simulations.

Chapter 1

Introduction

1.1 Background

The Arctic Ocean is the smallest and shallowest of the world's five oceans; it covers approximately 4 % of the surface area of the world ocean with an average depth of about 1200 m (Jakobsson, 2002). About half of the total area of the Arctic Ocean is comprised of deep basins centred around the North Pole, while the other half consists of continental shelves of North America and Eurasia (Jakobsson, 2002). Between these continents, there are straits that connect the Arctic Ocean to the Pacific and the Atlantic Oceans.

Perhaps the most prominent feature of the Arctic Ocean is the presence of sea ice that regulates the exchange of heat, moisture, and gases between the ocean and the atmosphere, thereby playing an important role in the global climate system and biogeochemical cycles (Vancoppenolle et al., 2013). Sea ice is also an important habitat for microbial communities that constitute the base of polar marine food webs. These sea ice habitats include melt ponds, surface ice, interior ice, bottom ice, platelet ice, and strand communities (Arrigo, 2014). Among these habitats, the bottom ice is typically the most biologically productive area where the ice temperature is relatively warm and rich in nutrients due to its proximity to the underlying seawater (Arrigo, 2014).

Microalgae that colonize the bottom few centimetres of sea ice are referred to as ice algae. The seasonal bloom of ice algae precedes that of phytoplankton residing in the underlying water column, as ice algae are acclimated to low ambient light conditions (Lavoie et al., 2005). Consequently, ice algae can temporarily dominate

the total (sea ice and pelagic) primary production over phytoplankton in some ice-covered regions (Gosselin et al., 1997). Furthermore, the earlier onset of the ice algal bloom affects pelagic and benthic ecosystems (Leu et al., 2015) in a variety of ways including: 1) providing food for pelagic and benthic grazers (Arrigo, 2014); 2) seeding pelagic blooms (Michel et al., 1993); 3) reducing the light penetration into the water column; and 4) drawing down nutrients in the upper water column. Quantifying these effects through observations, however, is often difficult in practice.

One of the by-products of marine primary production is dimethylsulfoniopropionate (DMSP), which is a soluble sulfur compound stored within cells for maintaining cell volume. In addition, DMSP is believed to act as a cryoprotectant, reducing the freezing point of ice algae (Kirst et al., 1991). DMSP is released from algal cells when exposed to stress related to large changes in ambient salinity, such as brine rejection associated with sea ice formation.

Algal production of DMSP has implications for both the global sulfur cycle and the climate system because the cleavage product of DMSP, dimethylsulfide (DMS), is the dominant oceanic source of sulfur emitted into the atmosphere (Lovelock et al., 1972) and consequentially influences the planetary albedo (Shaw, 1983), respectively. The latter process is possible because the oxidation of DMS in the atmosphere can lead to the formation of sulfate and sulfuric acid, that can scatter shortwave radiation, modify the radiative properties of clouds, and, in the case of sulfuric acid, form new cloud condensation nuclei (von Glasow and Crutzen, 2004).

The climatic role of DMS received much attention when Charlson et al. (1987) hypothesized that increased oceanic DMS emission (as a result of increased productivity under warmer climate) could counteract climate warming due to increased planetary albedo (through the chain of processes explained above). This negative feedback mechanism between marine algae and climate, known as the CLAW hypothesis (named after the initials of the four authors of Charlson et al., 1987), has stimulated the scientific community to investigate the possibility of biological regulation of global climate. While the mechanism proposed by the CLAW hypothesis now appears to be relatively unimportant at global scale (Quinn and Bates, 2011), biological regulation of climate is possible in regions where oceanic DMS emission is sufficiently high and the background concentration of aerosol is sufficiently low to promote DMS-derived new particle formation (e.g. Tesdal et al., 2016b). Recent field observations (Ghahremaninezhad et al., 2016; Willis et al., 2016; Sharma et al., 2012; Chang et al., 2011a; Rempillo et al., 2011; Park et al., 2017) indicate that these

conditions can be met in the Arctic. However, the limited spatio-temporal extent of these observations reduces confidence in generalizing the argument to a pan-Arctic context.

The spatio-temporal gaps in field measurements can be complemented by numerical modelling. In particular, numerical models can be used to construct a new climatology of surface seawater DMS concentrations that is free of spatio-temporal limitations, which is advantageous over the existing measurement-based climatologies (Kettle et al., 1999; Kettle and Andreae, 2000; Lana et al., 2011). Although climatologies based on numerical models exist (Tesdal et al., 2016a), much focus is given to their representativeness at global scale. More specifically, these climatologies are based on numerical models that lack representation of sea ice habitat that can substantially influence DMS dynamics in the Arctic (Levasseur, 2013; Mungall et al., 2016).

Prior to this dissertation, Elliott et al. (2012) was the only study that incorporated DMS production within sea ice habitat into a process-based numerical model; their study showed potential importance of DMS produced in the bottom ice to the pan-Arctic distribution of surface seawater DMS concentration. However, in their study, no attempt was made to provide the model-based DMS climatology or assess the relative contribution of the DMS production within the bottom ice and the upper water column to the oceanic emissions. Clearly, more research is needed to assess the implications of sea-ice algal DMS production for oceanic DMS emissions within the Arctic.

As a result of global warming, the Arctic Ocean has undergone substantial environmental changes in recent decades. One of the most striking changes is the decline of sea ice that has been happening at least since the late 1970s, but even more rapidly since around the late 1990s (Stroeve et al., 2012b). A straightforward consequence of the sea ice receding is an enhancement of the oceanic DMS emissions as it removes the barrier (i.e. sea ice) to air-sea gas exchange (Levasseur, 2013). The magnitude of this enhancement in the emissions, however, is highly uncertain owing to the complexity of the DMS dynamics in the Arctic Ocean.

1.2 Objectives

In this dissertation, I investigate the sea-ice and oceanic production and emissions of DMS, the dominant oceanic and biogenic source of atmospheric sulfur-containing

aerosols, in the Arctic. The specific objectives of the dissertation are as follows:

1. Develop a new process-based numerical model for Arctic sea-ice and pelagic ecosystems and associated DMS dynamics using a one-dimensional (1-D) modelling framework.

2. Identify key processes and parameters for ice algal production and its impacts on the underlying pelagic ecosystems.

3. Identify key processes and parameters for modelled DMS dynamics.

4. Assess the impacts of sea-ice biogeochemistry on modelled DMS dynamics.

5. Incorporate the sea-ice biogeochemical model developed within the 1-D framework into a three-dimensional (3-D) regional model.

6. Evaluate the model performance in simulating the decline of Arctic sea ice and broad spatial patterns of sea-ice and pelagic annual primary production in recent decades.

7. Compare and contrast the model-based DMS climatology with the observationally-based climatologies.

8. Examine the impacts of the recent decline of Arctic sea ice on the modelled DMS fluxes at the ice-sea and sea-air interfaces.

1.3 Outline

This dissertation is primarily composed of four research articles, each of which makes up an individual chapter. Chapter 2 addresses Objectives 1 and 2, and it has been published as the peer-reviewed research article Mortenson et al. (2017). Chapter 3 addresses Objectives 1, 3, and 4, and it has been published as the peer-reviewed research article Hayashida et al. (2017). Chapter 4 addresses Objectives 5 and 6, and it has been submitted to a peer-reviewed journal for publication. Chapter 5 addresses Objectives 6, 7, and 8, and it is planned to be submitted to a peer-reviewed journal for publication. Chapter 6 offers the conclusions of the dissertation.

1.4 Attribution statements

Given the collaborative nature of the work involved in the dissertation, this section is intended to provide a clear attribution of the work I have undertaken for each of the core chapters (Chapters 2-5).

Chapter 2 was co-designed by the lead author of Mortenson et al. (2017) and myself; Both individuals contributed equally to developing the model code, carrying out the experiments, analyzing the results, and writing the manuscript with inputs from the rest of the co-authors.

Chapter 3 was designed by myself; I developed the model code, carried out the experiments, analyzed the results, and wrote the manuscript with inputs from the co-authors.

Chapter 4 was designed by myself; I developed the model code, carried out the experiments, analyzed the results, and wrote the manuscript with inputs from the co-authors.

Chapter 5 was designed by myself; I developed the model code, carried out the experiments, analyzed the results, and wrote the manuscript with inputs from my supervisors.

Chapter 2

A model-based analysis of physical and biological controls on ice algal and pelagic primary production in Resolute Passage

The following chapter is a manuscript published as:

Mortenson, E., Hayashida, H., Steiner, N., Monahan, A., Blais, M., Gale, M., Galindo, V., Gosselin, M., Hu, X., Lavoie, D., and Mundy, C-J. (2017): A model-based analysis of physical and biological controls on ice algal and pelagic primary production in Resolute Passage, Elementa, https://doi.org/10.1525/elementa.229

The manuscript is repeated here with some adjustments to fit the format of the dissertation.

2.1 Abstract

A coupled 1-D sea ice-ocean physical-biogeochemical model was developed to investigate the processes governing ice algal and phytoplankton blooms in the seasonally ice-covered Arctic Ocean. The 1-D column is representative of one grid cell in 3-D model applications and provides a tool for parameterization development. The model was applied to Resolute Passage in the Canadian Arctic Archipelago and assessed with

observations from a field campaign during spring of 2010. The factors considered to limit the growth of simulated ice algae and phytoplankton were light, nutrients, and in the case of ice algae, ice melt. In addition to the standard simulation, several model experiments were conducted to determine the sensitivity of the simulated ice algal bloom to parameterizations of light, mortality, and pre-bloom biomass. Model results indicated that: (1) ice algae limit subsequent pelagic productivity in the upper 10 m by depleting nutrients to limiting levels; (2) light availability and pre-bloom biomass determine the onset timing of the ice algal bloom; (3) the maximum biomass is relatively insensitive to the pre-bloom biomass, but is limited by nutrient availability; (4) a combination of linear and quadratic parameterizations of mortality rate is required to adequately simulate the evolution of the ice algal bloom; and (5) a sinking rate for large detritus greater than a threshold of $\sim$ 10 m d^{-1} effectively strips the surface waters of the limiting nutrient (silicate) after the ice algal bloom, supporting the development of a deep chlorophyll maximum.

2.2 Introduction

Satellite records indicate that the minimum annual sea ice extent in the Arctic has been decreasing by more than 10% per decade since the late 1970s (Vaughan et al., 2013), which results in a longer and more widespread open-water season (Barber et al., 2015). In addition to the loss of sea ice, there has been a general shift in ice type, from thicker multiyear ice to younger and thinner first-year ice (Lindsay and Schweiger, 2015). These trends in ice type, cover, and timing have significant consequences for marine and sea-ice ecosystems and air-sea exchange, as well as broader implications for global climate. To reproduce recent changes and project future changes of sea ice related primary production in models, we need to be able to understand the driving processes and develop adequate model parameterisations. 1-D models are excellent tools to develop such parameterisations and test the system sensitivity to parameter variations.

In the Arctic, ice algae live in a relatively sheltered environment concentrated within the bottom few centimeters of the sea ice (Smith et al., 1990; Galindo et al., 2014; Brown et al., 2015a). Ice algal blooms occur at high latitudes where snow and ice-cover substantially reduce incident light to the bottom of the ice column. This environment, and the timing of ice algal blooms, suggest that they are shade-acclimated to low-light conditions (Kirst and Wiencke, 1995). The algae within the

ice can reach very high biomass (exceeding 1000 mg Chl a m^{-3}) that is up to two orders of magnitude greater than the underlying phytoplankton biomass (Galindo et al., 2014; Leu et al., 2015). Previous observational studies indicate that primary production by ice algae can make a substantial contribution to the total (sea ice and pelagic) primary production at various locations in the Arctic Ocean (Legendre et al., 1992; Gosselin et al., 1997). Ice algae are dependent on the ice as a habitat and also affect the ice through light absorption and its subsequent conversion to heat, and through production of extracellular polymeric substances (Riedel et al., 2006; Krembs et al., 2011). In addition, the termination of the ice algal bloom translates to nutrient release to, and possible seeding of, the phytoplankton bloom (Galindo et al., 2014) in the surface ocean.

One challenge for model studies of Arctic sea ice is that observations from the field are sparse due to the remote location and harsh environment. As a result, many parameters required to simulate biogeochemical processes in ice-covered regions are poorly constrained. In this modeling study, we have been able to take advantage of observations of ice algal blooms and environmental variables from several recent field campaigns at one location in order to better understand the processes constraining the simulation. To address the impact of remaining uncertainties, the modelled ice algal growth can be tested against variations in relevant parameters, with ranges based on measured or inferred uncertainty. Sensitivity analyses are a common way to assess the impact of specific processes or parameters on the whole system and evaluate the variables to which the system is most sensitive. Testing the model's sensitivity over a certain parameter range, based on observations, allows for an estimate of the importance of a given process, compared to others, and identification of parameters that need to receive focused observational attention to reduce the overall uncertainty of the system (Steiner et al., 2016). Several 1-D sea ice algal models have been developed in order to reproduce observations at particular locations (Lavoie et al., 2005; Pogson et al., 2011). Some sensitivity studies (e.g., Arrigo and Sullivan, 1994) show that lowering the ice algal nutrient supply (via a nutrient transport coefficient) can cause the ice algal ecosystem to become nutrient-limited, and identify a high sensitivity to the ice algal growth rate. Jin et al. (2006) identified a strong correlation between net primary production of ice algae and the initial nutrient concentration in the water column. Steiner et al. (2016) highlighted several components and parameters that lack either full understanding or observational constraints. Based on these previous studies, the following parameters were selected for testing in this study: the amount

of algae in the ice during the winter (pre-bloom biomass), photosynthetic efficiency of the ice algae in low light conditions, the strength of nutrient flushing during the ice algal bloom period, and the magnitude and form of mortality of the ice algae. While model studies suggest that ice algal seeding of an ice-associated pelagic bloom mainly affects the timing rather than the magnitude of the pelagic bloom (Jin et al., 2007; Tedesco et al., 2012) the link between ice algal and pelagic production remains an area of uncertainty and that we also address here.

Another challenge for both 1-D and 3-D modelling of sea ice ecosystems is the treatment of heterogeneous snow cover and how subgrid-scale heterogeneity affects light penetration to the bottom of the ice. In order to represent a grid cell average, this heterogeneity needs to be taken into account. Abraham et al. (2015) compared light penetration through a Rayleigh-distributed snow cover to a uniformly distributed snow cover, identifying substantial improvement to the grid-cell mean light transmission compared to observations. Light transmission to the bottom of the sea ice has been identified as a major problem in simulating ice algal growth, particularly during the period of snow decline (Arrigo and Sullivan, 1994; Lavoie et al., 2005; Pogson et al., 2011). In the present study, we test the impact of the newly-developed parameterization for light transmission through sea ice (Abraham et al., 2015) on ice algal growth.

With the broader objective of establishing a set of parameterizations that can be incorporated into a 3-D regional Arctic model (coupling sea-ice and the ocean along with associated ecosystems), this study uses a 1-D coupled sea ice-ocean physical-biogeochemical model to analyze the physical and biological controls on simulated ice algae and phytoplankton blooms. The analysis contains three distinct components: 1) Investigation of the impacts of subgrid-scale non-uniform snow depth distributions on the growth of ice algae by applying a new parameterization for light transmission through sea ice (Abraham et al., 2015); 2) assessment of the influences of ice algae on the simulated phytoplankton bloom by coupling and decoupling the sympagic and pelagic ecosystems; and 3) evaluating the sensitivity of the simulated ice algal bloom to a set of selected parameters and parameterizations following recommendations by Steiner et al. (2016). The test location for our model study is set in Resolute Passage in the Canadian Arctic Archipelago, based on the availability of a comparatively rich observational dataset at this location.

2.3 Methods

2.3.1 Model description

Physical model

The sea ice component of the coupled sea ice-ocean physical model is the 1-D thermodynamic model of Flato and Brown (1996) with recent updates from Abraham et al. (2015). These updates include new parameterizations for the light fields and heat fluxes through sea ice by accounting for a subgrid-scale snow depth distribution, melt ponds, and temperature-dependent extinction and transmissivity coefficients (see Appendix for a synopsis of these updates). These new parameterizations improved the evolution of the simulated light fields under the landfast ice in Resolute Passage during the melt period of 2002 (Abraham et al., 2015). In the present study, some of the optical parameters of the sea ice model were modified to improve the fit of the simulated results to observations at Resolute Passage. A set of retuned optical parameters is provided in Table 2.1. Although seasonal changes to the properties of snowfall have not been included in the present study, the snowfall rate has been varied with time based on specified precipitation data, by contrast to a prescribed constant rate as in earlier studies (Flato and Brown, 1996; Abraham et al., 2015).

The physical processes in the water column are simulated by the General Ocean Turbulence Model (GOTM) of Burchard et al. (2006). GOTM provides the physical quantities required for computation of biogeochemical variables in the water column, such as horizontal velocity fields, turbulent transport, photosynthetically active radiation (PAR), and temperature. Details of model parameterizations for these quantities are provided on the GOTM website (http://www.gotm.net).

Biogeochemical model

A biogeochemical model representing the lower-trophic level of sea ice and pelagic ecosystems in the Arctic was developed within the Framework for Aquatic Biogeochemical Models (Bruggeman and Bolding, 2014) to facilitate the coupling with the physical model described above. The schematic diagram of the biogeochemical model is shown in Figure 2.1. The sea ice component of the biogeochemical model simulates the temporal evolution of four state variables (ice algae, nitrate, ammonium, and silicate) in the sea ice skeletal layer. The ice algae module is based on Lavoie et al. (2005). It was updated in this study to account for potential algal growth reduction

Table 2.1: Extinction and transmissivity coefficients, as well as surface albedos used in this study

Symbol	Quantity	Value	Reference
$\kappa_{s,f}$	Extinction coefficient for freezing snow	14 m^{-1}	Grenfell and Maykut (1977)
$\kappa_{s,m}$	Extinction coefficient for melting snow	7.5 m^{-1}	Grenfell and Maykut (1977)
$\kappa_{i,f}$	Extinction coefficient for freezing sea ice	1.2 m^{-1}	Smith (1988)
$\kappa_{i,m}$	Extinction coefficient for melting sea ice	0.8 m^{-1}	Light et al. (2008)
κ_m	Extinction coefficient for melt ponds	0.5 m^{-1}	Abraham et al. (2015)
κ_{ia}	Extinction coefficient for ice algae	0.017 (mmol N $m^{-3})^{-1}$ m^{-1}	McDonald et al. (2015)
κ_{pd}	Extinction coefficient for phytoplankton and detritus	0.03 (mmol N)$^{-3})^{-1}$ m^{-1}	Lavoie et al. (2009)
$i_{0,s,f}$	Transmissivity coefficient for freezing snow	0.15	Vancoppenolle et al. (2010)
$i_{0,s,m}$	Transmissivity coefficient for melting snow	0.15	Vancoppenolle et al. (2010)
$i_{0,i,f}$	Transmissivity coefficient for freezing sea ice	0.5	Lavoie et al. (2005)
$i_{0,i,m}$	Transmissivity coefficient for melting sea ice	0.5	Lavoie et al. (2005)
$i_{0,m}$	Transmissivity coefficient for melt ponds	0.5	Abraham et al. (2015)
$\alpha_{s,f}$	Surface albedo of freezing snow	0.8	Vancoppenolle et al. (2010)
$\alpha_{s,m}$	Surface albedo of melting snow	0.7	Lavoie et al. (2005)
$\alpha_{i,f}$	Surface albedo of freezing sea ice	0.6	Within the range between Vancoppenolle et al. (2010) and Perovich et al. (2002)
$\alpha_{i,m}$	Surface albedo of melting sea ice	0.5	Vancoppenolle et al. (2010)
α_m	Surface albedo of melt ponds	0.3	Light et al. (2008)

due to nitrogen limitation, and separating the dissolved nitrogen pool into nitrate and ammonium to represent the range of biogeochemical processes within sea ice more realistically. At any given time, the growth of simulated ice algae is limited by one of four limiting factors: light, ice melt, silicate, or nitrogen. A limitation index for each factor is determined as a non-dimensional index that varies between 0 and 1 as in Lavoie et al. (2005). The ice algal growth rate is then determined by the minimum of the four indices multiplied by the temperature-dependent specific growth rate (Appendix A.1.2).

To study the sympagic-pelagic ecological interactions at the lower trophic levels, the sea ice biogeochemical model was coupled to a ten-compartment (small and large phytoplankton, microzooplankton, mesozooplankton, small and large detritus, biogenic silica, nitrate, ammonium, and silicate) pelagic biogeochemical model based on Steiner et al. (2006). This module was updated by including mesozooplankton as a prognostic variable and by partitioning detritus into small and large size classes. At the ice-water interface dissolved nutrients are exchanged by molecular diffusion. Ice algae released into the water column are treated similarly as in the coupled model of Lavoie et al. (2009): sloughed ice algae enter either the large phytoplankton pool in which they continue to grow or the large detritus pool in which they sink rapidly as aggregates. The equations and parameters for the coupled biogeochemical model are provided in Appendix A.1.2.

Experimental design

The 1-D model was applied to simulate ice algae and pelagic primary production within and under the landfast first-year sea ice in Resolute Passage, at a location with a water depth of 141 m. Resolute Passage was chosen for the study site because extensive field research has been conducted in the area (Cota et al., 1987; Lavoie et al., 2005; Papakyriakou and Miller, 2011; Galindo et al., 2014; Brown et al., 2015a; Geilfus et al., 2015). Specifically, model simulations were conducted for a location representative of the Arctic Ice Covered Ecosystem (Arctic-ICE) field campaign (74.71°N, 95.25°W). This field campaign took place during the spring of 2010 in order to study the physical and biological processes controlling the timing of ice algae and under-ice phytoplankton blooms (Mundy et al., 2014). The model was divided into 10 uniformly-spaced layers for sea ice and 100 layers for the upper 100 m of the water column. With the ultimate goal of implementing the parameterizations considered

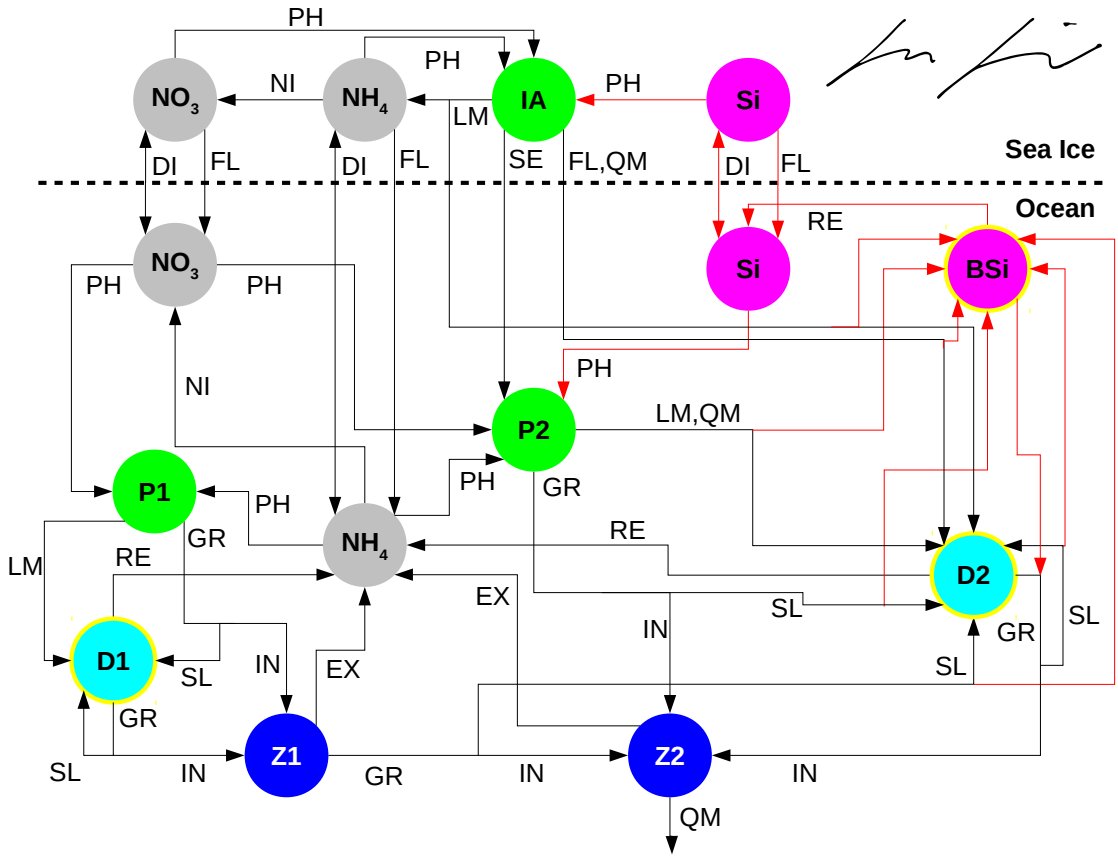

Figure 2.1: Schematic diagram of the coupled sea ice-ocean biogeochemical model. Circles represent the model state variables: nitrate (NO_3), ammonium (NH_4), silicate (Si), ice algae (IA), small phytoplankton (P1), large phytoplankton (P2), microzooplankton (Z1), mesozooplankton (Z2), small detritus (D1), large detritus (D2), and biogenic silica (BSi). Sinking variables are bounded by yellow circles. Black and red arrows represent paths of nitrogen and silicon transfers between the variables, respectively: photosynthesis (PH), nitrification (NI), diffusive mixing (DI), flushing (FL), seeding (SE), linear mortality (LM), quadratic mortatlity (QM), remineralization (RE), grazing (GR), ingestion (IN), sloppy feeding (SL, for inefficient grazing that leaves unconsumed but dead prey), and excretion (EX).

into regional or global ocean circulation models, we do not attempt to resolve small-scale under-ice processes finer than 1 m. In order to limit the ultimate computational burden, we compared the 10-layer model to 5- and 2-layer simulations, deciding that the minor differences (1–2%) in output did not justify curtailing the effort at this stage.

The model was integrated for 8 months (1 February – 30 September, 2010) with a timestep of 10 minutes, and forced with Environment Canada's hourly weather data (including surface air temperature, zonal and meridional wind speed at 10 m above the sea surface, surface air pressure, relative humidity, cloud cover, and precipitation) collected at the Resolute airport, located within 10 km of the study site. Ocean temperature, salinity, and horizontal velocity fields of the ocean were restored over the entire water column with restoring timescale of 1 day (temperature and salinity) and 10 minutes (horizontal velocity) to the output of a 3-D regional model simulation (NEMO-LIM2) used in Dukhovskoy et al. (2016). We chose to restore the model in order to tightly constrain the physical water column properties and thus focus on comparing biogeochemical components of the model. The initial snow and melt pond depths and ice thickness were set to 5, 0, and 55 cm, respectively. The initial concentration of ice algae was set to 1.0 mmol N m^{-3} (ca. 3.5 mg Chl *a* m^{-3}; the observed range of C:N:Chl *a* ratios is described in Appendix A.1.2). The initial concentration of nitrate (silicate) was set to a constant value of 7.2 mmol N m^{-3} (14.7 mmol Si m^{-3}) throughout the bottom ice and the water column, based on measurements of these nutrients during the Arctic-ICE 2010 field campaign (Mundy et al., 2014; Galindo et al., 2014). The initial concentrations of ammonium both in the sea ice and the water column were assumed to be small (e.g., Harrison et al., 1990), and hence, set to 0.01 mmol N m^{-3}. Similarly, the initial concentrations of all other pelagic biogeochemical state variables were set to 0.01 mmol N m^{-3} (mmol Si m^{-3} for biogenic silica) throughout the water column.

2.3.2 Observations

Observational data used to evaluate the model results include snow and melt pond depths, ice thickness, under-ice PAR, and chlorophyll *a* (Chl *a*). Measurements of these variables were conducted during May and June of 2010 as part of the Arctic-ICE field campaign. Observed snow and melt pond depths, ice thickness, and Chl *a* in the bottom 3 cm of sea ice were sampled at various sites of high, medium, and low

snow covers. The mean value of Chl *a* is therefore an estimate of the site average, as presented in Galindo et al. (2014), and is comparable to a grid cell average in a regional or global model. Concentrations of Chl *a* in the water column were determined by collecting samples at five depths (2, 5, 10, 25, and 50 m below the sea surface) using 5 L Niskin bottles and following the procedures outlined in Galindo et al. (2014). *In situ* time series data for daily-mean under-ice (2 m below sea surface) PAR were collected using two independent tethers moored to the sea ice below high ($>$ 40 cm prior to snowmelt onset) and low ($<$ 20 cm prior to snowmelt onset) snow cover sites (within 4 – 6 m of the CTD casts). Technical details of these PAR measurements are provided in Mundy et al. (2014). In addition to the tether measurements, instantaneous under-ice PAR was estimated by extrapolating the 20 m depth CTD-based PAR measurement to the surface following Frey et al. (2011). Casts of CTD and a biospherical 4 pi sensor were obtained daily through the main sampling hole within a heated tent on the sea ice. Details of the CTD-based under-ice PAR estimates are described in Gale (2014).

2.4 Results

Results are divided into three parts based on the types of model simulations conducted. The first subsection evaluates the performance of the standard run. The second subsection compares the result of the standard run with a simulation that excludes ice algae. The third subsection provides the results of parameter sensitivity experiments. Specific setups of these runs are described in each of these subsections.

2.4.1 Model evaluation

The standard run was conducted with the setup outlined in the previous section (Experimental Design) and by applying the Rayleigh distribution for representing the subgrid-scale snow depth variability (see Appendix A.1.1). Abraham et al. (2015) indicated a better fit for the Rayleigh distribution than gamma probability distribution based on observations from the Arctic-ICE 2010 study.

Snow and melt pond depths and ice thickness

In many previous 1-D model studies, the temporal evolution of snow depth was either prescribed to observed snow depth data (e.g., Lavoie et al., 2005; Pogson et al., 2011;

Palmer et al., 2014) or simulated by prescribing a constant snowfall rate (Flato and Brown, 1996; Abraham et al., 2015). In this study, snow depth was simulated by prescribing a variable snowfall rate based on observed precipitation data. The simulated and observed time series of snow and melt pond depths are shown in Figure 2.2a. The simulated snow depth increased occasionally as a result of snowfall events until the maximum depth (ca. 20 cm) was reached by mid-May. In the standard run, the simulated snow started melting toward the end of May and completely vanished within 3 weeks. Snowmelt resulted in the formation of melt ponds which reached a maximum depth of 5 cm shortly after the snow disappeared. Compared with the field measurements presented in Figure 2.2a, the timing of melt events was simulated reasonably with the distributed snow case.

Figure 2.2b shows the simulated and observed time series of ice thickness. In the standard run, simulated ice grew gradually to a maximum thickness of about 150 cm by early June and then started melting following the initial snowmelt. In the standard case, the distributed snow parameterization allows for snow-free areas, which allows the ice to start melting before all the snow has disappeared. The simulated ice vanished completely in early July after which the sea surface remained ice-free until late September. The simulated ice thickness agreed well with the observations throughout the sampling period (Figure 2.2b), whereas the ice break up in the simulation occurred a week earlier than in the observations (Galindo et al., 2014). This difference may be due to dynamic processes (e.g., wind-driven ridging and rafting) which are not accounted for in our 1-D model.

Surface area fractions and under-ice PAR

Simulation of the light penetration through snow and sea ice is crucial for simulating a reasonable ice algal bloom, as the initial phase of the bloom is typically limited by light (Gosselin et al., 1990; Lavoie et al., 2005; Leu et al., 2015). During the melt period, surface area fractions of simulated snow, melt ponds, and bare ice undergo changes that affect the amount of light reaching the ice base as indicated in Figure 2.3. In the standard simulation, the surface of the simulated ice was fully snow-covered prior to the snowmelt onset. Consequently, the simulated daily-mean under-ice PAR during this period was less than 1 μmol photons m^{-2} s^{-1}. This is lower than either of the tether measurements, but in good agreement with most of the CTD-based estimates. In the model, about 10% of the snow surface was replaced

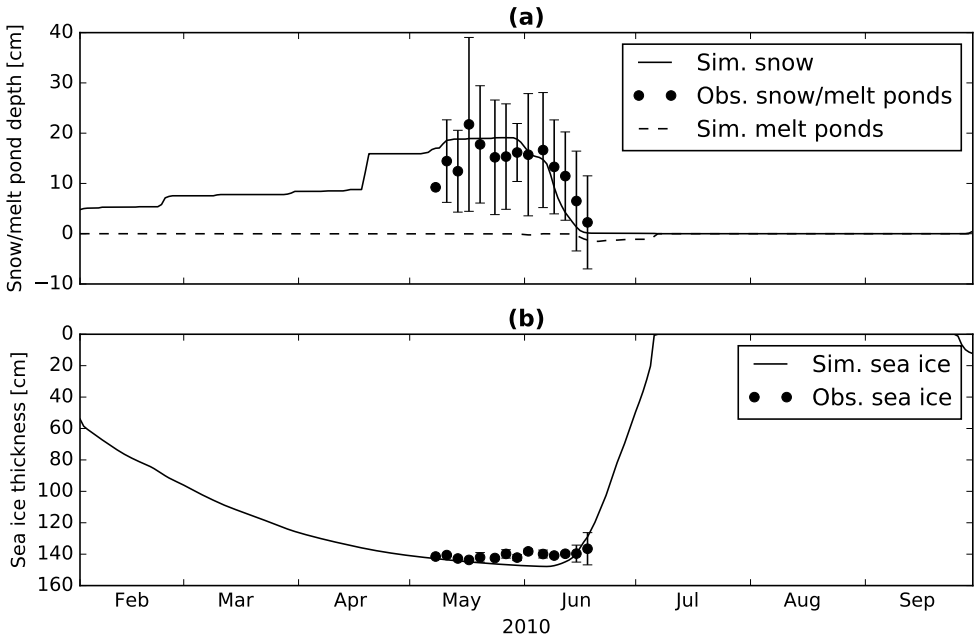

Figure 2.2: Simulated and observed snow depth, melt-pond depth, and ice thickness. Time series of (a) simulated daily-mean snow (solid line) and melt pond (dashed line) depths, observed snow/melt pond depth (circles), and (b) simulated daily-mean (line) and observed (circles) ice thickness. Circles represent the site-average values with one standard deviations indicated by vertical bars.

with melt ponds due to snowmelt during the first week of June, resulting in an increase of the daily-mean under-ice PAR to more than 1 μmol photons m^{-2} s^{-1}. This is comparable to the tether measurements at the high snow cover station, as well as to the CTD-based estimates. By June 9, the surface area coverage of simulated melt ponds increased to 30% (the maximum value prescribed by the model). Further loss of simulated snow resulted in emergence of bare ice, which covered 70% of the ice surface following the snow disappearance. The pulsed effect in melt pond area in mid-June (Figure 2.3a) reflects daily signals associated with daytime melting and overnight freezing (producing bare ice). The simulated under-ice PAR during this period exceeded 10 μmol photons m^{-2} s^{-1} (Figure 2.3b), which is comparable to both the tether and the CTD-based observations. As expected, the simulated gridbox-mean under-ice PAR was quantitatively closer to the CTD-based (site-average) estimates than the tether (point) measurements. Furthermore, the standard simulation successfully reproduced the smooth seasonal transition of under-ice PAR that is evident in the tether measurements during the melt period.

Sea ice ecosystem

Figure 2.4 shows the simulated time series of sea ice ecosystem variables. The standard run simulated an ice algal bloom that is comparable to the observations in terms of both the magnitude and timing of the bloom (Figure 2.4a). In the following, we discuss the dynamics of simulated sea ice ecosystem by partitioning the bloom into growth and decline phases.

The growth phase of simulated ice algal bloom lasted from late March to mid-May, while the bloom decline phase is from mid-May to late June. During the growth phase of the ice algal bloom, the simulated ice algal biomass in the standard run increased to 1050 mg Chl *a* m^{-3} (Figure 2.4a). This is within the range of observed values during peak ice algal biomass (800 – 1300 mg Chl *a* m^{-3} Galindo et al., 2014). Note that this wide range in the observed peak is due to sampling over different snow depth conditions, and that the modelled value falls near the center of the observed range. Until the end of April, simulated concentrations of nitrate and silicate in the ice decreased rapidly due to uptake by ice algae, while the simulated ammonium concentration increased as a result of remineralization of dead ice algal cells (Figure 2.4b). During this time, the ice algal growth rate declined slightly even though nutrients are not yet limiting, likely due to the quadratic term in the

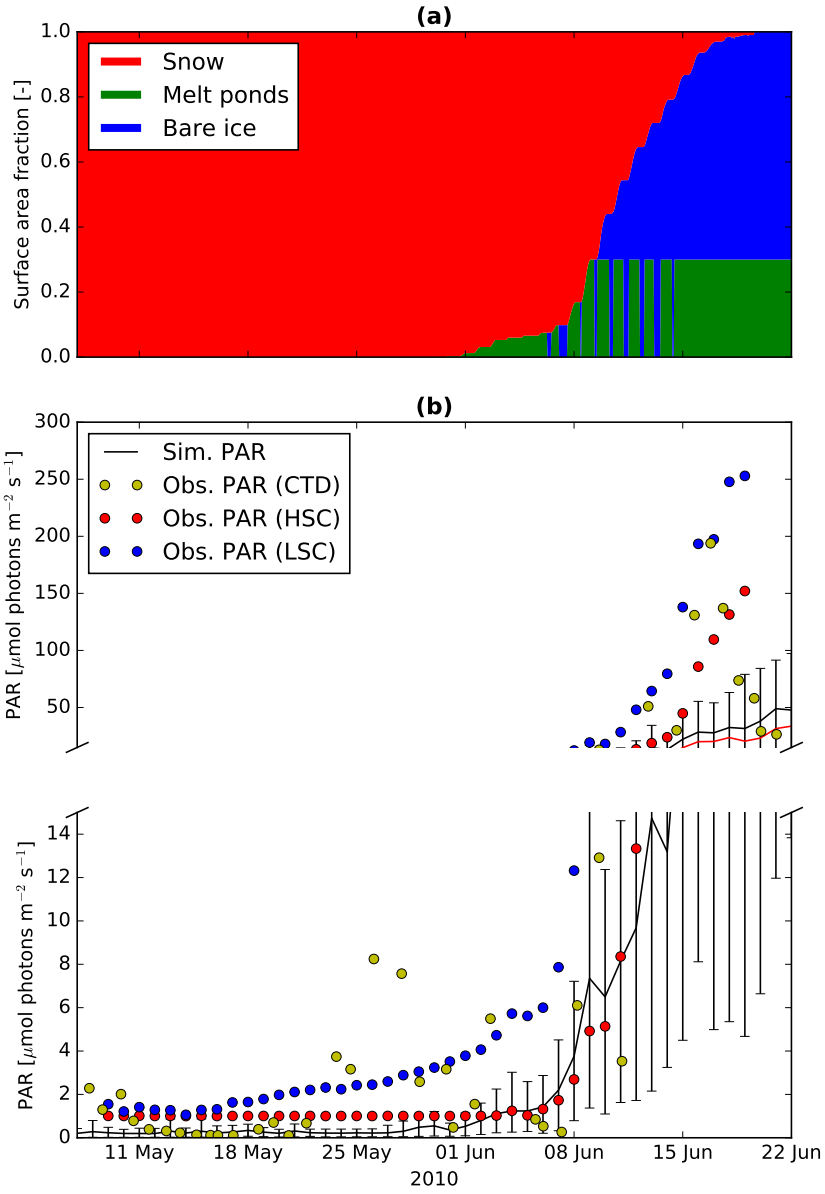

Figure 2.3: Simulated snow, melt-pond depth, and bare ice area, and simulated and observed PAR. Time series of (a) surface area fraction of simulated snow (red), melt ponds (green), and bare ice (blue) and (b) simulated daily-mean (line) and observed (circles) under-ice PAR during the Arctic-ICE 2010 study period. In (b), the units for the simulated PAR values were converted from W m^{-2} to μmol photons m^{-2} s^{-1} by a conversion factor of 4.56 following Lavoie et al. (2005). Vertical bars associated with the solid line represent the diurnal range of simulated under-ice PAR. Red and blue circles represent the daily-mean values measured using tethers deployed over high (HSC) and low (LSC) snow cover sites, respectively. Yellow circles are the instantaneous values based on CTD casts (CTD).

parameterization of mortality. Consequently, both nitrate and silicate concentrations recovered slightly until they were drawn down further by ice algae during the bloom peak in mid-May. The ice algal growth was generally light-limited during the growth phase (Figure 2.4c), except for a day in the beginning of May when the nitrate concentration reached about 0.5 mmol m^{-3} (Figure 2.4b).

At the peak of the ice algal bloom, simulated nutrient concentrations became extremely low, nearly 0 mmol m^{-3} for nitrate and ammonium and 1 mmol m^{-3} for silicate (Figure 2.4b). Consequently, the ice algal growth became nitrogen-limited following the peak (Figure 2.4c), and remained so until the end of the bloom in late June (Figure 2.4a). The simulated range of nitrate concentration (0 – 8 mmol m^{-3}; Figure 2.4b) matches the observed range reported in Galindo et al. (2014). By contrast, the simulated range of ammonium concentration (0 – 0.05 mmol N m^{-3}) is much smaller than the range typically observed in the bottom ice (e.g., Vancoppenolle et al., 2013). This discrepancy is most likely due to the fact that much of the ammonium found in the bottom ice is trapped in the ice matrix and therefore not accessible to ice algae residing in the brine phase of the ice (Vancoppenolle et al., 2013). The model simulates the remaining fraction of ammonium available for ice algae which is low in abundance due to rapid turnover of ammonium by production and removal processes. Figure 2.4d presents the time series of depth-integrated production rates by simulated ice algae and phytoplankton (i.e., sum of P1 and P2). The production rate of simulated ice algae was around 0.1 g C m^{-2} d^{-1} during the bloom peak in mid-May. The time-integrated production by ice algae and phytoplankton over the simulation period was about 4 and 60 g C m^{-2}, respectively. Hence, the primary production by simulated ice algae accounted for 6% of the entire sea ice and water column primary production. This fraction is within the range of the observational and model estimates for first-year Arctic sea ice (2 – 33%; Legendre et al., 1992; Gosselin et al., 1997; Lavoie et al., 2009).

Pelagic ecosystem

Figure 2.5 shows the comparison of simulated and observed time series of chlorophyll *a* concentrations in the upper 80 m of the water column. In mid-June, the model simulated an under-ice phytoplankton bloom in the upper 10 m of the water column (Figure 2.5a). This bloom was dominated by large phytoplankton (Figure 2.1b), and reached a peak concentration of 13 mg Chl *a* m^{-3} in late June. The timing,

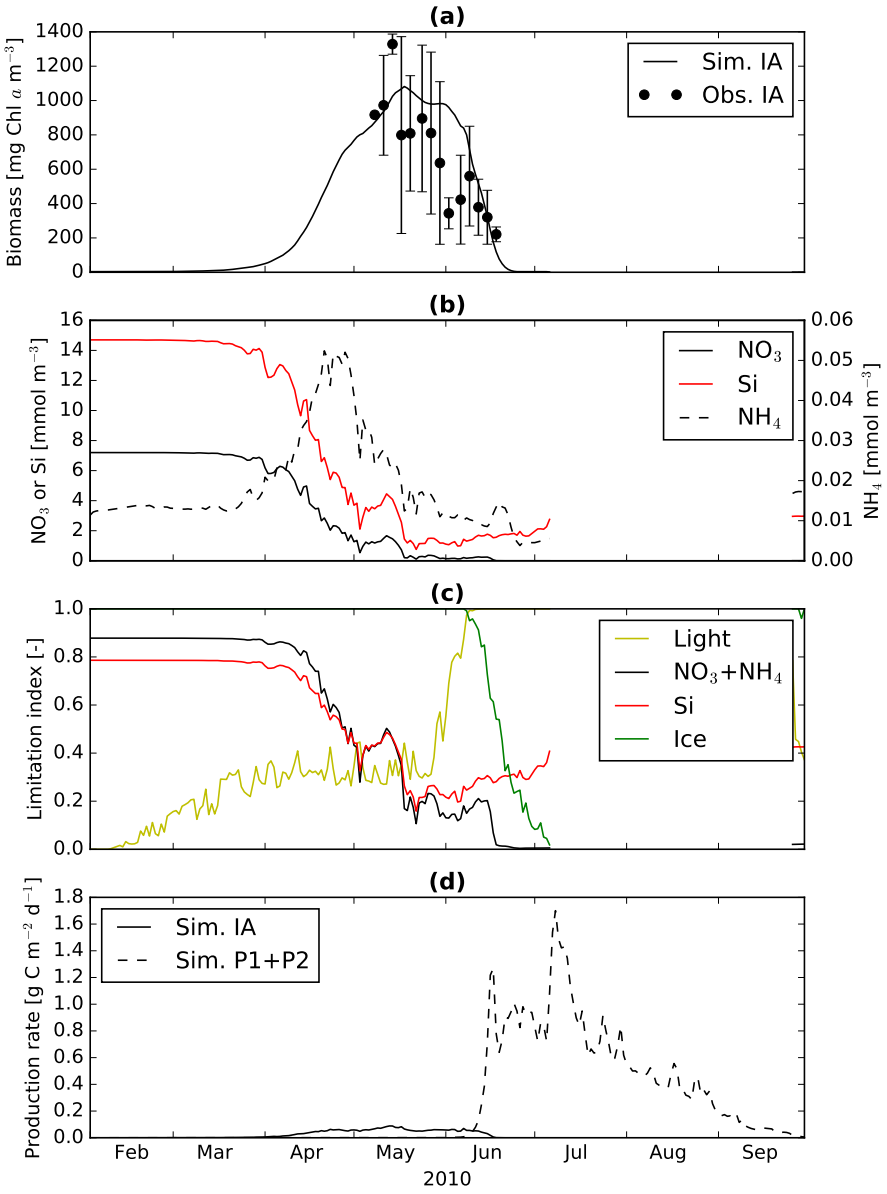

Figure 2.4: Simulated and observed ice algal biomass, nutrients, growth limitations, and simulated sympagic and pelagic production. Time series of (a) simulated (line) and observed (circles) Chl *a* concentrations in the bottom 3 cm of the sea ice, (b) simulated nitrate (solid black), ammonium (dashed black) and silicate (red) concentrations in the bottom 3 cm of sea ice, (c) simulated daily-mean growth limitation index for light (yellow), nitrogen (black), silicate (red), and ice melting (green), and (d) primary production rates of simulated ice algae (solid line) and phytoplankton (dashed line). In (a), circles represent the site-average values with one standard deviations indicated by vertical bars.

magnitude, and vertical extent of the simulated under-ice phytoplankton bloom are consistent with the observed bloom (Figure 2.5b), which was also dominated by large cells (Mundy et al., 2014). The simulated bloom migrated downward and formed a subsurface chlorophyll maximum of 18 mg Chl *a* m^{-3} at 15 – 40 m between late June and early July. During the ice-free period, increased light penetration allowed the deepening of the simulated subsurface chlorophyll maximum to a depth of 75 m where it maintained fairly high concentrations (>6 mg Chl *a* m^{-3}) until the end of August. The formation and subsequent deepening of a deep chlorophyll-maximum is a typical feature in the Arctic where surface nutrient concentrations are low in summer (the chlorophyll maximum typically follows the nitricline). No direct observations are available for this particular time period near Resolute to evaluate the deepening of the subsurface chlorophyll maximum simulated by the model. However, observations taken during the last decade in the Beaufort Sea and Canadian Archipelago show the subsurface chlorophyll maxima with depths ranging from 35 and close to 100 m depending on time and location measured (Tremblay et al., 2008; Carmack et al., 2010; McLaughlin and Carmack, 2010; Carmack and McLaughlin, 2011) which is also represented in model results (Steiner et al., 2015). The chlorophyll maximum in the Chukchi Sea tends to be much shallower (Brown et al., 2015b), while the deepest maxima have been observed in the Beaufort Sea. A maximum depth of 75 m for the deep chlorophyll maximum in the Canadian Arctic Archipelago is within the range of observations. Daily production rates corresponding to the under-ice phytoplankton bloom (1.2 g C m^{-2} d^{-1}) and the subsurface chlorophyll maximum (up to 1.6 g C m^{-2} d^{-1}) simulated by the model (Figure 2.4d) are comparable to the observed rates in Resolute Passage (1.1 g C m^{-2} d^{-1}; Mundy et al., 2014) and in the Beaufort Sea (1.4 g C m^{-2} d^{-1}; Mundy et al., 2009), respectively.

Figure 2.6a-c illustrates the temporal evolution of simulated dissolved nutrients in the upper 80 m of the water column. Prior to the development of the under-ice phytoplankton bloom in mid-June (Figure 2.5a), the concentrations of simulated nitrate (Figure 2.6a) and silicate in the upper 15 m (Figure 2.6c) were reduced as a result of uptake by ice algae. In contrast to nitrate and silicate, simulated ammonium concentrations increased slightly below the nitracline due to the remineralization of dead ice algal cells released into the water column (Figure 2.6b). In late June, these nutrients were drawn down by large phytoplankton, and decreased to < 1 mmol m^{-3} (nitrate; Figure 2.6a), < 0.04 mmol m^{-3} (ammonium; Figure 2.6b), and < 4 mmol m^{-3} (silicate; Figure 2.6c) in the upper 10 m of the water column. These

simulated nitrate and silicate concentrations are close to the values (0.2 mmol m^{-3} for nitrate+nitrite and 2.8 mmol m^{-3} for silicate) reported at the end of the sampling period (21 June) in Resolute Passage (Mundy et al., 2014). The simulated nutrient concentrations remained below these levels until the end of the simulation period (Figure 2.6a-c) because large detritus, which consists of dead cells of ice algae and large phytoplankton and fecal pellets, sinks quickly (50 m d^{-1}, following Lavoie et al., 2009) into the deeper water column before they could be remineralized in the upper water column. The rapid sinking of large detritus resulted in the accumulation of ammonium at depth below the nitracline from late June onwards (Figure 2.6b).

To demonstrate that the ice algal uptake and the nutrient removal in the water column are balanced in the model, the time series of depth-integrated (3 cm) cumulative nitrate uptake by ice algae is displayed with the depth-integrated cumulative nitrate drawdown and total uptake by phytoplankton in the upper 80 m of the water column (Figure 2.6d). Clearly, the total amount of nitrate consumed by ice algae is equivalent to the amount removed from the water column until the onset of the pelagic bloom in mid-June. The result demonstrates an important role of ice algae in reducing nutrient availability in the upper water column. This important aspect of sympagic-pelagic ecological coupling will be examined further in a later section. The decreasing trend of simulated nitrate in the water column during May and June (Figure 2.6a) is generally in good agreement with the observed nitrogen time series in the ice and underlying water column as reported in Galindo et al. (2014).

2.4.2 Sympagic-pelagic ecosystem coupling

In order to assess the impact of the simulated ice algal bloom on the underlying pelagic ecosystem, we conducted an additional simulation that turned off the ice algal bloom (referred to as the exclusion run). This scenario was established by setting the initial biomass of ice algae to zero, while all other aspects are identical to the standard run. Hence, the difference in the results between the standard and the exclusion runs represents the impact of ice algae on the pelagic ecosystem.

Figure 2.7 displays the comparison of the two runs in terms of Chl *a* concentrations in the upper 50 m of the water column. The differences between the two runs are most evident in late June, which correspond to the under-ice bloom in the upper 10 m of the water column (Figure 2.7c). Both the timing and magnitude of the bloom were affected by the presence/absence of ice algae. When ice algae were excluded

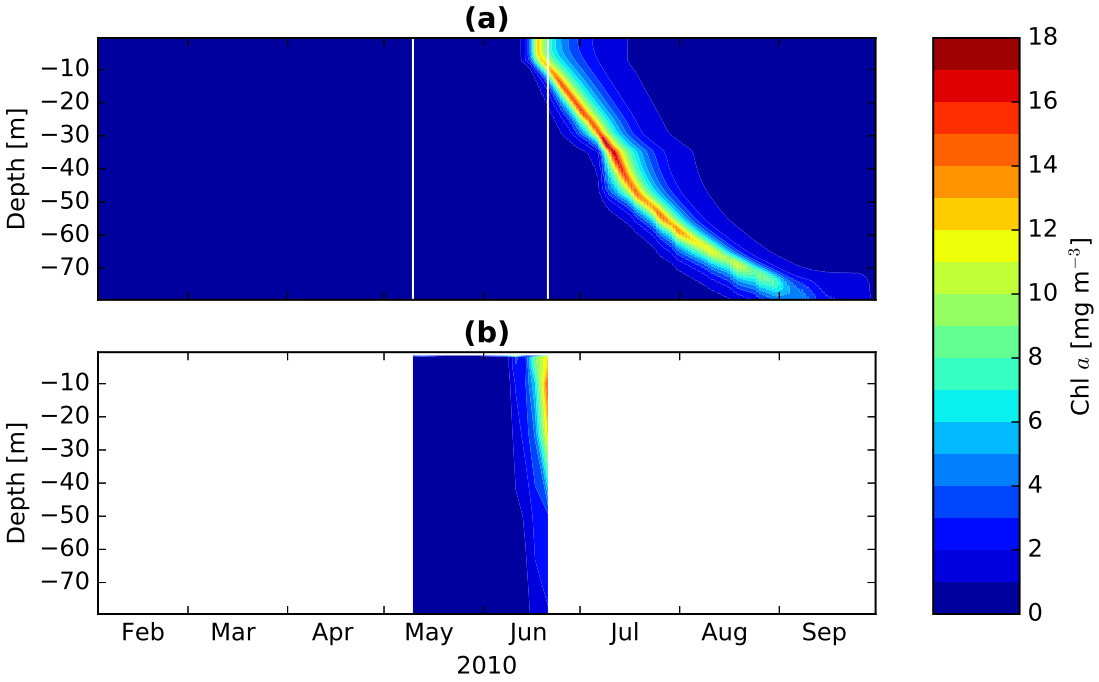

Figure 2.5: Simulated and observed Chl a concentration. Time series of (a) simulated and (b) observed Chl a concentrations in the upper 80 m of the water column.

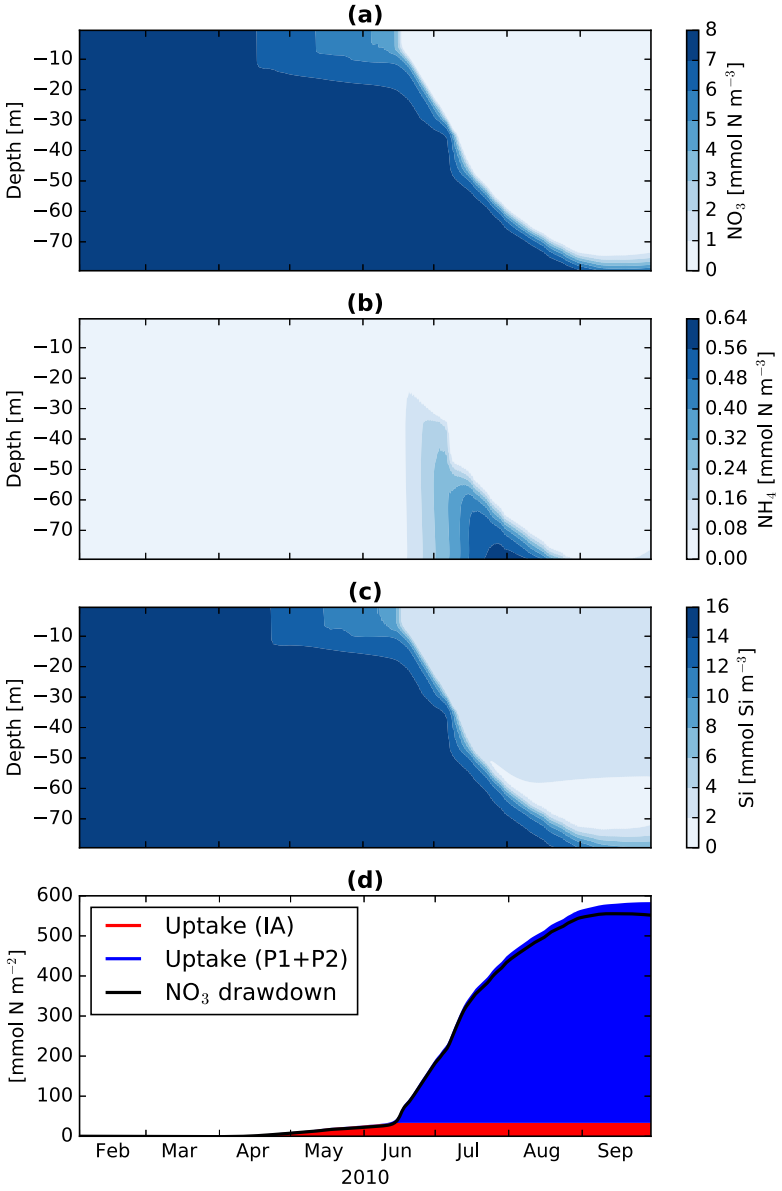

Figure 2.6: Simulated water column concentrations of nutrients and biological uptake and drawdown of nitrate. Simulated time series of (a) nitrate, (b) ammonium, and (c) silicate concentrations in the upper 80 m of the water column (depth of entire water column is 141 m). (d) Simulated time series of cumulative depth-integrated nitrate uptake and drawdown. In (d), areas filled in red represent the cumulative uptake by ice algae integrated over the bottom 3 cm of the ice skeletal layer, areas filled in blue represent the cumulative uptake by phytoplankton (P1 and P2) integrated over the upper 80 m of the water column, and the black line represents the cumulative amount of nitrate drawn down from the upper 80 m of the water column. Note that the sum of the two uptake terms (red+blue) does not balance with the drawdown during the ice-free period; the mismatch represents the uptake of nitrate entrained from the layer below 80 m.

from the simulation (Figure 2.7b), the onset of the under-ice bloom was delayed by a few days. This delay in the bloom onset is due to the lack of seeding by ice algae in the exclusion run (Chapter 3). Despite the delay in the development of the under-ice bloom, the exclusion run simulated a higher peak Chl *a* concentration (a difference of about 7 mg Chl *a* m^{-3}) than the standard run. The enhanced peak in the exclusion run is due to the absence of nutrient drawdown by ice algae (Figure 2.8), which implies a concentration difference of about 3 mmol N m^{-3} in the upper 10 m of the water column at the onset of the under-ice bloom. (It is not due to the absence of light-shading by the ice algae, as the pelagic bloom does not begin in the standard run until after the ice algal bloom has ended.). The effects of ice algae in the pelagic ecosystem appear to be relatively small below the upper 10 m of the water column, as there is no substantial difference in either Chl *a* or nitrate concentrations between the standard and the exclusion runs.

Sinking rate of large detritus

In the model, large detritus (D2) represents the non-living particulate matter originating mainly from ice algal and large phytoplankton cells. The simulated large detritus is assumed to sink at a constant rate (w_{d2}; Appendix A.1.2) which is faster than the sinking rate of small detritus. In the standard run, a sinking rate of 50 m d^{-1} was prescribed for large detritus following Lavoie et al. (2009). However, observations of this rate span a range of values. Onodera et al. (2015) observed sinking rates from 37 to more than 85 m d^{-1} for diatoms in the western Arctic Ocean. Higher and lower rates have also been measured, with sinking rates well over 100 m d^{-1} among Antarctic ice algal aggregates (Sibert et al., 2010) and near 20 m d^{-1} in lab tests with the common Arctic ice algae diatom *Nitzschia frigida* (Aumack and Juhl, 2015).

In this sensitivity analysis, we assessed the simulated phytoplankton response to a change in the D2 sinking rate. Runs with a slower sinking rate do not show much difference in the pelagic ecosystem until the sinking rate is lowered below a threshold of approximately 10 m d^{-1}. Above this threshold, large detritus is effectively removed from the euphotic layer and transported to depth before it can be remineralized (Figure 2.9a and b). Below that threshold, e.g., at $w_{d2} = 5$ m d^{-1}, a secondary sub-surface bloom, comprised of small phytoplankton (P1), forms after the first bloom (Figure 2.9c). This secondary bloom results from an increased supply of nitrogen. The dissolution rate from biogenic silica is an order of magnitude slower

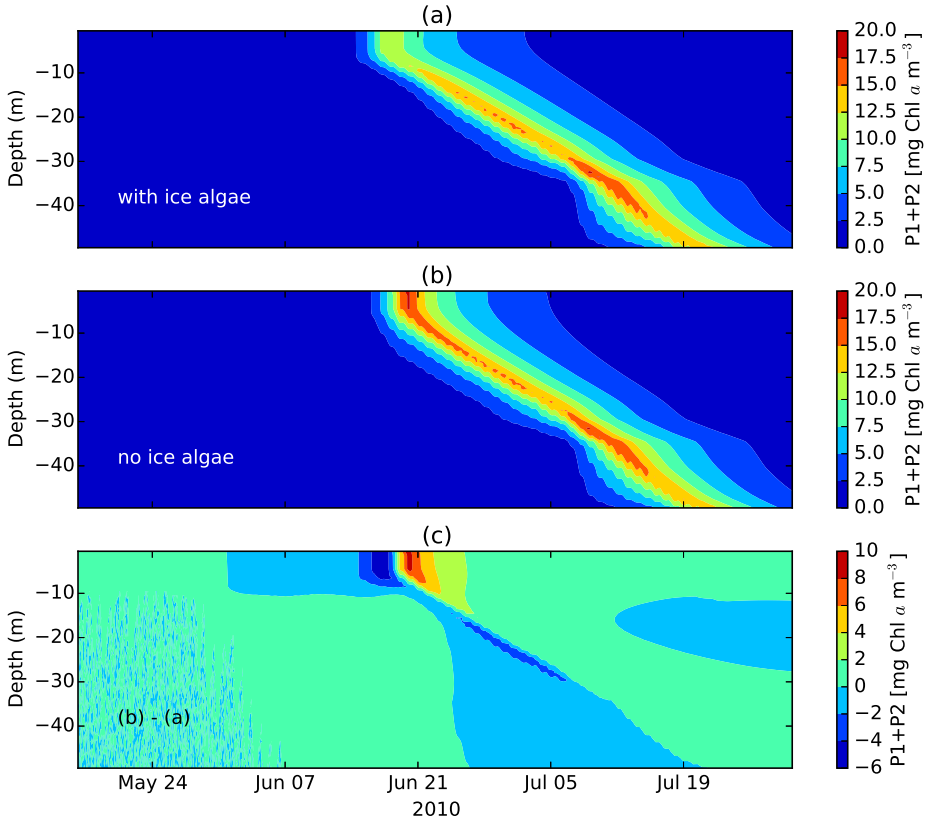

Figure 2.7: Water columm Chl *a* concentration when ice algae are present, absent, and the difference. Simulated phytoplankton bloom in the upper 50 m of the water column when ice algae are present (a), absent (b), and the difference (c). Phytoplankton are sum of large and small (P1 and P2) groups.

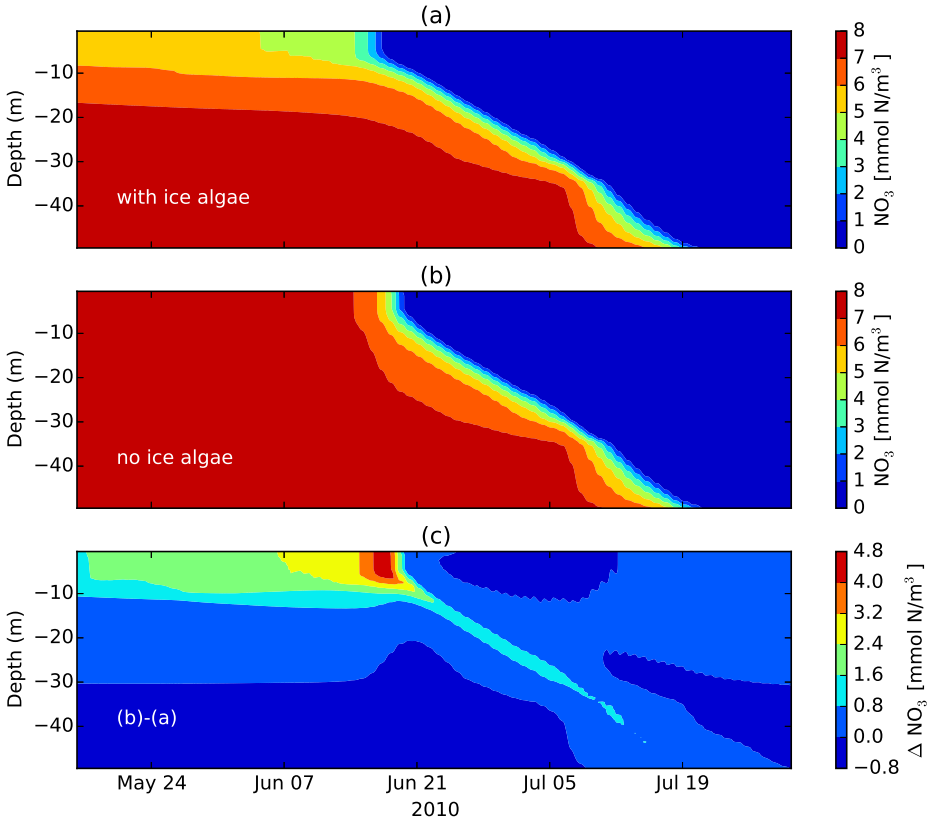

Figure 2.8: Water column nitrate when ice algae are present, absent, and the difference. Simulated NO_3 concentration in the upper 50 m of the water column when ice algae are present (a), absent (b), and the difference (c).

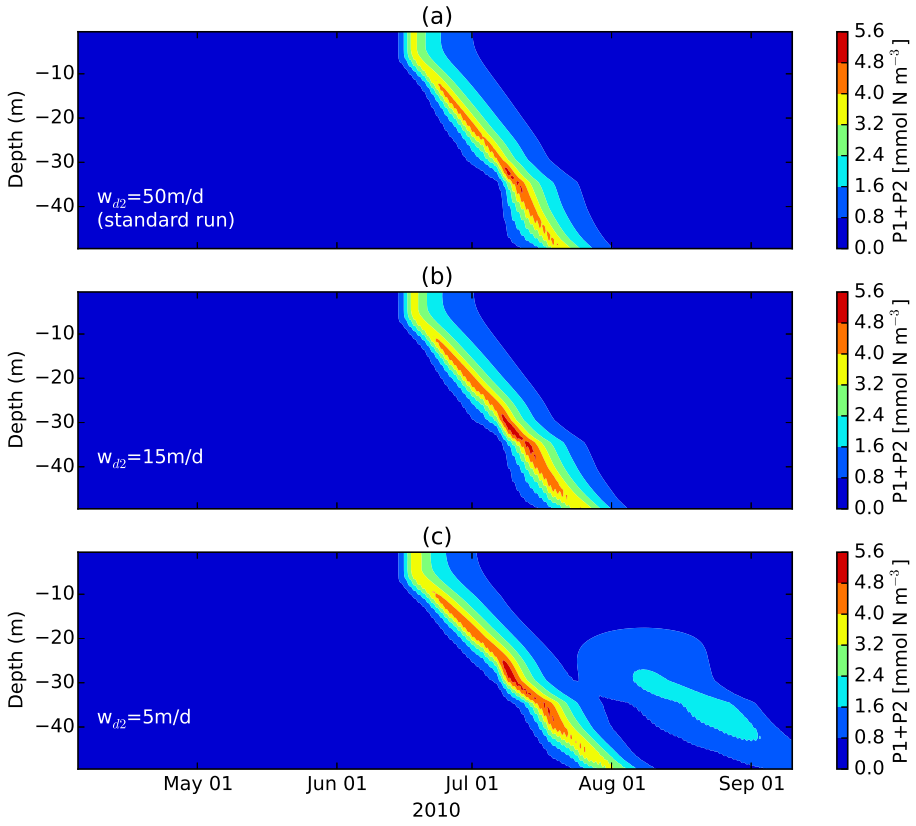

Figure 2.9: Phytoplankton in the water column with fast-sinking detritus. Simulated phytoplankton in the upper 50 m of the water column, with detritus (D2) sinking rate set at 50 m d^{-1} (a), 15 m d^{-1} (b), and 5 m d^{-1} (c). The first bloom is dominated by large phytoplankton (P2, diatoms) and the later bloom in (c) is dominated by small phytoplankton (P1, flagellates).

than remineralization of D2 (0.01 d^{-1}, and 0.3 d^{-1}, respectively, Table S2), and hence the second bloom does not allow for silicate-dependent large phytoplankton.

2.4.3 Sensitivity analyses for ice algae

Given the influence of simulated ice algae on the underlying pelagic ecosystem, it is of great interest to investigate the physical and biological controls on the simulated ice algal bloom (and subsequently on the underlying ecosystem). These controls are set via parameter values which are often not measured directly, but inferred from observed concentrations that are also not well constrained. Sensitivity analyses focus on

parameters that represent key uncertainties in the observational record. By varying each parameter over the range of observed (or estimated if not constrained by observations) uncertainty and determining which parameters have the strongest impact on properties of the simulated ice algal bloom, we can identify which observations would be most beneficial to improve our understanding of the system.

The growth of the ice algal bloom is dependent on both physical and biogeochemical processes. In the simulated ice algal bloom, several key parameters determine the strength of these influences. In the standard simulation, parameters controlling the onset, growth, maximum biomass, and bloom termination of the modelled ice algae have been adjusted to produce good agreement with observations. In this section, key parameters associated with over-wintering (pre-bloom) ice algal biomass, mortality, photosynthetic sensitivity, and nutrient limitation, are varied independently in order to determine the sensitivity of the simulated bloom.

The experiments testing photosynthetic efficiency (not shown) demonstrated that increasing photosynthetic efficiency does not increase the maximum biomass substantially, because of nutrient limitation. The experiments varying the ratio of intracellular silicate to nitrogen (also not shown) indicated that increasing the intracellular ratio Si/N ratio by $\sim$ 20% was enough for the ice algal growth to become silicate-limited instead of nitrogen-limited.

Pre-bloom algal biomass in the ice

In previous modelling, pre-bloom ice algal biomass has been estimated based on water column measurements during ice formation (Steiner et al., 2016), or from early bloom measurements (Lavoie et al., 2005; Pogson et al., 2011). It is possible that processes involved in ice formation can preferentially pick up marine particles, such as algal cells, and ice algal biomass concentrations up to 2 orders of magnitude higher than the underlying water column have been observed in sea ice in fall and winter (Różańska et al., 2008; Niemi et al., 2011).

The year-to-year variability in the amount of ice algae before the bloom may have a strong effect on the timing of the bloom onset. The timing of the onset of the simulated ice algal bloom (defined as when biomass exceeds 100 mg Chl a m^{-3}) depends on the pre-bloom, or over-wintering, concentration (Figure 2.10b). The pre-bloom concentration is implemented in the model as a minimum ice algal biomass. In the standard run, the pre-bloom concentration was set at 1 mmol N m^{-3} (or 3.533

mg Chl a m^{-3}) to match the observed bloom onset. This value is approximately 20% of the value used in Lavoie et al. (2009) of 0.5 mg Chl a m^{-2} (16.7 mg Chl a m^{-3}, assuming a 3 cm ice algal layer). This value was set for the more productive Beaufort Sea, but is an order of magnitude larger than that observed by Niemi et al. (2011) (0.1 mg Chl a m^{-3} for first-year ice in the Beaufort Sea). Because of the large difference between these estimates of the pre-bloom concentration, the simulation was run with pre-bloom concentrations at 200%, 150%, 50%, and 10% of the standard value in order to test the importance of this value for the onset and maximum concentration of the ice algal bloom. With pre-bloom concentrations of 50% (200%) of the standard value, the subsequent ice algal blooms are slightly later (earlier), with the biomass reaching 100 mg Chl a m^{-3} approximately 4 days later (earlier). It is evident that a multiplicative change in the pre-bloom biomass results in an additive offset in the time needed to reach a specified biomass (consistent with exponential growth through the earlier parts of the bloom).

Modelled ice algal blooms for runs with the pre-bloom ice algal biomass values an order of magnitude larger or smaller than the standard value (Figure 2.10b) indicate that, at higher pre-bloom biomass, the bloom occurs earlier, but the maximum biomass is not much greater than in the standard run because the growth is terminated by nutrient limitation. When the pre-bloom ice algal biomass is one-tenth of that in the standard run, the timing of the bloom onset is delayed and the bloom levels off (at the time of the maximum biomass in the standard run). This is because the NO_3 limitation in that time period is approximately 0.2 day^{-1} (not shown). In an idealized 12 hour day, and no other limitation, the daily averaged minimum limitation would be half of that (0.1 day^{-1}), which is roughly equal to the grazing rate.

These results are in agreement with those of Jin et al. (2006), who found that doubling the initial ice algal biomass does not affect the maximum biomass of the bloom, and results in an onset 3 – 5 days earlier. In addition, Pogson et al. (2011) found that using the observed low initial biomass under high snow cover caused underestimation of the simulated maximum biomass compared to observations.

Mortality

Mortality rate of marine algae is commonly parameterized as some combination of linear and quadratic terms. To our knowledge mortality rates have not been directly measured for ice algae and the contribution of linear and quadratic contributions

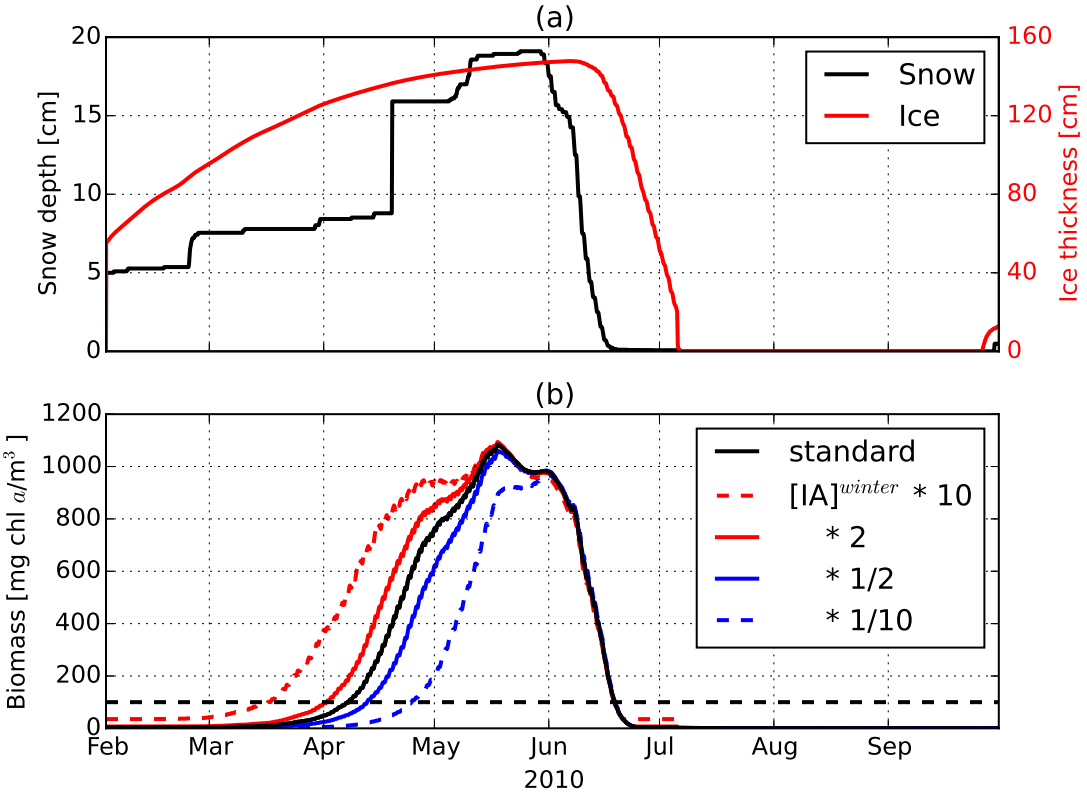

Figure 2.10: (a) Snow and ice thickness (cm). (b) Ice algal biomass with varying pre-bloom biomass. Pre-bloom biomass is set to 10, 2, 1/2, and 1/10 times that in the standard simulation (solid black line).

needs to be tested. Here, the mortality rate for ice algae (M; Appendix A.1.2) is defined as a function of biomass:

$$M = m_{lia} \exp(b_{ia}[T]_{ia}) + m_{qia}[IA] \tag{2.1}$$

where b_{ia}, $[T]_{ia}$, and $[IA]$ represent the temperature sensitivity coefficient, temperature in the ice skeletal layer, and ice algal biomass, respectively (see the Appendix for details). m_{lia} represents the rate constant for the temperature-dependent linear mortality and m_{qia} is the rate constant for the quadratic mortality. The linear term represents ice algal biomass-independent processes, in which a specified fraction of the population is lost per unit time. Lavoie et al. (2005) defined this term as the grazing rate on ice algae, and prescribed it at 10% of the growth rate. The quadratic term represents crowding effects, in that the fraction of biomass lost per unit time increases with higher biomass. (Although the quadratic formulation is a commonly used approach to representing the crowding effect of large phytoplankton cells (i.e., diatoms) in marine ecosystem models (e.g., Steiner et al., 2006; Aumont et al., 2015), we do not implement it in the case of small phytoplankton because they do not reach high enough densities.) Based on model tuning to match observations, m_{lia} and m_{qia} are respectively set to 0.03 d^{-1} and 0.00015 (mmol C m^{-3})$^{-1}$ d^{-1} in the standard run. As the simulated bloom grows, the population will have a quasi-exponential growth if the linear contribution to mortality varies slowly with time, and the biomass is small enough that the quadratic contribution to mortality is small.

Figure 2.11b presents the standard run along with multiple runs in which the linear and quadratic mortality parameters have been increased or decreased. As expected, when both parameters are increased (decreased), the simulated ice algae has a lower (higher) maximum biomass than the standard run. When the two are changed in opposite directions, the magnitude of the maximum biomass does not vary substantially, but the onset timing is earlier or later. In Figure 2.11c, the red box from Figure 2.11b is enlarged in order to show when the simulated ice algal bloom crosses the 100 mg Chl a m^{-3} threshold. With a 25% decrease (increase) to this parameter, the bloom reaches the 100 mg Chl a m^{-3} threshold 2 days earlier (later).

Dashed lines correspond to simulations in which the linear and quadratic mortality parameters have been changed in the same way. These different runs cross the 100 mg Chl a m^{-3} threshold at almost the same time, indicating that the bloom onset (when ice algal biomass is small) is relatively insensitive to the quadratic mortality term.

Therefore, these two mortality parameters can be adjusted to best fit observations for the timing of the bloom onset and magnitude of maximum biomass.

2.5 Discussion

The recent model study by Abraham et al. (2015) showed that grid-cell mean simulations of light and heat fluxes through sea ice could be improved by parameterizing the subgrid-scale snow depth variability, relative to simulations with spatially uniform snow depth distribution. These authors pointed out the need to examine biological responses to this new parameterization. In the first part of the present study, we investigated the impact of the new parameterization on simulated ice algae. The results indicate an improvement in simulating the ice algal bloom especially during the melt period, owing to an improvement in simulating the gradual increase in light availability to the ice algae. However, in this study, we are unable to further assess the impact of the new light parameterization on earlier stages of the bloom because the observed time series of ice algal biomass are confined mostly to the decline phase of the bloom. Measurements focusing on ice algal biomass during the onset and early growth of blooms are needed for assessing this impact.

As discussed in Arrigo (2014), the presence of ice algae affects several important processes in the underlying water column ecosystem. However, it is logistically difficult to isolate the contribution of ice algae from that of phytoplankton in terms of observed nutrient drawdown and biomass production. It is similarly difficult to observationally assess the seeding of the phytoplankton bloom by ice algae. Hence, process models become important tools to address questions like: *What if ice algae were excluded from a given environment?* In particular, the absence of advective processes in 1-D models allows focus on the *in situ* sympagic-pelagic ecosystem coupling. The present analysis demonstrated some of the influences of ice algae on the pelagic ecosystem. The results indicate that both the timing and magnitude of the simulated under-ice phytoplankton bloom are affected by the presence of ice algae. The timing of the bloom is affected due to seeding as a result of ice algal flushing, whereas the magnitude is affected due to the nutrient drawdown by the earlier ice algal bloom. These impacts of ice algae further influence other important biogeochemical processes, such as the production of dimethylsulfide (Chapter 3). Previous model studies also indicated the timing and magnitude of the ice-associated pelagic bloom as an important response to ice algal seeding Jin et al. (2007); Tedesco et al. (2012). However

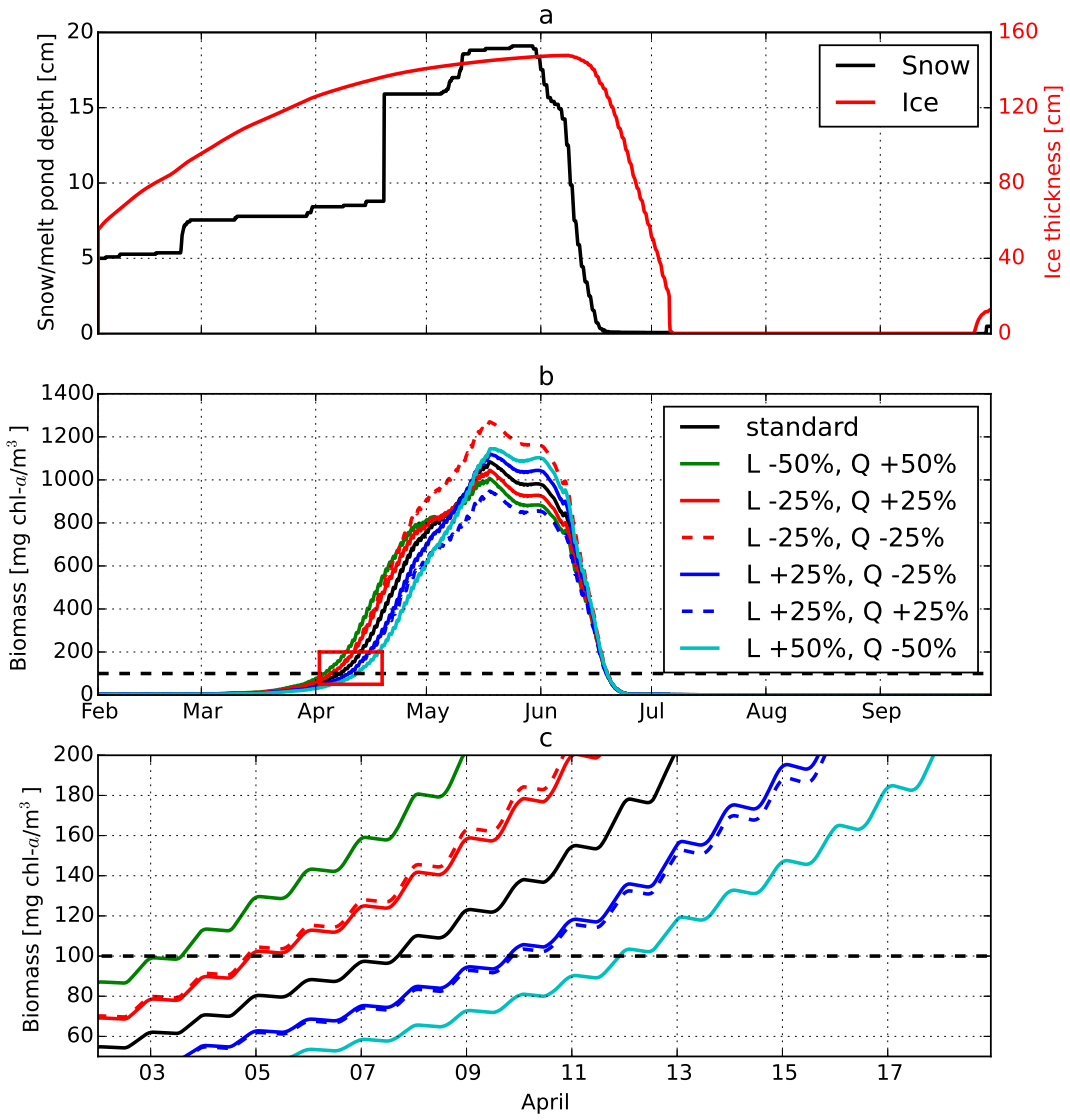

Figure 2.11: Snow and ice thickness, and ice algal biomass for varying mortality functions. (a) Snow and ice thickness (cm). (b) Ice algal biomass (mg Chl a m^{-3}) for different linear and quadratic mortality coefficients. The black solid line in (b) is the standard run, the dashed red (blue) line is the simulated bloom with both linear and quadratic dependencies decreased (increased) by 25%. The solid colored lines are for blooms with linear and quadratic dependencies changed in opposite directions, e.g., increased for linear and decreased for quadratic. The onset of the bloom in the red box in (b) is expanded in (c).

Jin et al. (2007) highlighted the importance of stratification, suggesting that sudden mixing events following ice melt would disrupt the ice-associated pelagic bloom. More quantitative estimates of the effects of ice algae on the underlying ecosystem can be achieved by conducting simulations (including the exclusion run) in a full 3-D model using the parameterizations considered in this study. Deal et al. (2011) and Jin et al. (2012) 3-D model applications highlight both high regional variability as well as the seasonal importance of ice algal primary production.

The model applies several simplified assumptions due to lack of observations in the ice. For instance, the simulated ice algal nitrogen uptake preference (p^{ia}_{no3} in Equation A.25) is constant throughout the simulation. However, Harrison et al. (1990) observed that nitrogen utilization by ice algal communities in Barrow Strait shifted from a nitrate- to an ammonium-dominated metabolism. In addition, the nitrification (NH_4 oxidation to NO_3) rate in sea ice is set to a constant rate, but actually varies with environmental conditions (Fripiat et al., 2014).

In both the modelled ice and water column, nutrient depletion due to phytoplankton uptake leads to near-zero concentrations of the limiting nutrient. Observations of post-bloom nutrient concentrations in an area with little horizontal transport could allow assessment of this result. The influence of horizontal advection on the nutrient drawdown below the ice could be assessed in 3-D model simulations.

The model results indicate that a combination of linear and quadratic mortality terms is required to adequately represent the development and decline of the ice algal bloom. The application of a quadratic mortality term implies a larger specific mortality at higher ice algal concentrations, representing lysis due to viral infection and other overcrowding processes that occur at higher ice algal concentrations. Additional field observations during the height of the bloom could help to constrain this term.

In the standard simulation, the growth of ice algae was initially limited by light, and then by nutrients (nitrate) during the peak and the decline of the bloom, which is consistent with the findings of previous studies (Mundy et al., 2014). The simulated under-ice bloom was similar to the observed bloom in terms of the magnitude, timing, and the species composition (dominated by diatoms, Galindo et al. (2014)). During the ice-free period, the simulated under-ice bloom was succeeded by the formation of a subsurface chlorophyll maximum. While this is a common feature in low-nutrient Arctic waters, observations are lacking for this particular time and location. It is possible that high tidal mixing could prevent a deep chlorophyll maximum from developing in particular regions.

The parameters were adjusted to this specific dataset (particular year, particular place). Applications for different years and locations, and subsequent implementation in a 3-D model, will indicate if some retuning may be necessary. A need for retuning would hint at processes that are incompletely understood and indicate whether further measurements to constrain the process are required.

2.6 Conclusions

This 1-D study is intended as a step in the development of a 3-D model, one of a growing number that incorporate biogeochemical processes in order to represent the sympagic ecosystem and its coupling to the underlying pelagic ecosystem.

In order to establish a set of parameterizations which can be transferred into a 3-D regional Arctic model which couples sea-ice, ocean and associated ecosystems, this 1-D model study investigates the physical and biological controls on sympagic and pelagic primary production using observations from Resolute Passage. Results of the standard simulation, including a snow distribution function allowing for a slow evolution towards bare ice and melt ponds, were generally in good agreement with the variability of snow/melt pond depths, ice thickness, under-ice PAR, and bottom-ice and seawater Chl *a* observed during the melt season in 2010. The simulated ice algal and under-ice phytoplankton blooms in the standard run were in reasonable agreement with the observations in terms of timing and magnitude.

Several findings can be taken from the sensitivity analyses. (1) Ice algal growth limits subsequent pelagic biomass in the upper water column by removing nutrients and limiting their availability to the phytoplankton, with a decrease of $\sim 50\%$ of the maximum phytoplankton concentration in the upper 10 m in the standard run relative to the run without ice algae. (2) Photosynthetic sensitivity and pre-bloom biomass determine the onset timing of the ice algal bloom. (3) The maximum biomass is relatively insensitive to the pre-bloom ice algal biomass. (4) A combination of linear and quadratic parameterizations of mortality rate is required to adequately simulate the evolution of the ice algal bloom, indicating that processes associated with each of these functional forms are occurring within the ice algal bloom phase. And (5), a large detrital (D2) sinking rate greater than a threshold of ~ 10 m d^{-1} effectively strips the upper water column of the potential to regenerate the limiting nutrient after the bloom by transporting it to depth. For this scenario a deep chlorophyll maximum develops, as is characteristic for low nutrient Arctic waters. A D2 sinking rate slower

than this threshold allows for a subsequent subsurface P1 bloom due to availability of ammonium (from detrital remineralization) after the initial (P2 dominated) pelagic bloom.

Measurements needed to better constrain the simulated ice algal bloom include ice algal concentration in winter, in situ mortality rate, and sinking rates for ice algal aggregates. This 1-D study is part of two subsequent 1-D studies, implementing sulfur (dimethyl sulfide, or DMS) and inorganic carbon cycles. The work in all three of these studies will be used as a basis for the implementation of ice algae, DMS, and carbon cycles into a 3-D coupled ice-ocean biogeochemical regional model of the Arctic Ocean.

Chapter 3

Implications of sea-ice biogeochemistry for oceanic production and emissions of dimethylsulfide in the Arctic

The following chapter is a manuscript published as:

Hayashida, H., Steiner, N., Monahan, A., Galindo, V., Lizotte, M., and Levasseur, M. (2017): Implications of sea-ice biogeochemistry for oceanic production and emissions of dimethyl sulfide in the Arctic, Biogeosciences, 14, 3129-3155, https://doi.org/10.5194/bg-14-3129-2017

The manuscript is repeated here with some adjustments to fit the format of the dissertation.

3.1 Abstract

Sea ice represents an additional oceanic source of the climatically active gas dimethylsulfide (DMS) to the Arctic atmosphere. To what extent this source contributes to the dynamics of summertime Arctic clouds is not known due to scarcity of field measurements. In this study, we developed a coupled sea ice-ocean ecosystem-sulfur cycle model to investigate the potential impact of bottom-ice DMS and its precursor

dimethylsulfoniopropionate (DMSP) on the oceanic production and emissions of DMS in the Arctic. The results of the 1-D model simulation were compared with field data collected during May and June of 2010 in Resolute Passage. Our results reproduced the accumulation of DMS and DMSP in the bottom ice during the development of an ice algal bloom. The release of these sulfur species took place predominantly during the earlier phase of the melt period, resulting in an increase in DMS and DMSP concentration in the underlying water column prior to the onset of an under-ice phytoplankton bloom. Production and removal rates by processes considered in the model are analyzed to identify the processes dominating the budgets of DMS and DMSP both in the bottom ice and the underlying water column. When openings in the ice were taken into account, the simulated sea-air DMS flux during the melt period was dominated by episodic spikes of up to 8.1 μmol m^{-2} d^{-1}. Further model simulations were conducted to assess the effects of the incorporation of sea-ice biogeochemistry on DMS production and emissions, as well as the sensitivity of our results to changes of uncertain model parameters of the sea-ice sulfur cycle. The results highlight the importance of taking into account both the sea-ice sulfur cycle and ecosystem in the estimates of DMS flux near ice margins and identify key uncertainties in processes and rates that should be better constrained by new observations.

3.2 Introduction

Dimethylsulfide (DMS) is a volatile biogenic compound that is produced primarily through ecological interactions in marine microbial food webs (Simó, 2001). Oceanic emissions of DMS are the largest natural source of sulfur in the atmosphere (Bates et al., 1992), thereby playing a crucial role in global sulfur cycling. Oceanic DMS emissions can play an important role in climate because oxidation products of DMS produce atmospheric aerosols and cloud condensation nuclei (CCN), therefore contributing to radiative forcing (Shaw, 1983). In 1987, Charlson et al. hypothesized that enhanced oceanic DMS emissions due to global warming could produce a negative feedback via increased scattering of incoming shortwave radiation by DMS-derived aerosols and CCN. Although this climate regulation by oceanic DMS emissions has been suggested to be of minor importance at global scale (Quinn and Bates, 2011), oceanic DMS emissions could still exert a significant influence on local climate in certain regions, such as the Arctic (Chang et al., 2011b; Levasseur, 2013).

During the mid-spring and summer (May-August), the Arctic atmosphere becomes

relatively free of anthropogenic aerosols due to increased wet deposition and decreased transport from lower latitudes (Croft et al., 2016). At the same time, concentrations of methanesulfonic acid (MSA), an oxidation product of DMS, have been observed to increase and peak at various locations north of 70° N (Sharma et al., 2012; Willis et al., 2016). The cleansing of the summertime Arctic atmosphere and the emergence of relatively high concentrations of MSA point towards oceanic DMS as the driver for the formation and growth of new particles (Sharma et al., 2012; Leaitch et al., 2013), along with other important biogenic sources of CCN, such as microgels (Orellana et al., 2011; Tjernström et al., 2014). Simultaneous measurements of sea surface and atmospheric DMS concentrations provide further evidence linking new particle formation events to oceanic DMS emissions (Chang et al., 2011b; Rempillo et al., 2011).

In addition to DMS produced within the water column, the presence of sea ice provides an additional source of oceanic DMS in the Arctic that can make a transient but potentially important contribution to the formation of sulfur-containing aerosols and clouds during the melt period (Levasseur et al., 1994; Levasseur, 2013; Mungall et al., 2016). Especially during spring (April-June), DMS and its precursor dimethylsulfoniopropionate (DMSP) can reach very high concentrations in the bottom layer of Arctic sea ice throughout the development of the ice algal bloom (Levasseur et al., 1994). Measurements of DMS and DMSP reveal concentrations in the bottom ice that are often 1 to 3 orders of magnitude larger than in the water column (Levasseur et al., 1994; Uzuka, 2003; Levasseur, 2013; Galindo et al., 2014, 2015). How much of this ice-related DMS eventually reaches the atmosphere is not known, but mechanisms have been suggested by which the DMS produced in the bottom ice supplies pulses of DMS into the pristine Arctic atmosphere during spring and therefore contributes significantly to the formation of new clouds in the Arctic (Levasseur et al., 1994). However, it is difficult in practice to measure the sea-air flux of DMS originating from the bottom ice alone and therefore to quantify the contribution of that flux relative to DMS produced within the water column. Process models can aid the understanding of the relevance of specific processes to the Arctic marine sulfur cycle as well as their likely spatio-temporal variability. To the best of our knowledge, only one previous study has incorporated the sea-ice sulfur cycle in model simulations (Elliott et al., 2012). This earlier study demonstrated that the DMS production in the bottom ice can supply a significant amount of DMS (exceeding 10 nmol L^{-1}) to the upper mixed layer at many locations in the Arctic Ocean. However, the importance

of the bottom-ice source relative to the production in the underlying water column was not assessed in this previous study, nor was an attempt made to provide the potential emissions to the atmosphere.

In the present study, we test the hypothesis that DMS and DMSP produced in the bottom ice can make a substantial contribution to marine production and emissions of DMS in the Arctic by developing a sulfur cycle module for the bottom ice and underlying water column. This module was embedded into a coupled sea ice-ocean ecosystem model to conduct various simulations which were compared to observations within landfast first-year ice in Resolute Passage during 2010.

3.3 Model description and experimental design

A sulfur cycle module for the bottom ice and the water column was developed and embedded into an existing coupled sea ice-ocean ecosystem model. The resulting coupled model was applied in a one-dimensional (1-D) configuration to conduct simulations of DMS and DMSP dynamics within and under the bottom layer of landfast first-year ice in Resolute Passage during 2010.

3.3.1 Ecosystem model

The coupled sea ice-ocean ecosystem model is described and evaluated in Chapter 2. In this earlier study, the model was used to study the physical and biological controls on the ice algal and under-ice phytoplankton blooms observed in Resolute Passage during the spring of 2010. The sea-ice component of the model is based on Lavoie et al. (2005) and consists of four prognostic variables including nitrate, ammonium, silicate, and ice algae. The model simulates the growth and decline of ice algae in the bottom layer of the sea ice, as well as the release of ice algae into the water column during the melt period. The oceanic component of the model is a ten-compartment (nitrate, ammonium, silicate, small and large phytoplankton, small and large zooplankton, small and large detritus, and particulate silica) lower-trophic level ecosystem model derived from Steiner et al. (2006). In the uppermost layer of the water column, the ocean ecosystem model is coupled to the sea-ice ecosystem model to represent the diffusive exchange of nutrients at the ice-water interface, as well as the release of living and dead ice algae into the water column as large phytoplankton and large detritus, respectively. The ecosystem dynamics are driven by physical pro-

cesses which are computed by a coupled sea ice-ocean physical model. The oceanic component of this model is the General Ocean Turbulence Model (GOTM), a public domain 1-D water column model (Burchard et al., 1999, 2006). Horizontal velocity fields, turbulent transports, photosynthetically active radiation (PAR), temperature, and salinity in the water column are simulated by GOTM and are provided for simulation of pelagic ecosystem and sulfur cycle dynamics. The sea-ice component is based on the 1-D thermodynamic model developed by Flato and Brown (1996), which consists of a single layer of snow and multi-layers of ice. In the present version, the model considers non-uniform snow thickness distributions and melt ponds, which improved the simulation of light fields under snow and sea ice (Abraham et al., 2015). Ice growth/melting rate, melt-pond areal fraction, and basal ice temperature are simulated by the sea ice model and are provided for simulation of bottom-ice ecosystem and sulfur cycle dynamics.

3.3.2 Sulfur cycle module

The ocean can be seen as an infinite reservoir of sulfur for the atmosphere, although its contribution to the atmospheric sulfur budget depends on how much of this reservoir can be converted into the volatile compound DMS. The structural design of the coupled sea ice-ocean sulfur cycle module developed in the present study was inspired mainly by two previous marine sulfur cycle models (Archer et al., 2004; Steiner and Denman, 2008). It should be emphasized that the sulfur cycle represented in this and earlier studies considers the cycling between DMSP and DMS only, and does not conserve total sulfur. However, total sulfur conservation is not a requirement because sulfur is not a limiting nutrient for primary producers and sea-air fluxes only depend on the concentration of DMS. Figure 3.1 shows the variables and processes represented in the model that are deemed most relevant for the production and removal of DMSP and DMS in the bottom ice and water column. DMSP in particulate (DMSPp) and dissolved (DMSPd) phases are simulated separately as they have distinct physical properties and ecological roles in sulfur cycling. For example, DMSPp released from the bottom ice is expected to sink quickly through the water column, whereas DMSPd likely remains in the under-ice meltwater lens upon its release from the bottom ice (Elliott et al., 2012; Galindo et al., 2014, 2015). Furthermore, only DMSPd can be assimilated by bacteria to produce DMS (Stefels et al., 2007). In the model, DMSPp is simulated diagnostically by assuming a fixed intracellular DMSP:Chlorophyll

a (Chl *a*) ratio for each of the simulated algal groups, while DMSPd and DMS are simulated prognostically. DMSPd is produced by cell lysis and exudation, and in the water column, by sloppy feeding, while it is removed by bacterial consumption and free DMSP-lyase. DMS is produced by bacterial DMSPd-to-DMS conversion and free DMSP-lyase, while it is removed by bacterial consumption, photolysis, and in open water conditions, by sea-to-air flux. Due to the absence of rate measurements within sea ice, most of the parameters prescribed for these simulated processes are taken from limited water column measurements (see Appendix A.2.1 for details). In the water column, all sulfur species are mixed between model layers with eddy diffusivities computed by the ocean physical model. At the ice-water interface, the sulfur species are coupled one way through the release of DMSP-containing ice algae, DMSPd, and DMS from the bottom ice into the uppermost layer of the water column. The concentrations of simulated sulfur species are computed at each model layer by a system of differential equations representing the budgets of these species, with parameterized expressions for the processes discussed above. A detailed description of the sulfur cycle module is presented in Appendix A.2.1. A detailed discussion of neglected physical and biogeochemical processes that may potentially be important to the sulfur cycle is presented in Section 3.4.3.

3.3.3 Study site

The focus of this study is landfast first-year ice in Resolute Passage, Nunavut, Canada. This site was chosen because of the availability of extensive datasets from previous field studies on ice-associated ecosystems and biogeochemistry (e.g. Smith, 1988; Levasseur et al., 1994; Lavoie et al., 2005; Michel et al., 2006; Mundy et al., 2014), including time series of sea-ice DMSP measurements (Galindo et al., 2014, see below). Furthermore, situated in the central Canadian Arctic Archipelago, Resolute Passage is representative of Arctic continental shelves which constitute more than 50 % of the total area of the Arctic Ocean (Jakobsson et al., 2003) and represent more than 80 % of the total primary production of the Arctic Ocean (Sakshaug, 2004). The landfast first-year ice found in Resolute Passage can reach a thickness of more than 2 m (e.g. Flato and Brown, 1996) and typically remains in the region until July (e.g. Galindo et al., 2014).

During May and June of 2010, measurements of DMSPp and DMSPd within and under the sea ice in Resolute Passage were carried out as part of a time-series ice

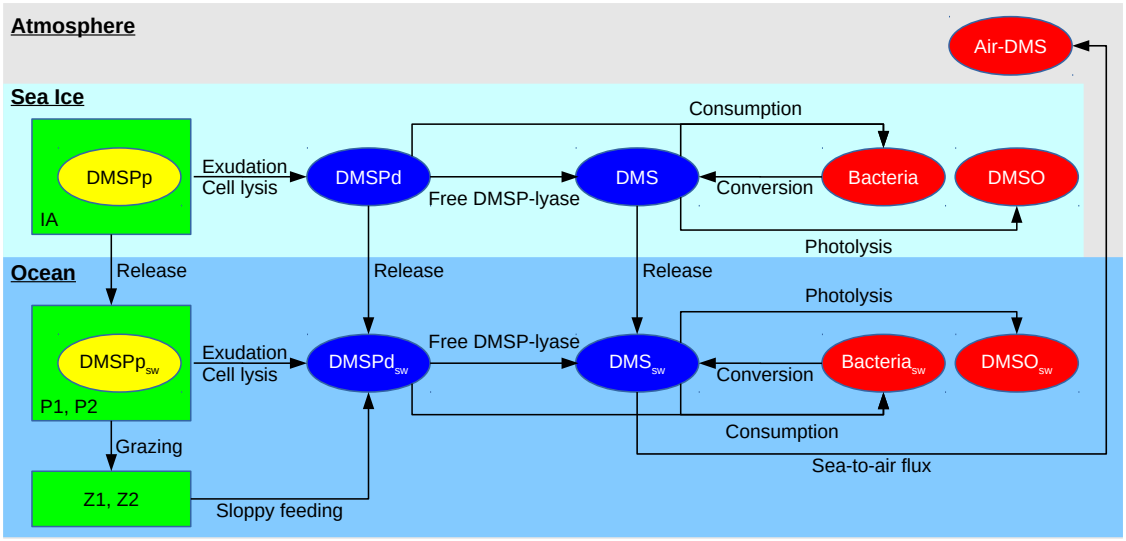

Figure 3.1: Schematic of the sea-ice and water column components of the sulfur cycle module. Variables in blue (yellow) are simulated prognostically (diagnostically), while the variables in red are not simulated but the relevant processes are parameterized. Variables in green are simulated prognostically by the ecosystem model. Arrows represent the physical and biogeochemical fluxes parameterized in the module.

study called the Arctic Ice-Covered-Ecosystem (Arctic-ICE) project (Galindo et al., 2014). As the sampling was done at a single location, it was deemed ideal to test our 1-D model for this Arctic-ICE 2010 study. Data from this field campaign were used to calibrate the parameters of the sulfur cycle module and evaluate the results of model simulations.

3.3.4 Model setup

The model developed in this study was applied to the study site of the Arctic-ICE 2010 field campaign (74°42.6' N and 95°15' W; Galindo et al., 2014). The vertical domain of the model was divided into 10 uniformly spaced layers for the sea ice and 100 uniformly spaced layers for the upper 100 m of the water column (the actual depth of the water column of the study site was 141 m; Galindo et al., 2014). The model was integrated with a time step of 10 minutes from 1 February to 6 July, 2010. At the surface, the model was forced with Environment Canada's hourly weather data (including surface 2-m air temperature, zonal and meridional wind speed at 10 m above the sea surface, surface air pressure, relative humidity, cloud cover, and precipitation; http://climate.weather.gc.ca/) collected at Resolute airport, which is located within 7 km of the study site. A meteorological station deployed at the study site only provided limited coverage (May and June) and a limited set of variables (air temperature and irradiance), however, 2 m air temperature measured at the airport (Fig. S1) compares well with the time series collected at the meteorological station (Fig. 2a of Mundy et al., 2014). Simulated temperature, salinity, and horizontal velocity fields were restored over the entire water column to the output of a simulation from a coupled 3-D regional sea ice-ocean circulation model (NEMO-LIM2; Dukhovskoy et al., 2016, and references therein) with restoring timescales of 1 day for temperature and salinity, and 10 minutes for horizontal velocity fields. Initial snow and melt pond depths and ice thickness set respectively to 5, 0, and 55 cm, result in simulations of these variables in good agreement with the measurements from the Arctic-ICE 2010 field campaign. Similarly, to simulate an ice algae bloom comparable to that in the the Arctic-ICE 2010 study, the initial biomass of ice algae was set to 3.5 μg Chl a L^{-1}. Although this value may seem high, previous studies report a wide range of Chl a concentrations in young sea ice (0.3-26.8 μg Chl a L^{-1}) that is often much higher than concentrations in the water column (e.g. Garrison et al., 1983). The thickness of the bottom-ice skeletal layer (in which the ecosystem and sulfur processes take place) was set to

3 cm and matches the vertical sampling resolution of Galindo et al. (2014). The initial concentrations of nitrate and silicate in the bottom ice and water column were respectively set to 7.2 μmol N L^{-1} and 14.7 μmol Si L^{-1}, based on measurements at the beginning of the Arctic-ICE 2010 field campaign (Mundy et al., 2014). The initial concentrations of ammonium in the bottom ice and water column, as well as the remaining ocean ecosystem model variables were set to 0.01 μmol N L^{-1} (μmol Si L^{-1} for particulate silica). The initial concentrations of DMSPd and DMS were assumed to be small, and were set to 0.1 nmol S L^{-1} in the bottom ice and water column.

3.3.5 Model experiments

Two types of model simulations were conducted in this study: standard and sensitivity runs. The standard run was designed to simulate the observed variability of physical and biogeochemical variables during the Arctic-ICE 2010 field campaign. Specifically, the performance of the standard run was evaluated by directly comparing the simulated results with the observed time series of snow and melt pond depths, ice thickness, Chl *a*, DMSPp and DMSPd in the bottom ice and upper water column. The default values of the sulfur cycle model parameters (Table 3.1) were calibrated to match the observations, starting from initial guesses based on both previous model studies and available field measurements in Arctic waters (see Appendix A.2.1).

Three types of sensitivity runs were designed to assess the impact of sea-ice biogeochemistry on the production and emissions of DMS under the ice. The first experiment evaluated the changes in the simulated under-ice DMSPd and DMS concentrations due to the presence or absence of sea-ice biogeochemistry. The second experiment explored the model uncertainty resulting from uncertainties in the parameters of the sea-ice sulfur cycle. The third experiment quantified the potential sea-air fluxes of DMS through openings in the ice during the melt period and the relative contributions of the sea-ice sulfur cycle and ecosystem to those fluxes. Details of the sensitivity runs are described in Section 3.4.2.

3.4 Results and discussions

3.4.1 Standard run

Snow, melt ponds, and sea ice

Figure 3.2a shows the simulated and observed time series of snow and melt pond depths and ice thickness. It is important to note that our model allows for subgrid-scale snow depth variability (Abraham et al., 2015), hence the simulated results are intended to represent an areal average over the study site (as would be the case for an individual grid cell in a global or regional model). Because the observations were taken at multiple locations with different snow depths on most days, the mean of these observations can be directly compared with the simulated results. During the winter and spring, the simulated snow depth increased as a result of occasional snowfall events until it reached about 20 cm in mid-May (black solid line; Fig. 3.2a). Simulated snow started melting at the end of May, and had disappeared completely by mid-June. The simulated snow depth is close to the observed site-average snow depth (black dots; Fig. 3.2a). The resulting melt water from the simulated snow contributed to the formation of simulated melt ponds that reached a mean depth of about 2 cm in late June (black dashed line; Fig. 3.2a). The timing of simulated melt pond formation is reasonable as melt ponds with similar depths were observed during the last two days of sampling, as indicated by the negative values in the observed snow depth range. The simulated ice thickness increased gradually until it reached about 145 cm in early June (red line; Fig. 3.2a). Simulated ice melt started shortly after the initiation of snowmelt and was complete by early July. The observed range of ice thickness was small indicating its homogeneity over the study site (red vertical bars; Fig. 3.2a), and is comparable to the simulated values. Furthermore, the timing of the simulated ice disappearance is close to the timing of the ice breakup observed in the field (mid-July; Galindo et al., 2014). This indicates a dominance of thermodynamic processes which is expected for the region (Flato and Brown, 1996).

Ice algae and phytoplankton

Figure 3.2b shows the simulated and observed time series of ice algal biomass in the bottom 3 cm of the sea ice and phytoplankton biomass averaged over the upper 10 m of the water column. The simulated ice algal biomass increased gradually from late March and reached about 1100 μg Chl a L^{-1} by mid-May (black line; Fig. 3.2b). The

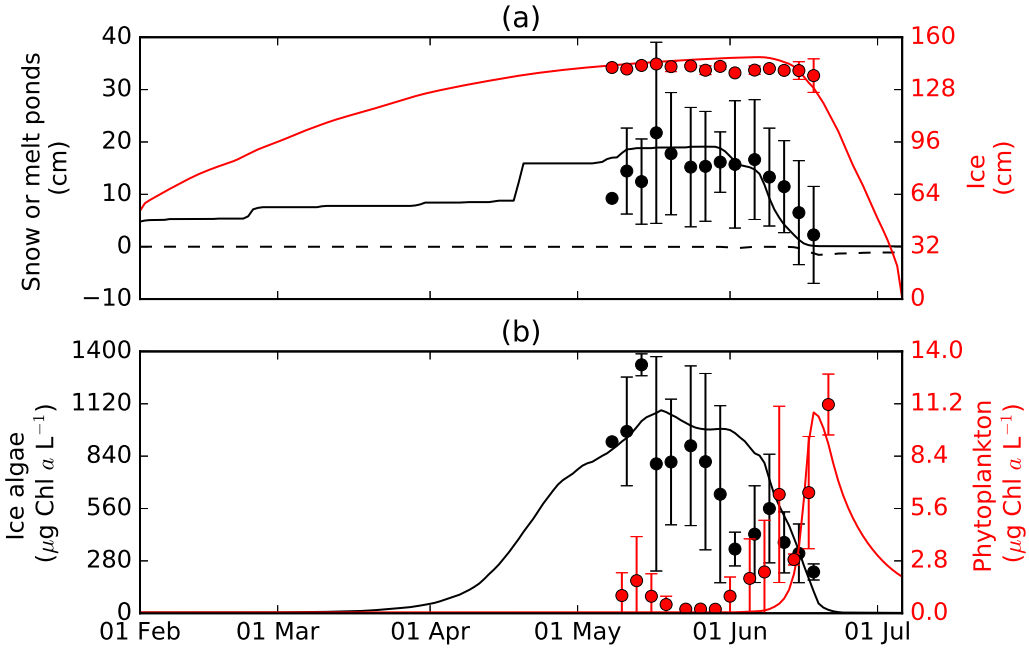

Figure 3.2: Simulated (lines) and observed (dots and bars) time series of (a) snow (black solid) and melt pond (black dashed) depths [cm] and ice thickness [cm] (red), and (b) ice algal biomass [μg Chl a l^{-1}] in the bottom 3 cm ice (black) and phytoplankton biomass [μg Chl a l^{-1}] averaged over the upper of the 10 m water column (red) in Resolute Passage during 2010. In (a), the negative values represent the depth of melt ponds. Also in (a), the observed values show the average (dots) and 1 standard deviation (vertical bars) of samples collected at three sites of high (>20 cm), medium (10-20 cm), and low (<10 cm) snow cover. In (b), the observed ice algal biomass shows the average (black dots) and 1 standard deviation (vertical bars) of samples collected in ice cores under high, medium, and low snow cover sites, while the observed phytoplankton biomass shows the average (red dots) with $\pm$ 1 standard deviation (vertical bars) of samples collected in seawater at 1.5, 2, 5, and 10 m depth. Note that the biomass for both ice algae and phytoplankton is expressed in terms of volumetric concentration. Hence, despite high concentrations in the sea ice, they are confined to a very small vertical range (3 cm) compared to those concentrations in the upper 10 m of the water column.

simulated ice algal biomass did not increase further due to nitrogen limitation and decreased rapidly due to release into the underlying water column associated with both flushing and basal melting during the melt period in June (Chapter 2). The simulated ice algal bloom terminated in late June, about two weeks prior to the simulated ice breakup (red line; Fig. 3.2a). Both the magnitude and temporal variations in the simulated ice algal bloom are generally comparable to the observations at the study site (black dots; Fig. 3.2a).

In the upper 10 m of the water column, the simulated phytoplankton biomass started increasing in early June and quickly reached a peak of about 11 μg Chl a L^{-1} in mid-June (red line; Fig. 3.2b). This simulated under-ice phytoplankton bloom was dominated by large cells and terminated due to nitrogen limitation (Chapter 2). These findings are consistent with observations that the bloom was numerically dominated by centric diatoms and led to the complete use of nitrate and nitrite (down to about 0.1 μmol L^{-1}) in the upper 10 m of the water column (Mundy et al., 2014). The timing and magnitude of the simulated under-ice phytoplankton bloom are generally comparable with the observations, except for those increases in the observed phytoplankton biomass during the first few sampling days in early May and during four sampling days in early June (red dots; Fig. 3.2b). Based on the bulk salinity measurements, Galindo et al. (2014) concluded that brine drainage was occurring prior to the snowmelt period, although the underlying mechanism for such an early occurrence is unknown. We speculate that the brine drainage was triggered by surface warming as seen by the presence of above-freezing air temperature between 15 and 18 May (Galindo et al., 2014). Nevertheless, the first model-observation mismatch in May was likely due to the release of ice algae by brine drainage, which was not simulated by our model. By contrast, the second mismatch in early June can not be explained by brine drainage, as the observed bulk salinity was fairly constant during this period (Galindo et al., 2014). Since this mismatch occurred during the snowmelt period, we hypothesize that the model might have underestimated the release due to flushing.

DMSPp, DMSPd, and DMS concentrations

Figure 3.3a shows the simulated and observed time series of the bottom-ice (3 cm) DMSPp concentration and the seawater DMSPp concentration averaged over the upper 10 m of the water column. The simulated DMSPp concentrations were determined

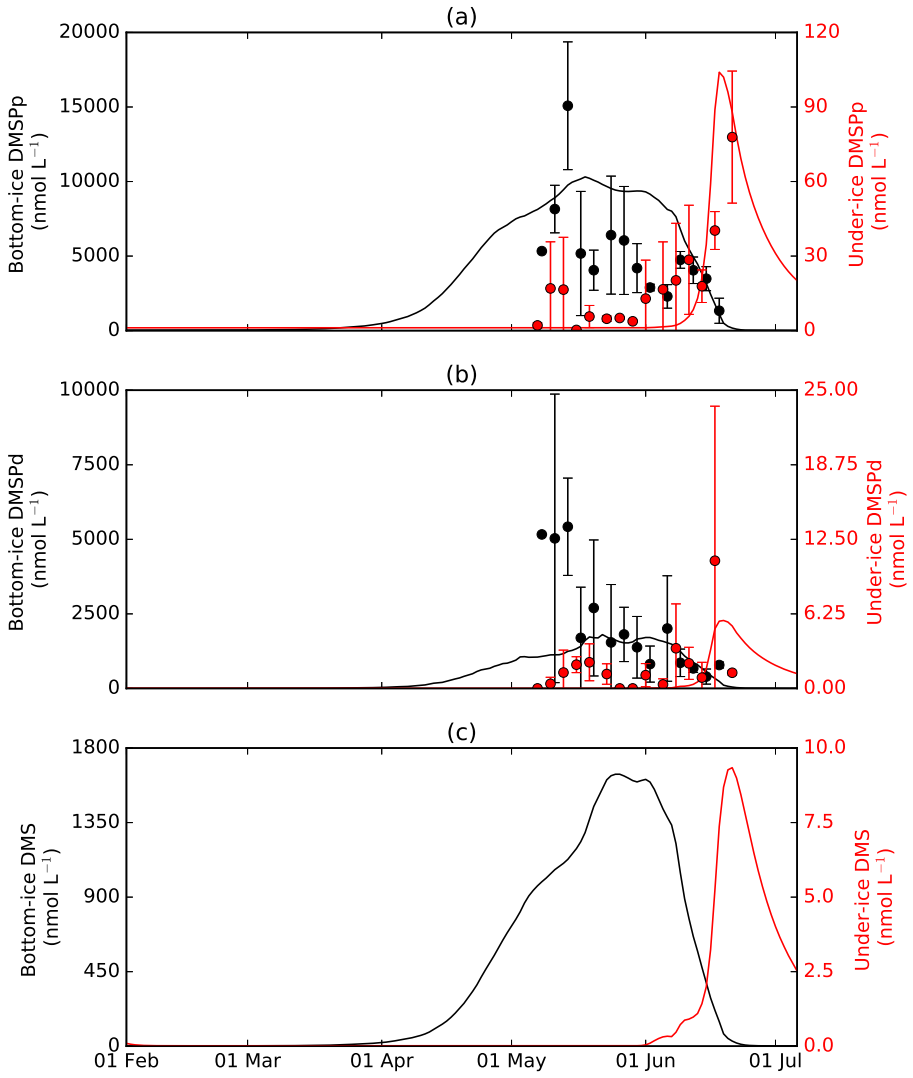

Figure 3.3: Simulated (lines) and observed (dots and bars) time series of (a) DMSPp, (b) DMSPd, and (c) DMS concentrations [nmol L^{-1}] in the bottom 3 cm ice (black) and averaged over the upper 10 m of the water column (red) in Resolute Passage during 2010. The observed bottom-ice values show the average (black dots) and 1 standard deviation (vertical bars) of samples collected in ice cores under high, medium, and low snow cover sites. The observed upper 10 m water column values show the average (red dots) with ± 1 standard deviation (vertical bars) of samples collected in seawater at 1.5, 2, 5, and 10 m depth.

by assuming fixed DMSPp-to-Chl *a* ratios, as the observations in Resolute Passage showed a strong linear relationship between DMSPp and Chl *a* concentrations both in the bottom ice and in the underlying water column ($r^2 = 0.9$; Galindo et al., 2014). In the standard run, these ratios were set to 9.5 nmol S:mg Chl *a* for ice algae and large phytoplankton, while the ratio of 100 nmol S:mg Chl *a* was prescribed for small phytoplankton (see Appendix A.2.1). Therefore, the temporal variability in simulated DMSPp in the bottom ice was identical to that of simulated ice algal biomass (black line; Fig. 3.2b). Similarly, in the absence of small phytoplankton, the temporal pattern of simulated DMSPp in the underlying water column follows closely that of simulated phytoplankton biomass dominated by large cells (red line; Fig. 3.2b). The simulated bottom-ice DMSPp concentration reached about 10^4 nmol L^{-1} at the peak of the simulated ice algal bloom in mid-May (black line; Fig. 3.3a). The observed bottom-ice DMSPp concentrations were highly variable during this period both spatially (vertical bars associated with black dots on each sampling day; Fig. 3.3a) and temporally (the range of black dots; Fig. 3.3a). The spatial variability likely reflects the patchiness of ice algae collected over sites of varying snow cover, while the temporal variability can be related to various stages of the ice algal bloom combined with the effect of brine drainage as discussed in the previous section. The simulated bottom-ice DMSPp concentrations were close to the site-average value observed on day 2, near the lower end of the observed range on day 3, and close to the upper end of the observed range on days 4, 6, and 7 of the sampling during May (black dots and associated vertical lines; Fig. 3.3a). During the melt period in June, the temporal variations in simulated bottom-ice DMSPp concentration closely followed the observed site-average values sampled on the last four days (black dots; Fig. 3.3a).

In the upper 10 m of the water column, the simulated seawater DMSPp concentration started increasing in June and peaked at about 100 nmol L^{-1} in mid-June (red line; Fig. 3.3a), coinciding with the simulated under-ice phytoplankton bloom (red line; Fig. 3.2b). The simulated values were close to the observed values throughout the sampling period except for days 2-3 and 9-12 (red dots; Fig. 3.3a). These mismatches are consistent with those found in the under-ice phytoplankton biomass time series, suggesting that they could be attributed to the lack of brine drainage effect (days 2-3) and a potentially underestimated effect of flushing in the model (days 9-12).

Figure 3.3b shows the simulated and observed time series of the bottom-ice DMSPd concentration and the seawater DMSPd concentration averaged over the upper

10 m of the water column. The simulated bottom-ice DMSPd concentrations gradually increased from early April to late May with a peak of about 1800 nmol L^{-1} (black line; Fig. 3.3b). During the melt period, the simulated bottom-ice DMSPd concentration decreased gradually and was near zero by late June. The simulated bottom-ice DMSPd closely followed the observed site-average values except for high values (about 5000 nmol L^{-1}) measured during the first three sampling days (black dots; Fig. 3.3b). Considering that brine drainage had occurred during these sampling days, it may have promoted the production of DMSPp and its conversion to DMSPd (and DMS) due to stress, which is not represented adequately in the model.

In the upper 10 m of the water column, the simulated DMSPd concentrations were near zero until the onset of the simulated under-ice bloom in June (red line; Fig. 3.2b). By contrast, the observed site-average DMSPd concentrations were above 1 nmol L^{-1} for four consecutive sampling days (from day 3 to 6) in May (red dots; Fig. 3.3b). This observed DMSPd increase prior to the melt period is consistent with the observed increases in under-ice Chl *a* and DMSPp, suggesting the influence of brine drainage (red dots on days 2 and 3; Fig. 3.3a). These increases in observed Chl *a*, DMSPp, and DMSPd in the upper 10 m of the water column gradually ceased and approached zero by the following sampling days (day 4 for DMSPp, day 5 for Chl *a*, and day 7 for DMSPd), which might be explained by a combination of the following two processes. First, some of ice algal cells and DMSPp released through brine drainage sank quickly into the water column. This argument is supported by a slight increase in observed Chl *a* and DMSPp at depths below 10 m on the following sampling days, and more prominently, by a larger increase in DMSPd at 50 m depth (ca. 1 nmol L^{-1}), which might suggest a degradation of DMSPp-containing ice algal cells (Figures 8 of Galindo et al., 2014). The other process contributing to the decreases in Chl *a*, DMSPp, and DMSPd in the upper 10 m of the water column could be the degradation of ice algal cells in the upper layer, which could explain the delay in the decrease in observed DMSPd relative to the decreases in Chl *a* and DMSPp.

In late June, the simulated DMSPd concentrations in the upper 10 m of the water column increased to about 6 nmol L^{-1} near the peak of simulated under-ice bloom (red line; Fig. 3.2b). This peak in simulated DMSPd was lower than the observed site-average value (about 11 nmol L^{-1}) from the second last sampling day. However, this observed site-average DMSPd value had a large standard deviation because a single high value (ca. 30 nmol L^{-1}) was measured at 1.5 m depth, while values measured deeper in the water column were much lower ($\leq$ 3 nmol L^{-1}). Given this observed

range, the simulated DMSPd peak is reasonable.

Figure 3.3c shows the simulated time series of the bottom-ice and the upper 10 m average of the water column DMS concentrations. The simulated bottom-ice DMS concentration increased gradually from April and reached about 1600 nmol L^{-1} in late May (black line; Fig. 3.3c). The timing of the simulated DMS peak lagged behind the simulated peaks of DMSPp and DMSPd by about one week. While no DMS observations were available to directly compare with the simulated DMS for this time period, the simulated DMS peak is close to the DMS concentration of 2000 nmol L^{-1} measured in the bottom ice in Resolute Passage at the end of the ice algal bloom in 2012 (Levasseur, 2013). The simulated bottom-ice DMS concentration remained close to its peak value until the beginning of June, then quickly decreased to near zero by late June.

In the upper 10 m of the water column, the simulated DMS concentrations increased gradually during early June and sharply during mid-June (red line; Fig. 3.3c). A few days after the simulated peaks of DMSPp and DMSPd in the upper water column, the simulated DMS reached its maximum value of about 9 nmol L^{-1} in late June. This peak value is within the range of surface seawater DMS concentration measured in the eastern Canadian Archipelago and Baffin Bay during July and August of 2014 (Mungall et al., 2016).

Production and removal rates of DMSPd and DMS

The variability of the simulated DMSPd and DMS concentrations is driven by a range of physical and biogeochemical processes that are generally not well constrained by observations. Reporting rates of processes simulated by the model will help interpret the observed features. Figure 3.4a shows the individual terms in the production and removal rates of simulated bottom-ice DMSPd. Prior to mid-May, simulated production rates by cell lysis and exudation increased to about 600 nmol L^{-1} d^{-1}, associated with the simulated ice algal bloom. However, the two rates differed twofold during the peak of simulated ice algal bloom. The production rate by cell lysis exceeded 1300 nmol L^{-1} d^{-1} as a result of increased ice algal biomass as well as nutrient stress in the bottom ice. On the other hand, the production rate by exudation remained around 600 nmol L^{-1} d^{-1} because its potential enhancement due to nutrient stress was offset by reduced primary production. The removal of simulated bottom-ice DMSPd was dominated by bacterial consumption, while the contributions of free DMSP-lyase and

release from bottom ice were minor. As parameterized in the model, the removal rate by bacterial consumption varied with the bottom-ice DMSPd concentration, and peaked at 1800 nmol L^{-1} d^{-1} in late May. Simulated removal rates by free DMSP-lyase were generally low, reaching up to 50 nmol L^{-1} d^{-1}) in late May. This value falls within the range observed in Antarctic sea ice brine samples (21-62 nmol L^{-1} d^{-1}; Asher et al., 2011). Simulated removal rates by release from bottom ice reached about 200 nmol L^{-1} d^{-1} during the melt period. We note that the simulated removal rates by bacterial consumption and free DMSP-lyase both have the same functional form (Appendix A.2.1), and therefore the differences in these rates were a straightforward consequence of choices of parameter values.

Figure 3.4b shows the production and removal rates of simulated DMSPd in the uppermost layer (0.5 m below the ice) of the water column. In early June, simulated production rates by release from bottom ice reached about 6 nmol L^{-1} d^{-1} and dominated the under-ice DMSPd budget, as other terms were relatively small due to low biological activity under the ice. During the simulated under-ice phytoplankton bloom in mid-June, both cell lysis and exudation made similar contributions (27-28 nmol L^{-1} d^{-1}) to the DMSPd production in the uppermost layer of the water column, with the peak in cell lysis lagging a few days behind the peak in exudation. Finally, the simulated DMSPd production rates by sloppy feeding were negligible (≤ 0.1 nmol L^{-1} d^{-1}) due to low zooplankton biomass during the melt period. No measurements of zooplankton biomass are available to observationally assess our simulated zooplankton biomass, although a previous study suggests high interannual variability in zooplankton biomass in Resolute Passage (Michel et al., 2006). The removal of simulated DMSPd in the uppermost layer of the water column was governed by bacterial consumption, which increased up to 35 nmol L^{-1} d^{-1} during the under-ice bloom. Simulated DMSPd removal rates by bacterial consumption were comparable to the rates measured under the ice in Resolute Passage during the melt period in 2012 (3 to 44 nmol L^{-1} d^{-1}; Galindo et al., 2015). Simulated DMSPd removal rates by free DMSP-lyase were negligible (below 1 nmol L^{-1} d^{-1}) in the uppermost layer of the water column throughout the simulation.

Figure 3.4c shows the production and removal rates of simulated bottom-ice DMS. The production of simulated bottom-ice DMS was dominated by bacterial DMSPd-to-DMS conversion, while the production by free DMSP-lyase was considerably less. The simulated DMS production rates by bacterial conversion were highest (about 350 nmol L^{-1} d^{-1}) during the peak of the ice algal bloom. Simulated DMS production

rates by free DMSP-lyase increased gradually with the accumulation of DMSPd in the bottom ice (black line; Fig. 3.3b), but remained below 50 nmol L^{-1} d^{-1} throughout the simulation. The removal of simulated DMS in the bottom ice was dominated by bacterial consumption, while photolysis and release from bottom ice became of comparable importance during the melt period. The simulated DMS removal rate by bacterial consumption reached about 325 nmol L^{-1} d^{-1} during the peak of ice algal bloom, balancing the DMS production by bacterial conversion. During the melt period, simulated DMS removal rates by bacterial consumption were reduced due to a decrease in DMSPd (black line; Fig. 3.3b), while the removal rates by photolysis and release from bottom ice briefly exceeded 50 nmol L^{-1} d^{-1}. The increase in simulated DMS removal rate by photolysis at the beginning of the melt period was caused by the increased light penetration through the ice. Despite the continuous melting of simulated snow and ice and the enhancement in light penetration, the removal rate by photolysis decreased sharply after its peak in early June due to the decrease in the bottom-ice DMS concentration (black line; Fig. 3.3c). In mid-June, the simulated DMS removal rate by release from bottom ice reached its peak. This peak value was comparable to the rates by other simulated processes at that time. Asher et al. (2011) measured gross DMS consumption rates in brine samples, which includes both rates of bacterial consumption and photolysis. Their reported values (57-250 nmol L^{-1} d^{-1}) are generally comparable to our simulated values, although the peak values are beyond their reported range.

Figure 3.4d shows the production and removal rates of simulated DMS in the uppermost layer of the water column. Similar to the simulated under-ice DMSPd budget, release from bottom ice dominated (>5 nmol L^{-1} d^{-1}) the under-ice DMS budget prior to the under-ice bloom (early June). During the same time period, the simulated DMS production rates by bacterial conversion were relatively low (0-1 nmol L^{-1} d^{-1}), which is consistent with the rates of 0-1.1 nmol L^{-1} d^{-1} measured in Resolute Passage during the initiation of the under-ice bloom in 2012 (Galindo et al., 2015). With the development of the under-ice boom, the simulated DMS production rates by bacterial conversion increased quickly and reached a peak of about 7 nmol L^{-1} d^{-1} in mid-June. Simulated DMS production by free DMSP-lyase had a negligible contribution (<0.2 nmol L^{-1} d^{-1}) throughout the simulation period, which is consistent with measurements in seawater samples collected under Antarctic sea ice (Asher et al., 2011). Removal of DMS in the uppermost layer of the water column was dominated by bacterial consumption which increased up to about 6 nmol

L^{-1} d^{-1} during the under-ice bloom. DMS removal by photolysis also increased during the same time period, but was relatively low (about 1 nmol L^{-1} d^{-1}). The combined removal rates by bacterial consumption and photolysis are comparable to the rate measured in seawater under Antarctic sea ice (Fig. 3 of Asher et al., 2011). Finally, it is important to note that, in the standard run, the loss of DMS by sea-to-air flux was prevented by the presence of ice, under the assumption that the surface was fully ice-covered throughout the simulation period. In Section 3.4.2, we will examine the effects of interstices in the ice on the simulated sea-to-air flux.

Due to the scarcity of rate measurements in ice-covered regions, it is challenging to evaluate the rates simulated by our model. Direct comparisons with rates that have been measured in sea ice brines and under-ice seawater samples (DMS conversion, bacterial DMSPd/DMS consumption, free DMSP-lyase) indicate that our simulated rates are in good agreement with the observed rates (Asher et al., 2011; Galindo et al., 2015). Certainly, further rate measurements in ice-covered regions will help build confidence in model-based estimates for production and removal rates of DMSPd and DMS within and under the sea ice. For simulated processes whose observed rates are not available, we find that the simulated rates in under-ice seawater (Figures 3.4b and d) are of the same order of magnitude as the observed rates in open-water environment (e.g. Galí and Simó, 2015), while the simulated rates in the bottom ice (Figures 3.4a and c) are a few orders of magnitude higher than those observed rates. Such results are expected for rates that are dependent on either DMSPd or DMS concentrations. For example, bacterial consumption rates and photolysis rates are generally known to follow Michaelis-Menten kinetics (Galí and Simó, 2015, and references therein), whose rates can be represented as a product of some rate constant and the DMSPd (DMS) concentration. Since all of these rate constants prescribed in our model are based on field measurements in open water environments (see Appendix A.2.1), the difference between the simulated rates in the bottom-ice/under-ice environment and the observed rates in the open-water environment reflects the difference in concentration, which differs by orders of magnitude.

3.4.2 Sensitivity runs

Incorporation of sea-ice biogeochemistry

In the standard run, we showed that the release of DMSPd and DMS from bottom ice dominated the DMSPd and DMS budgets in the underlying water column prior

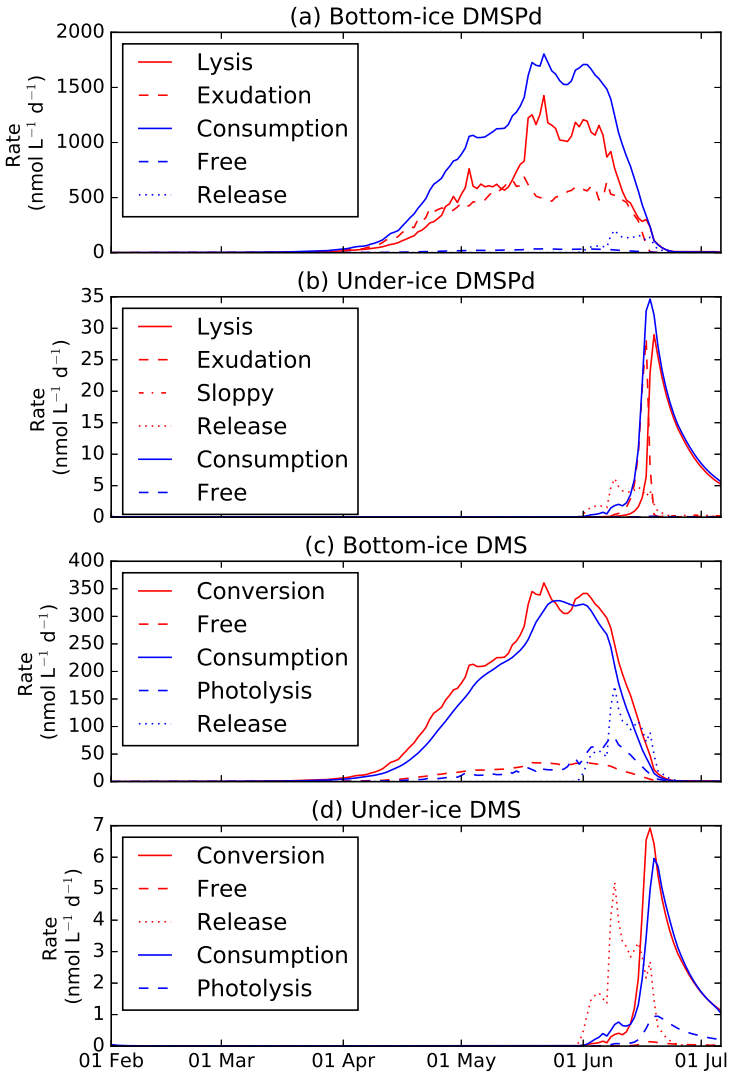

Figure 3.4: Simulated time series of daily mean production (red) and removal (blue) rates [nmol L^{-1} d^{-1}] of (a and b) DMSPd and (c and d) DMS (a and c) in the bottom 3 cm of ice and (b and d) in the uppermost layer (0.5 m below the ice) of the water column. In (a) and (b), the sources for DMSPd are cell lysis (Lysis; solid red), exudation (Exudation; dashed red), and sloppy feeding (Sloppy; dash-dot red in (b) only) while its sinks are bacterial DMSPd consumption (Consumption; solid blue) and free DMSP-lyase (Free; dashed blue). In (c) and (d), the sources for DMS are bacterial DMSPd-to-DMS conversion (Conversion; solid red) and free DMSP-lyase (Free; dashed red), while its sinks are bacterial DMS consumption (Consumption; solid blue) and photolysis (Photolysis; dashed blue). Release from the bottom ice (Release; dotted) is a sink for the bottom-ice DMSPd (a) and DMS (c), while it is a source for the under-ice DMSPd (b) and DMS (d).

to the onset of the under-ice phytoplankton bloom (Figs. 3.4b and 3.4d). To evaluate the changes in the simulated under-ice DMSPd and DMS concentrations due to this release, we conducted an additional simulation that excluded the sea-ice sulfur cycle module (NoIceSul; Fig. S2b). In other words, DMSPd and DMS in the bottom ice are not simulated in the NoIceSul run, and therefore there is no release of these sulfur compounds from the bottom ice during the melt period. It should be emphasized, however, that the sea-ice ecosystem module was still retained in this sensitivity run, hence the simulated ecosystem dynamics remained unchanged with respect to the standard run. The difference between the results of the standard and NoIceSul runs (i.e. Standard - NoIceSul; Fig. 3.5 and Table 3.2) thus represents the effect of the sea-ice sulfur cycle. As expected, the exclusion of the sea-ice sulfur cycle module resulted in a decrease in the under-ice DMSPd and DMS concentrations during most of the melt period (Fig. 3.5). The differences in these concentrations between the two runs were most evident from 1 June to 25 June, with peak differences of 0.5 (DMSPd) and 2.4 nmol L^{-1} (DMS) during the third week of June. Following 25 June, the concentration differences between the two runs became negligible, as the release from bottom ice declined toward the end of the melt period (Fig. 3.4). Over the simulation period, the incorporation of the sea-ice sulfur cycle resulted in 6 and 18 % increases in the respective under-ice DMSPd and DMS pools (Table 3.2). The increase in DMS was much greater than that of DMSPd because the rates of increase in the under-ice DMS due to the release from bottom ice were relatively high among the under-ice DMS budget terms. Rates of increase in under-ice DMSPd due to the release from bottom ice were smaller than the other under-ice DMSPd budget terms.

Besides the sea-ice sulfur cycle, it is possible that the incorporation of the sea-ice ecosystem itself can have an impact on the under-ice DMSPd and DMS concentrations (e.g. via changes in the nutrient availability in the surface ocean). To examine this possibility, we conducted an additional simulation that excluded the entire sea-ice biogeochemistry module (NoIceBgc; Fig. S2c), in which no release or uptake of any biogeochemical tracer from sea ice occurs. It is clear from Fig. 3.5 that the under-ice DMSPd and DMS concentrations simulated in the NoIceBgc run are much different from the results of the NoIceSul run, which implies a substantial contribution from the sea-ice ecosystem. In particular, the under-ice DMSPd and DMS concentrations in the NoIceBgc run were higher than the NoIceSul run from late June onward. The higher peaks in the under-ice DMSPd and DMS concentrations in the NoIceBgc run were associated with an under-ice phytoplankton bloom that was greater in magnitude

than the bloom in the standard or the NoIceSul run (Fig. 3.6a). In the standard run, the presence of ice algae resulted in reduced under-ice nitrate concentrations due to uptake by the sea-ice ecosystem (Fig. 3.6b). Consequently, the production rates of DMSPd and DMS associated with the under-ice phytoplankton bloom were higher, thereby yielding higher DMSPd and DMS concentrations under the ice in the NoIceBgc run.

On the other hand, prior to the under-ice bloom, the under-ice DMSPd and DMS concentrations were lower in the NoIceBgc run than in the standard run, because release of ice algal cells (Fig. 3.6c) that seed the under-ice bloom was absent (Fig. 3.6a). Our results therefore suggest that the incorporation of the sea-ice ecosystem promotes the under-ice DMSPd and DMS production by seeding the under-ice phytoplankton bloom, while it reduces the overall production by drawing down the available nutrients prior to the bloom. Over the simulation period, the incorporation of the sea-ice ecosystem resulted in a 16 % decrease in the under-ice DMS concentrations relative to the NoIceBgc run (Table 3.2). Note that although the shading effect of ice algae likely contributed to a delay in the under-ice bloom, an earlier onset of the bloom in the NoIceBgc run relative to the standard run (Fig. 3.6a) suggests that shading had less effec on the bloom than seeding. Furthermore, the effect of brine convection on nutrient dynamics (e.g. Vancoppenolle et al., 2010) was not taken into account in our model, which could further increase the difference between the standard and the NoIceBgc runs.

The results presented here suggest that the incorporation of sea-ice biogeochemistry (referring to both sea-ice sulfur cycle and ecosystem) has both direct and indirect effects on the under-ice DMSPd and DMS production. The direct effect is due to the incorporation of the sea-ice sulfur cycle, which increases under-ice DMSPd and DMS concentrations through the release of these sulfur species from the bottom ice. The indirect effect is due to the incorporation of sea-ice ecosystem which, depending on the phase of the under-ice phytoplankton bloom, increases or decreases the under-ice DMSPd and DMS concentrations. Over the simulation period, the incorporation of the sea-ice biogeochemistry resulted in a slight change (-1 %) in the under-ice DMS concentrations, as the direct and indirect effects nearly counteracted each other (Table 3.2). However, the transient increases prior to the under-ice bloom peak (up to 5.6 nmol L^{-1}) could still be a significant source of episodic sea-air flux of DMS. We will examine the effects of these increases in the under-ice DMS production on the flux in Section 3.4.2.

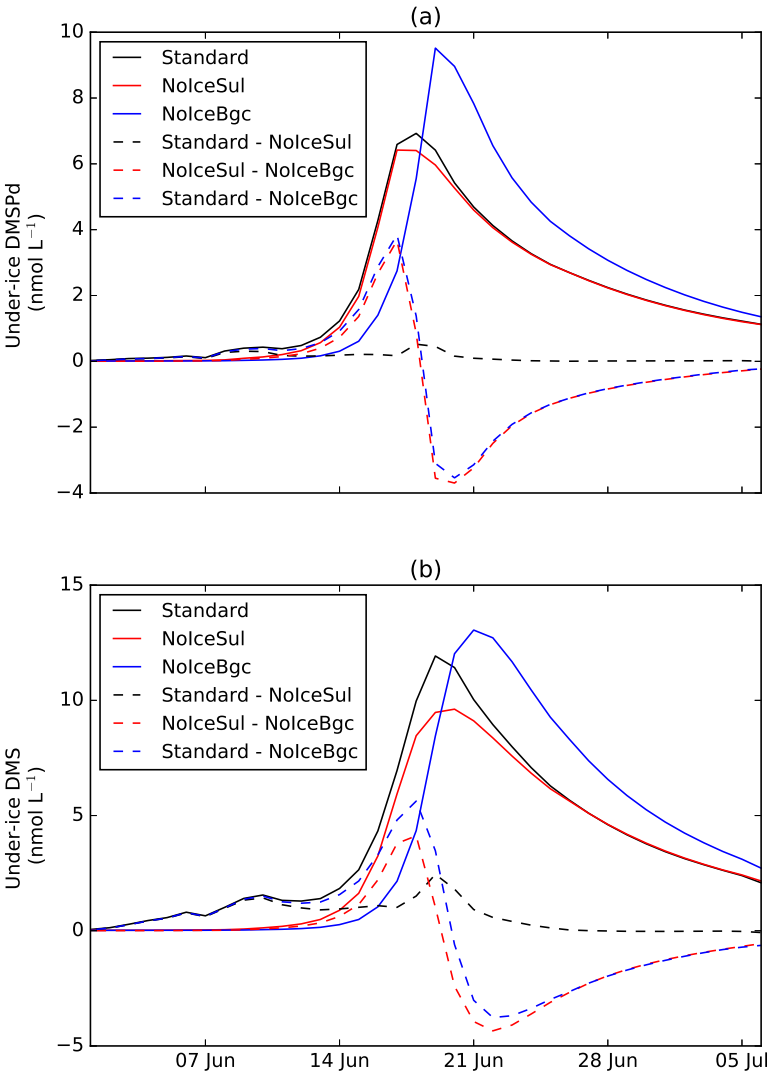

Figure 3.5: Simulated time series of (a) DMSPd and (b) DMS concentration [nmol L^{-1}] in the uppermost layer (0.5 m below the ice) of the water column during the melt period in 2010 for the standard run (Standard) and the sensitivity runs that exluded the sea-ice sulfur cycle (NoIceSul) and both the sea-ice sulfur cycle and ecosystem (NoIceBgc). Dashed lines represent the concentration difference between the two runs of interest. Positive differences represent enhancement in the concentration due to the incorporation of sea-ice sulfur cycle (Standard - NoIceSul), sea-ice ecosystem (NoIceBgc - NoIceSul), and both sea-ice sulfur cycle and ecosystem (Standard - NoIceBgc), respectively, while negative values represent reduction.

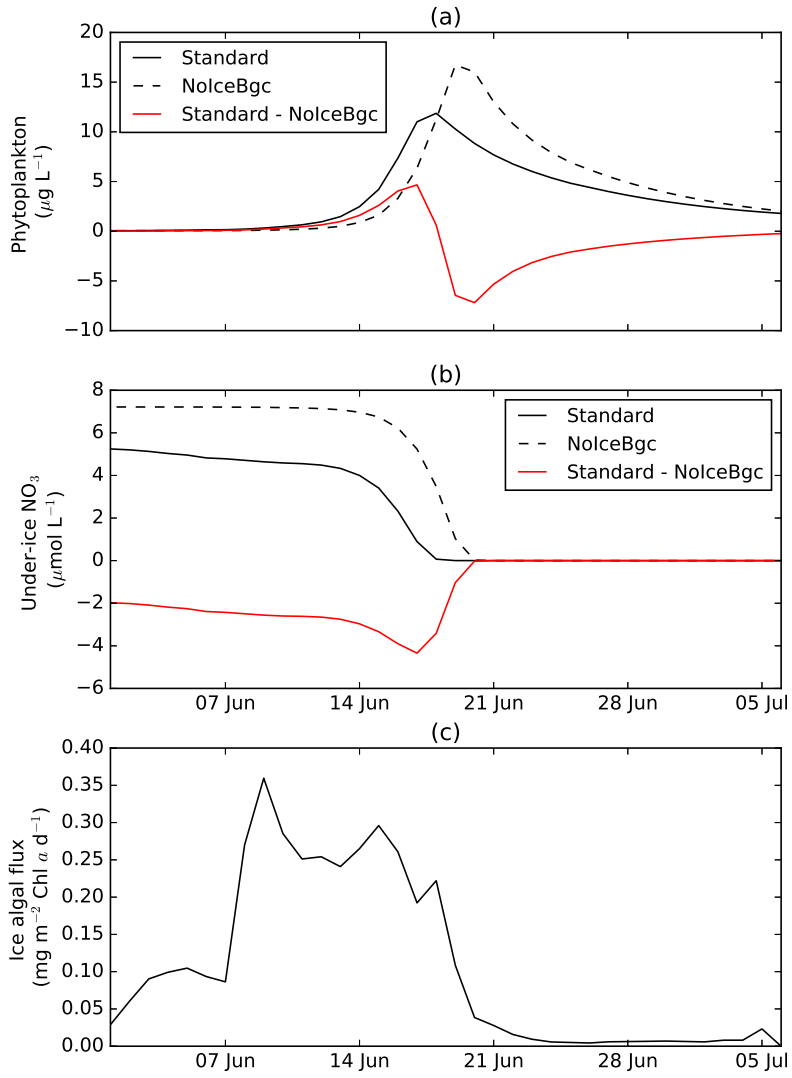

Figure 3.6: Simulated time series of (a) phytoplankton biomass [μg Chl a L^{-1}] and (b) nitrate concentration [μmol L^{-1}] in the uppermost layer (0.5 m below the ice) of the water column during the melt period in 2010 for the standard run (Standard) and the sensitivity run that exluded both the sea-ice sulfur cycle and ecosystem (NoIceBgc). (c) Ice algal flux [mg Chl a m^{-2} d^{-1}] entering the large phytoplankton pool in the uppermost layer of the water column. In (a) and (b), red lines represent the differences in phytoplankton biomass and nitrate concentration between the standard and sensitivity runs.

Parameter uncertainty

The results of the standard run are influenced by the choice of uncertain model parameters. The model parameters of the sea-ice sulfur cycle are especially poorly constrained due to the scarcity of rate measurements within sea ice (Stefels et al., 2012). Therefore, it is important to report the sensitivity of our model results to plausible changes in these parameters. We conducted five additional simulations to examine the respective changes in the simulated DMS concentrations in the bottom ice and underlying water column due to a doubling of the following five key parameters: intracellular DMSP:Chl *a* ratio (Case 1), DMS yield (Case 2), and rate constants for bacterial DMSPd consumption (Case 3), bacterial DMS consumption (Case 4), and photolysis (Case 5). Note that these parameter changes were applied only to the sea-ice sulfur cycle and not to the ocean sulfur cycle. We selected these five parameters considering that previous model sensitivity studies indicated their importance to marine sulfur cycle dynamics (Archer et al., 2004; Steiner and Denman, 2008).

The intracellular DMSP:Chl *a* ratio is defined here as the ratio of particulate DMSP (DMSPp) to Chl *a*. For sea-ice samples, there are only three studies that report values of this ratio (Levasseur et al., 1994; Bouillon et al., 2002; Galindo et al., 2014), while several other studies provide the ratio of total DMSP (DMSPt = DMSPp + DMSPd) to Chl *a* (Table 3.3). Our baseline value of 9.5 nmol:μg is taken directly from the Arctic-ICE study conducted in 2010. This value does not differ much from that obtained in the following year (9.4 nmol:μg; Galindo et al., 2014). By contrast, an earlier study in the same region gives a much lower value (2.7 nmol:μg; Levasseur et al., 1994), which is close to the mean ratio for pelagic diatoms (4 nmol:μg; Stefels et al., 2007). Reported DMSPt:Chl *a* ratios for ice diatoms range from 8.4 nmol:μg to 49 nmol:μg (Table 3.3), which suggests that DMSPp:Chl *a* ratios could vary over a similar range. Note that most of these reported values are potentially underestimated due to anticipated DMSP loss associated with cell rupture during the melting process used in making these measurements (Stefels et al., 2012). Given this wide range among various studies and potential bias in measurements due to the methodological challenges mentioned above, the doubled ratio of 19 nmol:μg in Case 1 was deemed reasonable in the natural environment. In Case 2, the DMS yield fraction was increased to 40 %, which was the upper limit of the measured range for the bottom section of Antarctic ice core samples (Stefels et al., 2012). The doubled DMS consumption rate constant of 0.4 d^{-1} in Case 4 is within the range of 0.1-0.5 d^{-1}

observed in the bottom ice of Antarctic sea ice (J. Stefels, University of Groningen, personal communication). To the best of our knowledge, there has been only one study measuring the bottom-ice parameter values tested in Cases 2 and 4, and no studies have measured the rate constants in the bottom ice considered in Cases 3 and 5. Doubling the values of these parameters is justified by the fact that the observed water column values of these parameters in the Arctic often differ by an order of magnitude (e.g., Luce et al., 2011; Galindo et al., 2015).

Figure 3.7 shows the simulated time series of bottom-ice and under-ice DMS concentrations in the standard and sensitivity runs. The results generally indicate that the parameter variations affected the magnitudes of the simulated DMS pools. The temporal patterns of DMS concentrations are more or less invariant, as they are controlled by the ecosystem dynamics. The parameter variations generally had greater impacts on the bottom-ice DMS concentrations than on those in the underlying water column (Table 3.4). For example, doubling the intracellular DMSP:Chl *a* ratio (Case 1) and the DMS yield fraction (Case 2) resulted in doubling (100 % increase) and near-doubling (91 % increase) of the bottom-ice DMS concentration, while the increases were lower (17 % and 12 %) in the uppermost layer of the water column. Nevertheless, doubling these parameters resulted in the largest change in the cumulative under-ice DMS concentration among the five sensitivity runs. A previous model study by Lefèvre et al. (2002) also found these two parameters to be the most influential, and several other studies support the strong influence of variations in the intracellular DMSP:Chl *a* ratio (Gabric et al., 1993; Archer et al., 2004; Steiner and Denman, 2008). Doubling the remaining parameters (Cases 3-5) had relatively small effects (<10 %) on the cumulative under-ice DMS. This result indicates that field measurements targeting the two most sensitive parameters (i.e. DMSPp:Chl *a* ratio and DMS yield) will have the largest influence on constraining model-based estimates of sea-ice sulfur cycle processes.

To a certain extent, these sensitivities (e.g. sign and/or relative magnitude of the change in DMS) could have been deduced from inspection of the model equations, in which it is evident that doubling a single parameter results in doubling the DMS production or removal rate of a certain process either directly (Cases 2, 4, and 5) or indirectly (by doubling the production rate of precursor DMSPp; Case 1). The only exception is Case 3, in which doubling the bacterial DMSPd consumption rate constant affects both the production of DMS by bacterial conversion and the removal of DMSPd by bacterial consumption. Because the two processes have the opposite

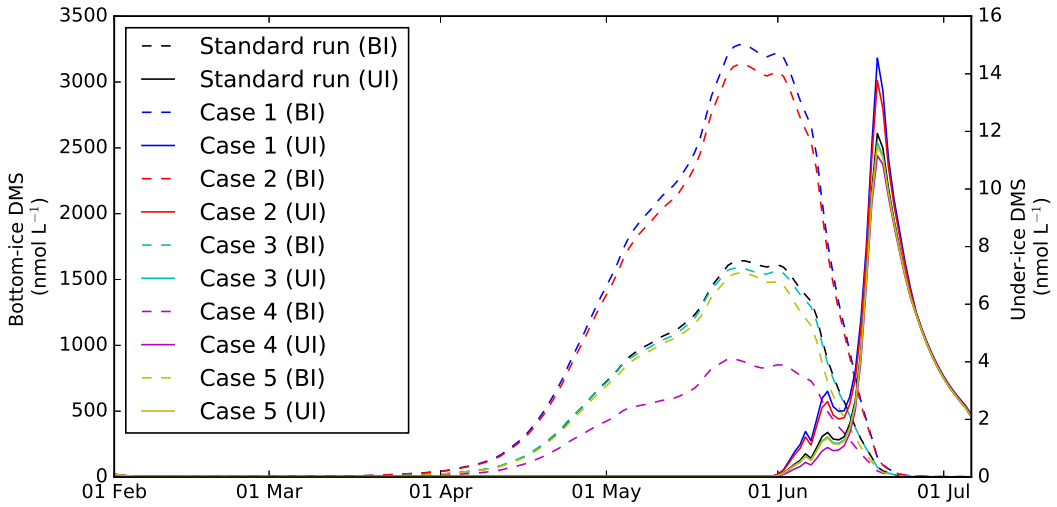

Figure 3.7: Simulated time series of bottom-ice (BI) and under-ice (UI; 0.5 m below the ice) DMS concentrations [nmol L^{-1}] during 2010 for: the standard run; Case 1: doubling the intracellular DMSP:Chl *a* ratio; Case 2: doubling the DMS yield fraction; Case 3: doubling the bacterial DMSPd consumption rate constant; Case 4: doubling the bacterial DMS consumption rate constant; and Case 5: doubling the photolysis rate constant.

effect on the rate of change in DMS, it is challenging to predict even the sign (increase or decrease) of the change in DMS. The result of the sensitivity run indicates that the impact of doubling this parameter is a slight decrease (2 %) in both the bottom- and under-ice DMS pools, and therefore the increases in the rates of the two processes are almost balanced. Although we cannot explain the magnitude of the percentage change in the DMS pools, we are confident that the net effect of doubling the bacterial DMSPd consumption rate constant on the DMS pools is a decrease because the model considers that only a fraction (i.e. the DMS yield fraction; set to 0.2 in this run) of DMSPd consumed by bacteria is converted to DMS, while the remaining fraction is lost to the sulfur pool. It is of particular importance to investigate the model sensitivity to variations in a parameter that has influence on multiple processes of the sulfur cycle, such as the bacterial DMSPd consumption rate constant. Although this is beyond the scope of the present study, it is worthwhile to mention that two parameters of ecological processes, namely active exudation fraction and cell lysis rate constant, have influence on both ecological and sulfur processes, and therefore deserve attention in future sensitivity studies.

Sea-air DMS flux during the melt period

In the uppermost layer of the water column, sea-air flux of DMS (μmol m^{-2} s^{-1}) was calculated as a function of areal fraction of open water (f_{ow}), gas transfer velocity (k_{dms}), and the concentration of seawater DMS (DMS_{wc}):

$$Flux = f_{ow} k_{dms} DMS_{wc} \tag{3.1}$$

This formulation assumes that the atmospheric DMS concentration is sufficiently low that it can be neglected. This assumption is common in both measurement- and model-based estimates of DMS flux (e.g. Rempillo et al., 2011; Tesdal et al., 2016a). The gas transfer velocity is parameterized following Nightingale et al. (2000). Note that this parameterization is based on measurements in open water, and therefore may not be suitable for ice-covered waters. However, we used the Nightingale et al. (2000) parameterization in order to better compare with previous flux estimates in the ice-covered Arctic that are all based on similar parameterizations. Future studies should take into account the effects of ice-associated processes on gas transfer velocity parameterizations (e.g. Loose et al., 2014). Also note that we do not take into account additional fluxes from other surface types, such as snow, bare ice, and melt ponds, which may provide an additional source of atmospheric DMS (Zemmelink et al., 2008; Nomura et al., 2012; Levasseur, 2013; Mungall et al., 2016).

In the standard run, it was assumed that when sea ice was present, the surface was fully ice-covered and f_{ow} was set to zero. Although this assumption is reasonable when conducting simulations at a single point in space, it is less reasonable over an entire grid cell due to subgrid-scale heterogeneity. In fact, as suggested by Levasseur et al. (1994), sea-air DMS flux can take place through openings in the ice (such as leads and cracks) and at the ice margin. Furthermore, laboratory, field, and model studies have suggested that flux of CO_2 through small scale areas of open water result in non-negligible fluxes in ice-covered regions (Loose et al., 2011; Else et al., 2012; Steiner et al., 2013). In order to quantify potential emissions of DMS through the open water in a partially ice-covered area, we conducted four additional standard runs with non-zero f_{ow} values (Table 3.5). In the first and second runs, values of 0.02 and 0.1 were selected to represent small and large leads within the ice (Lindsay and Rothrock, 1995; Steiner et al., 2013). In the third run, a value of 0.5 was prescribed to represent either an extensive opening in the ice or emissions near the ice margin (such that only a half of under-ice DMS can be advected to the ice margin and make

its way into the atmosphere). Finally, in the fourth run, a value of 1 was assigned to represent emissions right at the ice margin. Note that while these sensitivity runs are highly idealized (assuming partial or no ice cover for estimates of sea-air flux, but full ice cover in the biogeochemical model), they provide an indication on the impacts of open-water on the temporal variability of the DMS flux. Also, f_{ow} is included only in the DMS-flux parameterization, and has no influence on other physical or biogeochemical processes (such as surface heat flux). In order to evaluate the contribution of sea-ice biogeochemistry to the simulated flux, these four runs with non-zero f_{ow} values were also conducted for the NoIceSul and NoIceBgc cases.

During the melt period, observed winds were generally low to moderate, with daily means ranging from 1 to <10 m s^{-1} (Fig. 3.8). However, occasional strong winds were also measured as indicated by daily maximum wind speeds exceeding 20 m s^{-1}. The sea-air DMS flux simulated by the standard run using four different values of f_{ow} (Fig. 3.6b) was generally high in late June, with some maxima coincident with stronger winds as well as with peaks in under-ice DMS concentration (Fig. 3.6b). In particular, the simulated fluxes were notably high on 16, 21, and 26 June. In the case of emissions through partially open-water (f_{ow} = 0.02, 0.1, and 0.5), the simulated maximum flux (up to 0.3, 1.2, and 4.9 μmol m^{-2} d^{-1}, respectively; Table 3.5) were higher than the highest observational flux estimates over regions with similar open-water fractions during July and August of 1994 (0.1 μmol m^{-2} d^{-1} for f_{ow} = 0.03-0.06 and 1.2 μmol m^{-2} d^{-1} for f_{ow} = 0.25-0.3; Sharma et al., 1999), probably because the simulated maxima resulted partly from DMS associated with the under-ice bloom. In the cases of emissions near and at ice margins (f_{ow} = 0.5 and 1), the simulated maxima (of up to 4.9 and 8.1 μmol m^{-2} d^{-1}, respectively; Table 3.5) were comparable to the emissions under ice-free conditions estimated from previous oceanographic cruises in the Arctic (Leck and Persson, 1996; Sharma et al., 1999; Mungall et al., 2016). Furthermore, these simulated maxima exceeded the nucleation threshold of 2.5 μmol m^{-2} d^{-1}, above which the DMS flux has been suggested to be sufficiently high to promote new particle formation in pristine marine conditions (Pandis et al., 1994; Russell et al., 1994).

As expected, simulated sea-air fluxes were smaller in the NoIceSul run than in the standard run for each of the four f_{ow} values (Fig. 3.9b). The incorporation of sea-ice sulfur cycle affected the simulated fluxes most prominently during the first three weeks of June (Fig. 3.9d). The increase in the flux in the standard run relative to the NoIceSul run during this time period was due to the increase in the under-ice DMS

concentration due to the release of bottom-ice DMS, as discussed in Section 3.4.2. The relative flux enhancement was particularly important during the first two weeks of June, during which the simulated flux would otherwise remain close to zero as shown in Fig. 3.9b. During the third week of June, the first and second spikes in the flux time series increased by as much as 1.7 μmol m^{-2} s^{-1} in the case of f_{ow} = 1 (Table 3.5). Overall, the incorporation of sea-ice sulfur cycle resulted in a 20-26 % enhancement of DMS flux.

When both the sea-ice sulfur cycle and ecosystem modules were excluded from the model (NoIceBgc), the time course of the simulated flux was quite different from the NoIceSul runs (Fig. 3.9c), implying an active contribution from the sea-ice ecosystem to the flux. The difference between the two runs indicates that the incorporation of the sea-ice ecosystem results in an enhancement of flux between 13 and 19 June, followed by a reduction from 19 June onward (Fig. 3.9e). The three spikes in the flux time series of both the standard and NoIceSul runs were all affected by the incorporation of the sea-ice ecosystem: the first was enhanced by as much as 3.5 μmol m^{-2} s^{-1} (in the case of f_{ow} = 1), while the second and third spikes were reduced by the similar amount. These changes in fluxes were primarily driven by the changes in under-ice DMS concentrations (Fig. 3.5b). Overall, the incorporation of sea-ice ecosystem resulted in a 9-14 % reduction in the simulated flux relative to the NoIceBgc run (Table 3.5).

Lastly, the overall effect of incorporating sea-ice biogeochemistry on simulated DMS flux was examined by calculating the flux difference between the standard and NoIceBgc runs (Fig. 3.9f). The largest difference, occurring in the third week of June, was due to the incorporation of both sea-ice sulfur cycle and ecosystem (Figs. 3.9d and e). This difference resulted in an enhancement of the peak flux by as much as 5 μmol m^{-2} s^{-1} in the case of f_{ow} = 1. The largest negative difference coincided with the third spike, with a reduction in this spike by nearly 4 μmol m^{-2} s^{-1} in the case of f_{ow} = 1. Over the simulation period, the incorporation of the sea-ice biogeochemistry resulted in a 3-15 % flux enhancement (Table 3.5). Considering that the overall change in the under-ice DMS concentration due to the incorporation of sea-ice biogeochemistry was only -1 % (Section 3.4.2), this result demonstrates the potential importance of episodic fluxes to the cumulative DMS flux.

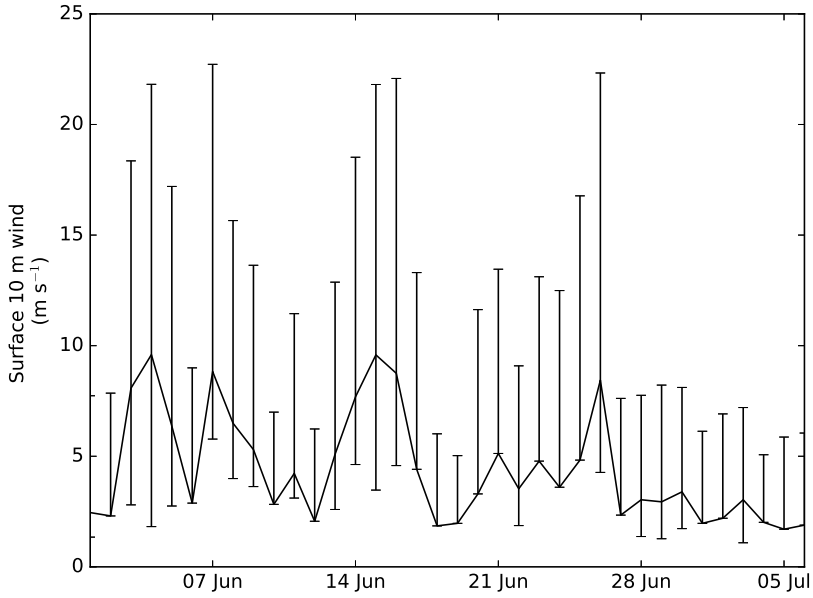

Figure 3.8: Time series of daily mean 10 m wind speed [m s^{-1}] observed at the Resolute airport (located within 7 km of the study site) during the melt period in 2010. The upper and lower vertical bars associated with the daily mean values represent the daily maximum and minimum values, respectively.

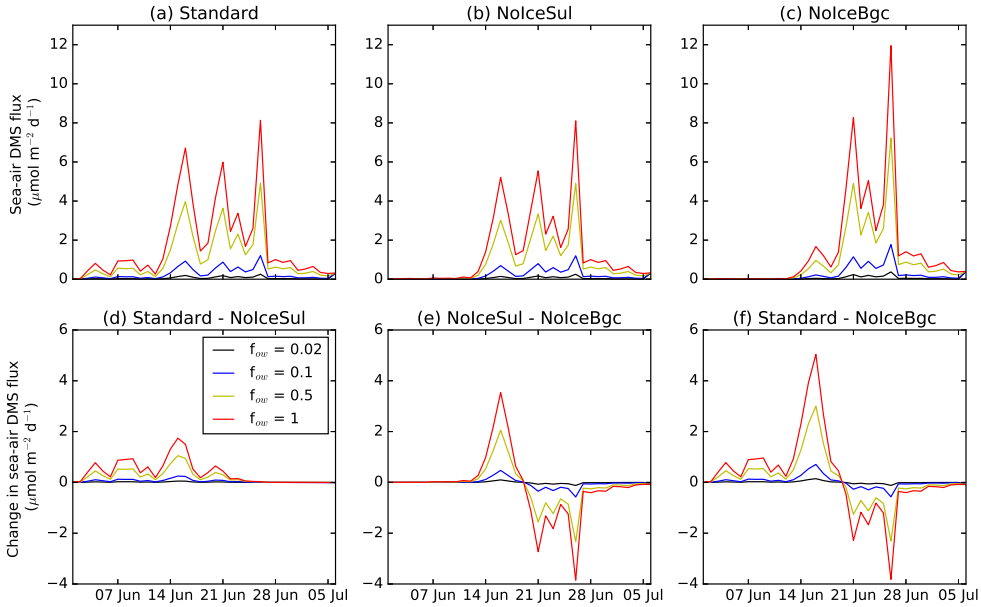

Figure 3.9: Simulated time series of sea-air DMS flux [μmol m^{-2} d^{-1}] for (a) the standard run and the sensitivity runs that excluded (b) the sea-ice sulfur cycle (NoIceSul) and (c) both the sea-ice sulfur cycle and ecosystem (NoIceBgc). Lower panels show the difference between (d) the standard and NoIceSul runs, (e) the NoIceSul and NoIceBgc runs, and (f) the standard and NoIceBgc runs, during the melt period in 2010. In (d), (e), and (f), positive values represent enhancement of the simulated sea-air flux due to the incorporation of the additional processes.

3.4.3 Limitations of the present study

The model used in the present study incorporated many of the important physical and biogeochemical processes within and under the sea ice (Fig. 3.1). However, there are additional processes that may potentially be important to the sea-ice sulfur cycle but are neglected in the present study. These processes are shown schematically in Fig. 3.10. We will discuss some of the challenges in implementing these processes in order to help guide further advances in sea-ice sulfur cycle studies.

First, the effects of brine drainage on the release of DMS and other biogeochemical tracers in the bottom ice were neglected in the model, which may have led to mismatches between simulated and observed phytoplankton biomass, DMSPp, and DMSPd under the ice prior to the snowmelt period in early May (Section 4.4). Existing parameterizations for brine drainage typically require representation of brine dynamics (e.g. Vancoppenolle et al., 2007, 2010). While a simplified brine drainage term was included in our model salinity calculation (following Vancoppenolle et al., 2009), implementing such parameterizations into our biogeochemical model was not desirable, as the goal of the present modelling excercise was to develop parameterizations that can be easily implemented into regional or global scale sea ice models, many of which do not explicitly simulate brine dynamics. In addition, the implementation of brine drainage effects on biogeochemical tracers will require modifications compared to the salinity formulations. Although our test run showed that adding these effects resulted in an improvement in the temporal evolution of ice algal biomass and DMSP (not shown), we excluded these parameterizations from the current configuration as the parameters are at this point poorly constrained (e.g. vertically averaged sea ice equilibrium tracer concentrations during brine drainage; see Eq. 19 of Vancoppenolle et al., 2009).

The production of DMSPd by sloppy feeding was neglected in the present study, as zooplankton grazing on ice algae was not considered in the ecosystem model (Chapter 2). Although previous field measurements provide evidence for zooplankton grazing on ice algae (Michel et al., 1996, and references therein), the importance of this process during the Arctic-ICE 2010 study is unknown due to the absence of zooplankton measurements. The previous sea-ice sulfur cycle model study by Elliott et al. (2012) suggests sloppy feeding as an important process for the DMSPd (and the subsequent DMS) production during the early stages of ice algal blooms. This argument is supported by a recent Antarctic ice study that found the DMSP content

in krill specimens (Damm et al., 2016). However, note that the DMSPd production by sloppy feeding in Elliott et al. (2012) and that of exudation in our study are parameterized similarly (both parameterizations have a linear dependence on simulated ice algal growth rate) and DMSPd production by exudation was neglected in Elliott et al. (2012). This indicates that model parameterizations might account for different processes in a similar way. Future observational studies are required to assess the relative importance of these two processes as well as the details of how they can be parameterized.

The production of DMS by dimethylsulfoxide (DMSO) reduction is not considered due to the lack of observational constraints on this process. This process has been suggested as a major pathway of DMS production in Antarctic sea ice (Asher et al., 2011). Asher et al. (2011) is the only study that has measured the rate constants of DMSO reduction in sea-ice brines.

A possible direct release of DMS by intracellular or extracellular DMSP-lyase activity of algae (Niki et al., 2000; Stefels, 2000; Alcolombri et al., 2015) is also disregarded. To the best of our knowledge, no studies have yet shown that diatoms, the dominant group of the bottom-ice algal community, possess DMSP-lyases. Thus, neglecting these processes seems plausible at least for bottom-ice sulfur cycle studies.

Recent studies on Arctic sea ice have shown that gas bubble formation and rise plays a dominant role in the dynamics of an inert gas (argon) within sea-ice brines when sea ice becomes permeable (Zhou et al., 2013; Moreau et al., 2014). As DMS can be present in the gas phase, this process may be a relevant sink for DMS present within brine channels. The present study neglected this process as no observations are available to constrain a parameterization for DMS.

Besides the sulfur cycle module, our model can be improved by further development of parameterizations for physical and ecological processes. For example, nutrient dynamics near the ice-water interface can be represented more realistically by explicitly resolving the role of brine convection (Vancoppenolle et al., 2010). Explicit representation of zooplankton grazing on ice algae would further advance the sea-ice ecosystem module. The refreezing of snow and the subsequent formation of superimposed ice were not simulated, although they were observed toward the end of the ArcticICE 2010 campaign. These processes have impacts on sea ice thermodynamics and light transmission through sea ice that indirectly affect the sea-ice sulfur cycle.

Lastly, we acknowledge the limitations of the assessment of model simulations in the present study. The model results were evaluated against observations coming from

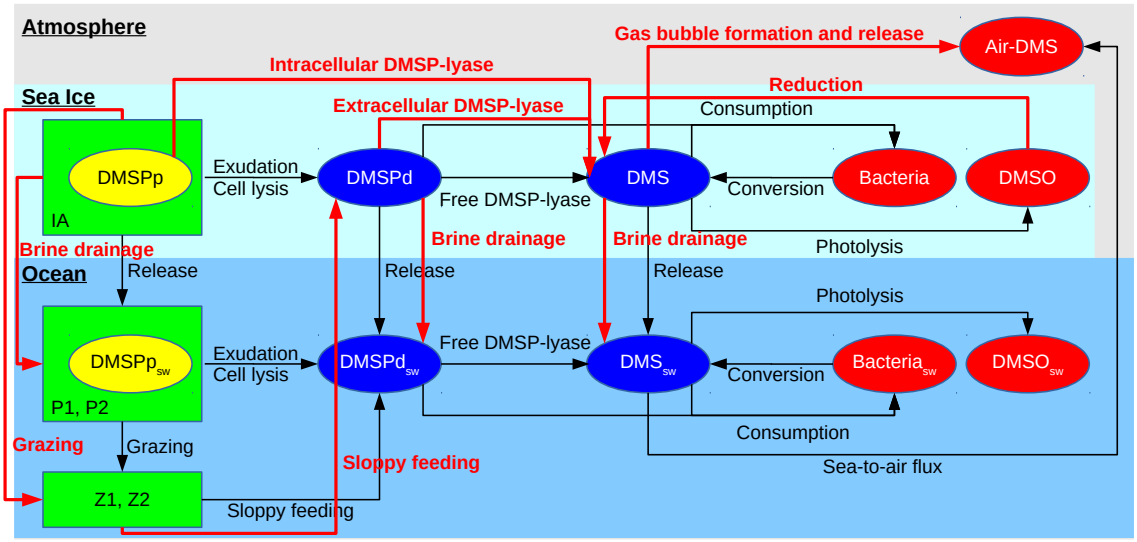

Figure 3.10: Same as Fig. 3.1, but with additional physical and biogeochemical fluxes suggested for future model development (red arrows).

a single time-series study. Therefore, an assessment of model's 'portability' (ability to simulate observed time series from a different year and/or region with the same parameters Friedrichs et al., 2007) is lacking. The scarcity of field measurements of dimethylated sulfur compounds within sea ice makes this task extremely challenging. Clearly, more field measurements, and particularly, high-resolution time-series of dimethylated sulfur compounds within sea ice (e.g. Tison et al., 2010; Galindo et al., 2014, 2015; Carnat et al., 2016) are needed to assess the portability of 1-D sea-ice sulfur cycle models and further constrain the model parameters and parameterizations.

3.5 Conclusions

In the present study, we investigated the implications of sea-ice biogeochemistry for production and emissions of DMS in the Arctic Ocean. Our model is able to capture reasonably well the limited set of observational data available, and suggests that the sea-ice sulfur cycle and ecosystem have considerable impact on DMS production under the ice, and therefore should not be overlooked in estimates of oceanic DMS emissions, especially near ice margins. Specifically, the sea-ice sulfur cycle increased under-ice DMS concentration directly by release of bottom-ice DMSPd and DMS into the underlying water column, while production in the water column was both

enhanced and reduced by interactions with the sea-ice ecosystem, at different phases of the under-ice phytoplankton bloom. In the case of first-year landfast ice in Resolute Passage, incorporation of the sea-ice sulfur cycle resulted in an 18 % enhancement of DMS concentrations under the ice and a 20-26 % enhancement of sea-air DMS flux during the melt period. By contrast, incorporation of a sea-ice ecosystem resulted in an overall reduction in under-ice DMS production (16 %) as well as emissions to the atmosphere (9-14 %). The overall effect of sea-ice biogeochemistry (both sulfur cycle and ecosystem) is negligible for under-ice DMS production (-1 %), but it increases emissions by 8-20 %. In the vicinity of ice margins, spikes in sea-air flux of DMS originating from the bottom ice and underlying water column were comparable to some of the local maxima in the summertime flux estimated for ice-free waters in the Arctic.

We acknowledge the simplified representation of the complex reality of the sea-ice sulfur cycle dynamics considered in our model, and note that the results of model simulations are subject to uncertainties in the model parameters and parameterizations. Furthermore, our model results are representative for a particular year, location, and specific environmental conditions. A few suggestions for future model development are to: 1) incorporate state dependence of bacterial parameters that are important to the sea-ice sulfur cycle dynamics, such as the bacterial DMS yield fraction; and 2) parameterize the effects of additional relevant processes, such as brine drainage, gas bubble release, sloppy feeding, and DMSO reduction.

To improve model-based estimates of oceanic DMS emissions in the Arctic under present-day and future climates, we make the following recommendations for future studies: both the sea-ice sulfur cycle and ecosystem should be incorporated into model simulations at a regional (pan-Arctic) scale; and more field time-series measurements of dimethylsulated sulfur compounds and key parameters of sea-ice sulfur cycle within sea ice (i.e. DMSPp:Chl *a* ratio and DMS yield fraction) should be conducted to further assess the model performance and refine the representation of essential processes. Ultimately, ocean circulation models incorporating both the sea-ice sulfur cycle and ecosystem should be coupled to atmospheric chemistry transport models in order to explore the possibility of regional climate regulation by oceanic DMS emissions within the Arctic.

Table 3.1: List of the coupled sea ice-ocean sulfur cycle model variables and parameters

Symbol	Description	Units	Value
Variable			
A_{mp}	Melt-pond area fraction	-	
$DMSPp$, $DMSPp_{wc}$	DMSPp concentration	nmol L^{-1}	
$DMSPd$, $DMSPd_{wc}$	DMSPd concentration	nmol L^{-1}	
DMS, DMS_{wc}	DMS concentration	nmol L^{-1}	
Γ_{z1}^{p1}	Grazing rate of zooplankton on phytoplankton	d^{-1}	
H_i	Sea ice thickness	m	
L_{nut}, L_{nut}^{p1}, L_{nut}^{p2}	Nutrient limitation index	-	
PAR, PAR_{wc}	Photosynthetically active radiation	W m^{-2}	
ρ_{wc}	Seawater density	kg m^{-3}	
μ, μ_{p1}, μ_{p2}	Algal growth rate	s^{-1}	
T_{z_0}	Seawater temperature in the uppermost layer	$^\circ$ C	
U_{10}	Wind speed at 10 m	m s^{-1}	
Parameter			
r_{mp}	Melt-pond drainage rate	m d^{-1}	0.0175
f_{active}, f_{active}^{p1}, f_{active}^{p2}	Active exudation fraction	-	0.05, 0.05, 0.05
f_{sloppy}^{z1}, f_{sloppy}^{z2}	Sloppy feeding fraction	-	0.3, 0.3
f_{yield}, f_{yield}^{wc}	Bacterial yield	-	0.2, 0.2
h_{bi}	Thickness of the biologically-active bottom ice layer	m	0.03
$h_{photolysis}$, $h_{photolysis}^{wc}$	Photolysis half-saturation constant	W m^{-2}	1, 1
h_{z_0}	Thickness of the uppermost layer of the water column	m	1
k_{dms}, k_{dms}^{wc}	Bacterial DMS consumption rate constant	d^{-1}	0.2, 0.5
k_{dmspd}, k_{dmspd}^{wc}	Bacterial DMSPd consumption rate constant	d^{-1}	1, 5
k_{free}, k_{free}^{wc}	free DMSP-lyase rate constant	d^{-1}	0.02, 0.02
k_{lysis}, k_{lysis}^{p1}, k_{lysis}^{p2}	Cell lysis rate constant	d^{-1}	0.03, 0.03, 0.03
$k_{photolysis}$, $k_{photolysis}^{wc}$	Photolysis rate constant	d^{-1}	0.1, 0.1
q, q_{p1}, q_{p2}	Intracellular DMSP-to-Chl a ratio	nmol S:μg Chl a	9.5, 100, 9.5
ρ_i	Sea ice density	kg m^{-3}	913
ρ_{me}	Sea ice density in equivalent meltwater	kg m^{-3}	1000

Table 3.2: Sensitivity of simulated under-ice DMS concentration to the incorporation of the sea-ice sulfur cycle and ecosystem. Overall change was calculated as the difference in the time-integrated under-ice DMS concentrations between the two runs of interest and dividing it by the time-integrated under-ice DMS concentration in the run being subtracted.

Runs to be compared (Implications of the comparioson)	Maximum concentration difference [nmol L^{-1}]	Overall change [%]
Standard - NoIceSul (Impact of sea-ice sulfur cycle)	2.4	18
NoIceSul - NoIceBgc (Impact of sea-ice ecosystem)	4.1	-16
Standard - NoIceBgc (Impact of sea-ice biogeochemistry)	5.6	-1

Table 3.3: Reported mean DMSPp:Chl *a* and DMSPt:Chl *a* ratios (mmol:g) for diatom-dominated sea-ice samples.

Ratio	Location (Arc./Ant.)[a]	Season[b]	Method[c]	Reference
DMSPp:Chl *a* (Particulate DMSP-to-chlorophyll *a* ratio)				
2.7	Resolute Passage (Arc.)	Spring 1992	Melting	Table 1 of Levasseur et al. (1994)
1.9	Baffin Bay (Arc.)	Spring 1998	Melting	Bouillon et al. (2002)
9.5	Resolute Passage (Arc.)	Spring 2010	Melting	Fig. 10a of Galindo et al. (2014)
9.4	Resolute Passage (Arc.)	Spring 2011	Melting	Fig. 10a of Galindo et al. (2014)
DMSPt:Chl *a* (Total DMSP-to-chlorophyll *a* ratio)				
8.4[d]	Weddell Sea (Ant.)	Spring 1988	Melting	Table 1 of Kirst et al. (1991)
22[e]	Southern Ocean (Ant.)	Winter-Spring 1997	Melting	Trevena et al. (2000)
37[e]	Prydz Bay (Ant.)	Spring 1997-1998	Melting	Trevena et al. (2003)
20	Barrow (Arc.)	Winter-Spring 2002	Melting	Uzuka (2003)
49	Weddell Sea (Ant.)	Spring 2004	Dry-crushing	Fig. 6a of Tison et al. (2010)

[a] Arc.: Arctic; Ant.: Antarctica
[b] Winter: Jan.-Mar. (Jul.-Sep.) for Northern (Southern) Hemisphere
[b] Spring: Apr.-June. (Oct.-Dec.) for Northern (Southern) Hemisphere
[c] Either melting or dry-crushing as described by Stefels et al. (2012).
[d] Average of brown ice and ice core samples.
[e] Calculated based on mean DMSPt and Chl *a* values given in Table 6 of Trevena et al. (2003).

Table 3.4: Sensitivity of simulated bottom-ice and under-ice DMS concentration to doubling of model parameters. Changes in the bottom-ice and under-ice DMS were calculated by subtracting the time-integrated DMS in the sensitivity run from the time-integrated DMS in the standard run and dividing the difference by the time-integrated DMS in the standard run.

Run	Description	Change in the bottom-ice DMS	Change in the under-ice DMS
Case 1	Doubling the intracellular DMSP:Chl *a* ratio	100 %	17 %
Case 2	Doubling the DMS yield fraction	91 %	12 %
Case 3	Doubling the bacterial DMSPd consumption rate constant	-2 %	-2 %
Case 4	Doubling the bacterial DMS consumption rate constant	-44 %	-5 %
Case 5	Doubling the photolysis rate constant	-8 %	-2 %

Table 3.5: Sensitivity of simulated sea-air DMS fluxes to the open-water fraction and to the incorporation of sea-ice biogeochemistry. Overall changes were calculated by taking the difference between the two runs of interest and dividing it by the cumulative flux in the subtracted run.

Open-water fraction [-]	0.02 (Small lead)	0.1 (Large lead)	0.5 (Near ice margin)	1 (At ice margin)
	Maximum flux [μmol m^{-2} d^{-1}]			
(Standard)	0.3	1.2	4.9	8.1
	Maximum flux difference [μmol m^{-2} d^{-1}]			
(Standard - NoIceSul)	0.1	0.2	1.1	1.7
(NoIceSul - NoIceBgc)	0.1	0.5	2.1	3.5
(Standard - NoIceBgc)	0.1	0.7	3.0	5.0
	Overall change [%]			
(Standard - NoIceSul)	20	24	26	26
(NoIceSul - NoIceBgc)	-14	-13	-11	-9
(Standard - NoIceBgc)	3	8	12	15

Chapter 4

CSIB v1: a sea-ice biogeochemical model for the NEMO community ocean modelling framework

The following chapter is a manuscript under review for Geoscientific Model Development as:

Hayashida, H., Christian, J.R., Holdsworth, A.M., Hu, X., Monahan, A.H., Mortenson, E., Myers, P.G., Riche, G.J.R., Sou, T., and Steiner, N.S.: CSIB v1: a sea-ice biogeochemical model for the NEMO community ocean modelling framework, Geoscientific Model Development Discussions, https://doi.org/10.5194/gmd-2018-191

The manuscript is repeated here with some adjustments to fit the format of the dissertation.

4.1 Abstract

Numerical models are a useful tool for studying marine ecosystems and associated biogeochemical processes in ice-covered regions where observations are scarce. To this end, CSIB v1 (Canadian Sea-ice Biogeochemistry version 1), a new sea-ice biogeochemical model has been developed and embedded into the Nucleus for European Modelling of the Ocean (NEMO) modelling system. This model consists of a three-compartment (ice algae, nitrate, and ammonium) sea-ice ecosystem and a two-

compartment (dimethylsulfoniopropionate and dimethylsulfide) sea-ice sulfur cycle which are coupled to pelagic ecosystem and sulfur-cycle models at the sea ice-ocean interface. In addition to biological and chemical sources and sinks, the model simulates the horizontal transport of biogeochemical state variables within sea ice through a one-way coupling to a dynamic-thermodynamic sea-ice model (LIM2). The model results for 1979 (after a decadal spin-up) are compared to observations and previous model studies for a brief discussion on the model performance. Furthermore, this paper provides discussion on technical aspects of implementing the sea-ice biogeochemistry and assesses the model sensitivity to 1) the temporal resolution of the snowfall forcing data, 2) the representation of light penetration through snow, 3) advective and eddy-diffusive horizontal transport of sea-ice biogeochemical state variables, and 4) light attenuation by ice algae. The sea-ice biogeochemical model has been developed within the generic framework of NEMO to facilitate its use within different configurations and domains, and can be adapted for use with other NEMO-based submodels such as LIM3 and PISCES. The model experiment beyond 1979 is underway to perform a more comprehensive model evaluation and examine the interannual and interdecadal variability over the recent decades.

4.2 Introduction

Biogeochemical processes at the sea ice-ocean interface play an active role in polar marine ecosystems and global cycling of important chemical elements and compounds. For example, microalgae that colonize the base of sea ice in spring can have a strong influence on primary production of phytoplankton through light attenuation, nutrient drawdown, and seeding as well as on secondary production by providing a food source for grazers (Arrigo, 2014). Furthermore, these ecological processes regulate the production and removal of greenhouse gases (e.g. carbon dioxide and nitrous oxide) and other climatically-important gases (e.g. dimethylsulfide) in ice-covered regions, and the exchange of these gases with the overlying atmosphere (Vancoppenolle et al., 2013).

However, our current understanding of many of these processes remains limited due to both logistical and technical challenges for field observations (Miller et al., 2015). Mechanistic models representing sea-ice biogeochemistry can both fill gaps between sparse measurements and aid in the interpretation of these measurements. Furthermore, these models can be used in systematic intercomparisons that can build

confidence in our understanding of polar marine science such as has been done for pelagic ecosystem models (e.g. Popova et al., 2012; Jin et al., 2015).

Although considerable effort has been invested in developing mechanistic models for sea-ice bigeochemistry over the last three decades following the pioneering work of Arrigo et al. (1991), most of these models were applied in one-dimensional (1D) frameworks, and the results are therefore limited to particular locations (see Vancoppenolle and Tedesco, 2016). Only a few of these models have been applied in three-dimensional (3D) framework coupled to either a regional or global sea ice-ocean general circulation model (see Table 4.1 for a list of 3D model configurations developed for pan-Arctic studies). More efforts toward developing such 3D sea-ice biogeochemical models are needed to better understand the large-scale variability in biogeochemical processes within sea ice and their role in underlying pelagic and benthic ecosystems.

In this study, we present CSIB v1 (Canadian Sea-Ice Biogeochemistry version 1), a new sea-ice biogeochemical model implemented into the Nucleus for European Modelling of the Ocean (NEMO), a state-of-the-art modelling framework for oceanographic research (`www.nemo-ocean.eu`). To the best of our knowledge, Tedesco et al. (2017) is the only previous study in which a sea-ice biogeochemical module has been coupled to NEMO. However, the coupling was done in an offline configuration in that study. An important advance of the present study is that the module is written within the NEMO code to allow in-line coupling (i.e. physical dynamics are computed simultaneously with biogeochemistry) and the computation of the horizontal transport of sea-ice biogeochemical state variables. These implementations allow more realistic simulation of sea-ice biogeochemistry. The main objectives of the present study are to: describe the development of the coupled model in a pan-Arctic configuration (Section 4.3); evaluate the results of a multi-year reference simulation (Section 4.4); and assess the model sensitivity to modifications of parameters and parameterizations (Section 4.5). Key findings of the present study are summarized in Section 4.6.

4.3 Model description and setup

The fundamental constituents of NEMO are the following three submodels: ocean physics, sea-ice physics, and ocean biogeochemistry. In the present study, we adopted version 3.4 of NEMO (NEMO v3.4; Madec, 2008) and developed within it an additional submodel, sea-ice biogeochemistry. Technical details on the code structure of

Table 4.1: Comparison of pan-Arctic 3D sea-ice biogeochemical model configurations developed in various framework. dx: the horizontal resolution; dzo: the vertical resolution of the uppermost water column; dzi: the thickness of ice algal skeletal layer; i_0: the fraction of incoming shortwave radiation that penetrates through the snow surface; Shading: attenuation of light by ice algae; Runoff: river discharge of nitrate.

Reference	Framework	dx	dzo	dzi	$i_{0,snow}$	Shading	Runoff
Dupont (2012)	MOM	$\sim$ 50 km	3.45 m	5 cm	0	no	yes
Jin et al. (2012)	POP	$\sim$ 40-50 km	10 m	3 cm	0	no[a]	no[a]
Watanabe et al. (2015)	COCO	$\sim$ 5 km	2 m	2 cm	1[a]	no	no[a]
Castellani et al. (2017)	MITgcm	$\sim$ 28 km	10 m	5 cm	0.3	yes	no
This study	NEMO	10-14.5 km	1 m	3 cm	0.15	yes	no

[a]Confirmed through personal communication with the lead author.

the model developed in this study are provided in Appendix A.3.1 for those who are interested in using the newly-added sea-ice biogeochemical module.

4.3.1 Ocean and sea ice physics (OPA-LIM2)

The physical ocean submodel is the Océan PArallélisé (OPA), which is a free-surface, hydrostatic, primitive-equation model developed for regional and global oean circulation studies (Madec, 2008). OPA is coupled to the submodel for sea-ice physics, namely the Louvain-la-Neuve sea Ice Model (LIM). The present study uses version 2 of LIM (LIM2; Fichefet and Maqueda, 1997; Bouillon et al., 2009) , consisting of a three-layer (one for snow and two for ice) dynamic-thermodynamic model.

To model ambient light available for ice algae and under-ice phytoplankton properly, we modified the module that computes the shortwave radiative transfer through snow and sea ice as shown schematically in Figure 4.1. In this module, the unreflected fraction (1-a) of the incoming shortwave radiation (F_{sw}) is parameterized as either being absorbed within a thin layer of surface snow and/or ice (defined as having thickness of 10 cm in NEMO v3.4) or penetrating through the snow and/or ice interior underneath this layer. This penetrating fraction is determined by a coefficient, i_0, which is set to zero in the presence of snow in the default configuration of LIM2 following Maykut and Untersteiner (1971). While this assumption of complete blockage of light may be a reasonable approximation for thermodynamic processes of snow and sea ice, this approximation is problematic for modelling sea-ice biogeochemistry. Specifically, the assumption implies that primary producers can not photosynthesize until snow disappears completely, which is inconsistent with the findings of many field observations that measure high algal biomass at the base of snow-covered sea ice (e.g. Leu et al., 2015). Furthermore, i_0 has been set to non-zero values in other sea-ice models in the case of thin or melting snow (Flato and Brown, 1996; Abraham et al., 2015). For these reasons, we use a non-zero value of i_0 and parameterize the light transmission through the snow column below the specified surface layer following the Beer-Lambert law. The value of i_0 was set to 0.15 following the 1D sea-ice biogeochemical modelling work of Vancoppenolle et al. (2010). The attenuation coefficient of snow was set to 10 m^{-1}, which falls within the observed range for melting and freezing snow (Grenfell and Maykut, 1977). Model sensitivity to i_0 is discussed in Section 4.5.2.

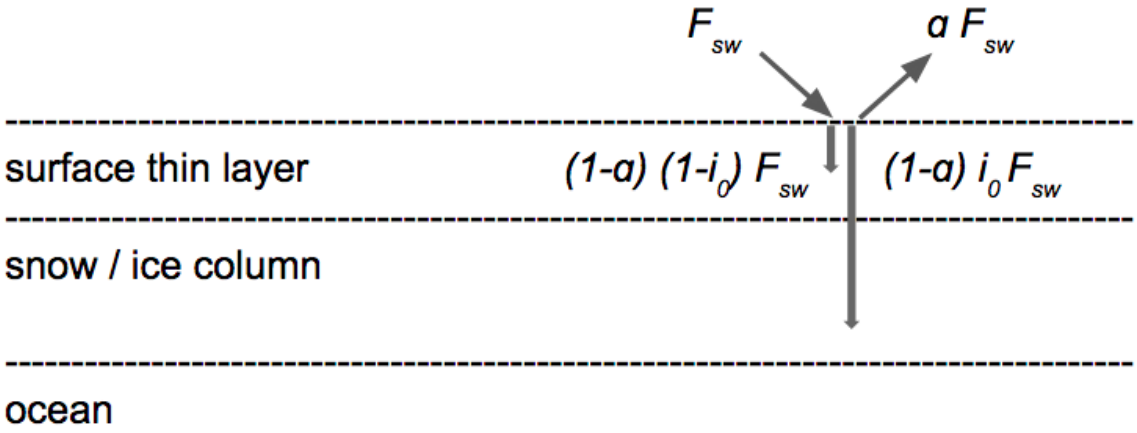

Figure 4.1: Shortwave radiative transfer through snow and sea ice modified from Figure 3.4 of Vancoppenolle et al. (2012). F_{sw} represents the incoming shortwave radiation, a fraction of which is reflected due to the surface albedo of snow or ice (a). The remaining radiation is either absorbed within the surface thin layer ($(1-a)(1-i_0)F_{sw}$) or penetrates into the snow and/or ice column below this layer ($(1-a)i_0F_{sw}$).

4.3.2 Ocean biogeochemistry (CanOE)

The submodel for ocean biogeochemistry adopted in the present study is the Canadian Ocean Ecosystem Model (CanOE), developed by the ocean modelling group at the Canadian Centre for Climate Modelling and Analysis (Appendix A.3.2). This model has been developed for the latest version of the Canadian Earth System Model (Arora et al., 2011), which will be used in the next phase of the Coupled Model Intercomparison Project (CMIP6). CanOE simulates the lower trophic levels of marine ecosystems (nutrients, phytoplankton, zooplankton, and detritus) and biogeochemical cycling of key elements (carbon, oxygen, nitrogen, and iron). This model is built around the basic code structure of the Pelagic Interactions Scheme for Carbon and Ecosystem Studies version 2 (PISCES-v2), the default submodel for ocean biogeochemistry of NEMO (Aumont et al., 2015). One advantage of CanOE over PISCES-v2 is that it is computationally more efficient as a result of having fewer state variables (19 vs 24) and fewer computationally expensive parameterizations (Appendix A.3.2). In the present study, we made two modifications to CanOE. The first modification is the addition of an ocean sulfur-cycle module and the second modification is the parameterization of the photosynthetically active radiation (PAR).

Addition of an ocean sulfur cycle

Figure 4.2 shows a schematic of CanOE including the ocean sulfur cycle and the sea-ice biogeochemistry. The sulfur cycle module consists of two state variables: dissolved dimethylsulfoniopropionate (DMSPd) and dimethylsulfide (DMS). The ocean sulfur cycle is one-way coupled to CanOE as sulfur cycle processes depend on the state of the ecosystem, but not vice versa. The ocean sulfur-cycle module is based on that of Chapter 3 with the following two modifications. First, the cellular DMSP content of modelled phytoplankton is derived from their carbon content as opposed to the chlorophyll content as in Chapter 3. This change was made because there are more observation-based estimates of the intracellular DMSP-to-carbon (DMSP:C) ratio than the DMSP-to-chlorophyll a ratio (e.g. Stefels et al., 2007). The DMSP:C ratios for small and large phytoplankton (respectively high and low DMSP producers) are set to 12 and 4 mmol:mol. The ratio for small phytoplankton falls within the observed range for non-diatom species (Stefels et al., 2007), while that of large phytoplankton is derived by converting the DMSP:Chl ratio of 9.5 mmol:mol (Hayashida et al., 2017) using the intracellular C:Chl-a ratio of 28 g:g (Mortenson et al., 2017).

Also, the parameterization of sea-to-air flux of DMS was modified to account for the non-linear dependence of the flux on the open-water fraction (Loose et al., 2009):

$$F = f_{ow}^{0.4} k_{dms} DMS \tag{4.1}$$

where F is the DMS flux (μmol m^{-2} s^{-1}), f_{ow} is the open-water fraction (-), k_{dms} is the gas transfer velocity (m s^{-1}), and DMS (nM) is the DMS concentration in the uppermost layer of the water column.

Correction to the fractionation of under-ice PAR

The second modification to CanOE was made to the PAR fraction of incident solar radiation. PAR is the shortwave radiation in the 400-700 nm wavelength range, which is available for photosynthesis. In CanOE, PAR reaching the sea surface is 43% of the downwelling shortwave radiation, a well established estimate for PAR in open water (e.g. Morel, 1988). However, this assumption underestimates PAR reaching the sea surface under sea ice. The shortwave radiation penetrating through snow and ice is almost entirely PAR, as radiation outside of the 400-700 nm range is absorbed by the snow and ice (e.g. Zeebe et al., 1996). Thus, we have set the fraction of the downwelling shortwave radiation to unity when computing the sea-surface PAR under sea ice.

4.3.3 Sea-ice biogeochemistry

The submodel for sea-ice biogeochemistry is a modified version of a three-compartment (ice algae, nitrate, and ammonium) ecosystem of Chapter 2 and a two-compartment (DMS and DMSPd) sulfur cycle of Chapter 3.

Sea-ice biogeochemical processes are assumed to take place in a layer of fixed thickness at the ice base. The governing equation for any sea-ice biogeochemical state variable is:

$$\frac{\partial X}{\partial t} = -\nabla \cdot \left(\overrightarrow{U} X \right) + D \nabla^2 X + \mathrm{SMS}\left(X\right) \tag{4.2}$$

where X denotes the concentration of the state variable, $\overrightarrow{U}$ denotes the horizontal velocity field of sea ice, and D denotes the horizontal eddy diffusion coefficient. The first two terms on the right hand side of Equation 4.2 represent tendencies associ-

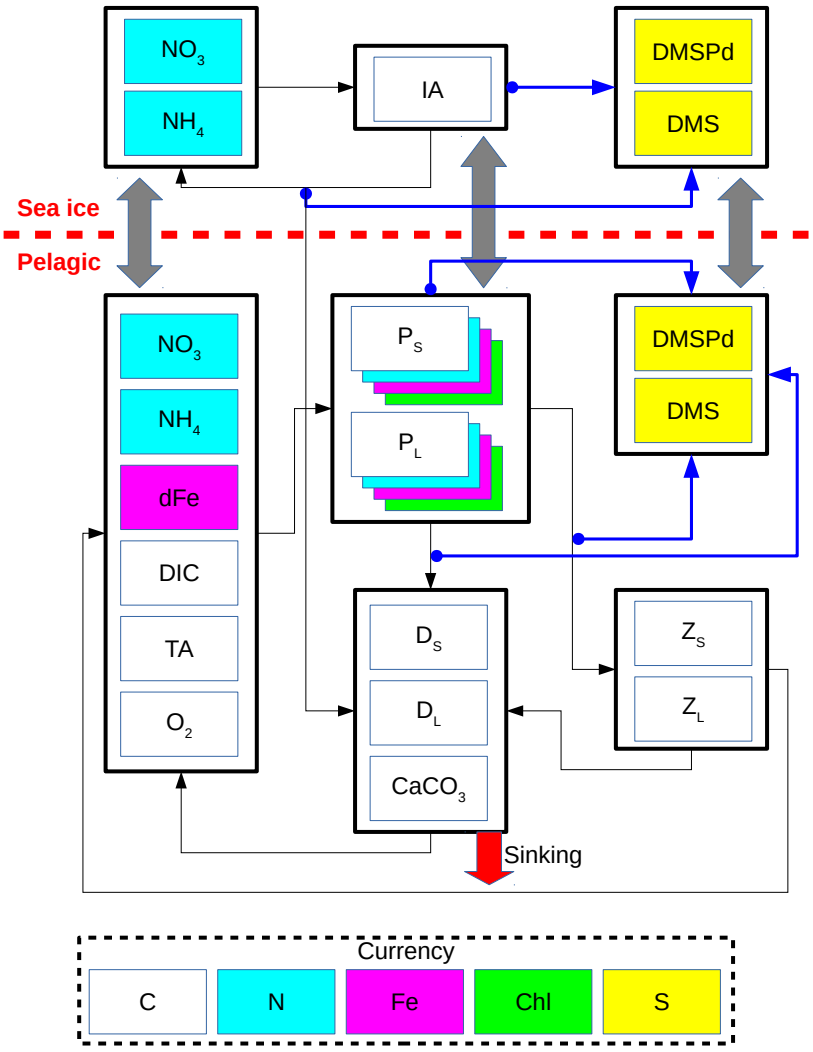

Figure 4.2: Schematic of the CanOE pelagic ecosystem model and associated sea-ice biogeochemistry and pelagic sulfur-cycle modules. Black arrows indicate fluxes of carbon (C)/nitrogen (N)/iron (Fe) between compartments; blue arrows indicate sources of dissolved dimethylsulfoniopropionate (DMSPd); gray arrows indicate ice-ocean fluxes of nitrate (NO_3), ammonium (NH_4), ice algae (IA)/large phytoplankton (P_L), DMSPd, and dimethylsulfide (DMS). Flows of dissolved oxygen (O_2) are opposite to those of dissolved inorganic carbon (DIC) and are not explicitly illustrated. Detritus (D_S and D_L) and zooplankton (Z_S and Z_L) are denominated in C units but have implicit N and Fe pools according to fixed elemental ratios; phytoplankton (P_S and P_L) have separate state variables for each currency. O_2 and total alkalinity (TA) are their own currencies, but are shown as white here for simplicity; their sources and sinks follow well established stoichiometry relative to those of DIC. Sources and sinks of TA associated with the nitrogen cycle (Wolf-Gladrow et al., 2007) are included but not shown in the figure. The state variables dFe and $CaCO_3$ represent dissolved iron and calcium carbonate, respectively. The currencies Chl and S represent the chlorophyll *a* and sulfur, respectively.

ated with horizontal motion of sea ice (Section 4.3.3). The third term represents biological and chemical sources and sinks. Note that while LIM2 computes the impact of mechanical redistribution (i.e. deformation due to ridging/rafting) on sea ice physical properties, these processes are neglected in computations of the sea ice biogeochemical state variable tendencies in the present study as the model uses a simple representation of the sea-ice biogeochemical layer as a layer of fixed thickness (3 cm) at the ice base.

Horizontal transport

Horizontal transport of sea-ice biogeochemical state variables is computed simultaneously and in the same way as the sea ice physical properties of LIM2 (i.e., snow and sea ice volume, heat content, and areal coverage). Specifically, it is done by solving the advection-diffusion equation for sea ice. Advection refers to the transport associated with the resolved motion of sea ice, and is computed using the scheme of Prather (1986). Diffusion, on the other hand, is a model artefact designed for numerical stability, although it can be considered as random component of sea-ice motion analogous to turbulence in fluids (Thorndike, 1986; Rampal et al., 2009, 2016). Diffusion is computed within the ice pack by evaluating the second-order diffusive operator using the Crank-Nicholson scheme (Crank and Nicolson, 1996), while it is set to zero at the ice edge. The horizontal diffusion coefficient (D) is set to 5 m^2 s^{-1}, as suggested byVancoppenolle et al. (2012). Readers are referred to Vancoppenolle et al. (2012) for further description of these processes. The impacts of advection and diffusion on modelled sea-ice biogeochemical state variables are discussed in Section 4.5.3.

New ice formation

Newly-formed ice is assumed to contain the same concentrations of biogeochemical state variables as those in the underlying water column. Thus, the concentration of any sea-ice biogeochemical state variable is updated as follows:

$$X = \frac{SIC_{t-1}}{SIC_t} X^* + \frac{SIC_t - SIC_{t-1}}{SIC_t} X_{ui} \tag{4.3}$$

where SIC_{t-1} and SIC_t respectively denote the sea-ice concentrations in the previous and current time step. X^* denotes the concentration of the sea-ice biogeochemical state variables after the computation of advection and diffusion but prior to the com-

putation of biological and chemical sources and sinks. X_{ui} denotes the concentration of the biogeochemical state variable in the uppermost layer of the water column under the ice. Equation 4.3 neglects the density difference between sea ice and seawater, and therefore violates mass conservation. However, this simplification has negligible effect on ocean biogeochemistry given the relatively-thin sea-ice biogeochemical layer (see Chapter 3). For ice algae only, a minimum biomass threshold is set at 10 mmol C m^{-3} in order to mimic reasonable overwintering biomass (Chapter 2).

Biological and chemical sources and sinks

The biological and chemical processes represented as sources and sinks of the sea-ice biogeochemical state variables are described in detail in Chapter 2 and Chapter 3. For the ecosystem component, these processes include photosynthesis, mortality, and remineralization of dead organic matter. The growth rate of ice algae is dependent on ambient temperature, PAR, and nutrient concentrations (nitrate and ammonium). Note that the growth rate dependence on ice melt considered in Chapter 2 has been neglected in the present study because: 1) our preliminary results indicated that ice algal blooms were generally insensitive to it; 2) the parameterization for ice melt limitation was applied for a specific location and might not be appropriate for other locations; and 3) the parameterization lacks observational evidence.

In addition to the computation of biological and chemical sources and sinks, processes relevant to the ice-ocean fluxes are computed, including molecular diffusive exchange of nutrients, release of all state variables into the water column due to basal ablation, and flushing of these variables by flow of water through the ice from rainfall and surface ablation.

4.3.4 Experiments

In this study, we consider six model experiments (Table 4.2). The first experiment is a reference simulation (EXP0), designed to be the most realistic model solution that best agrees with observations. The 11-year duration of EXP0 is considered sufficient for the spin up of sea-ice and near-surface pelagic variables based on previous Arctic biogeochemical model studies (e.g. Dupont, 2012; Jin et al., 2012). The setup of EXP0 is described below. The rest of the experiments (EXP1-5) are designed to assess the sensitivity of the model simulations to changes in uncertain forcing data and parameter values.

Table 4.2: List of model experiments

Name	Description	Duration
EXP0	Reference simulation.	1969-1979
EXP1	Same as EXP0 except that the atmospheric forcing was replaced by the CORE-II dataset.	1969-1979
EXP2	Same as EXP0 except that the snowfall and total precipitation for 1969-1978 were replaced by the original DFS dataset (i.e. daily-mean climatology).	1969-1979
EXP3	Same as year 1979 of EXP0 except that the light penetration through snow was impeded (i.e. i_0 was set to zero as in the original LIM2).	1979
EXP4	Same as year 1979 of EXP0 except that the advection and diffusion of sea-ice biogeochemical state variables were neglected (i.e. set to zero).	1979
EXP5	Same as year 1979 of EXP0 except that the shading effect of ice algae was neglected (i.e. set to zero).	1979

Domain

The model domain is based on the North Atlantic and Arctic (NAA) configuration developed by the ocean modelling group at the University of Alberta (`http://knossos.eas.ualberta.ca/xianmin/anha/model_configuration.html#naa`). This configuration was built on the curvilinear orthogonal coordinate system of NEMO that has been successfully applied to study the freshwater budget of the Arctic Ocean in present (Hu and Myers, 2013) and future climates (Hu and Myers, 2014), as well as to investigate pelagic ecosystem processes in the Canada Basin (Steiner et al., 2015). The NAA domain includes the Arctic Ocean, the Canadian Arctic Archipelago, the northern Bering Sea, the northern North Atlantic Ocean, and the Nordic Seas (Figure 4.3). The horizontal resolution of the 568 $\times$ 400 grid varies from 10 km along the North American boundary to 14.5 km along the Eurasian boundary. Vertically, the ocean is divided into 46 layers with variable resolution, from approximately 1 m in the uppermost layer to 255 m in the bottommost layer. This vertical resolution is finer than that of the original NAA configuration in the upper layers (Figure 4.4). The bathymetry is based on the 1 arc-min global relief data (ETOPO1; Amante and Eakins, 2009) as described by Hu and Myers (2013). For numerical stability, each ocean grid cell is set to have at least 7 vertical levels, corresponding to a depth of approximately 20 m.

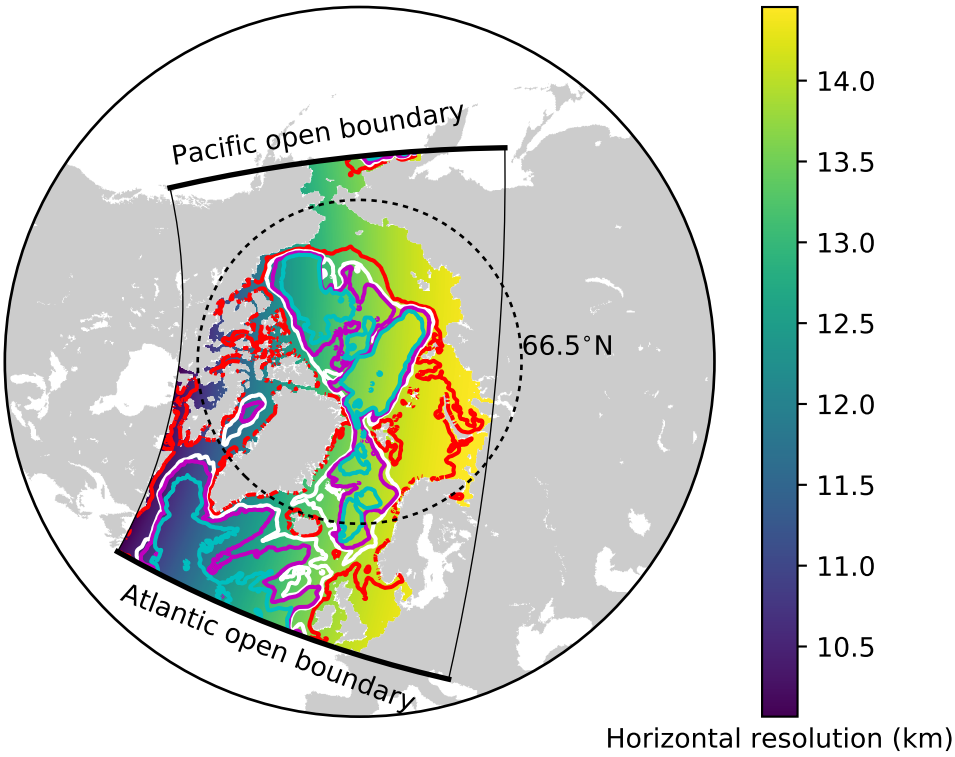

Figure 4.3: The domain of the North Atlantic and Arctic (NAA) configuration. The colour map represents the horizontal resolution and the contour lines denote the isobaths at 100 m (red), 1000 m (white), 2000 m (magenta), and 3000 m (cyan). The thick (thin) solid black lines indicate the locations of Atlantic and Pacific open (North American and Eurasian closed) boundaries.

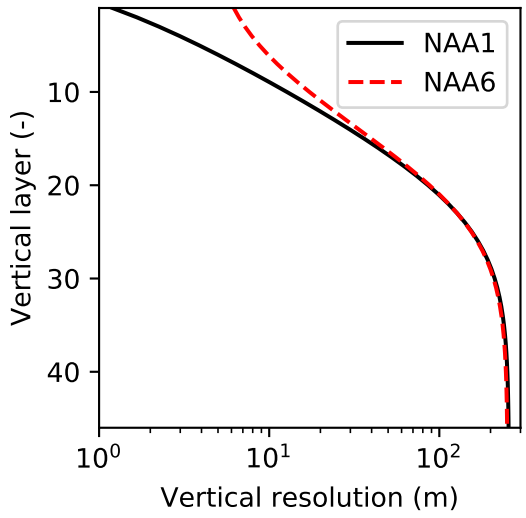

Figure 4.4: Comparison of the vertical resolution of the ocean model between the original NAA configuration (NAA6, i.e. approximately 6 m in the uppermost layer) and the configuration adopted in the present study (NAA1, i.e. approximately 1 m in the uppermost layer). Note the log scale on the x axis.

Initial and lateral boundary conditions, runoff, and atmospheric forcing

The ocean was initialized from rest with temperature and salinity fields for January 1969 derived from the Ocean Reanalysis System 4 (ORAS4; Balmaseda et al., 2013). The initial snow depth, ice thickness, and ice concentration were respectively set to 0.1 m, 2.5 m, and 0.95 for grid cells with temperatures within 2 °C of the seawater freezing point. Elsewhere, these values were set to zero. The initial concentrations of nitrate, dissolved inorganic carbon, and total alkalinity were taken from the annual-mean fields of the GLobal Ocean Data Analysis Project version 2 (GLODAP2; Lauvset et al., 2016). The initial concentrations of dissolved oxygen were set to the annual-mean fields from the World Ocean Atlas 2013 Version 2 (WOA13; Garcia et al., 2014). The initial concentration of dissolved iron was set to 0.6 nM in the entire domain (Aumont et al., 2015). Because the model simulation starts at a time of low biological production (i.e. January 1), the remaining biogeochemical state variables in the ocean were initialized uniformly in space to arbitrarily low values. The initial concentrations of sea-ice biogeochemical state variables were set to the same values as their respective variables in the uppermost layer of the ocean.

Open boundary conditions were applied by a radiation-relaxation algorithm (Madec, 2008) along the Atlantic and Pacific boundaries of the model domain, while the other two boundaries (along North America and Eurasia) were assumed to be closed (Figure 4.3). The boundary temperature, salinity, and zonal and meridional current fields were interpolated from the interannual monthly-mean fields of ORAS4. The open boundary conditions for ocean biogeochemical state variables were the same as their initial conditions. The relaxation timescales were set to 1 day for inflow and 15 days for outflow. These values are identical to those used in Dupont et al. (2015), but differ from the original NAA configuration (Hu and Myers, 2013). Our preliminary experiments suggested that these changes were needed to prevent salinity drift. Because the feature to prescribe the open boundary conditions for the sea-ice prognostic variables was not available in NEMO version 3.4, these were set to zero for the sea-ice prognostic variables of LIM2 as well as the sea-ice biogeochemical state variables; this feature is available in the subsequent version of NEMO (version 3.6).

River discharge of freshwater was derived from the interannual monthly-mean product of Dai and Trenberth (2002). The river discharge of biogeochemical state variables was neglected, and therefore, was not addressed in this study. Additional external supplies of nutrients (dust deposition and sediment mobilization)

were neglected due to the lack of reliable data. Partial pressure of carbon dioxide in the atmosphere was derived from the monthly-mean Mauna Loa CO_2 data (`https://www.esrl.noaa.gov/gmd/ccgg/trends/data.html`).

The surface atmospheric conditions used to drive the sea-ice and ocean model simulations were derived from the Drakkar Forcing Set 5.2 (DFS; Dussin et al., 2016). The DFS dataset is high resolution in space (0.7°) and time (3-hourly for zonal and meridional wind speed at 10 m height and air temperature and specific humidity at 2 m height; and daily for incoming shortwave and longwave radiation, total precipitation, and snowfall). It is based on a combination of ERA-40 and ERA-interim reanalysis products (Uppala et al., 2005; Dee et al., 2011). The original DFS dataset (`http://servdap.legi.grenoble-inp.fr/meom/DFS5.2/ALL`) has missing data flags which cause a simulation crash in some years. As a substitute, we used a modified version provided by Clark Pennelly at the University of Alberta (personal communication). Furthermore, in EXP0, the DFS snowfall and the total precipitation for year 1979 were used repeatedly for the simulation over the period 1969-1978, as opposed to the 1979-2012 daily climatology (due to the lack of adequate observations to construct the dataset for those years individually; Dussin et al., 2016). This modification was necessary to simulate adequate snow depths (discussed further in Section 4.5.1).

Additional settings

The time step of the model integration was 20 minutes. Unlike Hu and Myers (2013), no additional treatments for modelled temperature, salinity and wind-stress fields near the open boundaries were necessary since no obvious drift was apparent in the simulated fields. Table 4.3 displays some of the model parameters that were modified from their default values in NEMOv3.4. For a complete list of the parameters, readers are referred to the source-code repository (`www.gitlab.com/hakasehayashida/canoe-dms/tree/version1/CONFIG/cmoc08_naa1/EXP00`). The coefficients for horizontal eddy diffusion for oceanic and sea-ice tracers (rn_aht_0, ahi0, and rn_ahtrc_0) were reduced to keep diffusion relatively small compared to resolved dynamical processes, as recommended by Vancoppenolle et al. (2012). The other two parameters (hiccrit and pstar) were adjusted to improve the modelled sea ice volume and extent. Lastly, two parameters of CanOE (Tref and chldeg) were adjusted to simulate reasonable annual primary production in the Arctic Ocean.

Table 4.3: List of selected model parameters in the NEMO namelists

Name	Description	Unit	Value
	namelist		
rn_aht_0	Horizontal eddy diffusivity for oceanic active tracers	m^{-2} s^{-1}	5
	namelist_ice_lim2		
ahi0	Horizontal eddy diffusivity for sea-ice properties	m^{-2} s^{-1}	5
hiccrit	Thickness of newly-formed ice	m	0.6
pstar	Ice strength parameter	N m^{-2}	23,000
	namelist_top		
rn_ahtrc_0	Horizontal eddy diffusivity for passive tracers	m^{-2} s^{-1}	5
	namelist_pisces		
Tref	Reference temperature for photosynthesis, grazing, and remineralization	°C	10
chldeg	Chlorophyll oxidation rate	d^{-1}	0

Output

The output of the model experiments was saved as annual means for the first ten years (1969-1978) and five-day means for the final year (1979). Ice (snow) volume was defined as the sum of the product of grid-cell-mean ice thickness (snow depth) and the grid-cell area. Ice extent was defined as the areal sum of all grid cells with an ice concentration of at least 0.15. Primary productivity within sea ice was quantified in terms of depth-integrated (bottom 3 cm) gross primary productivity (GPP), whereas primary productivity within the water column was expressed in terms of depth-integrated (upper 90 m) net primary productivity (NPP). GPP was used for ice algae because the linear loss term for ice algae in our model accounts for processes other than just respiration, and therefore NPP cannot be derived simply by subtracting the linear loss term from the photosynthetic growth (i.e. GPP). In any case, the difference between NPP and GPP may be small for ice algae, as a previous incubation experiment suggests that NPP accounts for 60 to 100 % of GPP in the bottom layer of Arctic sea ice (Table 4 of Gosselin et al., 1997). Any grid cell whose ice concentration is 0.15 or greater was considered "under-ice" following Zhang et al. (2010). To investigate the interannual variability in pan-Arctic primary productivity, the ice algal GPP, phytoplankton NPP, and under-ice NPP were integrated annually and horizontally to derive respective pan-Arctic annual quantities. The term pan-Arctic is defined here as the region north of the Arctic Circle (66.5 °N). The pan-Arctic mean refers to an area-weighted average over the region north of the Arctic Circle. This

areal restriction allows consistent comparison to some previous studies (e.g. Legendre et al., 1992; Jin et al., 2012).

PIOMAS and SIIV3 data products

The modelled sea-ice properties were evaluated against the following observationally-based data products: the the Pan-Arctic Ice Ocean Modeling and Assimilation System (PIOMAS) and Sea Ice Index Version 3 (SIIV3) data products. Although these products are considered here as the best data products presently available, note that they have their own biases that could result in mismatches with our model results.

PIOMAS is a regional coupled sea ice-ocean circulation model that assimilates some observational data (Zhang and Rothrock, 2003; Schweiger et al., 2011). The daily-mean time series of PIOMAS ice volume were obtained from `www.psc.apl.uw.edu/research/projects/arctic-sea-ice-volume-anomaly/data`. The monthly-mean ice thickness and ice concentration gridded data products of PIOMAS were also used for spatial comparison (Dirkson et al., 2016).

SIIV3 provides an estimate for ice extent based on sea-ice concentration fields derived from passive microwave radiometers (Windnagel et al., 2017). The daily-mean SIIV3 ice extent time series were obtained from the National Snow and Ice Data Center website (`www.nsidc.org/data/G02135/versions/3`). For the year 1979, this data product is available for 182 days (i.e. every other day on average), which is sufficient to compare with the 5-day-mean model output.

4.4 Reference simulation (EXP0)

4.4.1 Interannual variability during spin up

The annual-mean time series of modelled snow and ice volumes, ice extent, seawater nitrate concentration, and ice algal and phytoplankton biomass over the 11 years of EXP0 are shown in Figure 4.5. This time period can be considered as sufficiently long to spin up some of these quantities, while others may require additional years to spin up. However, none of these quantities reach a steady state in the current setup as the model was driven by interannual surface and lateral boundary conditions. The aim of the present analysis is to diagnose potential drifts by examining the temporal variability starting from the initial year. No substantial drifts, such as monotonic increase/decrease, are simulated in any of the quantities considered.

The annual-mean modelled snow volume stabilized around 0.8×10^3 km^3 after an initial drop of about 0.1×10^3 km^3 from year 1969 to 1970 (Figure 4.5a), indicating a spin-up period of a year or so. In contrast, the annual-mean modelled ice volume variations showed an initial reduction during 1969-1971 followed by an overall increase during 1973-1979. The relatively short duration of this simulation does not allow us to distinguish between trends and slow interannual variability, so we cannot determine if the ice volume has spun up based solely on this analysis; this is addressed in a follow up study. A previous pan-Arctic regional model study of Watanabe (2013) showed a spin-up period of 10 years for modelled ice volume based on a simulation using a fixed annual cycle of atmospheric forcing and restoring of temperature and salinity.

Modelled ice extent showed a decrease in the first 6 years followed by a stabilization in the last 5 years, suggesting that this quantity spun up at year 1975 (Figure4.5b). This spin-up time is similar to that found in the pan-Arctic model study of Jin et al. (2012), in which their modelled ice area and extent became comparable to the observations after the first 6 years of simulation.

Annual-mean modelled seawater nitrate concentration integrated over the upper 90 m of the water column showed both increases and decreases during the 11 years (Figure4.5b), although the size of the fluctuation ($\sim$20 mmol N m^{-2}) is small relative to its mean state ($\sim$490 mmol N m^{-2}). Similarly to ice volume, a longer simulation would be needed to distinguish between trends and interannual variability in the modelled nitrate concentration. A previous pan-Arctic model study of Dupont (2012) indicated a spin-up period of at least a decade for nitrate in the upper 100 m water column for the model domain he considered. The modelled primary producers (ice algae and phytoplankton) appear to have spun up within a year of the model simulation, as their annual primary production fluctuates around a steady mean following the first year (Figure 4.5c).

4.4.2 Comparison of sea-ice physical properties with PIOMAS and SIIV3 during the year 1979

Seasonal variability

To assess the performance of the model simulation of sea ice, the seasonal variability of modelled ice volume and extent in EXP0 were compared to PIOMAS and SIIV3 (Figure4.6a and b) for the year 1979. This year corresponds to the first full year available for these data products. The ice volume in both EXP0 and PIOMAS was

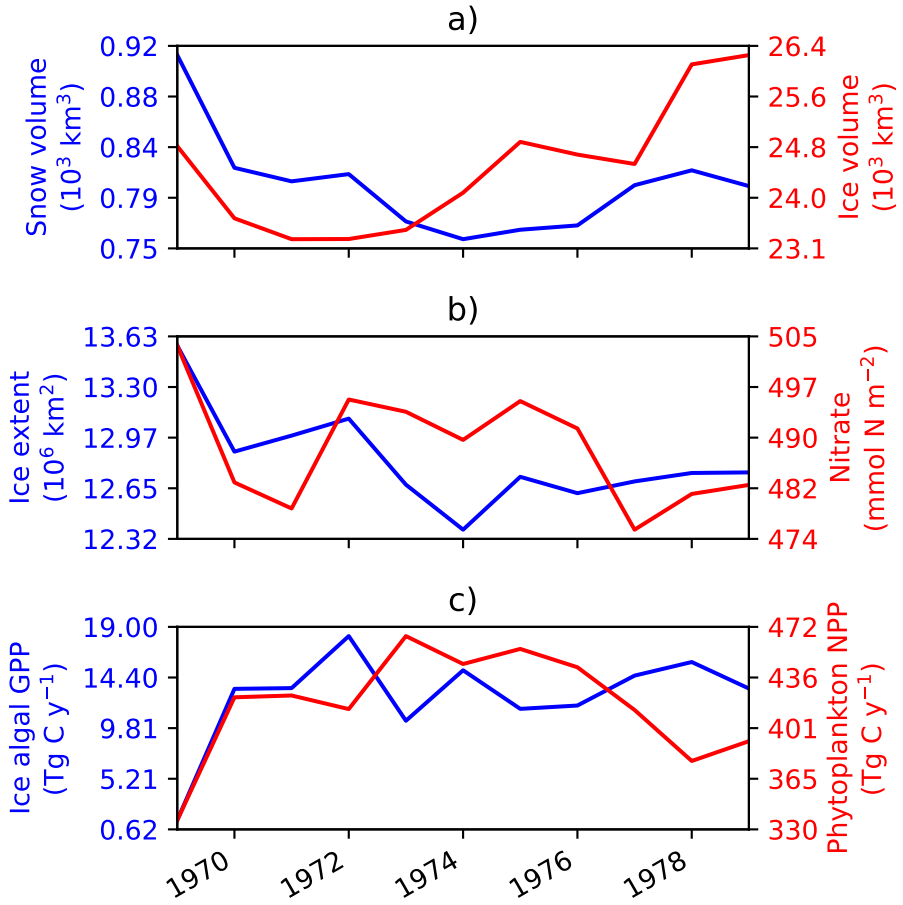

Figure 4.5: Time series of annual-mean modelled a) snow and ice volumes, b) ice extent and depth-integrated (90 m) seawater nitrate concentration, and c) depth-integrated (3 cm) ice algal GPP and depth-integrated (90 m) phytoplankton NPP in EXP0. The depth-integrated quantities represent averages over the entire model domain.

at its annual maximum in late April (April 25 vs 28) and at its annual minimum in September (September 10 vs 21). The ice extent in EXP0 and SIVV3 was at its annual maximum in March (March 24 vs 1) and at its annual minimum in September (September 25 vs 21). Given the difference in the frequency of the model output and these data products (5-day vs daily), the timings of the ice volume maximum and the ice extent minimum are comparable. The most prominent disagreement is in the timing of the ice extent maximum in which EXP0 lags by a few weeks. The seasonal recession of Arctic sea ice started later in EXP0 partly because our domain excludes lower-latitude regions that were ice-covered in 1979 (e.g. the Sea of Okhotsk and the Gulf of Saint Lawrence), and the seasonal retreat of sea ice in these areas occurred earlier (confirmed using the Sea Ice Spatial Comparison Tool: `www.nsidc.org/arcticseaicenews/sea-ice-comparison-tool`).

The ice volume is slightly higher in EXP0 than PIOMAS throughout the year, with the largest difference of about 3000 km^3 taking place in May-June. The ice extent, on the other hand, is generally lower in EXP0 than SIIV3, and their difference is greater than 1×10^6 km^2 during the season of greatest extent (December-May). Much of this difference can be attributed to the fact that the model domain excludes regions that are usually ice covered during that period, such as Hudson Bay (covering a surface area of 1.23×10^6 km^2) and the Sea of Okhotsk (1.58×10^6 km^2). During the remainder of the year, the modelled ice extent is in closer agreement with SIIV3 (especially in August-September).

Spatial variability

Figure 4.7 shows the spatial variability in modelled March- and September-mean ice thickness fields in EXP0 and PIOMAS. The extent of modelled Arctic sea ice can be inferred from the location of the ice edge, defined here as the 0.15 contour of ice concentration (Figure 4.7a,b,d,e). Overall, the locations of the ice edge within our model domain are similar between EXP0 and PIOMAS for both March and September. Beyond the model domain, the ice coverage in March extends to Hudson Bay and the Sea of Okhotsk in PIOMAS (Figure4.7b). The March-mean ice thickness distribution in EXP0 includes a band of >5-m-thick ice along the coast of the Canadian Arctic Archipelago extending east to Greenland, and a region of relatively thick ice ($\sim$4 m) in the Arctic Basin north of the East Siberian Sea (Figure4.7a). The band is also present in PIOMAS, although it is restricted to the north of Greenland (Figure4.7b).

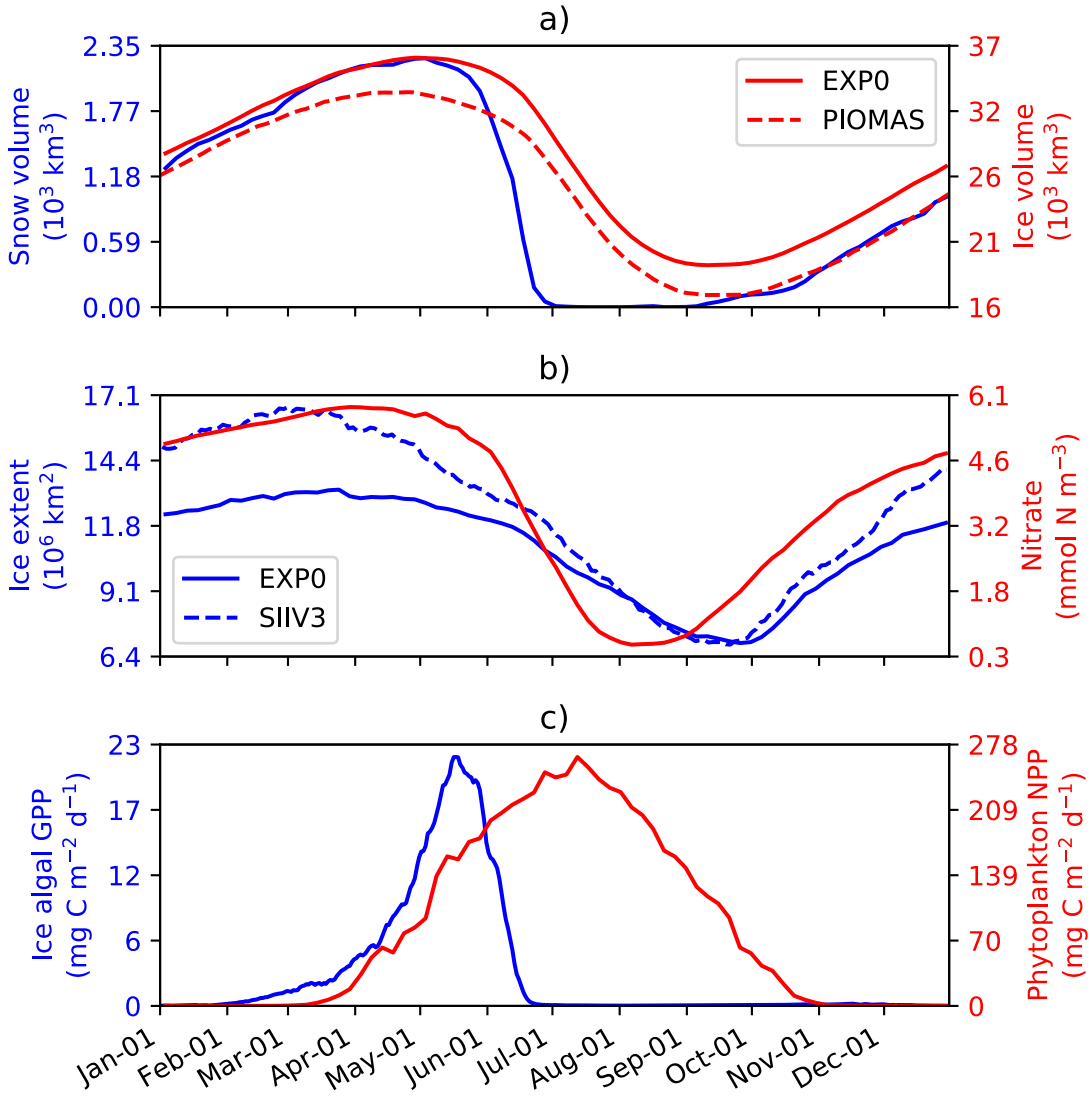

Figure 4.6: Time series of 5-day-mean modelled a) snow and ice volumes, b) ice extent and pan-Arctic-mean surface seawater nitrate concentration, and c) pan-Arctic ice algal GPP and phytoplankton NPP during 1979 in EXP0. The dashed lines in a) and b) represent the daily-mean ice volume and extent of PIOMAS and SIIV3, respectively.

The thick ice region in the Arctic Basin north of the East Siberian Sea, on the other hand, is absent in PIOMAS. Besides these regions entailing the band and the thick ice region, EXP0 generally simulated thicker ice than PIOMAS in the Greenland Sea and various shelf regions (Figure4.7c). On the other hand, EXP0 simulated thinner ice than PIOMAS on the Canadian Polar Shelf, and in the Chukchi Sea, the Barents Sea, the Kara Sea, and an area near the North Pole (Figure4.7c).

In September, the most notable features in the ice thickness distribution are the presence of thinner (<2 m) ice in an area near the North Pole in EXP0 (Figure 4.7d), and thick (>5 m) ice along the coast of Siberia in PIOMAS (Figure 4.7e). The latter feature seems unrealistic considering that: it is thicker in September than in March; and it is thicker than the multi-year ice present along the band north of the Canadian Arctic Archipelago and Greenland. Both of these features constitute negative ice thickness anomalies in the model relative to PIOMAS (Figure 4.7f). The difference is also negative and large (∼3 m) in the Canadian Polar Shelf; this could be due to the fact that the horizontal resolution of PIOMAS (∼22 km; Zhang et al. (2010)) is too coarse to resolve the circulation through these relatively narrow channels, resulting in the simulation of too thick first-year ice in this region at this particular time of the year. The ice thickness is greater in EXP0 than in PIOMAS in the Arctic Basin, part of the East Siberian Sea, and the Laptev Sea as well as along the eastern coast of Greenland.

4.4.3 Primary productivity of ice algae and phytoplankton

Seasonal variability

Figure 4.6 shows the seasonal variability in modelled pan-Arctic-mean ice algal GPP and phytoplankton NPP during 1979 (panel c) along with relevant environmental factors (panels a and b). Ice algal GPP started increasing in early February, peaked in mid May, sharply declined in late May-early June, and was near zero by late June. The start of the decline of the ice algal GPP coincided with the decline of the ice volume (Figure 4.6a) demonstrating that the decline was driven by the release of ice algae as a result of ice melt. The seasonal progression of the ice algal production is similar to Jin et al. (2012). The phytoplankton NPP started increasing in early March, peaked in early July, and decreased to near zero by the end of October (Figure 4.6d). At the peak in phytoplankton NPP, the pan-Arctic-mean surface seawater nitrate concentration was below 1 mmol N m^{-3} and remained so until the end of August

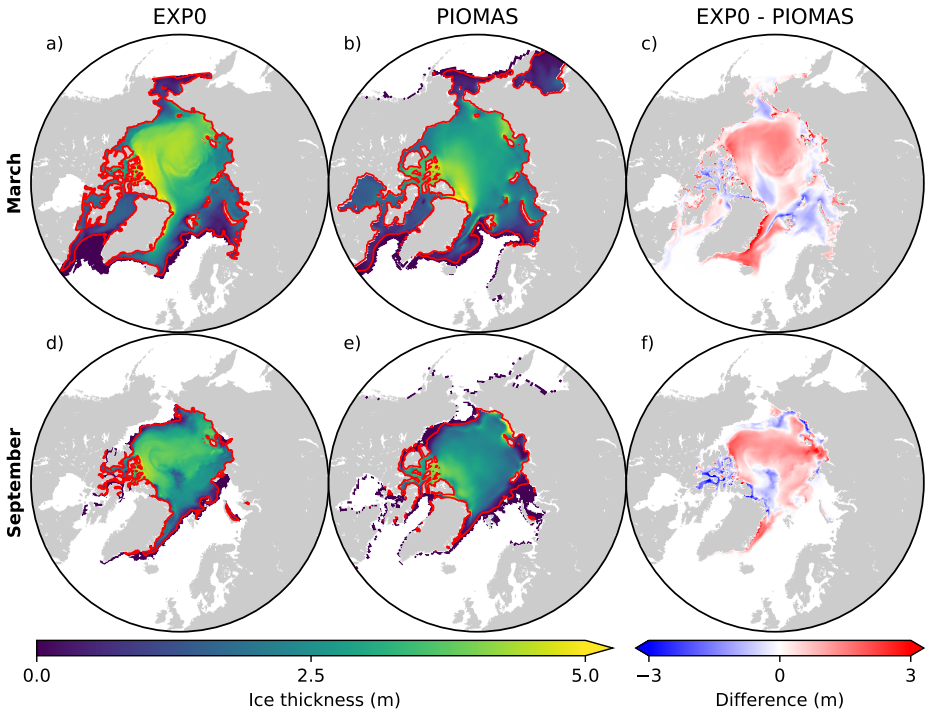

Figure 4.7: Spatial distributions of monthly-mean ice thickness in EXP0 (a,d) and the PIOMAS product (b,e) and their difference (c,f) for March and September in 1979. The red lines represent the ice edge, defined here as the 0.15 contour of ice concentration. In c) and f), the comparison is restricted to the NAA domain.

(Figure 4.6b).

Spatial variability

Figure 4.8 shows the spatial distribution of annual-mean snow depth, surface seawater nitrate concentration, ice algal GPP, and phytoplankton NPP for 1979. The largest values of ice algal annual GPP (>10 g C m^{-2} y^{-1}) are present in the coastal regions of Baffin Bay, the Canadian Polar Shelf, the Chukchi Sea, the East Siberian Sea, and the Kara Sea (Figure 4.8c). All of these regions have relatively thin snow (less than 0.1 m; Figure 4.8a), demonstrating the control of light on ice algal growth. In contrast, the nutrient control on ice algal production is less pronounced; although high ice algal GPP usually concides with high surface seawater nitrate, it is also present in a few areas where the nitrate levels are relatively low (Baffin Bay and Chukchi Sea; Figure 4.8b). Overall, ice algal production is mostly confined to shelf regions (water depth <100 m; Figure 4.3), consistent with previous model studies (Deal et al., 2011; Dupont, 2012; Jin et al., 2012, 2018). However, the values reported in Deal et al. (2011), Jin et al. (2012), and Jin et al. (2018) are representative of NPP, while those of Dupont (2012) and the present study represent GPP; comparisons should be made with this difference in mind.

There are a few noteworthy similarities and differences in the spatial variability in modelled ice algal annual production between the present study and previous model studies. All studies show a moderate-to-high level of ice algal production in Baffin Bay. In contrast, disagreement in the ice algal production is found along the eastern coast of Greenland and in the Bering Sea; the values along the eastern coast of Greenland are moderate (5-10 g C m^{-2} y^{-1}) in Deal et al. (2011) and Jin et al. (2012), while they are low (less than 5 $^{-2}$ y^{-1}) in Dupont (2012), Jin et al. (2018), and the present study. Similarly, although Bering Sea is identified as a region of high ice algal production by Deal et al. (2011), Jin et al. (2012), and Jin et al. (2018), Dupont (2012) and the present study simulate low ice algal production in this region. A possible explanation for the lower ice algal production in this region in the latter studies is due to an insufficient nutrient supply from the Pacific boundary as discussed in Dupont (2012). Lastly, the recent study by Jin et al. (2018) finds the Sea of Okhotsk to be a region of elevated ice algal annual production, which we are unable to assess in the present study due to the limited model domain.

The modelled phytoplankton annual NPP is high (>100 g C m^{-2} y^{-1}) in the

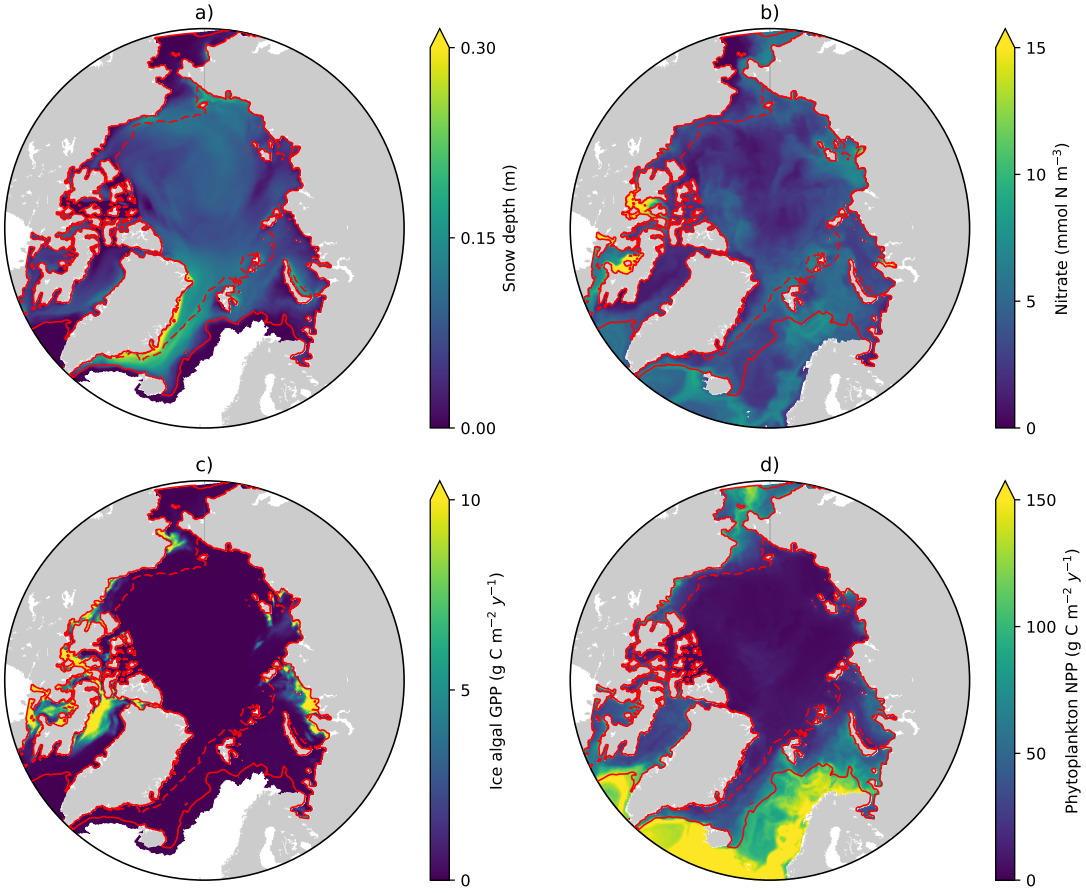

Figure 4.8: Spatial distribution of annual-mean a) snow depth and b) surface seawater nitrate concentration, and c) depth-integrated (bottom 3 cm) ice algal annual GPP and d) depth-integrated (upper 90 m) phytoplankton annual NPP in 1979 in EXP0. The solid and dashed red lines represent the 0.15 contour of monthly-mean ice concentration in March and September, respectively.

Atlantic and the Pacific sectors with little to no ice cover, moderate (50-100 g C m^{-2} y^{-1}) in the shelf seas along the North American and the Eurasian continents, and low (<50 g C m^{-2} y^{-1}) in the interior of the Arctic Ocean (Figure4.8d). These findings are in both qualitative and quantitative agreement with the results of five different models and satellite-based estimates (Figure 1 of Popova et al., 2012).

Interannual variability

The modelled pan-Arctic ice algal annual GPP in EXP0 ranged from 10.5 to 18.2 Tg C y^{-1} for the period 1970-1979, excluding the initial spin-up year. While this value

is on the lower end of the range of observation-based NPP estimates (9-73 Tg C y^{-1}; Legendre et al., 1992), it is close to the decadal mean of the annual NPP (10.1 Tg C y^{-1} for 1998-2007) simulated by Jin et al. (2012). The pan-Arctic estimates by Legendre et al. (1992) are quite speculative as they are based on the integration of a single ice algal production value over a specified ice area (discussed in detail in Deal et al. (2011)). The close agreement between the two model-based estimates suggests that the lower end of the observation-based estimates is more plausible than their upper end. Although the upper end accounts for contribution from mat and strand communities that are not represented in our model, their contribution to the pan-Arctic production should be small as their spatial distribution is generally localized (e.g., Assmy et al., 2013). Direct comparisons with the results of Deal et al. (2011) and Dupont (2012) are not possible because the reported values in those studies include contributions from below the Arctic Circle. The modelled pan-Arctic phytoplankton annual NPP in EXP0 ranged from 378 to 465 Tg C y^{-1}, which is in line with the observation-based estimate (>329 Tg C y^{-1}; Total High Arctic) of Sakshaug (2004), the satellite-based estimate (419 Tg C y^{-1} for 1998-2006) of Pabi et al. (2008), and the model-based estimate (627 Tg C y^{-1} for 1998-2006) of Jin et al. (2012).

4.4.4 Vertical distribution of salinity, nitrate, chlorophyll *a*, and DMS in the upper water column

The seasonal variability of pan-Arctic-mean seawater salinity, nitrate, chlorophyll *a*, and DMS in the upper 15 m of the water column is shown in Figure 4.9. During the summer, a prominent freshening of the uppermost layer occurs as a result of ice melt (Figure 4.9a). This freshening results in formation of a thin layer of low-salinity water known as a meltwater lens, which strengthens stratification and reduces mixing with the underlying water column. The formation of the lens coincides with the bloom of modelled phytoplankton, resulting in the depletion of nitrate first in the uppermost model layer and then in the underlying layers (Figure 4.9b). Nutrient depletion in the near surface waters then results in formation of subsurface chlorophyll *a* and DMS maxima during the latter half of July (Figure 4.9c and d).

These ice-associated physical and biogeochemical processes took place within a relatively shallow upper water column (∼10 m), and would have been impossible to simulate with a model of coarse vertical resolution. It is for this reason that the near-surface vertical resolution of the NAA configuration considered in the present

study is finer than that of the original configuration (6 m in the uppermost layer; Hu and Myers, 2013). Although modelling these small-scale processes probably has negligible effect on bulk quantities such as depth-integrated NPP, it can have an impact on processes at the air-sea or ice-sea interface (e.g. gas fluxes). To illustrate this point, the time series of modelled pan-Arctic-mean seawater DMS concentration in the uppermost layer of the water column (about 1 m) was compared with the concentration averaged over the top four layers (about 12 m) as a proxy for values simulated by a coarse-vertical-resolution model (Figure 4.10).

DMS concentration is higher in the uppermost layer than in the 12-m layer throughout most of April-September, but slightly lower in August (Figure 4.10b). The concentration difference is largest (up to about 20 %) in June-July. The highest DMS concentrations are found in the upper 1 m until the formation of the subsurface maximum (Figure 4.9c). Overall, annual-mean DMS concentration averaged over the upper 12 m of the water column is 9 % lower than in the upper 1 m. Considering that this difference is present primarily during the ice melt period, and therefore that the sea-surface DMS is released into the atmosphere, the sea-to-air DMS flux would be underestimated by a similar amount using the 12-m resolution time series.

4.5 Sensitivity experiments (EXP1-5)

4.5.1 Snowfall forcing frequency (EXP1 and 2)

Two sensitivity experiments (EXP1 and EXP2) were performed with the identical setup as EXP0 except for a change to the atmospheric forcing. In EXP1, all the forcing fields were replaced by the CORE-II dataset used in the original NAA configuration (Hu and Myers, 2013). In EXP2, the snowfall and total precipitation fields over the period 1969-1978 were replaced by their respective 1979-2012 daily climatological values as in the original DFS dataset (Dussin et al., 2016).

A comparison of the pan-Arctic-mean snowfall rates between the CORE-II and DFS datasets illustrates the differences between these datasets (Figure 4.11a). The monthly CORE-II dataset varies from approximately 1 to 2.4 mm d^{-1}, while the range of the DFS dataset is three times as large (from near 0 to about 4.4 mm d^{-1} for the year 1979) most likely due to the difference in the temporal resolution of the datasets. The lack of high frequency variability in the DFS daily climatology is evident from the comparison of the DFS dataset between 1969-1978 and 1979. The daily climatology

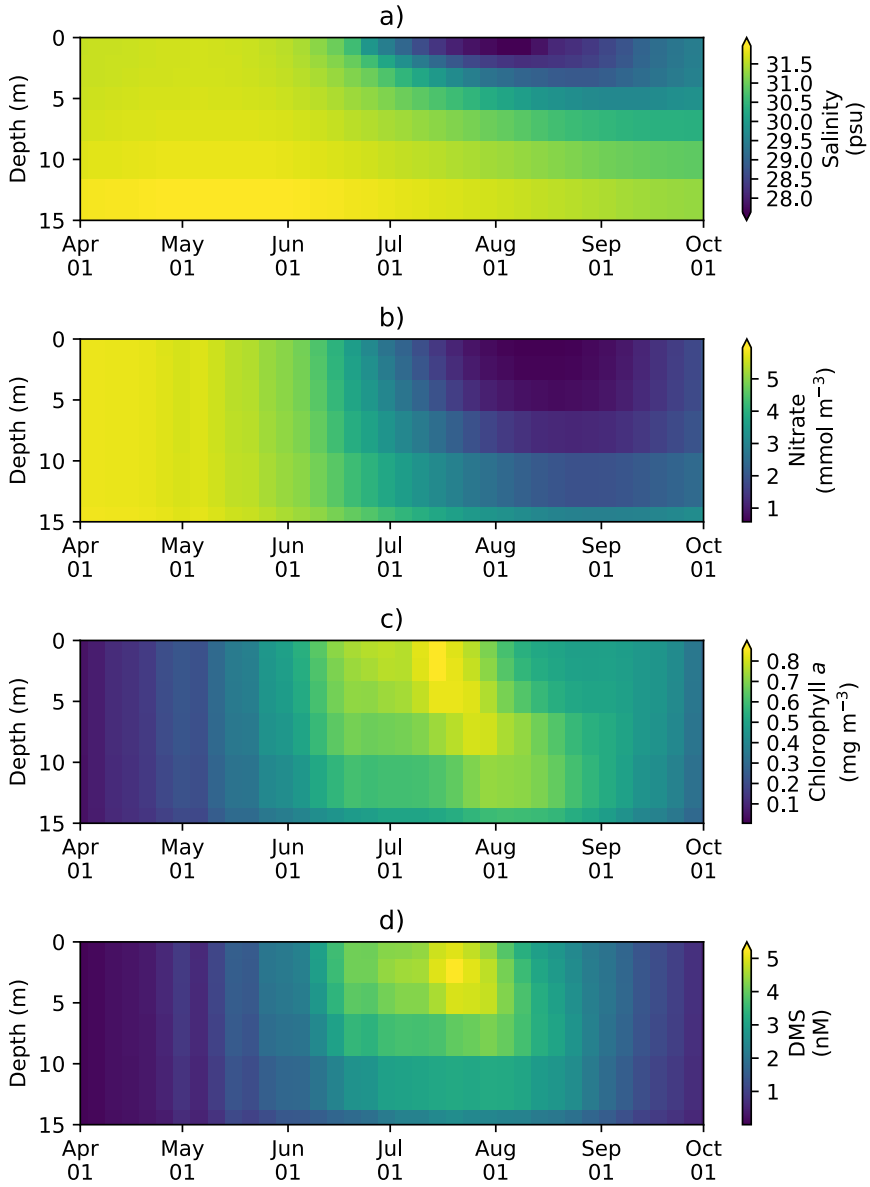

Figure 4.9: Time series of 5-day- and pan-Arctic-mean seawater a) salinity, and concentrations of b) nitrate, c) chlorophyll *a*, and d) DMS in the upper 15 m of the water column during April-September in 1979 of EXP0.

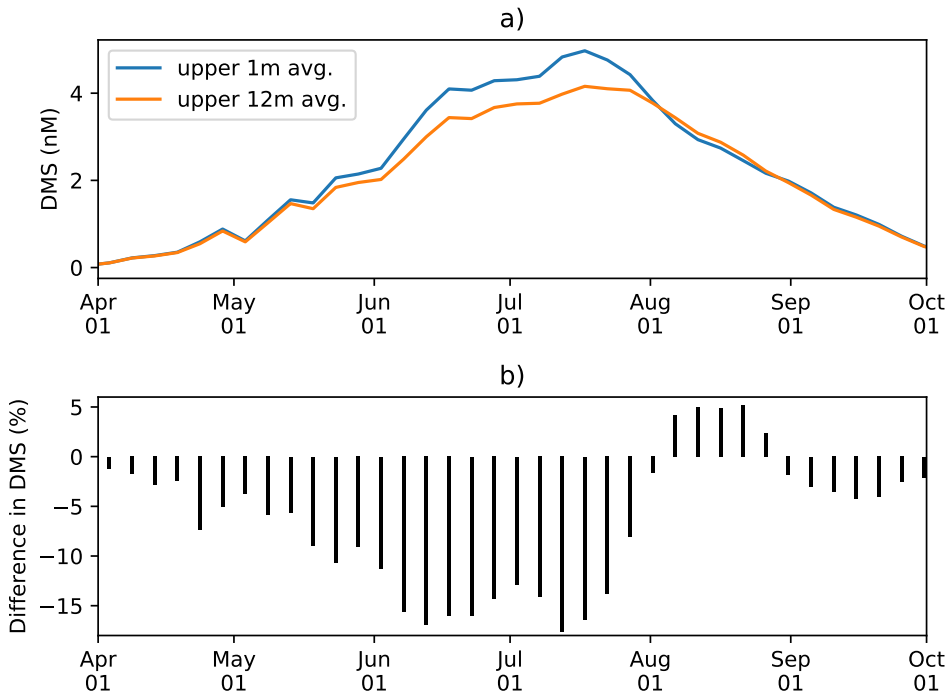

Figure 4.10: a) Time series of 5-day- and pan-Arctic-mean seawater DMS concentration a) in the uppermost layer (∼1 m; blue) and averaged over the upper four layers (∼12 m; orange) during April-September in 1979 of EXP0. b) The percentage difference between the two time series (the 1-m average minus the 12-m average, divided by the 1-m average).

ranges approximately from 0.2 to 2.2 mm d^{-1}, less than half of the range for the individual daily averages for 1979. The annual-mean CORE-II snowfall rate is higher than that of the DFS dataset in all of these years. The annual mean of the DFS daily climatology is slightly greater than that of the individual daily averages for 1979.

Figure 4.11b shows a comparison of the modelled pan-Arctic annual-mean snow depth among EXP0, EXP1, and EXP2. The snow depth was substantially lower in EXP1 and EXP2 than in EXP0 throughout the period 1969-1979, except for 1969 (in which year the snow depth is affected by its initial value). In EXP2, the extremely-low snow depth somewhat recovered in 1979.

Figure 4.11c-e shows a spatial comparison of the modelled annual-mean snow depth over the period 1970-1978 (excluding the first and last year of simulation). There is a clear difference in the distribution between EXP0 and the other two experiments; the ice pack was generally covered by moderate amount of snow ($\sim$0.1 m) in EXP0, while in EXP1 and EXP2, most regions were nearly snow-free. These results of the latter two experiments are inconsistent with the available snow depth climatology indicating the presence of considerably thicker (>0.2 m) annual-mean snow cover over the Arctic Basin (Warren et al., 1999). As a result of these biases, the modified DFS dataset was used as the reference simulation, rather than the CORE-II dataset or the original DFS dataset.

It is interesting that the modelled pan-Arctic annual-mean snow depth was higher in EXP0 than EXP1 even though the prescribed annual-mean snowfall rate was consistently higher in the latter experiment (Figure 4.11a). Furthermore, the recovery of the modelled snow depth in 1979 of EXP2 is also interesting given that there is essentially no change in the total snowfall amounts between 1978 and 1979. These results indicate a high sensitivity of the modelled snow depth to the temporal resolution of the snowfall dataset. This interpretation is reinforced by the fact that the modelled snow depth is also sensitive to the parameter nn_fsbc, which defines the frequency of the computation of surface boundary conditions and sea-ice physics relative to that of ocean dynamics. Figure 4.12 compares the annual-mean modelled snow depths for year 1970 of EXP2 with those of the simulations that varied nn_fsbc from the default value of 1 (i.e. the time step for surface boundary condition and sea-ice physics is identical to the ocean time step) to 5 and 10 (i.e. surface boundary condition and sea-ice physics are computed at every 5 and 10 ocean time steps, respectively). We found that setting nn_fsbc to 5 or 10 increased the modelled snow depth quite remarkably (Figure 4.12). This high sensitivity to the choice of nn_fsbc is somewhat

unexpected given that the tested range (1-10 time steps or 20-200 minutes) is far less than the temporal resolution of the CORE-II dataset. Perhaps there is a non-linear temporal dependence in the surface boundary treatment or the sea-ice dynamics. A more detailed analysis of the model sensitivity to nn_fsbc is outside the scope of this study.

4.5.2 Light penetration through snow column (EXP3)

Figure 4.13 compares the modelled sea-ice physical and biogeochemical properties in 1979 in EXP0 with those of EXP3, in which i_0 for snow was set to the default LIM2 value of zero. The results for modelled snow and ice volume were almost identical between the two experiments (Figure 4.13a), indicating a low sensitivity of these physical quantities to the change in i_0. On the other hand, an appreciable difference in the modelled bottom-ice PAR prior to the melt season in June results in a large difference in the modelled ice algal GPP (Figure 4.13b). By construction, ice algal GPP in EXP3 is restricted to snow-free regions, so an increase in the ice algal GPP due to the change in i_0 reflects production in snow-covered regions (Figure 4.13c). The pan-Arctic ice algal annual GPP of EXP3 is 3.5 Tg C y^{-1}, only about a quarter of the value obtained in EXP0. This value is much lower than those obtained in previous studies (see Section 4.4.3). This result emphasizes the importance of correct representation of the light penetration through snow, and shows that the original LIM2 provides inadequate light for ice algal growth, resulting in insufficient ice algal GPP. Note that the default value of i_0 is also set to zero in LIM3 (Vancoppenolle et al., 2012).

Previous 3D sea-ice biogeochemical models differed in their choices of values for i_0 (Table 4.1). The studies of Dupont (2012) and Jin et al. (2012) set this value to zero, yet their values for simulated ice algal productivity were relatively high. However, these models used special parametarizations for irradiance and light limitation, respectively, which likely resulted in realistic ice algal primary production values despite the lack of light penetration through snow. Dupont (2012) imposed a minimum lead fraction of 0.01 in any grid cell, supplying enough ambient light for ice algal growth. In Jin et al. (2012), the light limitation parameter (the ratio of light-limited slope and maximal photosynthetic rate; see Table 2 of Jin et al., 2006) was set to a very high value, nearly double the upper limit of the observed range reported in Table 2 of Lavoie et al. (2005). This reduction in light limitation allows the modelled ice algae

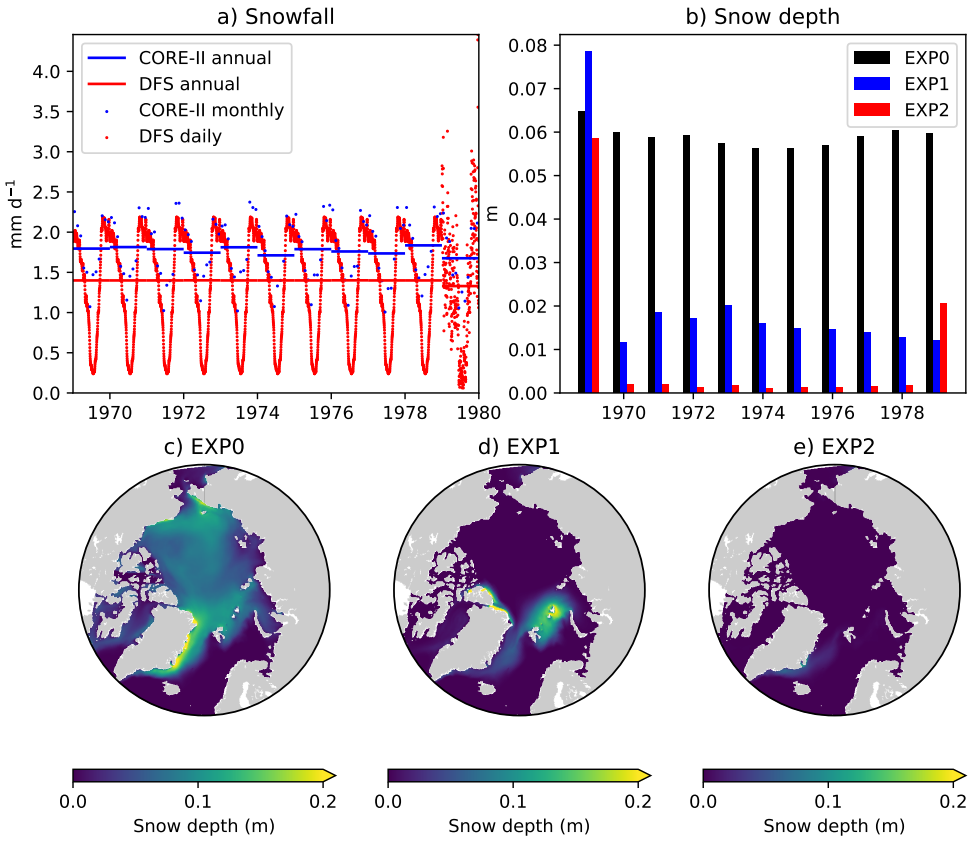

Figure 4.11: Model sensitivity to snowfall forcing frequency. Time series of pan-Arctic-mean a) prescribed snowfall rate of the CORE-II (blue) and DFS (red) datasets and b) modelled annual-mean snow depth in EXP0 (black), EXP1 (blue), and EXP2 (red). Spatial maps of modelled annual-mean snow depth for the period 1970-1978 in c) EXP0, d) EXP1, and e) EXP2. The units for the snowfall rate was converted from kg m^{-2} s^{-1} to mm d^{-1} using a constant snow density of 330 kg m^{-3}, which is the value assumed in LIM2.

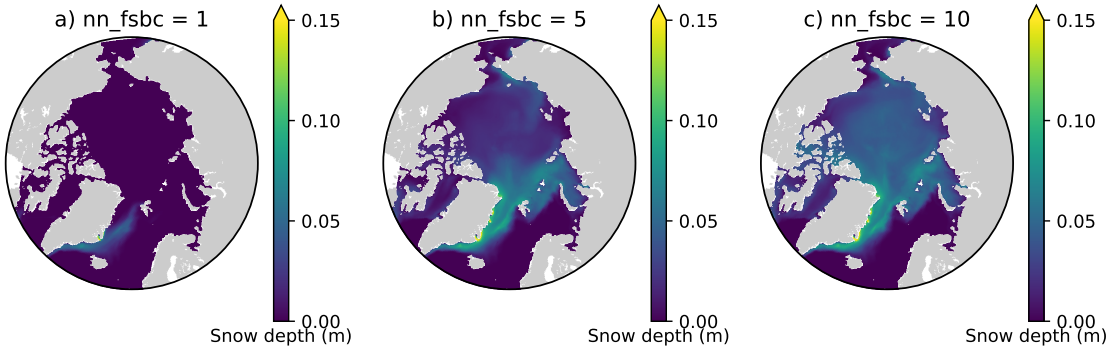

Figure 4.12: Sensitivity of modelled snow depth to the parameter nn_fsbc, which defines the frequency of the computation of surface boundary conditions and sea-ice physics relative to that of ocean dynamics. Spatial distribution of annual-mean modelled snow depth for 1970 when nn_fsbc is set to a) 1 (default), b) 5, and c) 10.

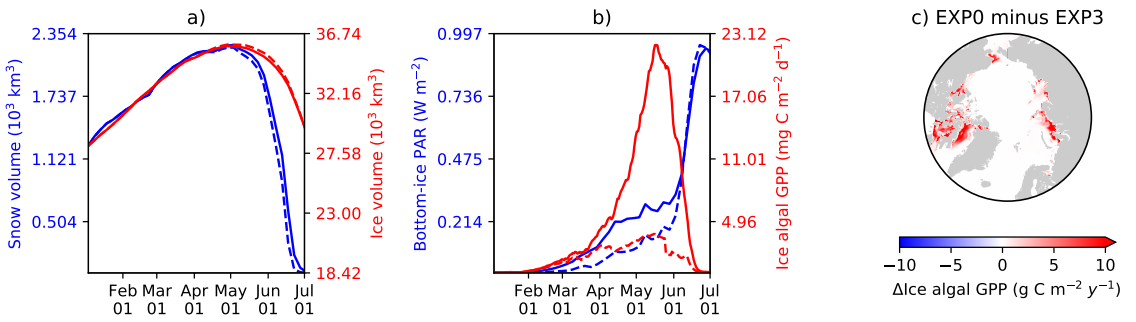

Figure 4.13: Model sensitivity to light penetration through snow. Time series comparison of modelled 5-day-mean a) snow volume (blue) and ice volume (red) and b) bottom-ice PAR (blue) and ice algal GPP (red) in 1979 between EXP0 (solid) and EXP3 (dashed). c) Spatial distribution of the difference in the ice algal annual GPP between EXP0 and EXP3.

to grow faster even under low light conditions.

Two other regional modelling studies prescribed non-zero values of i_0. Castellani et al. (2017) set i_0 to 0.3 based on the measurements over snow-free ice surface (Grenfell and Maykut, 1977). As such, this value should be viewed as an overestimate. Similarly, the light penetration through snow was also overestimated in Watanabe et al. (2015), as i_0 was effectively unity in their study. Using these higher i_0 reduces light limitation, and hence enhances ice algal primary production.

To the best of the authors' knowledge, no studies have ever reported an observed value for i_0. For a snow-free ice surface, Grenfell and Maykut (1977) reported the values ranging between 0.18 and 0.63 depending on both the ice type and whether the incoming shortwave radiation is direct or diffuse. Observation-based estimates of i_0 would be useful in order to reduce the uncertainty of ice algal and under-ice phytoplankton growth in models.

4.5.3 Horizontal transport of sea-ice biogeochemical state variables (EXP4)

EXP4 was conducted with the identical model formulation as EXP0 except that the advection and eddy diffusion of sea-ice biogeochemical state variables were neglected. Note that the advection and diffusion of sea-ice physical state variables were retained in EXP4, so there is no difference in the these variables between EXP0 and EXP4.

A time series comparison of the modelled pan-Arctic-mean bottom-ice nitrate and

ice algal GPP for 1979 shows that these quantities are always higher in EXP0 than EXP4 (Figure 4.14a). The pan-Arctic annual-mean bottom-ice nitrate and the ice algal annual GPP are higher in EXP0 than EXP4 by 2 and 16 %, respectively.

Although the overall effect is an enhancement, the spatial distribution shows regions of local increase and decrease (Figure 4.14c-d). The difference in nitrate concentration between the two experiments is relatively high off the west coast of Baffin Island, where the bottom-ice nitrate concentration is relatively high in EXP0 (Figure 4.14b), whereas the difference is relatively small on the Canadian Polar Shelf (Figure 4.14c). The difference in ice algal GPP is relatively high in regions of high ice algal GPP except for the Canadian Polar Shelf (Figure 4.14d), which is a region of relatively slow ice motion (Figure 4.14e). A possible explanation for these spatial differences is that the horizontal transport of sea ice takes ice algae out of regions of high productivity into regions of low productivity, opening up space for new growth in the productive regions.

4.5.4 Shading of ice algae (EXP5)

In EXP5, the shading effect of ice algae on light transfer through the ice was neglected in order to assess its impact on under-ice NPP. On the pan-Arctic scale, there is almost no effect, as shown in Figure 4.15a. The differences in the pan-Arctic- and annual-mean under-ice PAR and the pan-Arctic under-ice annual NPP between EXP0 and EXP5 are 2 % and 1 %, respectively.

Consistent with the patchiness of the ice algal distribution (Figure 4.8c), the shading effect is rather localized as shown in Figure 4.15b-e. The influence on under-ice PAR is assessed for the month of the ice algal bloom peak (May; Figure 4.6c). By construction, the spatial distribution of the difference in the under-ice PAR between EXP0 and EXP5 is simply a reflection of ice algal abundance (Figure 4.15c). Similarly, a general decrease in the under-ice NPP is found due to shading in the regions of high modelled ice algae. However, in some regions, shading results in a slight increase in under-ice NPP. A possible explanation for this phenomenon is that the reduction in nutrient drawdown under regions of large ice algal biomass enhances nutrient advection into regions of low ice algal biomass.

The shading effect of ice algae was recently examined in the model study of Castellani et al. (2017). Their results showed that the effect has greater influence at higher latitudes due to low ambient light. Furthermore, they hypothesized that the onset of

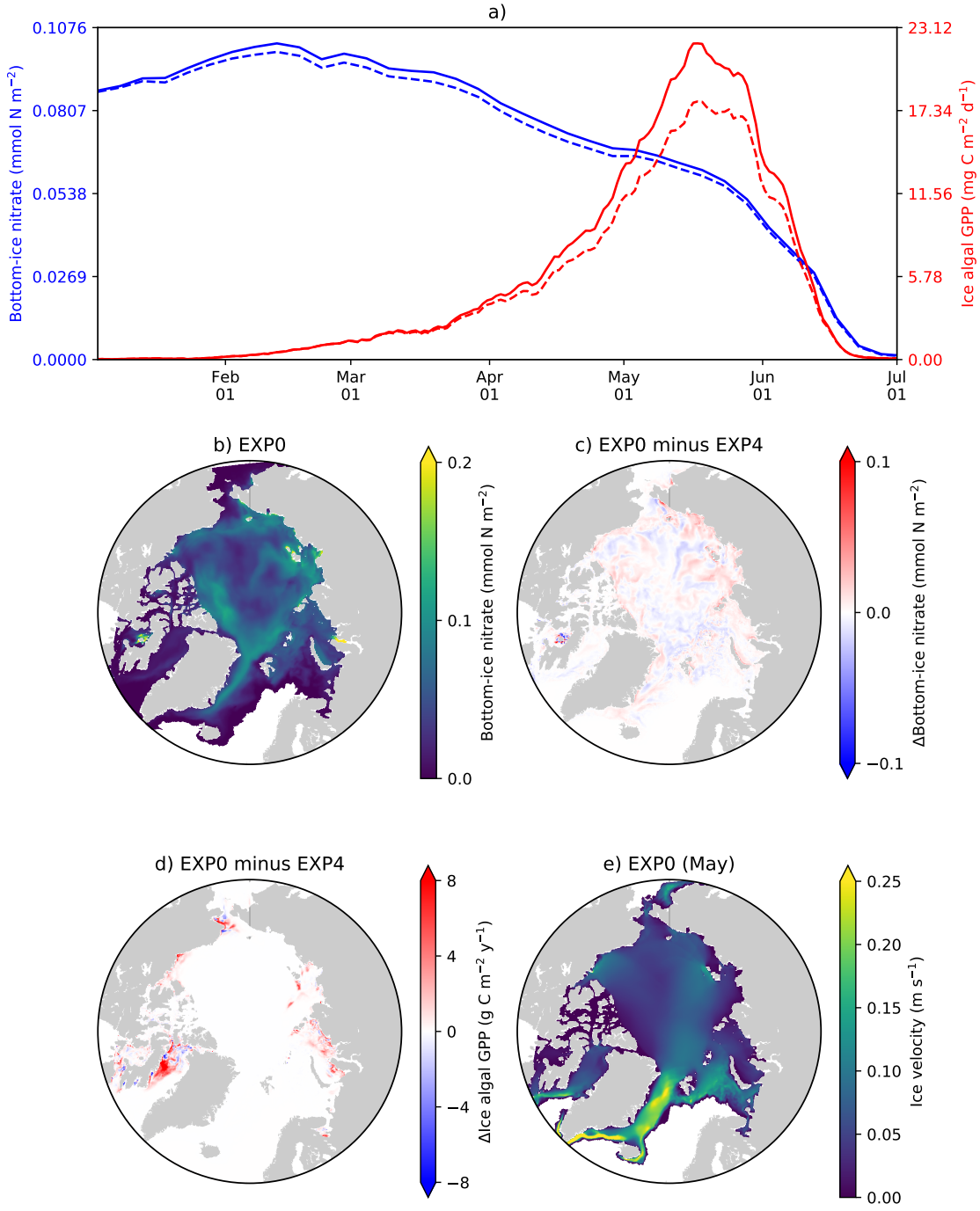

Figure 4.14: Model sensitivity to the advection and diffusion of sea-ice biogeochemical state variables. a) Time series comparison of 5-day- and pan-Arctic-mean modelled bottom-ice nitrate (blue) and ice algal daily GPP (red) during January-June of 1979 between EXP0 (solid) and EXP4 (dashed). Spatial maps of the annual-mean bottom-ice nitrate in b) EXP0 and c) its difference between EXP0 and EXP4, d) the difference in the ice algal annual GPP between EXP0 and EXP4, and e) the magnitude of the ice velocity during May.

the under-ice phytoplankton bloom north of 80°N can be delayed by up to 40 days depending on how their modelled under-ice PAR is affected by shading.

It is difficult to directly compare the results of the present study with those of Castellani et al. (2017), primarily due to the difference in the definition of the term under-ice. As described in Section 4.3.4, in the present study, a grid cell is considered "under-ice" as long as the ice concentration is 0.15 or above. Because of the strong light attenuation by snow and ice, the under-ice PAR defined in the present study is therefore dominated by the light through the open-water fraction. Consequently, the under-ice NPP is controlled by the light through the open-water fraction and does not show a strong influence by the shading of ice algae.

To carry out an analysis comparable to that of Castellani et al. (2017), we calculated the onset of under-ice phytoplankton bloom as follows. A bloom onset is defined as the day when bottom-ice PAR exceeds 0.4 W m^{-2} and remains above this value at least for 30 days. This threshold for bottom-ice PAR corresponds to the limit for under-ice algal growth considered in Castellani et al. (2017), assuming an unit conversion (from μmol photon m^{-2} s^{-1} to W m^{-2}) factor of 1/4.56 (Lavoie et al., 2005). Figure 4.16 shows the spatial variability in the under-ice bloom onset based on the definition above. The bloom took place mostly in seasonally ice-covered regions, while it was absent in most of the pack ice (as indicated by white regions). Unlike Castellani et al. (2017), the under-ice bloom north of 80°N was absent even without the shading effect. The absence of the bloom in our simulation is due to the presence of snow in this region; despite the extremely low quantity (< 0.01 m; data not shown), it kept the light level below the threshold for the bloom to occur. The median value of the onset is on the 155th day (June 6) when the shading is accounted (Figure 4.16a), while it is 10 days earlier without the shading effect (Figure 4.16b).

Figure 4.16c shows the spatial variability in the delay in the under-ice bloom onset caused by the ice algal shading. The values range from 5 to 275 days; in some places, the bloom is prevented completely. The present study does confirm the finding of Castellani et al. (2017) that the shading effect is spatially variable and can have a strong impact on the phytoplankton bloom under the ice of high ice algal biomass. However, given the patchiness of ice algal distribution and the control of the light through the open-water fraction, the impact of the shading on the estimate for the pan-Arctic under-ice annual NPP is negligible.

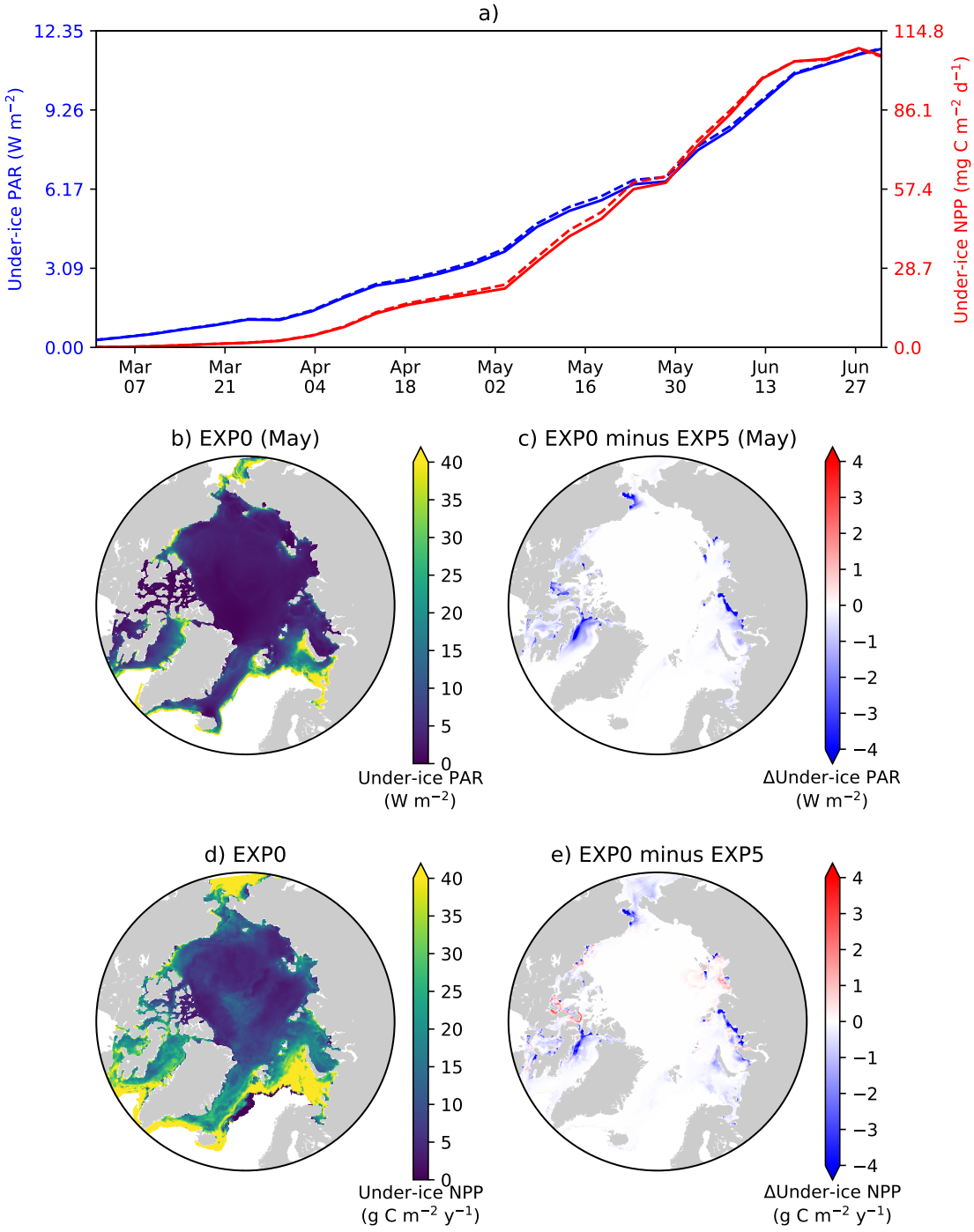

Figure 4.15: Model sensitivity to shading by ice algae. a) Time series comparison of modelled pan-Arctic- and 5-day-mean under-ice PAR (blue) and NPP (red) between EXP0 (solid) and EXP5 (dashed) during 1979. Spatial maps of b) monthly-mean under-ice PAR in May in EXP0 and c) its difference from EXP5, d) the under-ice annual NPP in EXP0, and e) its difference from EXP5.

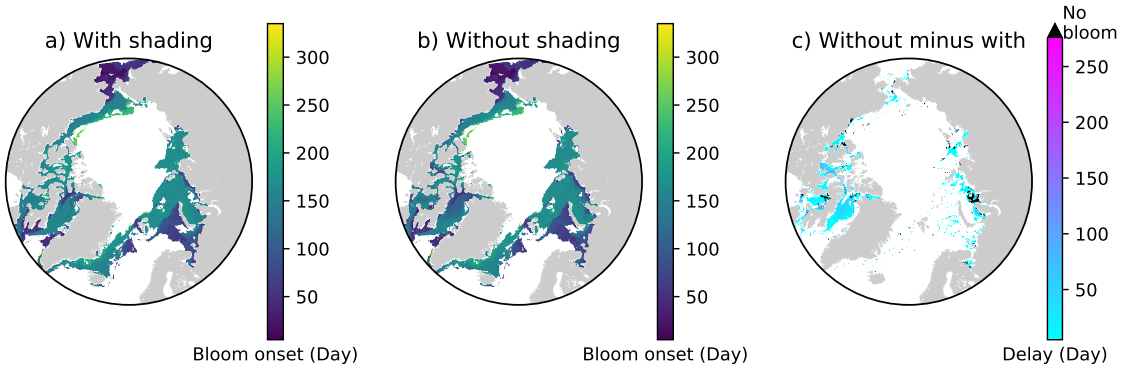

Figure 4.16: Effects of ice algal shading on the onset of under-ice phytoplankton bloom. Spatial maps showing the bloom onset (as the day from January 1) when the ice algal shading is a) considered and b) neglected and c) the difference between the two cases representing the delay due to the shading in 1979 in EXP0. In c), "No bloom" refers to regions in which the bloom was present in b) but not in a). See the main text for the definition of bloom onset.

4.6 Conclusions

In the present study, we have developed a sea-ice biogeochemistry module which is coupled to NEMO. A number of modifications to the sea-ice physical model used in the standard distribution of NEMO (LIM2), to the ocean biogeochemical model (CanOE), and to the existing pan-Arctic configuration (NAA) were necessary to properly simulate the physical and biogeochemical processes in ice-covered regions. Results of the reference simulation (EXP0) agreed well with observations and previous studies in terms of simulated ice volume and extent and the pan-Arctic annual primary production of ice algae and phytoplankton. Adopting a high vertical resolution in the upper water column was found to be necessary to properly represent the effects of a meltwater lens on surface nutrients and the formation of a subsurface chlorophyll maximum. Furthermore, the vertical resolution was shown to have an effect on the magnitude of the modelled surface seawater DMS concentration ($\sim$10 % annually and up to $\sim$20 % seasonally), which in turn influences DMS emissions. Results of the sensitivity experiments demonstrated that: LIM2 requires high-frequency (daily) snowfall forcing data to simulate realistic snow depth (EXP1 and 2); the assumption of no light penetration through snow in LIM2 is unrealistic for simulating an adequate ice algal bloom (EXP3); horizontal transport of sea ice contributes to an enhancement of the pan-Arctic ice algal annual GPP by 16 % (EXP4); and attenuation of light by ice algae has local influence on under-ice NPP but is negligible when estimating larger-scale quantities (e.g. pan-Arctic under-ice annual NPP) (EXP5). The modifications to LIM2, CanOE, and NAA adopted in the present study are also applicable to other submodels and configurations of NEMO (e.g. LIM3, PISCES, ORCA) as the code structures are similar, and therefore, can be incorporated into future pan-Arctic biogeochemical studies. The sea-ice biogeochemical module developed in the present study has been embedded into NEMO in a generic way (see Appendix A.3.1), and can therefore be easily coupled to the aforementioned submodels. To our knowledge, such a development has not been done previously within NEMO. Further sensitivity experiments and observational constraints are needed to refine the important parameters (e.g. i_0) for sea-ice biogeochemistry.

Chapter 5

Spatio-temporal variability in modelled sea-ice and oceanic dimethylsulfide production and fluxes in the Arctic over the period 1979-2015

5.1 Abstract

Recent field observations in various parts of the Arctic suggest that oceanic emissions of dimethylsulfide (DMS) may play a dominant role in the radiative forcing of Arctic aerosols and clouds during late spring and summer. In ice-covered seas, DMS is produced not only in the water column, but also in various sea ice habitats. The ongoing recession of sea ice cover is expected to enhance oceanic DMS emissions in the Arctic, although the magnitude of this increase is highly uncertain. In the present study, a coupled three-dimensional sea ice-ocean regional circulation model was used to perform a multi-decadal (1969-2015) simulation of physical and biogeochemical processes relevant to the production and fluxes of sea-ice and oceanic DMS in the Arctic. The results of the latter 37 years of the simulation were compared with available data products based on field and satellite measurements and other model simulations to evaluate the model performance. The model reasonably simulated the decline of Arctic sea ice, the magnitude and the general spatial patterns of the pan-

Arctic sea-ice and pelagic annual primary production, and the mean seasonal cycle and the spatial distribution of the pan-Arctic surface seawater DMS climatology. The challenges in the comparison of the DMS climatologies are discussed, demonstrating the need to update the *in situ* measurement-based and satellite-derived climatologies by incorporating data acquired by recent field campaigns. The analysis of the modelled ice-to-sea and sea-to-air DMS fluxes revealed different responses to the accelerated decline of Arctic sea ice over the recent decades (1996-2015). In particular, the pan-Arctic ice-to-sea annual DMS flux showed no trend, whereas the sea-to-air flux exhibited an increase of around 40 % over the past two decades. The driving mechanisms for these recent trends are discussed. It is concluded that further model developments and projections are needed to better address the climate change impacts on oceanic DMS emissions in the rapidly-changing Arctic.

5.2 Introduction

Dimethylsulfide (DMS) is the most abundant volatile sulfur compound in the ocean (Simó, 2001), The production of DMS results from the enzymatic cleavage of dimethylsulfoniopropionate (DMSP), which is an osmolyte produced by marine algae (Stefels et al., 2007). Oceanic emissions of DMS are the main source of biogenic aerosols, and therefore, play an important role in radiative forcing and atmospheric chemistry (Andreae and Crutzen, 1997). In particular, recent observational studies suggest that oceanic DMS emissions may exert a strong influence on regional climate in the Arctic during late spring and summer, as they play a dominant role in aerosol composition and new particle formation in the region (Chang et al., 2011b; Rempillo et al., 2011; Sharma et al., 2012; Ghahremaninezhad et al., 2016; Mungall et al., 2016; Willis et al., 2016; Park et al., 2017). However, these studies are limited both spatially and temporally, and the applicability of these proposed conclusions to the broader Arctic remains unknown.

One of the main challenges in Arctic DMS research is the poor spatio-temporal coverage of surface seawater DMS concentration measurements; direct measurements in ice-covered regions are logistically difficult, while indirect measurements via remote sensing are restricted to open water. As a result, the existing climatologies of seawater DMS concentrations in the Arctic Ocean were primarily constructed by the extrapolation of the measurements from lower latitudes (Kettle et al., 1999; Kettle and Andreae, 2000; Lana et al., 2011). Given the spatial heterogeneity of DMS con-

centration in the Arctic (Levasseur, 2013), such an approach is not ideal to derive the surface seawater DMS concentration fields that feed into atmospheric and Earth System model simulations.

Another approach to acquire surface seawater DMS concentration fields is via numerical modelling. Models apply knowledge based on limited measurements to produce simulations over time periods and spatial domains that are beyond the capacity of field observations. Only a handful of papers in the existing literature focus on modelling DMS production in the Arctic Ocean (Gabric et al., 1999; Jodwalis et al., 2000; Gabric et al., 2005; Qu and Gabric, 2010; Elliott et al., 2012; Qu et al., 2016). Among these previous studies, Elliott et al. (2012) was the only study that: 1) incorporated sea-ice biogeochemistry; and 2) could address the spatial variability in surface seawater DMS concentrations. However, this earlier study did not address the temporal variability in DMS concentration nor attempt to quantify oceanic DMS emissions.

The decline of Arctic sea ice is one of the most striking consequences of ongoing climate change, and has implications for oceanic emissions of DMS in the Arctic. Using a box model, Gabric et al. (2005) projected an 86% increase in DMS emissions from the Barents Sea between the late 20th and the 21st centuries, owing to both significant loss of ice cover and warming of sea-surface temperature (with consequent reduction in the gas solubility). Similarly, a global model simulation under the Representative Concentration Pathway scenario 4.5 (Six et al., 2013) indicates that DMS emissions will increase in polar regions north (south) of 60°N(S), while a reduction in DMS emissions is projected for the lower latitudes. However, these earlier studies either focused on a confined region in the Arctic (Gabric et al., 2005) or did not provide a thorough analysis for the Arctic (Six et al., 2013). Furthermore, the spatial resolution of the global model used in the latter study might be inadequate to resolve important processes for the Arctic region (Chapter 4).

In the present study, a multi-decadal simulation using the 3-D coupled sea ice-ocean physical-biogeochemical model developed in Chapter 4 was performed to investigate the spatio-temporal variability in sea-ice and oceanic DMS production and fluxes in the Arctic over the period 1979-2015. Specific objectives of this study are to: 1) evaluate the model performance in simulating recent trends in sea-ice physical properties and associated changes in primary productivity of ice algae and phytoplankton; 2) compare and contrast surface seawater Arctic DMS climatology products based on three different approaches (*in situ* measurements, remote sensing, and

numerical modelling); and 3) investigate the response of modelled ice-to-sea and sea-to-air DMS fluxes to anthropogenic warming and the recent decline of Arctic sea ice.

5.3 Methods

5.3.1 Model simulation

A numerical model simulation was conducted for 47 years from January 1, 1969, to December 31, 2015 using the pan-Arctic regional configuration of the NEMO modelling system described in Chapter 4. The set up of the model simulation is identical to the reference simulation (EXP0) of Chapter 4, except that: the simulation spans additional 37 years with prescribed annually-varying surface and lateral boundary conditions (Appendix A.4.1); and the following updates were made to improve the model simulation. First, I added river runoff of nitrate, total alkalinity, and dissolved organic and inorganic carbon by constructing their annual-mean concentration fields based on measurements from major Arctic rivers (see Appendix A.4.2 for details). Second, I removed the iron limitation on photosynthetic growth of small and large phytoplankton to avoid spurious reduction in primary productivity that may arise due to the lack of external supply (dust deposition and river input) of dissolved iron in the current model set up. This change has a negligible effect on the results of Chapter 4 given the short span of the simulations, but was deemed necessary for the multi-decadal simulation carried out in the present study. This change is also justified by the fact that iron is generally not the limiting factor for phytoplankton growth for the Arctic domain (Zahariev et al., 2008; Aumont et al., 2003, 2015). Third, I removed the effect of nutrient stress on the DMSP content of small phytoplankton as Stefels et al. (2007) suggested that the DMSP production of high DMSP-producing algae, such as small phytoplankton in the present study, are not affected much by nutrient limitation. Lastly, I changed the values of the following model parameters from the values used in Chapter 4 in order to fine tune the modelled ice volume and extent: the thickness of newly-formed ice (*hiccrit*; from 0.6 m to 0.5 m); and the ice strength parameter (*pstar*; from 23,000 N m^{-2} to 30,000 N m^{-2}). My preliminary simulations indicate that: the modelled ice volume and extent are directly proportional to *hiccrit* within the range 0.3-0.8 m; and the modelled ice extent is inversely proportional to *pstar*, while the modelled ice volume is insensitive to the choice of

pstar within the range 23,000-45,000 N m^{-2}.

5.3.2 Validation data products

For the evaluation of modelled sea-ice physical properties, I obtained the Pan-Arctic Ice Ocean Modeling and Assimilation System (PIOMAS) product and the Sea Ice Index Version 3 (SIIV3). PIOMAS is a regional coupled sea ice-ocean circulation model that assimilates observational data (Zhang and Rothrock, 2003; Schweiger et al., 2011). The monthly-mean time series of PIOMAS ice volume were obtained from `www.psc.apl.uw.edu/research/projects/arctic-sea-ice-volume-anomaly/data`. Additionally, the monthly-mean ice thickness and concentration gridded data products of PIOMAS (Dirkson et al., 2016) were used for spatial comparison. To perform a grid-to-grid comparison, these spatial fields were interpolated onto the model grid using a Fortran-based interpolation tool called SOSIE (SOSIE is Only a Surface Interpolation Environment; `https://brodeau.github.io/sosie`). SIIV3 provides ice extent time series based on sea-ice concentration estimates from passive microwave radiometers (Windnagel et al., 2017). The monthly-mean ice extent time series were obtained from `www.nsidc.org/data/G02135/versions/3`.

For the evaluation of modelled surface seawater DMS concentration fields, I obtained two data products that are based on *in situ* measurements (the L11 climatology; Lana et al., 2011) and remote sensing (the G18 climatology; Martí Galí, Laval University, personal communication). The L11 climatology is regarded as the most-up-to-date global data product, incorporating over 47,000 seawater DMS measurements collected during 1972-2009. This data product is available in 1° longitude by 1° latitude grids, and comes in two forms: discrete and standard. The discrete climatology is an un-extrapolated product, whereas the standard climatology is an extrapolated product of the discrete climatology (see Lana et al. (2011) for details). Both products were downloaded from `https://www.bodc.ac.uk/solas_integration/implementation_products/group1/dms`.

The G18 climatology was constructed using a remote sensing algorithm that relies on satellite-derived chlorophyll *a*, light penetration regime, and sea-surface PAR (Galí et al., 2018). The temporal coverage of the data used to construct the G18 climatology is 2003-2016. In addition to the G18 climatology, I used satellite-derived fields of absorption coefficient at 412 nm, a proxy for coloured dissolved organic matter (CDOM) concentration, to screen out grid cells with very high CDOM concentration,

indicative of conditions where the algorithm provides poor estimates of chlorophyll *a* due to strong terrestrial influence. This error translates into DMS estimates, but not proportionally, because of the way the algorithm handles high chlorophyll *a* (see Galí et al. (2015) and Galí et al. (2018) for details). Both the G18 climatology and the corresponding CDOM climatology were provided by Martí Galí (Laval University, personal communication) and use an equal-area sinusoidal projection with a resolution of 27.84 km.

Although other DMS climatologies based on global model simulations could be used for comparison, I excluded these products because their evaluations tend to focus on the overall pattern around the globe without giving much attention to polar regions. Consequently, these global models tend to underestimate the DMS concentration in the Arctic Tesdal et al. (2016a) except for one model (e.g. Vogt et al., 2010) which incorporated the cryoprotection effect on DMSP quota. However, in that study, the DMS concentration was rather too high compared to the L11 climatology for the Arctic domain Tesdal et al. (2016a), while in contrast, the modelled chlorophyll distribution was much lower than the satellite-derived product (Vogt et al., 2010). Therefore, the performance in simulating the fundamental biogeochemical tracers for DMS dynamics is considered rather poor for the Arctic domain.

5.3.3 Trend analysis

Trends in modelled time series were determined using a simple least squares linear regression. Residuals are defined as the differences between the model solution and the regression line. Computationally, this analysis was performed using a Python library called SciPy, or more specifically, a function called numpy.linalg.lstsq. The associated root-mean-square difference (RMSD) was determined by taking the square root of the average of squared residuals. In the context of the present study, RMSD is a measure of interannual variability, although it may still include a non-linear trend.

5.4 Results

The analysis presented here focuses on the region within the Arctic Circle (66.5°N) and the period 1979-2015, which excludes the first decade of the standard run (1969-1978) considered as a spin-up.

5.4.1 Sea-ice physical properties

Ice extent and volume time series

Figure 5.1 compares the time series of modelled September-mean Arctic sea-ice extent (volume) with the SIIV3 (PIOMAS) product over the period 1979-2015. In general, both the interannual variability and trends agree well between the model and those data products.

The model simulated higher ice extent than the SIIV3 product throughout this period (Figure 5.1a); the mean absolute difference between the model and the SIIV3 product is 0.9×10^6 km^2. The trend in the modelled ice extent is -0.7×10^6 km^2 per decade, while that of SIIV3 is -0.8×10^6 km^2 per decade (dashed lines in Figure 5.1a); the difference between the two trends is about 13%. The interannual variability in the modelled ice extent agrees well with that of the SIIV3 product, as indicated by a strong correlation between these time series (ρ =0.94, where ρ denotes the Pearson's correlation coefficient defined as the covariance of the two de-trended time series divided by the product of their standard deviations).

The modelled ice volume is quantitatively similar to the PIOMAS product throughout the period except for 1983-1997, during which the modelled ice volume is consistently higher than the PIOMAS product (Figure 5.1b). The mean absolute difference between the model and the PIOMAS product is 1.5×10^3 km^3 over the period 1979-2015. The trend in the modelled ice volume is -2.5×10^3 km^3 per decade, while that of the PIOMAS product is -3.2×10^3 km^3 per decade (dashed lines in Figure 5.1b); the difference between the two trends is about 25%. The Pearson's correlation coefficient for the de-trended ice volume time series between the model and the PIOMAS product is 0.89, indicating a strong agreement in the interannual variability between the two results.

Ice concentration and thickness fields

Figure 5.2 (Figure 5.3) compares the spatial variability in the climatological September-mean ice concentration (thickness) fields and their trends and RMSDs over the period 1979-2013 between my model simulation and the PIOMAS product. For the most part, the spatial patterns are in qualitative agreement that: the locations of ice edges are comparable (black lines; Figure 5.2a,b); relatively thick (>2 m) ice is present along the northern coast of the Canadian Arctic Archipelago and Greenland (Figure 5.3a,b); the trends in both fields are almost entirely negative and are generally

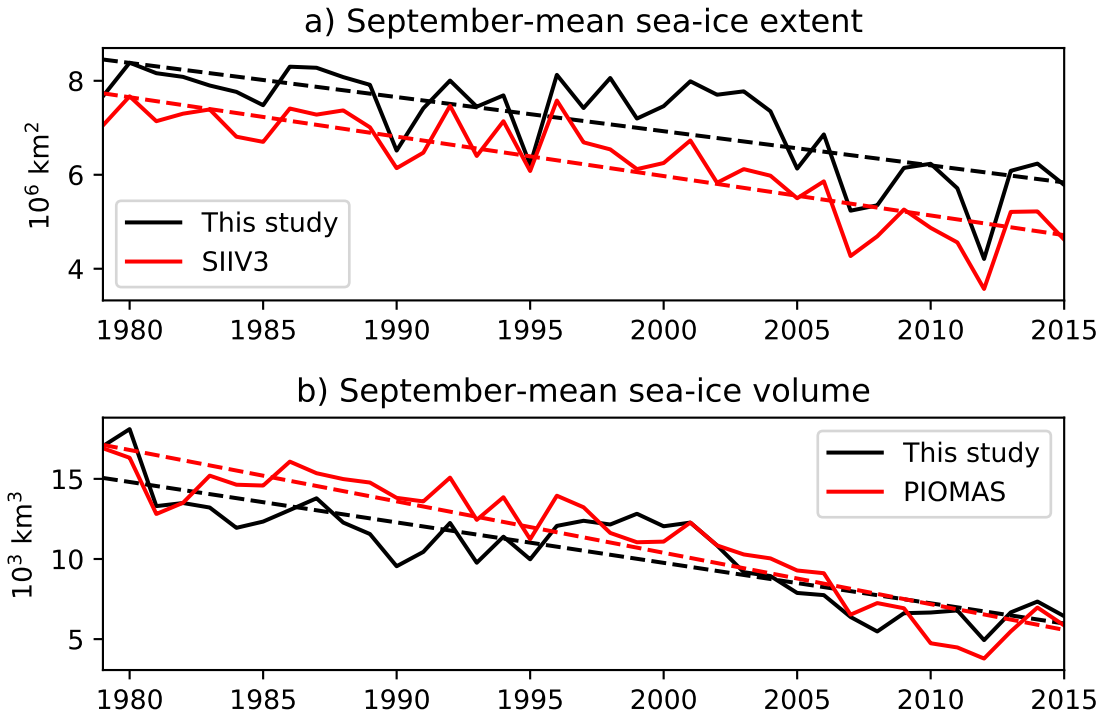

Figure 5.1: Time series comparison of September-mean a) sea-ice extent between the model (black) and the PIOMAS product (red) and b) the sea-ice volume between the model (black) and SIIV3 (red) over the period 1979-2015. Dashed lines represent the linear trends over the entire period.

higher in marginal ice zones than in the pack ice (Figure 5.2d,e and Figure 5.3d,e); and the RMSDs in both fields are relatively high in regions of strong negative trends (Figure 5.2g,h and Figure 5.3g,h).

Our model generally simulated higher ice concentration and thickness near the ice margins and lower ice concentration and thickness in the pack ice compared to the PIOMAS product (Figure 5.2c and Figure 5.3c). The largest ice concentration and thickness difference is apparent in the Canadian Polar Shelf; this difference may be caused by the difference in the simulation of flow through narrow channels owing to the spatial resolution difference between my model (∼10 km in the Canadian Polar Shelf; Figure 4.3) and PIOMAS (∼22 km; Zhang et al., 2010). The magnitude of the negative trends in most of the Arctic Basin and the Canadian Polar Shelf is lower in my model simulation than the PIOMAS product (Figure 5.2f and Figure 5.3f). The magnitude of the RMSD is higher overall in my model simulation than the PIOMAS product (Figure 5.2i and Figure 5.3i), indicating a higher interannual variability in my modelled sea-ice physical properties.

5.4.2 Annual primary production

Ice algae

Modelled sea-ice annual gross primary production (GPP) integrated over the Arctic Circle ranges from 6 Tg C y^{-1} to 21 Tg C y^{-1} with a mean and standard deviation of 13±3 Tg C y^{-1} over the period 1979-2015 (Figure 5.4a). No obvious trend is apparent from the time series, although the interannual variability appears to be higher in the latter half of the simulation. To compare my results with those of earlier studies, I derived the equivalent annual net primary production (NPP) from the modelled GPP values by assuming that NPP represents 76% of GPP. This fraction represents the average of the ratios of the particulate production to the total (particulate plus dissolved) production of organic carbon in the four incubation experiment carried out in the bottom layer of Arctic sea ice (Gosselin et al., 1997). The equivalent modelled sea-ice annual NPP ranges 4.6-16 Tg C y^{-1} (Table 5.1), which falls within the lower end of the *in situ* measurement-based estimates of Legendre et al. (1992); this comparison is reasonable considering that much of the upper end of the estimates represent contributions from strand and mat communities that are not explicitly represented in my model. Furthermore, the modelled mean sea-ice annual NPP over the period 1979-2015 (9.9±2.3 Tg C y^{-1}) matches (within one standard deviation) the

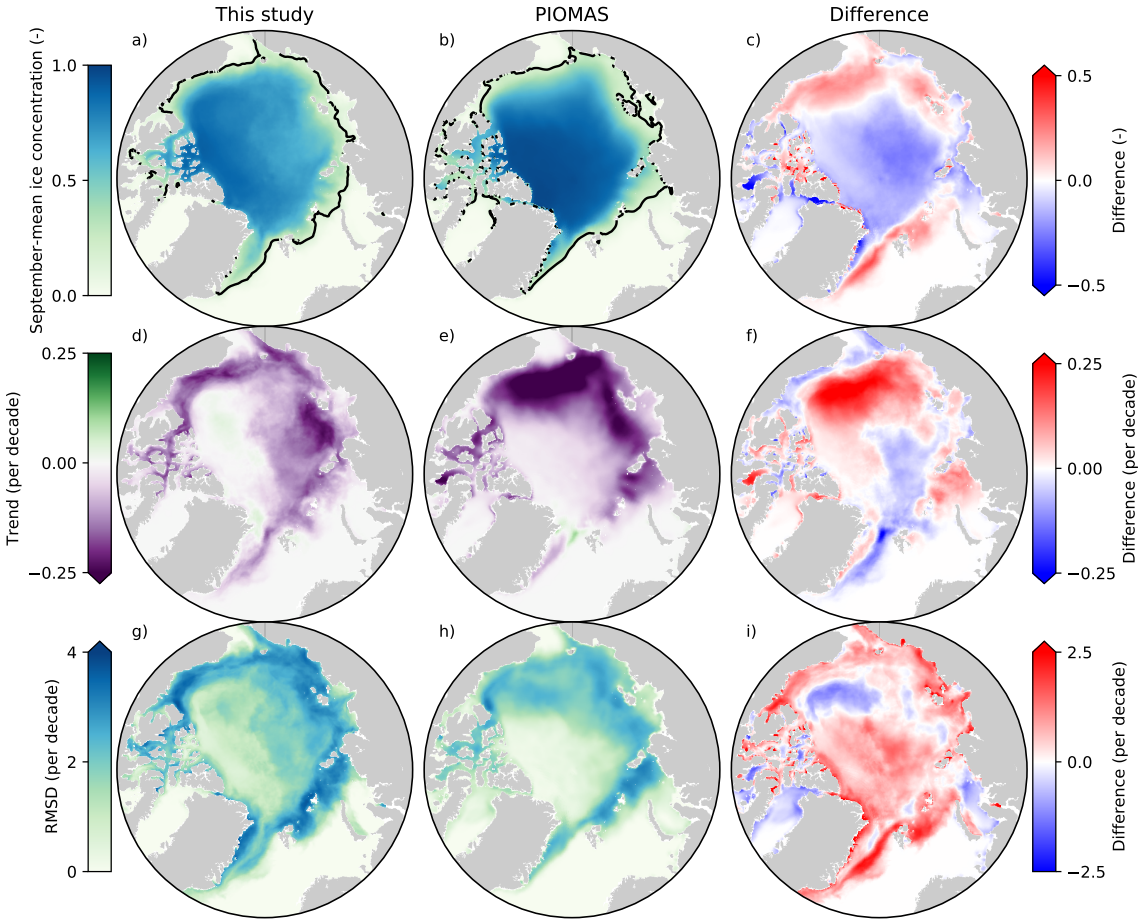

Figure 5.2: Spatial distributions of September-mean ice concentration fields averaged over the period 1979-2013 (top row) and its trend (middle row) and RMSD (bottom row) over the same period. Left column: my model. Middle column: PIOMAS. Right column: difference between my model and PIOMAS.

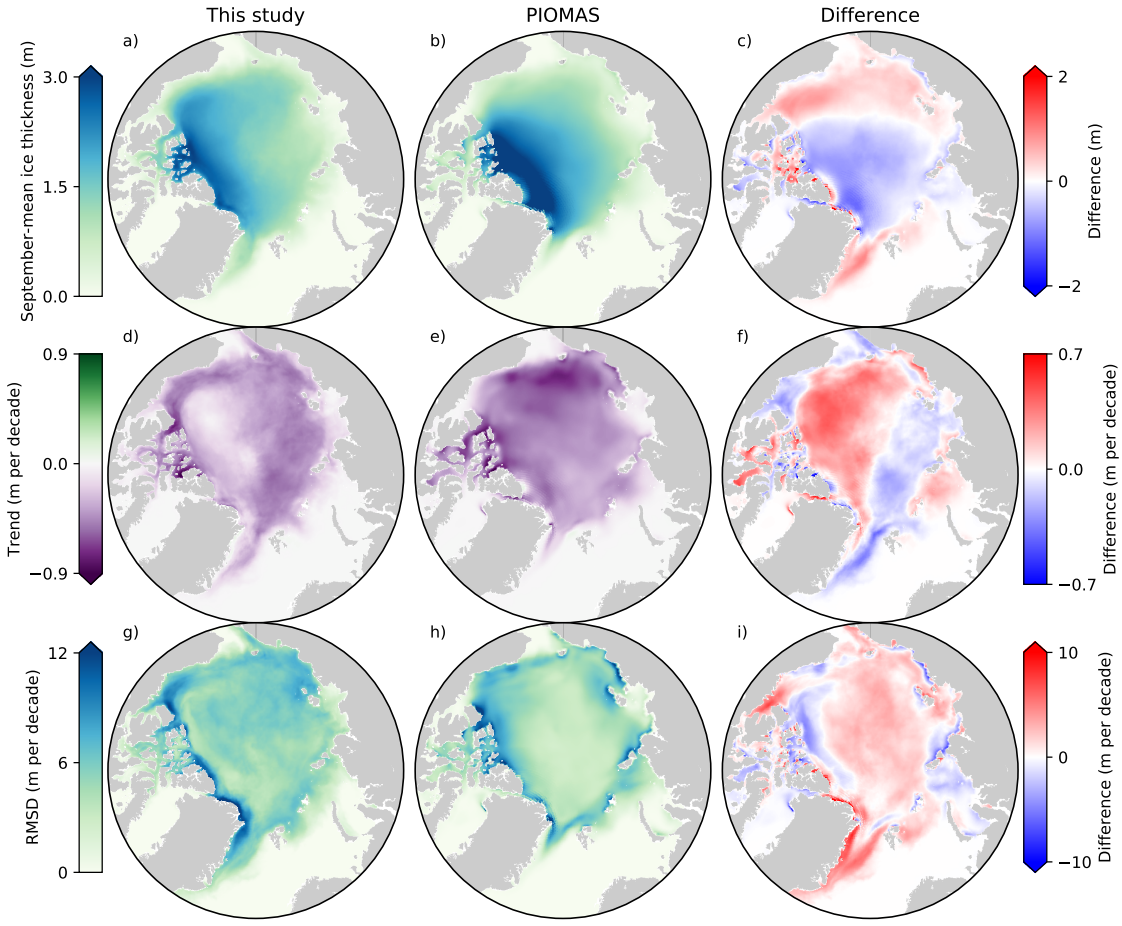

Figure 5.3: As Figure 5.2, but for ice thickness.

Table 5.1: Comparison of pan-Arctic sea-ice and pelagic annual net primary production estimates. Both the range and the mean ±1 standard deviation (in square brackets) are quoted from my model simulation, and either one (whichever is available) is quoted from previous studies. Note that the definition of the term pan-Arctic differs among studies, but is roughly the region north of the Arctic Circle.

Value (Tg C y^{-1})	Method	Temporal coverage	Reference
Ice algae			
4.6-16 [9.9±2.3][a]	Model	1979-2015	This study
9-73	*in situ* measurements	Unknown	Legendre et al. (1992)
[10.1±2]	Model	1998-2007	Jin et al. (2012)
Phytoplankton			
481-957 [674±129]	Model	1979-2015	This study
[>893][b]	*in situ* measurements	Unknown	Sakshaug (2004)
[993±94]	Satellite	1998-2007	Hill et al. (2013)
460-608	Satellite	1998-2012	Arrigo and van Dijken (2015)
456-682	Model	1988-2007	Zhang et al. (2010)
[627±51]	Model	1998-2007	Jin et al. (2012)
[626±20]	Model	1990-2006	Popova et al. (2012)

[a]The values are converted from GPP to NPP by assuming that the latter represents 76% of GPP. See the main text in Section 5.4.2 for explanation.

[b]This value represents the sum of the values quoted from Table 3.7 of Sakshaug (2004), excluding the contributions from Hudson Bay, Labrador Sea, Icelandic Sea, Bering oceanic, and Okhotsk Sea that are, for the most part, located south of the Arctic Circle.

mean value over the period 1998-2007 from the simulation of Jin et al. (2012). The results of other model studies (e.g. Deal et al., 2011; Dupont, 2012) are not directly comparable because the values quoted in those studies included contributions from regions that are beyond the spatial domain of my model configuration (e.g. Hudson Bay).

Figure 5.4b shows the spatial distribution of modelled sea-ice annual GPP averaged over the period 1979-2015. In general, the values are high in shelf regions, especially in the southern Canadian Polar Shelf. In contrast, the values are generally low in the Arctic Basin, the Greenland Sea, the Norwegian Sea, and the Barents Sea. These spatial patterns are consistent with the findings of my previous simulation (EXP0; Chapter 4) as well as other model studies (Deal et al., 2011; Dupont, 2012; Jin et al., 2012, 2018).

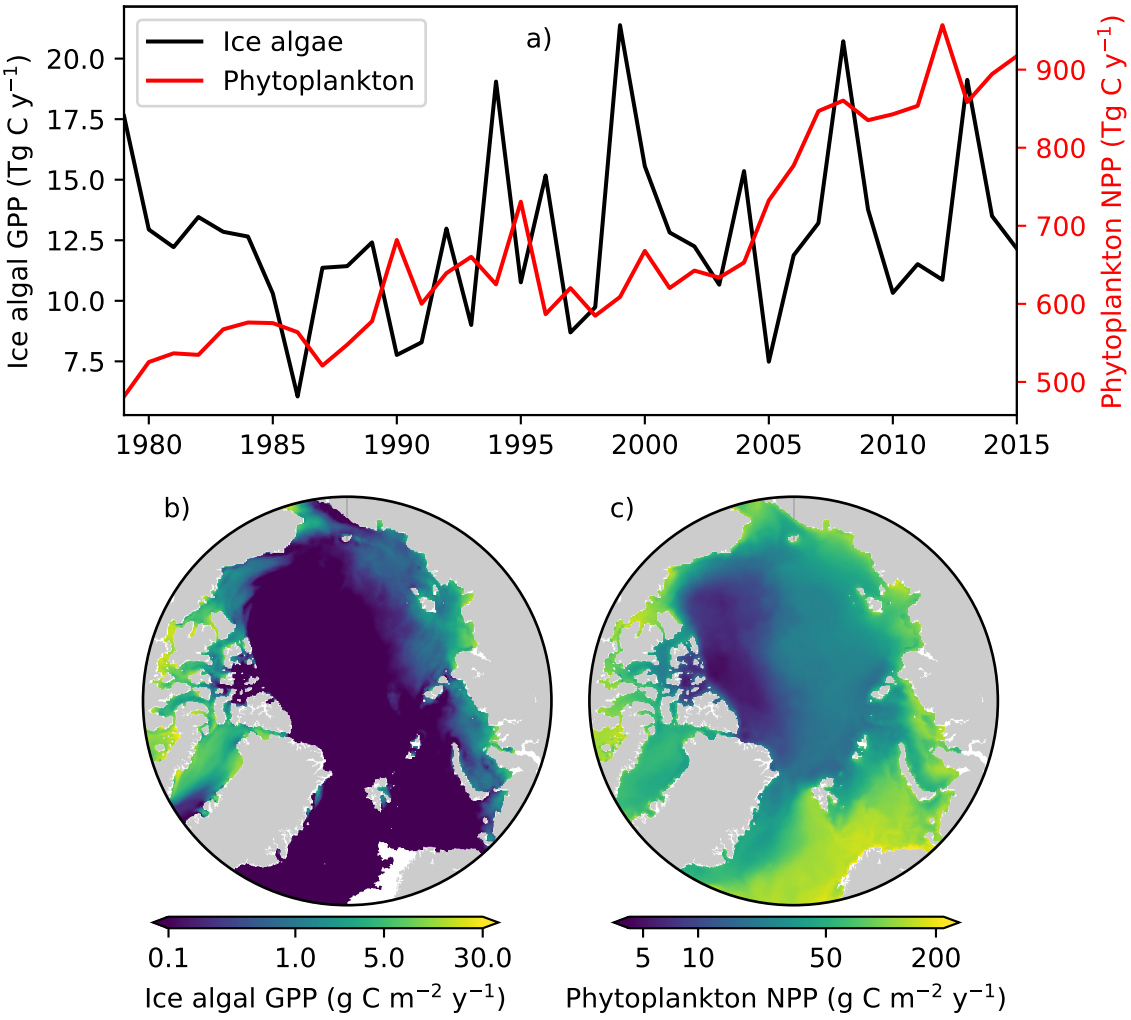

Figure 5.4: a) Time series of modelled bottom-3-cm sea-ice annual GPP (blue) and upper-90-m pelagic annual NPP integrated within the Arctic Circle. Spatial distributions of modelled b) sea-ice annual GPP and c) pelagic annual NPP averaged over the period 1979-2015. Note the log scales in these spatial maps.

Phytoplankton

Modelled pelagic annual NPP integrated north of the Arctic Circle ranges from 481 to 957 Tg C y^{-1} with a mean of 674 ($\pm$129) Tg C y^{-1} over the period 1979-2015 (Figure 5.4a). The time series shows a general increase, which is consistent with the findings of the previous studies based on remote sensing (Arrigo and van Dijken, 2015) and model simulation (Zhang et al., 2010). Compared to the previous satellite and model studies, my model simulated a higher range (Table 5.1), which is reasonable given the wider temporal coverage. The modelled mean value agrees well with the results of previous model studies (Jin et al., 2012; Popova et al., 2012), while it is substantially lower than the estimates based on *in situ* measurements (Sakshaug, 2004) and a remote sensing estimate that accounts for subsurface production (Hill et al., 2013). However, the latter two estimates are uncertain primarily due to spatially and temporally limited observations. Furthermore, some studies (Arrigo and Dijken, 2011; Ardyna et al., 2013) regard the contribution of subsurface chlorophyll maxima to the pan-Arctic annual NPP as negligible, and so the estimate by Hill et al. (2013) is open to debate.

Figure 5.4c shows the spatial variability in modelled pelagic annual NPP averaged over the period 1979-2015. In general, the values are high in lower-latitude regions that are either ice free or covered by thin ice (Figure 5.3a). By contrast, the values are generally low in the Arctic Basin, and are extremely low (below 10 Tg C y^{-1}) in the Canada Basin and the northern part of the Canadian Polar Shelf and north of Greenland that are covered by thick ice (Figure 5.3a). These spatial patterns generally agree well with most of the model results and the satellite-derived product presented in Popova et al. (2012).

5.4.3 Surface seawater DMS climatology

Caveats to the comparison

Figure 5.5 shows the spatial distributions of monthly-mean surface seawater DMS concentration fields of my model-based climatology (Column C), the standard L11 climatology (Column B), and the G18 climatology (Column D). Comparisons with the standard L11 climatology and the G18 climatology need to be carried out with caution for a few reasons. First, the standard L11 climatology is an interpolated/extrapolated gridded product that is based on essentially no data in the Arctic (Figure 5.5 Column

A). In other words, the standard L11 climatology in the Arctic relies heavily on the extrapolation of data from lower latitudes. Nevertheless, the standard L11 climatology deserves attention because it is the most commonly used product for prescribing the DMS emissions in atmospheric and Earth System models. The G18 climatology also suffers from limited number of observations in ice-covered regions where remotely sensed estimates of chlorophyll *a* (and subsequent DMS) concentrations are not available. This limitation is illustrated by the lack of data in ice-covered regions in the G18 climatology (Column D). In addition to the issue of data availability, the G18 climatology is affected by signal contamination from CDOM originating from rivers. This bias is illustrated by the co-occurrence of high DMS concentrations (Column D) and high CDOM concentrations (Column E) in regions of strong river influence. Another issue is that both the L11 climatology and the G18 climatology are representative of open-water environments, which differs from my model-based climatology that incorporates both open-water and under-ice DMS concentrations. There are also issues with the representativeness of climatological (long-term-mean) monthly-mean values in the L11 climatology due to limited temporal coverage of measurements incorporated into the climatology. Lastly, a direct comparison of the standard L11 climatology to my model-based climatology and the G18 climatology is problematic as the former is based on point measurements, which exhibit much higher variability than model-based and satellite-derived quantities which are representative of grid-cell averages.

Mean seasonal cycle

Figure 5.6 shows the monthly-mean time series of surface seawater DMS concentration averaged within the Arctic Circle for the model-based climatology, the standard L11 climatology and the G18 climatology. The three climatology products agree that the pan-Arctic-mean DMS concentration is relatively high during May-August. The time series of the model-based climatology (blue bars) are in qualitative agreement with the time series of the standard L11 climatology (yellow bars), although the timing of the annual peak differs by a month (June vs May). The earlier peak in the standard L11 climatology is a consequence of the extrapolation of datasets from lower latitudes (discussed in more detail below). The time series of the G18 climatology (red bars) show substantially higher values than the other climatologies in June and July partly due to the fact that the former mask out the ice-covered areas for the computation

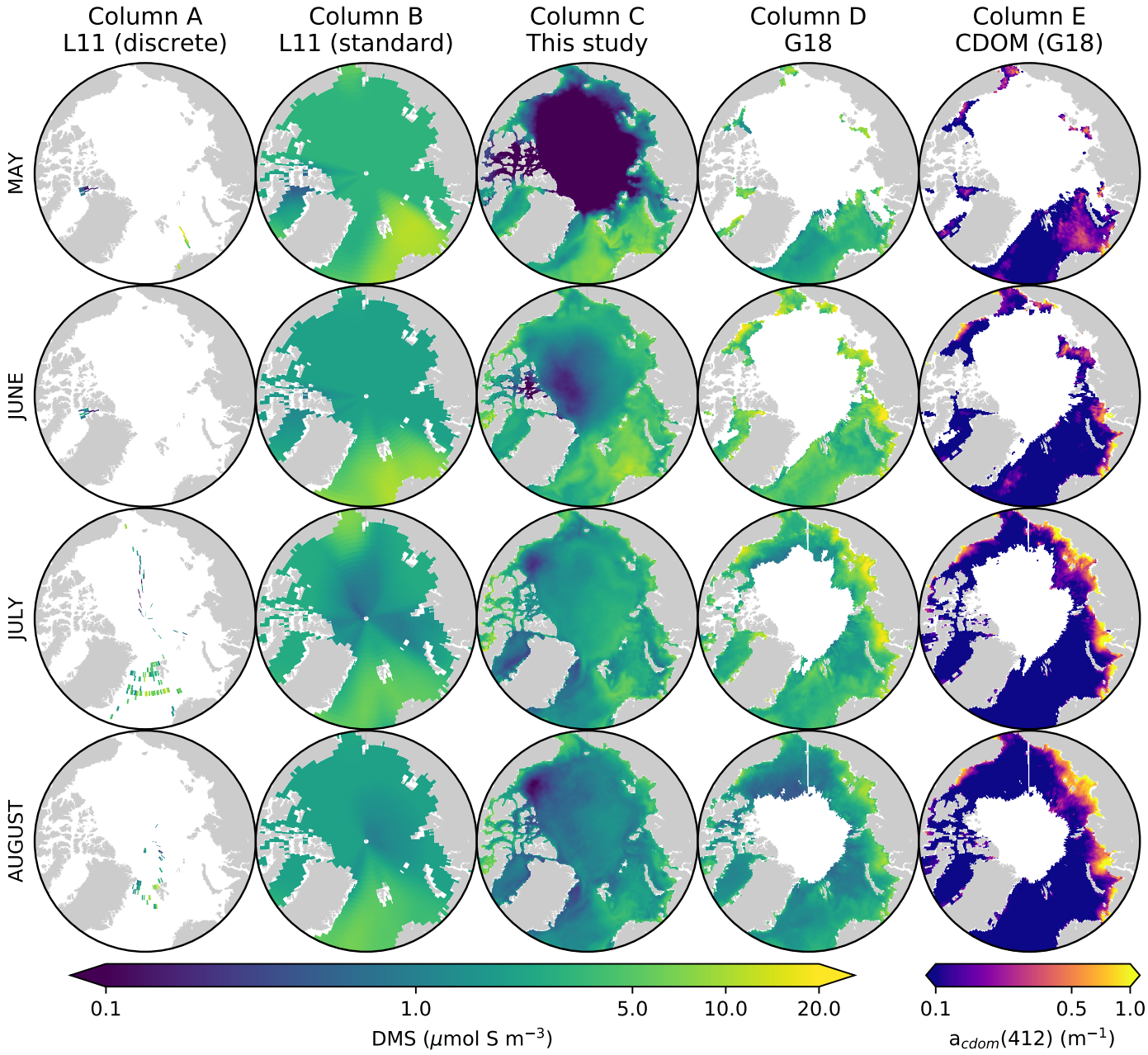

Figure 5.5: Spatial distributions of the surface seawater DMS climatology products for the months of May-August within the Arctic Circle. Columns A and B are respectively based on the *in situ* measurement-based discrete and standard (interpolated/extrapolated) L11 climatologies; Column C is the model-based climatology (1979-2015); and Column D is the satellite-derived G18 climatology (2003-2016). Column E is the climatology of the absorption coefficient at 412 nm (a proxy for CDOM concentration) corresponding to the G18 DMS climatology. In Columns D and E, white regions indicate missing data due to the presence of sea ice. Note the log scales on the DMS concentration.

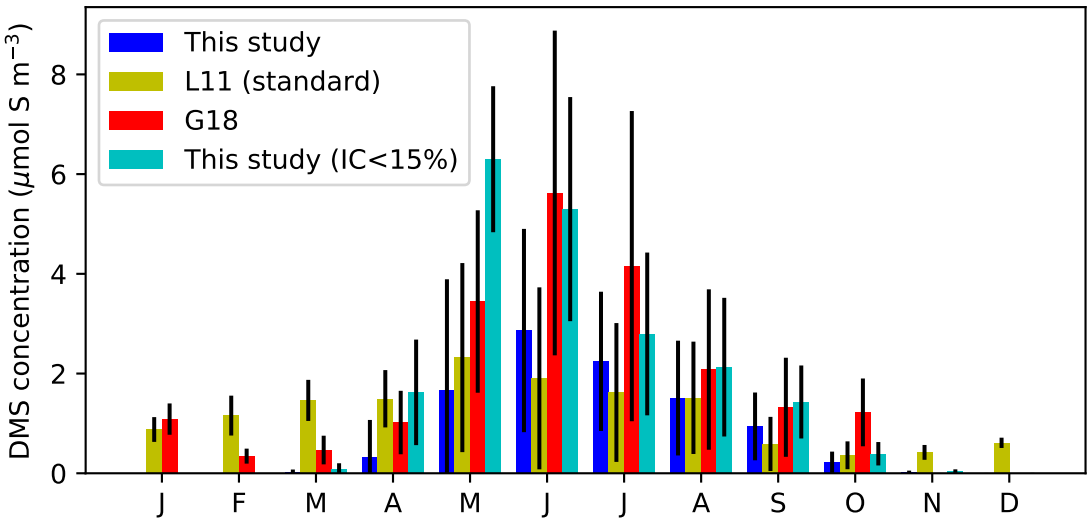

Figure 5.6: Time series of the spatial mean seasonal cycle of surface seawater DMS concentration within the Arctic Circle for my model simulation, the standard L11 climatology, and the G18 climatology. Colour bars show the mean values and associated black errorbars represent ±1 standard deviation of the spatial distribution. To make a consistent comparison with the G18 climatology, I also show the modelled mean concentration in open water (defined here as the region where ice concentration is less than 15%; cyan bars). Note that blue and cyan bars are difficult to see for November-March because the mean values are close to zero, whereas the red bars are absent for November-December because no data are available within the Arctic Circle in the G18 climatology for these months.

of the pan-Arctic-mean concentration. To make a consistent comparison with the G18 climatology, I calculated the pan-Arctic-mean concentration representative of the open-water areas for the model-based climatology (cyan bars); the resultant time series are comparable to the G18 climatology, although the timing of the annual peak differs (May vs June).

Spatial variability

Regional differences in the climatologies are illustrated in Figure 5.5. I focus on the spatial variability in the timing and magnitude of the annual peak in surface seawater DMS concentration that takes place mostly in May-July.

First, the model-based climatology shows that DMS concentration in the northern North Atlantic has an annual peak of 10-20 μmol S m^{-3} in May-June, in agreement with the standard L11 climatology. The G18 climatology shows a distinct peak in

June rather than both in May and June. The L11 climatology for this region in May is governed by the measurements in the Barents Sea. The L11 climatology for June, however, is unreliable for this region because it is based on the extrapolation of datasets from lower latitudes as indicated by the absence of local measurements (Column A).

Second, the model-based climatology shows the annual peak in June-July for the Chukchi Sea and the Eurasian shelves (East Siberian, Laptev, Kara) with peak concentrations ranging from 5 to 10 μmol S m^{-3}. This timing is consistent with the G18 climatology but the peak concentrations differ by at least 10 μmol S m^{-3} for most of the Eurasian shelves; I assume that part of this difference is due to the signal contamination by CDOM in the G18 climatology. The L11 climatology shows that the DMS concentrations in the Chukchi Sea peak in July. This result is based on local measurements, the values of which are comparable to the peak concentrations in the model-based climatology. The peak month for DMS in the Eurasian shelves in the L11 climatology is May, which is a bias owing to the extrapolation of peak concentrations in the North Pacific (Lana et al., 2011).

Lastly, the model-based climatology indicates July as the peak month for DMS in the Arctic Basin (except for the Beaufort Sea, which is at peak in June) with a peak concentration of $\sim$5 μmol S m^{-3}. The timing of this peak does not match that of the L11 climatology (May), but this is again likely due to the extrapolation bias. In the model-based climatology, July is also the peak month for the Canadian Polar Shelf ($>$20 μmol S m^{-3}). The timing of this peak is in agreement with the L11 climatology, although no local measurements are incorporated into the climatology of this region for this month. A comparison with the G18 climatology for these ice-covered regions is not possible due to limited spatial coverage.

Comparison with the discrete L11 climatology

Given the extrapolation bias in the standard L11 climatology, the model-based climatology can be better evaluated through a direct comparison with the discrete L11 climatology at locations where observations are available (Column A; Figure 5.5). Figure 5.7 shows the scatter plot of this comparison for May-August. The dashed line represents a slope of unity; the data which lie on this line indicate a perfect match between the model-based climatology and the discrete L11 climatology. The correlation between the modelled and observed DMS is weak. The model-based climatology

generally overestimates the low DMS concentrations (<1 μmol S m^{-3}) of the discrete L11 climatology in the Baffin Bay (May and June; Column A; Figure 5.5) and the Arctic Basin (July and August). On the other hand, the model-based climatology consistently underestimates the concentrations exceeding 4 μmol S m^{-3} in the discrete L11 climatology, which correspond to data from the Barents Sea (May), the Chukchi Sea (July), and the Greenland Sea (July and August).

Although the discrete L11 climatology has no extrapolation bias, the direct comparison with the model-based climatology is still problematic owing to some of the caveats mentioned above, particularly the fact that the L11 climatology is based on point measurements, which display much higher variability than model quantities which represent grid-cell averages. The discrete L11 climatology also has not yet incorporated the data from some recent field campaigns (e.g. Mungall et al., 2016; Jarníková et al., 2018).

5.4.4 Ice-to-sea and sea-to-air DMS fluxes

Seasonal variability

Figure 5.8 shows the seasonal variability in modelled ice-to-sea and sea-to-air DMS fluxes integrated within the Arctic Circle. The ice-to-sea flux is at its annual peak in May and moderately high in June relative to the remainder of the year. The sea-to-air flux is relatively high throughout May-September. The sea-to-air flux at its annual peak (June) is about 20-fold higher than the ice-to-sea flux in May, indicating that the latter represents a negligible source of DMS to the water column at a pan-Arctic scale. Note that my model does not have a representation for ice-to-air flux, such as the emissions from melt ponds (Gourdal et al., 2018), that can make an additional contribution to the atmospheric inventory.

Spatial variability

Figure 5.9 shows the spatial variability in modelled ice-to-sea and sea-to-air annual DMS fluxes within the Arctic Circle. In general, the spatial patterns in the ice-to-sea (sea-to-air) flux resemble those of annual primary productivity within sea ice (water column) previously shown in Figure 5.4. The ice-to-sea flux is relatively high (more than 10 μmol S m^{-2} y^{-1}) in Baffin Bay, Chukchi Sea, and shelf regions near the Eurasian and the North American continents, while it is near zero in the Norwegian

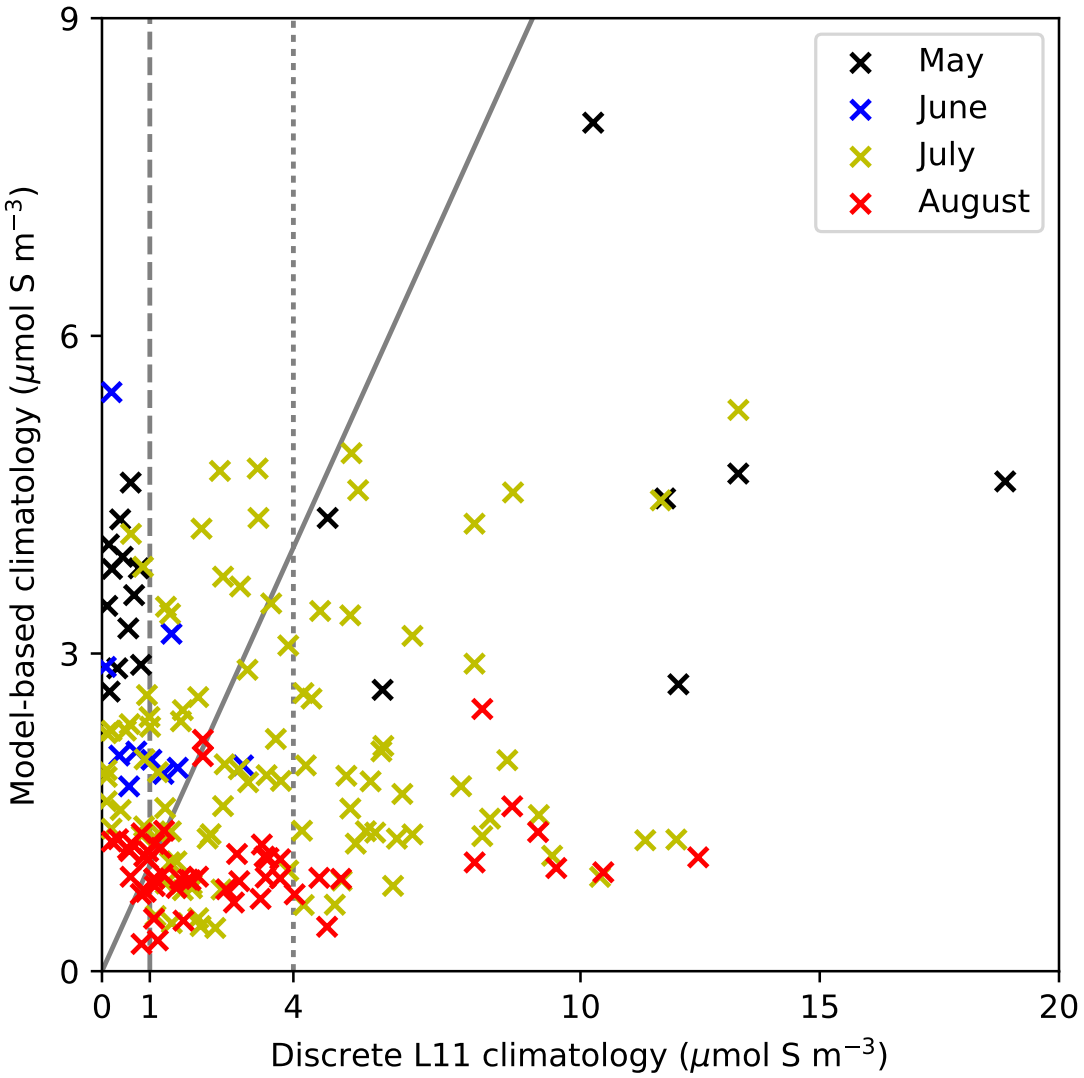

Figure 5.7: Scatter plot comparison between the model-based climatology and the discrete L11 climatology of surface seawater DMS concentration north of the Arctic Circle. Colours distinguish the datasets by month. To aid in the interpretation of the plot, grey lines are drawn which represent a slope of unity (solid) and the concentration in the discrete L11 climatology at 1 and 4 μmol S m^{-3} (dashed and dotted), respectively.

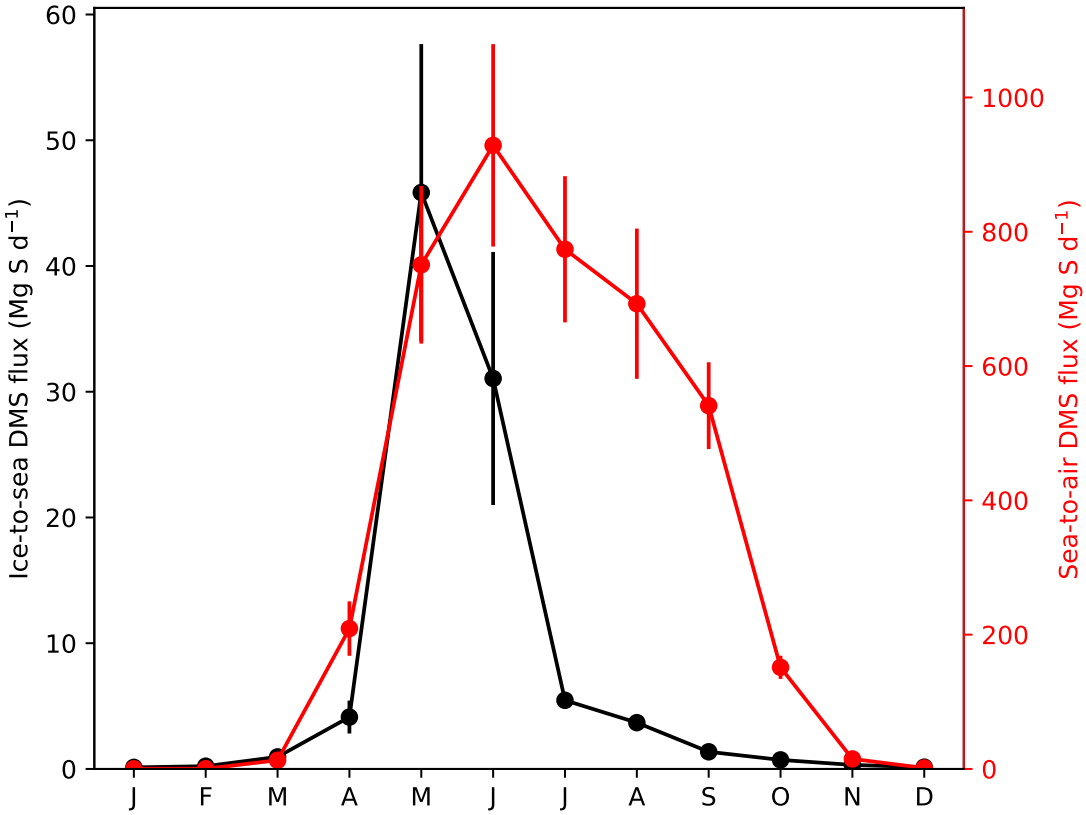

Figure 5.8: Seasonal cycle of modelled a) ice-to-sea and b) sea-to-air annual DMS flux integrated over the Arctic Circle. Dots represent the mean values and error bars represent ± 1 standard deviation of the integrated fluxes over the period 1979-2015.

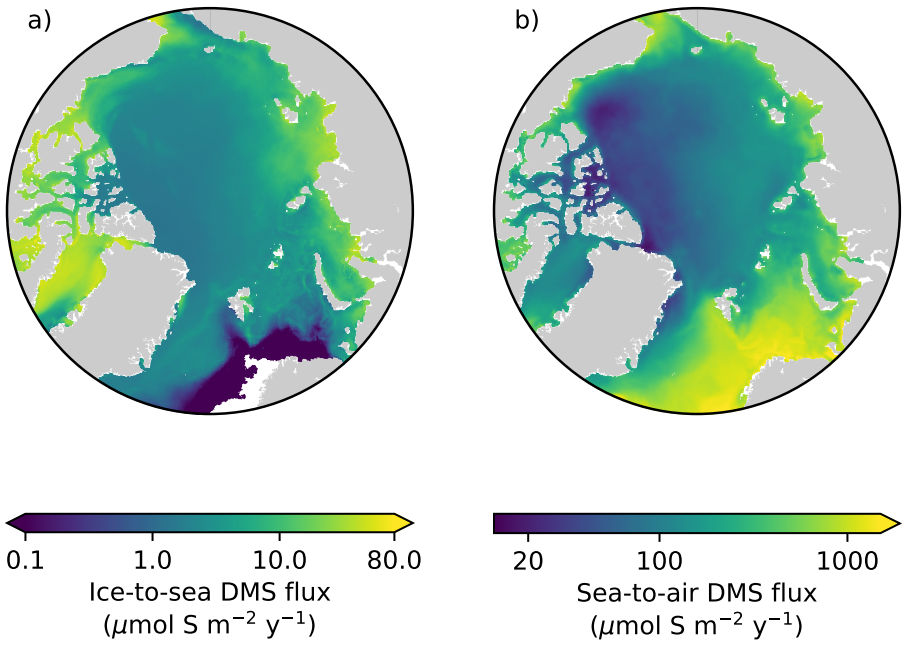

Figure 5.9: Spatial distributions of modelled a) ice-to-sea and b) sea-to-air annual DMS flux averaged over the 1979-2015 period. Note the log scales on these maps.

and Barents Seas (Figure 5.4a). In contrast, these seas represent regions of high DMS emissions from the ocean to the atmosphere, as the sea-to-air flux exceeds 1000 μmol S m^{-2} y^{-1} (Figure 5.4b). The sea-to-air flux is similarly high in shelf areas of the Kara Sea, the Laptev Sea, the East Siberian Sea, the Chukchi Sea, the Beaufort Sea, and the Canadian Polar Shelf. The sea-to-air flux is generally low (20 μmol S m^{-2} y^{-1} or less) in regions that are covered by thick ice ($\sim$2 m or more; Figure 5.3a).

Interannual variability and trends

Figure 5.10a and Figure 5.10b show the interannual variability in modelled ice-to-sea and sea-to-air annual DMS fluxes integrated over the Arctic Circle, respectively. The ice-to-sea flux ranges from 1.9 to 4.6 Gg S y^{-1} with a mean of 2.9 ($\pm$0.5) Gg S y^{-1} over the period 1979-2015 (black lines; Figure 5.10a), while the sea-to-air flux ranges from 0.10 to 0.15 Tg S y^{-1} with a mean of 0.12 ($\pm$0.01) Tg S y^{-1} over the same

period (black lines; Figure 5.10b). There is no particularly strong trend in these time series. To compare the modelled sea-to-air DMS flux with estimates based on the L11 climatology, I also integrated the modelled flux over the region north of 60°N. The resulting average flux of 0.24 (±0.02) Tg S y^{-1} over the period 1979-2015 is somewhat lower than the estimates of Lana et al. (2011) and Wang et al. (2018), both of which find 0.3 Tg S y^{-1} over the same spatial domain.

To assess longer-term variability in the modelled fluxes, I calculated the 10-year centred moving averages of these fluxes, which are shown as solid red lines in Figure 5.10. The 10-year moving average of the ice-to-sea flux is more or less constant from the late 1990s (Figure 5.10a). In contrast, the interdecadal variability in the sea-to-air flux shows a quasi-linear monotonic increase since about 2000 (dashed red lines; Figure 5.10b). To assess the relationship with ice conditions, I did the same calculation for the modelled ice concentration averaged north of the Arctic Circle and over the spring-summer season (Figure 5.10c). The spring-summer season is defined here as April-September, which are the months most relevant for DMS fluxes (Figure 5.8). The variability in the 10-year centred moving average of the ice concentration shows a quasi-linear monotonic decrease since the decadal-moving-average period 1996-2005, coinciding with the beginning of the quasi-linear monotonic increase in the sea-to-air DMS flux. Furthermore, this timing coincides with the beginning of the accelerated decline of Arctic sea ice (Stroeve et al., 2012b).

To quantify the trends in the modelled fluxes and ice concentration, I conducted a simple linear regression on the interannual time series of these variables over the period 1996-2015 (yellow lines; Figure 5.10). I chose to calculate the trend since 1996, as it corresponds to the start of the rapid sea ice decline. The slopes of the regression lines are: 0.02 Gg S y^{-1} per decade for the ice-to-sea flux (Figure 5.10a); 0.02 Tg S y^{-1} per decade for the sea-to-air flux (Figure 5.10b); and -0.06 per decade for the ice concentration (Figure 5.10c). Tthe ice-to-sea flux has remained more or less constant (1 % increase) over the last 20 years (1996-2015), while the sea-to-air flux (ice concentration) has increased (decreased) by 37 % (17 %).

The inverse relationship between the sea-to-air DMS flux and the ice concentration over the last two decades of the simulation period suggests a strong influence of the sea ice retreat on the DMS emissions. By construction, this relationship makes sense as sea-to-air flux is inversely proportional to ice concentration. There is a strong negative correlation between the two over the years of simulation (Figure 5.11). By contrast, the ice-to-sea DMS flux is essentially constant over the same period, suggesting an

offsetting effect of the sea ice retreat on ice algal production (and the subsequent DMS production and release from sea ice).

5.4.5 Spatial variability in the trend over the period 1996-2015

To investigate spatial variability in the trends in the modelled ice-to-sea and sea-to-air DMS fluxes over the last two decades of the simulation, I computed the linear trends in these fluxes and a set of other modelled and prescribed quantities for the the spring-summer season (April-September averages) on every grid cell over the same period (Figure 5.12 and 5.13).

The spatial patterns of the trends in modelled ice-to-sea DMS flux (Figure 5.12a) resemble those of modelled sea-ice DMS concentration (Figure 5.12b) and ice algal biomass (Figure 5.12c), indicating that changes in the ice-to-sea DMS flux are driven by sea-ice DMS production rather than ice melt. Regions of increasing and decreasing trends are mostly confined to the marginal ice zone, while the trends are near zero in the pack ice owing to relatively low production in this light-limited area (Figure 5.4b). The spatial patterns of trends in these variables are inversely related to those of modelled snow depth in the Canadian Polar Shelf and the Pacific Arctic (Figure 5.12d), suggesting a strong control of snow on light-limited ice algal production in these regions. The Pacific Arctic also experiences a strong decrease in modelled ice concentration (Figure 5.12e) and thickness (Figure 5.12f). While these processes have opposite effects on ice algal production, the impact of the thinning of sea ice and snow pack outweighs the lateral retreat of sea ice, resulting in an increase in ice algal biomass and subsequent formation and release of DMS.

Figure 5.13a shows the spatial variability in the trend in modelled sea-to-air DMS flux, in which regions of increases predominate, especially near the Pacific and Atlantic inflows. These spatial patterns resemble those of the trends in modelled DMS concentration (Figure 5.13b), and generally match the spatial patterns of the trends in modelled sea-surface phytoplankton and zooplankton biomass (Figure 5.13c and Figure 5.13d, respectively). Furthermore, these spatial patterns are consistent with those of the trends in modelled sea-surface temperature (Figure 5.13e) and PAR (Figure 5.13f), which suggests that the increase in the phytoplankton and zooplankton biomass is due to a combination of warming and increased ambient light levels. Furthermore, the warming of sea-surface temperature enhances the flux by reduc-

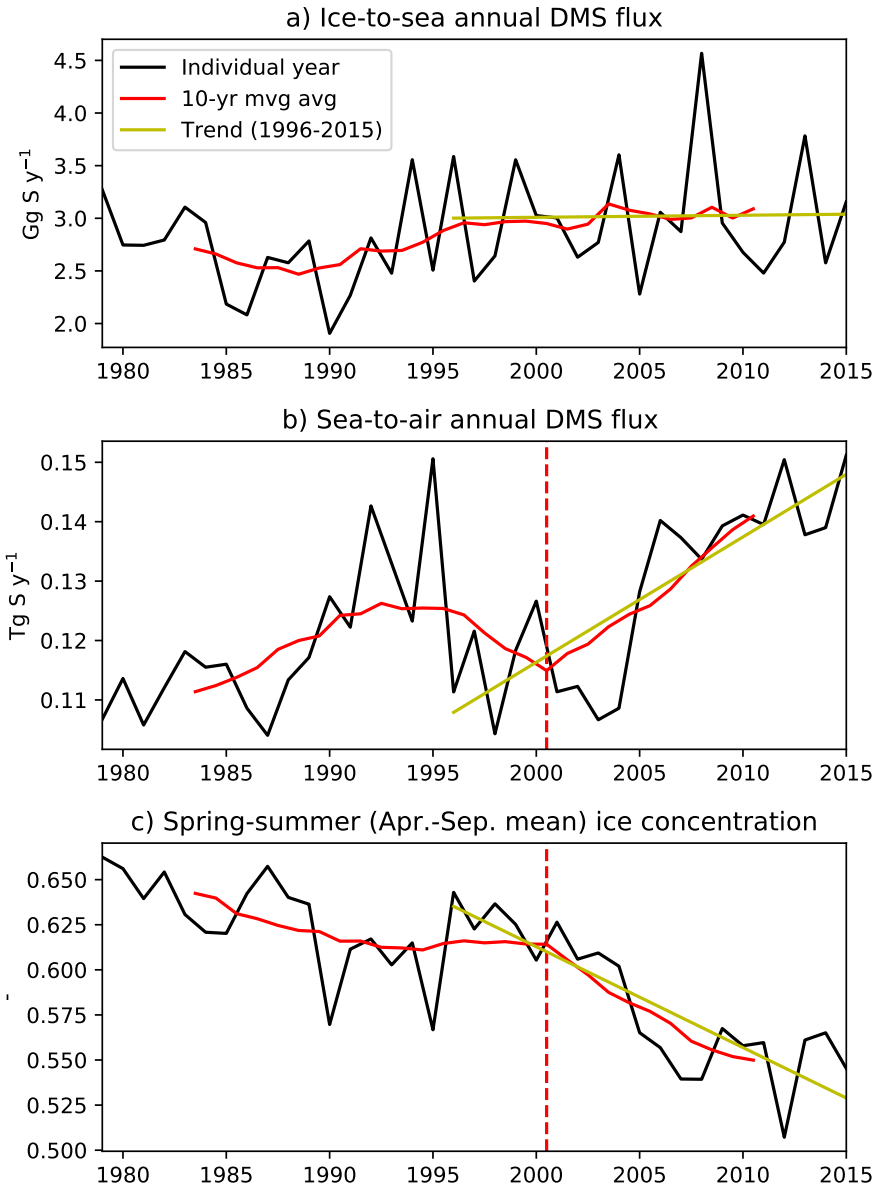

Figure 5.10: Time series of modelled a) ice-to-sea and b) sea-to-air annual DMS flux integrated over the Arctic Circle, and c) modelled spring-summer (April-September mean) ice concentration averaged over the Arctic Circle, over the period 1979-2015. Black lines represent the values for individual years; red lines represent 10-year centred moving averages; yellow lines represent linear trends over the period 1996-2015; and dashed red lines in b) and c) indicate the decade 1996-2005 at which the moving averages of the sea-to-air flux and the ice concentration started to show a quasi-linear monotonic increase and decrease, respectively.

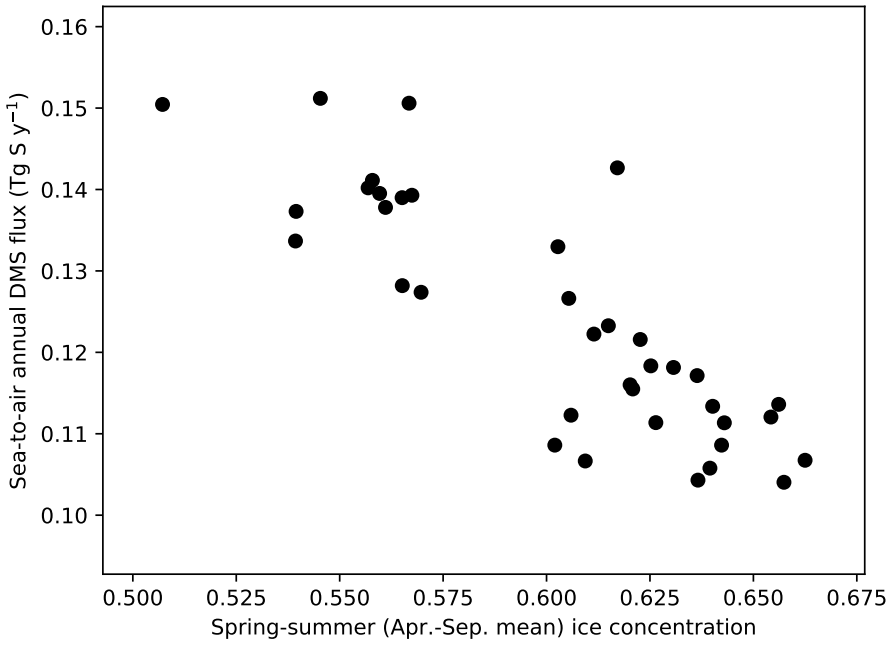

Figure 5.11: Scatter plot comparison of modelled annual sea-to-air DMS flux integrated within the Arctic Circle and spring-summer (April-September mean) ice concentration averaged within the Arctic Circle over the period 1979-2015.

ing gas solubility. All of these processes stem from the decline of sea ice, which is generally more pronounced near the Pacific and Atlantic inflows (Figure 5.12e and Figure 5.12f). Lastly, I examined the spatial variability in the trends in modelled sea-surface nitrate concentration (Figure 5.13g) and prescribed surface wind speed (Figure 5.13h), and found no strong correspondence with the spatial patterns of the trend in the phytoplankton biomass and the sea-to-air DMS flux, indicating that these factors are generally of secondary importance to primary production and DMS emissions within the Arctic Circle. Co-occurrence of strong increases in wind speed and DMS emissions in a few regions (e.g. the Amundsen Gulf and the Barents Sea) suggests a localized importance of the changes in the magnitude of the wind speed. Similarly, changes in nitrate may have impacted the DMS emissions regionally (e.g. north of Chukchi Sea), as indicated by the co-occurrence of increases in the surface seawater concentrations of nitrate, phytoplankton, and DMS.

5.5 Discussion and conclusions

In this study, I analyzed a multi-decadal pan-Arctic model simulation of sea-ice and ocean physical and biogeochemical processes relevant to the production and emission of the climatically-important trace gas DMS. The model performance was evaluated by comparing with available data from field measurements, remote sensing, and model simulations. These comparisons have demonstrated the model's skill in simulating the decline of Arctic sea ice and the broad spatial distributions of ice algal and phytoplankton primary production and surface seawater DMS concentration within the Arctic Circle over recent decades. However, these comparisons are affected by the spatial and temporal limitations of these data products, owing to logistical and methodological challenges in *in situ* measurements (Miller et al., 2015) and the inability of remote sensing algorithms to consider conditions under ice. A more thorough comparison requires more measurements in these ice-covered regions in future studies.

The comparisons of surface seawater DMS climatology products have highlighted the challenge in the evaluation of the model due to the scarcity of data in the *in situ* measurement-based L11 climatology and the satellite-derived G18 climatology. Despite this difficulty, the comparisons have shown reasonable agreement among these data sets in terms of the mean seasonal cycle within the Arctic Circle and the spatial variability in the timing and magnitude of the annual peak in DMS concentrations. To improve the evaluation of the model performance and the remote sensing algorithm,

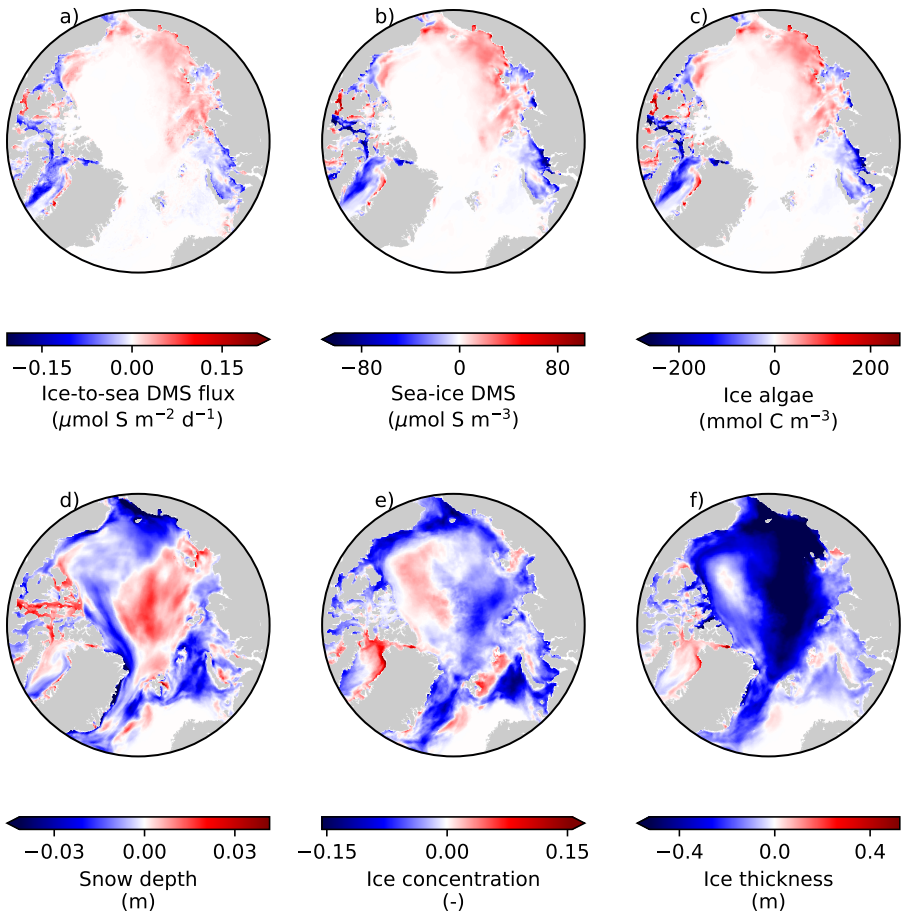

Figure 5.12: Spatial distributions of linear trends in modelled spring-summer (i.e. April-September mean) a) ice-to-sea DMS flux, b) sea-ice DMS concentration, c) ice algal biomass, d) snow depth, e) ice concentration, and f) ice thickness over the period 1996-2015. The trend here represents the slope of a regression line which is derived by conducting a simple linear regression at each grid point.

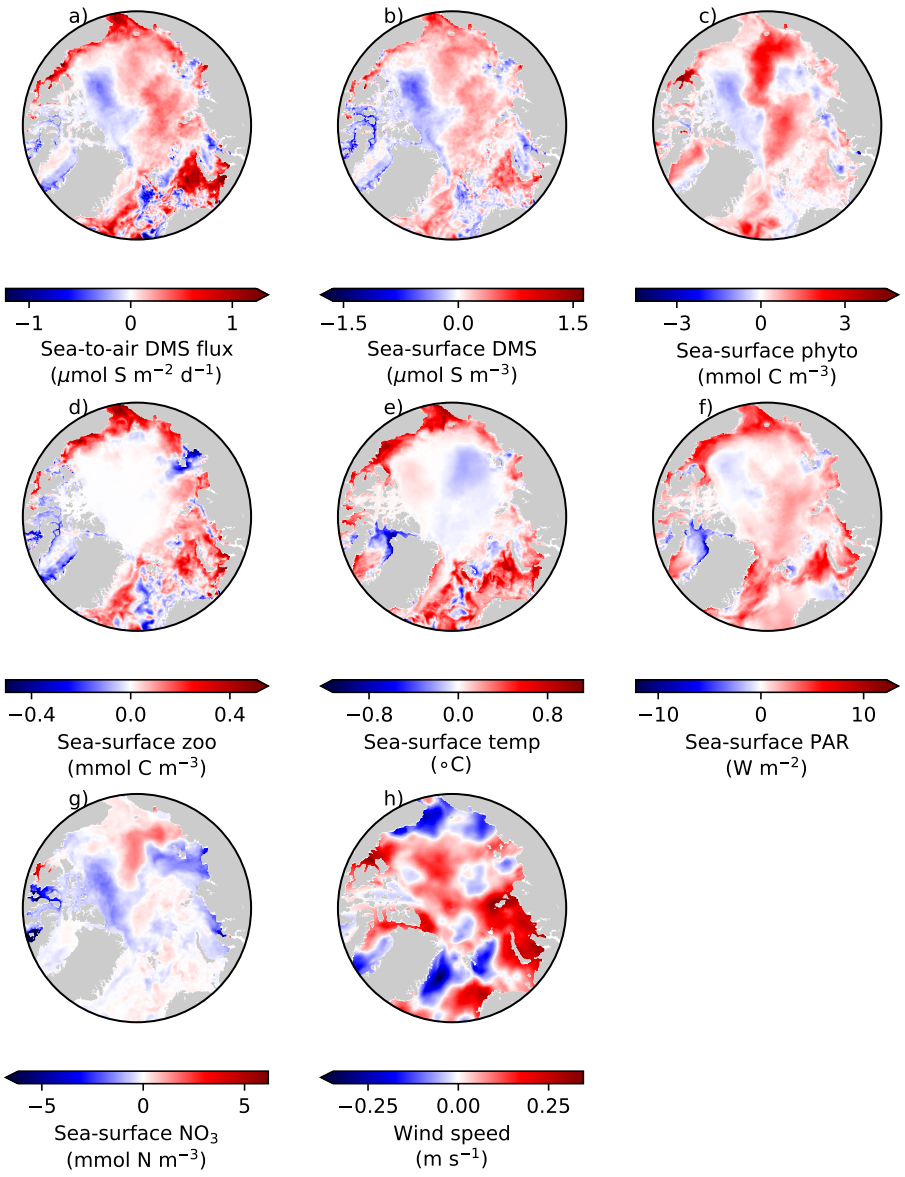

]

Figure 5.13: Same as Figure 5.12, but for a) sea-to-air DMS flux, b) sea-surface DMS concentration, c) sea-surface phytoplankton biomass, d) sea-surface zooplankton biomass, e) sea-surface temperature, f) sea-surface PAR, g) sea-surface nitrate concentration, and h) prescribed surface wind speed.

I encourage the development of an update to the almost decade-old L11 climatology (Lana et al., 2011). Specifically, data collected from recent field campaigns of the NETCARE (www.netcare-project.ca), GEOTRACES (www.geotraces.org), ArCS (www.arcs-pro.jp/en), and GRENE (www.nipr.ac.jp/grene/e) projects, can substantially improve the quality of the climatology in the Arctic Ocean, as these projects focused on collecting data in regions lacking data in the L11 climatology, such as the Canadian Polar Shelf in July-August.

The analysis of trends in modelled ice-to-sea and sea-to-air DMS fluxes north of the Arctic Circle have shown different responses of these fluxes to the recent decline of sea ice. The pan-Arctic ice-to-sea DMS flux shows no trend owing in part to the counteracting effects of sea ice thickness and extent decline on ice algal production. Another important factor for ice algal production (and therefore, the ice-to-sea DMS flux) is snow depth, which has been shown to exert regional control on light-limited ice algal production. By contrast, the pan-Arctic sea-to-air DMS flux has shown an increasing trend essentially driven by the loss of sea ice that promotes biological production, and consequently oceanic DMS production and emissions.

Previous studies (Levasseur et al., 1994; Elliott et al., 2012; Hayashida et al., 2017) have suggested the potential importance of DMS produced within sea ice for oceanic DMS emissions. However, two of these earlier studies were limited in space and time, and cannot be generalized with confidence to the pan-Arctic context. The model study by Elliott et al. (2012) incorporated sea-ice DMS production into a pan-Arctic regional model, and showed that DMS produced in the bottom layer of Arctic sea ice can supply a substantial amount of DMS (over 10 μmol S m^{-3}) to the underlying water column. However, on top of various assumptions and simplifications involved in their model (e.g. retention of icemelt DMS in the uppermost water column and diagnostic representation of oceanic DMS production; see Section 5.2), they lacked the representation of sea-to-air DMS flux, and were unable to present direct evidence for the importance of sea-ice DMS production to oceanic DMS emissions.

Our model simulation, which relaxes some of the assumptions involved in the model study of Elliott et al. (2012), suggests that sea-ice DMS production makes a very small contribution to oceanic DMS emissions at a pan-Arctic scale. However, this analysis is unable to assess the relative contribution of sea-ice DMS production to the oceanic DMS emissions. This assessment requires another set of sensitivity simulation that excludes the sea-ice representation of DMS from the model (such as done in Chapter 3), which will be investigated in a follow-up study. Furthermore,

some additional sources/sinks of DMS are not incorporated into my model (discussed in Chapter 3), such as direct release of DMS from the sea ice to the atmosphere (Levasseur et al., 1994).

The representation of DMS emissions in current atmospheric and Earth System models relies on the L11 or earlier climatologies (Kettle et al., 1999; Kettle and Andreae, 2000), which are based on extremely limited data for the Arctic domain. Moreover, these climatologies lack potentially substantial interannual variability and trends, as indicated by my model simulation (approximately 40 % increase in the DMS emissions north of the Arctic Circle over the period 1996-2015). The sensitivity of Arctic sulfate aerosols and clouds to the interannual variability and trends in the DMS climatology can be investigated using my model output in future regional atmospheric model studies.

Current climate models project that Arctic sea ice will continue to decline throughout the 21st century (Stroeve et al., 2012a). Based on this projection and my simulation, it is anticipated that the pan-Arctic sea-to-air DMS flux will continue to increase as long as primary production (and subsequent DMS production) is not reduced by nutrient limitation, which can be caused by shoaling of the surface mixed layer (Gabric et al., 2005; Steiner et al., 2015). This process would also decrease the ice-to-sea DMS flux by suppressing the ice-sea flux of nutrients, and therefore, its trend may be different from that of the last two decades. Given the spatial variability in the trends in the ice-to-sea and sea-to-air DMS fluxes in my model simulation, I recommend that projections of these fluxes for the Arctic domain should be carried out using a regional or global model rather than a one-dimensional box or column model. Furthermore, my trend analysis emphasizes strong linkages among ambient environmental conditions (snow, sea ice, and seawater temperature), ecosystems (primary/secondary production), and DMS production/fluxes. Hence, incorporating potential changes in ecological processes driven by climate change into DMS models is an important step towards an improvement on the projection of oceanic DMS emissions and their impacts on aerosol and clouds. For example, poleward expansion of *Emiliania huxleyi* (Winter et al., 2014) and potential increase in the abundance of *Phaeocystis pouchetii* in the Fram Strait (Nöthig et al., 2015; Soltwedel et al., 2016) and the Canadian Arctic (Michel Gosselin, Institut des sciences de la mer de Rimouski, personal communication) under ongoing climate change are processes that deserve attention in the development of DMS models for the Arctic, because these haptophytes are high DMSP producers (Stefels et al., 2007).

Chapter 6

Conclusions

In the Arctic, oceanic emissions of DMS may exert a strong influence on the local climate by modifying the strength of the radiative forcing by aerosol and clouds. Suggestions that this is an important effect, however, are based on a few observational studies that are spatially and temporally confined, and its relevance to the whole Arctic remains open to question. To address this issue, I developed a numerical model representing sea-ice and oceanic DMS production to investigate the spatial, seasonal, and interannual variability in DMS emissions in the Arctic.

Initial development was performed within a 1-D column modelling framework, which is an important tool for the development of 3-D regional/global models. In this dissertation, I developed a sea-ice biogeochemical model including DMS production within the GOTM-FABM 1-D framework, and then incorporated this model into a pan-Arctic configuration of the NEMO 3-D framework. To my knowledge, such a model has not previously been implemented in either of these frameworks. As both GOTM-FABM and NEMO are open-source and community-based state-of-the-art frameworks for ocean modelling, it is anticipated that the sea-ice biogeochemical model developed in this dissertation will be used in future studies, and the strategies for coupling the model with the pelagic component provide a technical guideline for future model development (e.g. implementation of sympagic-pelagic-benthic coupling).

Sea-ice biogeochemistry is a crucial component of ecosystems and DMS production in polar oceans. The 1-D sensitivity simulations demonstrated the role of ice algae in shaping the subsequent phytoplankton blooms through seeding and nutrient drawdown. Furthermore, these simulations showed notable contribution of sea-ice biogeochemistry to DMS production in the underlying water column and its potential

emissions to the overlying atmosphere. These emissions are possible due to accumulation of DMS under the ice and its sudden release with opening leads. This simulated springtime DMS flux is comparable to some of the observed maxima in the summertime flux in the Arctic, and is considered sufficient to trigger new particle formation. While DMS has not been detected as a source of ice-nucleating particles (INPs), other ice algal materials (e.g., aggregates, exudates, and extracellular polymeric substances) have been speculated as potential sources of INPs (Irish et al., 2017). Therefore, the springtime flux of DMS and other ice algal products can influence the properties of ice clouds (as opposed to liquid clouds in the summer), and may have disproportionate importance for radiative forcing from the subsequent summertime flux. Furthermore, the springtime DMS flux can affect the summertime flux by influencing the light availability for phytoplankton growth, thereby proposing a link between ice algae and phytoplankton via the CLAW hypothesis at a seasonal time scale. This potential role of DMS and other ice algal products in ice-cloud nucleation is an interesting area for future research.

Another aspect of 1-D modelling is that it is an excellent tool to develop new parameterizations and assess the model sensitivity to parameters that are poorly constrained by observations. Compared to previous Arctic DMS model studies, the model parameters were better constrained in this dissertation by reflecting the results of the recent field measurements in the Arctic. In agreement with previous model studies, the 1-D sensitivity simulations indicated that key controlling parameters for DMS production are the algal cellular quota of DMSP and the bacterial DMS yield fraction. As these parameters are dependent on environmental factors, model representations of processes entailing these parameters can be improved by developing new parameterizations through collaboration among modellers, experimentalists, and observationalists.

The 1-D model simulations also emphasized the importance of light-relevant processes and parameters to ice-covered ecosystems and DMS production. Specifically, it was demonstrated that: resolving sub-grid-scale snow depth distribution improved the simulation of grid-cell-mean PAR reaching the bottom layer of sea ice, and therefore, also improved the simulation of the ice algal bloom; the onset of the modelled ice algal bloom was largely controlled by the parameters concerning the photosynthesis of ice algae; and DMS production within sea ice showed high sensitivity to the bacterial activity parameters. Furthermore, the assumption of light transmission through the snow column in classical sea-ice models was challenged by the inadequate simulation

of ice algal annual primary production in one of the 3-D model sensitivity simulations. These results highlight important processes for sea-ice optics and ice algal production that can be better represented in models.

The 3-D model simulated declines of Arctic sea ice and spatio-temporal variability in the sea-ice and pelagic annual primary production within the Arctic Circle over recent decades that are comparable to available data from field measurements, remote sensing, and other model simulations. These findings demonstrated the model's skill in simulating the governing physical and biogeochemical processes for DMS production in the Arctic Ocean as well as the applicability of the sea-ice biogeochemical model developed in the 1-D modelling framework to the broader 3-D modelling framework. In particular, the model results are in close agreement with other recent model studies. The agreement among different models builds confidence in the estimates of certain quantities, which helps narrow the range of old estimates (e.g. pan-Arctic ice algal NPP; Legendre et al., 1992) that are based on spatial extrapolation of a single ice algal production value.

The model-based DMS climatology was in broad agreement with the *in situ* measurement-based and the satellite-derived climatologies in terms of the magnitude of the mean seasonal cycle within the Arctic Circle, but not so in terms of the spatial variability in the timing of the annual peak in DMS concentrations. One critical issue with the current comparison is the extrapolation bias in the *in situ* measurement-based climatology owing to the scarcity of data in the Arctic Ocean. Specifically, the *in situ* measurement-based climatology is dominated by the more abundant data from the lower latitudes, resulting in an earlier onset of annual peak in DMS concentrations in the Arctic compared to the model-based climatology. As such, the model could augment the interpretation of the *in situ* measurement-based climatology especially over the region of missing data. Another issue with the current comparison is that these climatologies may not be directly comparable given different underlying assumptions on the structure of the models (empirical vs prognostic) and spatial scale of sampling (grid point vs box). These inherent differences cause individual biases that potentially impacted the comparison. Given the increased efforts to measure DMS concentrations in the Arctic Ocean over the past few years, it is time to update the existing *in situ* measurement-based climatology with these recently-acquired datasets. Such a new climatology would improve not only the quality of the comparison with the model-based and satellite-derived climatologies, but also the quality of atmospheric and Earth System model simulations. Similarly, a

sophisticated DMS model such as the one developed in this dissertation can be used to create a model-based climatology for atmospheric and Earth System models. The advantages of the modelling approach here is that it has no extrapolation bias and that it can be applied for the future (projection).

The acceleration in the decline of Arctic sea ice over the past two decades (since the late 1990s) is a well-established feature of anthropogenic climate change, and the respective impacts on DMS emissions were assessed with the developed model tool. The trend analysis over 1996-2015 indicated that the modelled pan-Arctic ice-to-sea annual DMS flux was relatively constant over this period due to the counteracting effects of reductions in both Arctic sea ice extent and thickness on ice algal production and the subsequent release of DMS from the bottom ice. The results also indicated that the ice-to-sea flux was strongly influenced by trends in snow depth that affects light-limited ice algal production in certain regions. On a pan-Arctic scale, this flux represents an insignificant source of annual oceanic DMS emissions. However, this flux can dominate the oceanic DMS emissions in areas where the ice algal production is high while the pelagic primary production is relatively low, which may be hidden in regional and/or annual averages. Furthermore, the contribution of sea-ice DMS production to the oceanic emissions might have been higher if the model accounted for additional sources, such as emission from melt ponds and the direct release from the sea ice to the atmosphere. These could be quantified in follow-up model studies.

The response of the modelled pan-Arctic sea-to-air annual DMS flux to the acceleration in the Arctic sea ice decline, on the other hand, was a consistent increase due to enhanced oceanic DMS production and emissions. In other words, the consequence of climate warming is an enhancement in the DMS emissions in the Arctic. This finding therefore supports the first step in the biological-climate linkage proposed by the CLAW hypothesis. The atmosphere is fairly clean in the Arctic except during winter due to biomass burning for heating and late summer due to (increasing amounts of) wildfires. If we assume that the summertime background concentration of aerosol particles remains low during this period, the increase in the DMS flux should be the driver for the new particle formation and the subsequent cloud formation/modification in the Arctic. While this response was postulated by previous studies, this dissertation demonstrates it by 3-D modelling for the first time. Whether this increase will continue with Arctic sea ice decline throughout this century can be addressed by extending the simulation into the future. Continued model development is recommended in parallel with such projections in order to account for potential

climate change impacts on ecological processes that control DMS production. Ultimately, the strength of regional climate feedbacks due to ice algae and phytoplankton in the Arctic can be explored by Earth System Model simulations that have prognostic representation of sea-ice and oceanic production of DMS and emissions to the atmosphere. This dissertation provides a step toward such an implementation.

Appendix A

Additional Information

A.1 Additional information for Chapter 2

A.1.1 Parameterizations for subgrid-scale snow depth distribution and light penetration through snow, sea ice, and melt ponds

To improve light and heat flux estimates through sea ice in regional and global models, Abraham et al. (2015) applied two kinds of one-parameter probability density functions for describing subgrid-scale snow depth variability: Rayleigh and gamma distributions. In this study, the Rayleigh distribution is used in model simulations since Abraham et al. (2015) indicated a better fit with observed snow depth evolution. The probability density function for the Rayleigh distributed snow ($pdf(h)$) is defined as

$$pdf(h) = \frac{\pi h}{2h_s^2} \exp\left(-\frac{\pi h^2}{4h_s^2}\right), \tag{A.1}$$

where h is the snow depth (m) and h_s represents the gridbox-mean snow depth (m), which is simulated by the sea ice model. The light transmission through snow and sea ice is described by the Beer-Lambert law, which is defined in a generalized form as:

$$I(z) = I_0 \exp(-\kappa z), \tag{A.2}$$

where $I(z)$ is the radiation at depth z (m) below the surface (W m^{-2}) and κ is the extinction coefficient of the medium (m^{-1}). I_0 represents the amount of incident light that penetrates into the snow/ice/melt ponds surface (W m^{-2}), which is defined in a generalized form as

$$I_0 = SWR(1-\alpha)i_0, \tag{A.3}$$

where SWR is the incident shortwave radiation (W m^{-2}), α is the surface albedo (dimensionless), and i_0 is the transmissivity coefficient (dimensionless). For a fully snow-covered surface of non-uniform snow depth, the gridbox-mean light intensity at the snow base is obtained by averaging the Beer-Lambert law over all snow depths weighted by the relative probabilities:

$$\bar{I}_s = SWR\,(1-\alpha_s)\,i_{0,s}\int_0^\infty pdf(h)\exp(-\kappa_s h)\mathrm{d}h, \tag{A.4}$$

where α_s, $i_{0,s}$, and κ_s respectively represent the albedo, the transmissivity coefficient, and the extinction coefficient for snow.

During melt periods, the ice surface may have different covers, such as snow, bare ice, and melt ponds. To account for different surface conditions in the parameterization of the gridbox-mean light intensity at the ice surface, Abraham et al. (2015) accounted for these different surface conditions within a grid box by introducing surface area fractions of snow (A_s), bare ice (A_i), and melt ponds (A_m), such that

$$A_s + A_i + A_m = 1. \tag{A.5}$$

The parameterizations for A_s, A_i, and A_m are described in Abraham et al. (2015). The gridbox-mean light intensity at the ice surface ($\bar{I}_{top}$) is then defined as a sum of the incident light that has: 1) penetrated through snow; 2) reached the bare ice; and 3) penetrated through melt ponds. Hence, $\bar{I}_{top}$ is given by

$$\bar{I}_{top} = A_s\bar{I}_s + A_i I_{0,i} + A_m I_{0,m}\exp\left(-\kappa_m h_m\right) \tag{A.6}$$

where $\bar{I}_s$ is Equation A.4. κ_m and h_m are the extinction coefficient and the depth of melt ponds, respectively. $I_{0,i}$ and $I_{0,m}$ respectively represent the amounts of incident

light that penetrates through the ice and melt ponds surface:

$$I_{0,i} = SWR(1-\alpha_i)i_{0,i} \tag{A.7}$$

$$I_{0,m} = SWR(1-\alpha_m)i_{0,m} \tag{A.8}$$

where α_i and α_m are the albedos and $i_{0,i}$ and $i_{0,m}$ are the transmissivity coefficients for sea ice and melt ponds, respectively. The optical parameters used in this study are listed in Table A.1. Note that different values for the extinction coefficients and albedos are set between the freezing and melting phases of snow and sea ice. To allow a smooth transition between the values under the freezing and melting phases, the extinction coefficients and albedos of snow and sea are defined based on Abraham et al. (2015) as

$$\kappa_s = \frac{\kappa_{s,f}+\kappa_{s,m}}{2} + \frac{\kappa_{s,m}-\kappa_{s,f}}{2}\tanh\left(T-273.15°\mathrm{C}\right) \tag{A.9}$$

$$\kappa_i = \frac{\kappa_{i,f}+\kappa_{i,m}}{2} + \frac{\kappa_{i,m}-\kappa_{i,f}}{2}\tanh\left(T-273.15°\mathrm{C}\right) \tag{A.10}$$

$$\alpha_s = \frac{\alpha_{s,f}+\alpha_{s,m}}{2} + \frac{\alpha_{s,m}-\alpha_{s,f}}{2}\tanh\left(T-273.15°\mathrm{C}\right) \tag{A.11}$$

$$\alpha_i = \frac{\alpha_{i,f}+\alpha_{i,m}}{2} + \frac{\alpha_{i,m}-\alpha_{i,f}}{2}\tanh\left(T-273.15°\mathrm{C}\right) \tag{A.12}$$

Following Zeebe et al. (1996), it is assumed that only PAR penetrates into the ice interior, while the radiation outside of PAR bands is absorbed by the uppermost layer of snow, bare ice, or melt ponds. Therefore, the gridbox-mean PAR at the ice base ($\overline{PAR}_{bot}$) is defined as

$$\overline{PAR}_{bot} = \bar{I}_{top}\exp(-\kappa_i h_i) \tag{A.13}$$

where h_i is the sea ice thickness. Finally, the gridbox-mean PAR in the water column under the ice ($\overline{PAR}_{ui}(z)$) is first attenuated by ice algae before it reaches the uppermost layer of the water column, and is further reduced as it penetrates through each model layer due to absorption and scattering by seawater itself, as well as by phytoplankton and detritus:

$$\overline{PAR}_{ui}(z) = \overline{PAR}_{bot}\exp\left(-\kappa_{ia}[IA]h_{ia} - \kappa_{ui}z_{sw}\right) \tag{A.14}$$

where κ_{ia} is the extinction coefficient of ice algae, $[IA]$ is the ice algal biomass, and

h_{ia} is the thickness of the ice skeletal layer, which are all defined in the next section. z_{sw} is the depth of seawater under the ice. κ_{ui} is the total extinction coefficient in the water column defined as

$$\kappa_{ui} = \kappa_{sw} + \kappa_{pd} \int_0^{z_{sw}} (P1 + P2 + D1 + D2)\, \mathrm{d}z \tag{A.15}$$

where κ_{sw} and κ_{pd} are the extinction coefficients for seawater and for both phytoplankton and detritus. κ_{sw} is computed by the GOTM model assuming the Jerlov type I (Burchard et al., 2006). The concentrations of phytoplankton ($P1$, $P2$) and detritus ($D1$, and $D2$) at the given model layer are defined in the next section.

A.1.2 Ecosystem model equations

The coupled sea ice-ocean biogeochemical model consists of 14 state variables (Figure 1 and Table A.1). Nitrogen is used as the currency for the model state variables other than $[Si]_{ia}$, $[Si]$, and $[BSi]$, which are expressed in silicon units. For comparison with observations, conversion from nitrogen (N) to Chl *a* and carbon (C) are required. For small phytoplankton (P1), the Redfield C:N ratio of 106:16 (mol:mol) following Redfield et al. (1963) and a fixed C:Chl *a* ratio of 50:1 (wt:wt) following Lavoie et al. (2009) are used. For ice algae and large phytoplankton (IA and P2), a fixed C:N ratio of 106:12 (mol:mol) following Palmer et al. (2014) and a fixed C:Chl *a* ratio of 28:1 (wt:wt) following Lavoie et al. (2009) were used. In Lavoie et al. (2009), the C:Chl *a* ratio of 28:1 (wt:wt) was used for ice algae, while 50:1 (wt:wt) was used for phytoplankton (corresponding to P2 in this study) assuming that ice algae was more acclimated to low light conditions. However, in this study, prescribing different C:Chl *a* ratios between IA and P2 would result in the violation of mass conservation of chlorophyll *a* in P2 because IA and P2 are coupled through the flushing of ice algae to enter the P2 pool, and also because chlrophyll *a* is not modeled explicitly. We represent the photoacclimation of IA relative to P2 by prescribing different values of photosynthetic parameters. The parameters for the ecosystem model are listed in Table A.3.

Sea ice component

The sea ice biogeochemical model consists of four state variables: ice algae, nitrate, ammonium, and silicate. The equation for ice algae is

$$\frac{\partial}{\partial t}[IA] = \mu_{ia}[IA] - M[IA] - \left(\frac{[R_{ice}] + f_{pond} r_{pond}}{z_{ia}}\right)[IA], \tag{A.16}$$

where $[IA]$ is the ice algal biomass in the bottom 3 cm of the skeletal layer (mmol N m^{-3}). The first term in Equation A.16 represents the growth of ice algae due to primary production. The rate of ice algal growth (μ_{ia}) depends on the ambient temperature of the bottom ice ($[T]_{ia}$ in °C) following Eppley (1972), as well as on the minimum value among the four limitation functions (L_{nit}, L_{sil}, L_{lig}, and L_{ice}):

$$\mu_{ia} = \mu_{ia}^{max} \ln(2) \exp(b_{ia}[T]_{ia}) \min\left(L_{nit}, L_{sil}, L_{lig}, L_{ice}\right), \tag{A.17}$$

where μ_{ia}^{max} represents the specific growth rate and b_{ia} is the temperature sensitivity coefficient for the ice algal growth. Following Lavoie et al. (2005), μ_{ia}^{max} and b_{ia} are set to 0.85 d^{-1} and 0.0633 $°C^{-1}$. The nitrogen (L_{nit}) and silicon (L_{sil}) limitation functions are based on the Monod formulation (Monod, 1949):

$$L_{nit} = \frac{[NO_3]_{ia} + [NH_4]_{ia}}{k_n + [NO_3]_{ia} + [NH_4]_{ia}} \tag{A.18}$$

$$L_{sil} = \frac{[Si]_{ia}}{k_s + [Si]_{ia}} \tag{A.19}$$

where $[NO_3]_{ia}$, $[NH_4]_{ia}$, and $[Si]_{ia}$ respectively represent the concentrations of nitrate (mmol N m^{-3}), ammonium (mmol N m^{-3}), and silicate (mmol Si m^{-3}) in the bottom 3 cm of the ice skeletal layer. k_n and k_s are the half-saturation constants for nitrogen and silicon uptake, which are set to 1 mmol N m^{-3} and 4 mmol Si m^{-3} following Lavoie et al. (2005), respectively. The light limitation function (L_{lig}) is formulated following Lavoie et al. (2005):

$$L_{lig} = \tanh\left(\frac{\alpha^{ia}}{P_m^{ia}}[PAR]_{ia}\right) \tag{A.20}$$

where α^{ia} is the photosynthetic efficiency (mg C (mg Chl a)$^{-1}$ h^{-1} (μmol photons m^{-2} s^{-1})$^{-1}$), P_m^{ia} is the maximum photosynthetic rate (mg C mg Chl a^{-1} h^{-1}), and $[PAR]_{ia}$ is the PAR (in μmol photons m^{-2} s^{-1}) penetrating the ice algae skeletal

layer, which is computed by the sea ice thermodynamic model. Lavoie et al. (2005) used various values (0.1-0.45) for the ratio of α^{ia} and P_m^{ia} depending on snow cover. We set the ratio of these two photosynthetic parameters (α^{ia}/P_m^{ia}) to 0.44, based on the results of our sensitivity studies.

The ice growth/melt limitation function (L_{ice}) is formulated similarly to Lavoie et al. (2005):

$$L_{ice} = \max\left(1 - \frac{[R_{ice}]}{C_m}, 0\right) \tag{A.21}$$

where $[R_{ice}]$ is the ice growth/melt rate at the ice base (m s^{-1}) computed by the physical model (see Flato and Brown (1996) for details) and C_m is the critical ice growth/melt rate, which is set to 0.015 m d^{-1} following Lavoie et al. (2005).

The second term in Equation A.16 represents the loss due to mortality. The mortality rate of ice algae (M) includes both linear and quadratic dependence on the ice algal biomass:

$$M = m_{lia} \exp(b_{ia}[T]_{ia}) + m_{qia}[IA] \tag{A.22}$$

where m_{lia} is the rate constant for the temperature-dependent linear mortality and m_{qia} is the rate constant for the quadratic mortality. We set m_{lia} and m_{qia} to 0.03 d^{-1} and 0.00015 d^{-1}, based on the results of our sensitivity studies.

The last term in Equation A.16 represents the loss due to flushing. There are four sources of meltwater that contributes to flushing: ice meltwater originating from the 1) top, 2) interior, and 3) bottom of the sea ice; and 4) snow meltwater that drains out of melt ponds. The sum of the ice melt rates (R_{ice}) and the areal fraction of melt ponds (f_{pond}) are computed by the physical model (see Flato and Brown (1996) and Abraham et al. (2015) for details). r_{pond} represents the drainage rate of meltwater in the melt ponds, which is set to 0.0175 m d^{-1} following Taylor and Feltham (2004). Finally, z_{ia} is the thickness of the ice skeletal layer, which is set to 0.03 m in this study.

The equations for nitrate ($[NO_3]_{ia}$) and ammonium ($[NH_4]_{ia}$) in the ice skeletal

layer (mmol N m^{-3}) are defined as:

$$\frac{\partial}{\partial t}[NO_3]_{ia} = -\mu_{ia}[IA]p^{ia}_{no3}\frac{[NO_3]_{ia}}{[NO_3]_{ia}+[NH_4]_{ia}} + r_{nit}[NH_4]_{ia} - \frac{f_{pond}r_{pond}}{z_{ia}}[NO_3]_{ia} + \frac{D}{h_\nu}\left(\frac{[NO_3]-[NO_3]_{ia}}{z_{ia}}\right) \quad (A.23)$$

$$\frac{\partial}{\partial t}[NH_4]_{ia} = -\mu_{ia}[IA]\left(1-p^{ia}_{no3}\right)\frac{[NO_3]_{ia}}{[NO_3]_{ia}+[NH_4]_{ia}} - r_{nit}[NH_4]_{ia} - \frac{f_{pond}r_{pond}}{z_{ia}}[NH_4]_{ia} + \frac{D}{h_\nu}\left(\frac{[NH_4]-[NH_4]_{ia}}{z_{ia}}\right) + f_{lia}m_{lia}exp(b_{ia}[T]_{ia})[IA] \quad (A.24)$$

The first term in Equation A.23 and Equation A.24 represents the loss due to uptake by ice algae. To discriminate the uptake of nitrate from that of ammonium, the relative preference index (p^{ia}_{no3}) based on Denman (2003) is defined as:

$$p^{ia}_{no3} = \frac{\nu_n}{\nu_n + [NH_4]_{ia}}, \quad (A.25)$$

where ν_n represents the half-saturation constant for preferential uptake of nitrate, which is set to 0.2 mmol N m^{-3} following Denman (2003). The second term in Equation A.23 and Equation A.24 represents the nitrification, which is a source for nitrate and a sink for ammonium. In this study, a first order reaction is assumed for this process in the sea ice with a rate constant of 0.01 d^{-1}. The third term in Equation A.23 and Equation A.24 represents the loss due to flushing, which is formulated in a similar manner as the flushing of ice algae. The fourth term in Equation A.23 and Equation A.24 represents the diffusive exchange at the ice-ocean interface, where $[NO_3]$ and $[NH_4]$ are the concentrations (mmol N m^{-3}) of nitrate and ammonium in the uppermost layer of the water column. D is the molecular diffusion coefficient for dissolved nutrients at the ice-water interface, which is set to 4.7×10^{-8} m^2 s^{-1} (Rebreanu et al., 2008). The exchange rate at the ice-water interface depends on the molecular sublayer thickness (h_ν) defined as:

$$h_\nu = \frac{\nu}{u_\tau}, \quad (A.26)$$

where ν is the kinematic viscosity of seawater, which is set to 1.85×10^{-6} m^2 s^{-1} (Lavoie

et al., 2005). u_τ represents the friction velocity, which is defined as

$$u_\tau = \left(\frac{|\tau|}{\rho_o}\right)^{1/2}, \tag{A.27}$$

where τ is the ice-ocean stress and ρ_0 is the seawater density. Following Goosse and Fichefet (1999), τ is defined as

$$\tau = \rho_o C_{io} |u_i - u_o| \left(u_i - u_o\right), \tag{A.28}$$

where C_{io} is the drag coefficient at the ice-ocean interface, which is set to 0.0054 (Shirasawa and Ingram, 1997). u_i and u_o are the magnitudes of horizontal velocity fields of ice and surface water, respectively. Substituting Equations A.27 and A.28 into Equation A.26 gives:

$$h_\nu = \frac{\nu}{|u_i - u_o|} C_{io}^{-\frac{1}{2}}, \tag{A.29}$$

where u_o is computed by the physical ocean model, and we assume $u_i = 0$ for landfast ice considered in this study.

The fifth term in Equation A.24 represents the remineralization of dead ice algal cells. A direct transfer from ice algae to ammonium is implemented here due of lack of representation of detritus pool in the sea ice. It is assumed that only a fraction (f_{lia}) of linear mortality enters the ammonium pool, while the remaining fraction is released into the water column and enters the large detritus pool. In this study, f_{lia} is set to 0.3.

The equation for silicate ($[Si]_{ia}$) in the ice skeletal layer (mmol Si m^{-3}) is given by:

$$\frac{\partial}{\partial t}[Si]_{ia} = -q_{si2n}\mu_{ia}[IA] - \frac{f_{pond} r_{pond}}{z_{ia}}[Si]_{ia} + \frac{D}{h_\nu}\left(\frac{[Si] - [Si]_{ia}}{z_{ia}}\right) \tag{A.30}$$

where the first term represents the uptake by ice algae, the second term represents the flushing, and the third term represents the diffusive mixing at the ice-ocean interface. The uptake rate is converted from nitrogen to silicon units by assuming a fixed nitrogen-to-silicon intracellular ratio (q_{si2n}) of 1.7 mol Si:mol N based on Mundy et al. (2014). $[Si]$ represents the concentration of silicate in the uppermost layer of the water column (mmol Si m^{-3}).

Oceanic component

The ocean biogeochemical model consists of ten state variables: small and large classes of phytoplankton, zooplankton, and detritus, biogenic silica, nitrate, ammonium, and silicate. The equations for small and large phytoplankton are:

$$\frac{\partial}{\partial t}[P1] = \mu_{p1}[P1] - \Gamma_{z1}\frac{[P1]}{F_{z1}}[Z1] - M_{lp1}[P1] + \frac{\partial}{\partial z}\left(K_z\frac{\partial[P1]}{\partial z}\right) \tag{A.31}$$

$$\begin{aligned}\frac{\partial}{\partial t}[P2] = {} & \mu_{p2}[P2] - \Gamma_{z2}\frac{[P2]}{F_{z2}}[Z2] - M_{lp2}[P2] + \frac{\partial}{\partial z}\left(K_z\frac{\partial[P2]}{\partial z}\right) \\ & - m_{qp2}[P2]^2 + f_{seed}\left([R_{ice}] + r_{pond}\right)[IA]\frac{z_{ia}}{z_{oc}}\delta_{z,z_1}\end{aligned} \tag{A.32}$$

where $[P1]$ and $[P2]$ respectively represent the biomass of small and large phytoplankton (mmol N m^{-3}). The first term in Equations A.31 and A.32 represent the growth due to primary production. The growth rates of phytoplankton (μ_{p1} and μ_{p2}) depend on the ambient temperature, nutrient and light conditions:

$$\mu_{p1} = \mu_{p1}^{max} Q_{10p}^{([T]-10)/10} \min\left(L_{nit}^{phy}, L_{lig}^{p1}\right) \tag{A.33}$$

$$\mu_{p2} = \mu_{p2}^{max} Q_{10p}^{([T]-10)/10} \min\left(L_{nit}^{phy}, L_{lig}^{p2}, L_{sil}^{p2}\right) \tag{A.34}$$

where μ_{p1}^{max} and μ_{p2}^{max} represent the maximum specific growth rates, which are set to 0.5 and 2.0 d^{-1}, respectively (Steiner et al., 2006). The temperature dependence is based on the Q10 formulation with a Q10 factor (Q_{10p}) of 1.55 (Suzuki and Takahashi, 1995). $[T]$ is the ambient seawater temperature (°C), which is simulated by the physical model. The nutrient limitation functions are based on the Monod function (Monod, 1949):

$$L_{nit}^{phy} = \frac{[NO_3] + [NH_4]}{k_n + ([NO_3] + [NH_4])} \tag{A.35}$$

$$L_{sil}^{p2} = \frac{[Si]}{k_{si} + [Si]} \tag{A.36}$$

where the same half-saturation constants are used between the sea ice and ocean biogeochemical modules. The light limitation functions are defined as

$$L_{lig}^{p1} = 1 - \exp\left(-\alpha^{p1}/P_m^{p1}[PAR]\right) \tag{A.37}$$

$$L_{lig}^{p2} = 1 - \exp\left(-\alpha^{p2}/P_m^{p2}[PAR]\right) \tag{A.38}$$

where α^{p1} and α^{p2} represent the photosynthetic efficiency and P_m^{p1} and P_m^{p2} represent the maximum photosynthetic rate. In this study, the ratios of photosynthetic parameters (i.e., α^{p1}/P_m^{p1} and α^{p2}/P_m^{p2}) are set to 0.07 for both phytoplankton groups. $[PAR]$ represents the photosynthetically active radiation in the water column (μmol photons m^{-2} s^{-1}) which is defined in the previous section. The second term in Equations A.31 and A.32 represent the loss due to grazing by zooplankton. The The rates of small and large zooplankton (Γ_{z1} and Γ_{z2}) are defined as

$$\Gamma_{z1} = \gamma_{z1} Q_{10z}^{([T]-10)/10} \frac{F_{z1}^2}{k_{z1}^2 + F_{z1}^2} \tag{A.39}$$

$$\Gamma_{z2} = \gamma_{z2} Q_{10z}^{([T]-10)/10} \frac{F_{z2}^2}{k_{z2}^2 + F_{z2}^2} \tag{A.40}$$

where γ_{z1} and γ_{z2} represent the maximum specific grazing rates, which are set to 1 d^{-1} for both zooplankton groups in this study. The Q10 factor for zooplankton (Q_{10z}) is set to 2.14 (Buitenhuis et al., 2006). k_{z1} and k_{z2} represent the half-saturation constants for grazing, which are set to 1 mmol N m^{-3} for both zooplankton groups in this study. F_{z1} and F_{z2} respectively represent the available food sources for small and large zooplankton, which are defined as

$$F_{z1} = [P1] + f_{d1}[D1] \tag{A.41}$$

$$F_{z2} = [P2] + f_{d2}[D2] + f_{z1}[Z1] \tag{A.42}$$

where f_{d1} represents the grazing preference of small zooplankton on small detitus. f_{d2} and f_{z2} represent the grazing preferences of large zooplankton on small and large detritus, respectively. f_{d1}, f_{d2}, and f_{z1} are all set to 0.5 following Steiner et al. (2006).

The third terms in Equations A.31 and A.32 represent the linear mortality of small and large phytoplankton. Assuming a temperature depnedence following the same Q10 formulation, the rates of linear mortality are given by:

$$M_{lp1} = m_{lp1} Q_{10p}^{([T]-10)/10} \tag{A.43}$$

$$M_{lp2} = m_{lp2} Q_{10p}^{([T]-10)/10} \tag{A.44}$$

where m_{lp1} and m_{lp2} represent the rate constants for linear mortality of small and large phytoplankton, respectively. In this study, both of these rates are set to 0.03 d^{-1}.

The fourth terms in Equations A.31 and A.32 represent the vertical mixing of small and large phytoplankton at a given model layer with those in the adjacent (upper and/or lower) layers. K_z represents the vertical eddy diffusivity coefficient, which is calculated by the physical ocean model.

The fifth term in Equation A.32 represents the quadratic mortality of large phytoplankton, which depends on a rate constant, m_{qp2}. In this study, m_{qp2} is set to 0.05 d^{-1} (mmol N m^{-3})$^{-1}$. The sixth term in Equation A.32 represents the source for large phytoplankton due to seeding of ice algae. Following Lavoie et al. (2009), it is assumed that a certain fraction (f_{seed}) of ice algae flushed into the water column enters the large phytoplankton pool, while the remaining fraction (1 - f_{seed}) enters the large detritus pool. In this study, f_{seed} is set to 0.1, assuming that 10% of ice algae flushing results in large phytoplankton seeding. h_{oc} is the thickness of the uppermost layer of the ocean model (i.e., 1 m in this study), and δ_{z,z_1} is the Kronecker's delta which equals 1 in the uppermost layer of the ocean (z_1), while it is set to 0 elsewhere:

$$\delta_{z,z_1} = \begin{cases} 0 & \text{if } z \neq z_1 \\ 1 & \text{if } z = z_1 \end{cases} \tag{A.45}$$

The equations for small and large zooplankton are defined as

$$\frac{\partial}{\partial t}[Z1] = a_1 \Gamma_{z1}[Z1] - M_{lz1}[Z1] - \Gamma_{z2}\frac{f_{z1}[Z1]}{F_{z2}}[Z2] + \frac{\partial}{\partial z}\left(K_z \frac{\partial [Z1]}{\partial z}\right) \tag{A.46}$$

$$\frac{\partial}{\partial t}[Z2] = a_2 \Gamma_{z2}[Z2] - M_{lz2}[Z2] - m_{qz2}[Z2]^2 + \frac{\partial}{\partial z}\left(K_z \frac{\partial [Z2]}{\partial z}\right) \tag{A.47}$$

where $[Z_1]$ and $[Z_2]$ respectively represent the biomass of small and zooplankton (mmol N m^{-3}).

The first terms in Equations A.46 and A.47 represent the sources due to ingestion, which are proportional to the zooplankton grazing. a_1 and a_2 respectively represent the assimilated fractions of grazing by small and large zooplankton, both of which are set to 0.7 following Lavoie et al. (2009).

The second terms in Equations A.46 and A.47 represent the sinks due to linear mortality. The rates of zooplankton linear mortality (M_{lz1} and M_{lz2}) are parameter-

ized in the same way as those of phytoplankton:

$$M_{lz1} = m_{lz1} Q_{10z}^{([T]-10)/10} \tag{A.48}$$

$$M_{lz2} = m_{lz2} Q_{10z}^{([T]-10)/10} \tag{A.49}$$

where the rate constants for linear mortality of small and large zooplankton (m_{lz1} and m_{lz2}) are both set to 0.03 d^{-1} (Lavoie et al., 2009).

The third term in Equation A.46 represents the loss of small zooplankton due to (carnivorous) grazing by large zooplankton. The third term in Equation A.47 represents the loss of large zooplankton due to quadratic mortality which is parameterized in the same way as the quadratic mortality of large phytoplankton with a rate constant (m_{qz2}) of 0.1 d^{-1} (mmol N m^{-3})$^{-1}$ in this study.

The fourth terms in Equations A.46 and A.47 respectively represent the vertical mixing of small and large zooplankton. The equations for small and large detritus,

as well as biogenic silica are given by

$$\begin{aligned}\frac{\partial}{\partial t}[D1] &= (1-a_1)\,\Gamma_{z1}[Z1] + M_{lp1}[P1] - \Gamma_{z1}\frac{f_{d1}[D1]}{F_{z1}}[Z1] \\ &\quad - R_{d1}[D1] - w_{d1}\frac{\partial[D1]}{\partial z} + \frac{\partial}{\partial z}\left(K_z\frac{\partial[D1]}{\partial z}\right) \qquad \text{(A.50)}\\ \frac{\partial}{\partial t}[D2] &= (1-a_2)\,\Gamma_{z2}[Z2] + M_{lp2}[P_2] - \Gamma_{z2}\frac{f_{d2}[D2]}{F_{z2}}[Z2] \\ &\quad - R_{d2}[D2] - w_{d2}\frac{\partial[D2]}{\partial z} + \frac{\partial}{\partial z}\left(K_z\frac{\partial[D2]}{\partial z}\right) + m_{qp2}[P_2]^2 \\ &\quad + (1-f_{seed})\left([R_{ice}] + r_{pond}\right)[IA]\frac{z_{ia}}{z_{oc}}\delta_{z,z_1} \\ &\quad + (1-f_{lia})\,m_{lia}exp(b_{ia}[T]_{ia})[IA]\frac{z_{ia}}{z_{oc}}\delta_{z,z_1} \\ &\quad + m_{qia}[IA]\frac{z_{ia}}{z_{oc}}\delta_{z,z0} \qquad \text{(A.51)}\\ \frac{\partial}{\partial t}[BSi] &= q_{si2n}\left((1-a_2)\,\Gamma_{z2}[Z2] + M_{lp2}[P_2] - \Gamma_{z2}\frac{f_{d2}[D2]}{F_{z2}}[Z2]\right) \\ &\quad - R_{bsi}[BSi] - w_{d2}\frac{\partial[BSi]}{\partial z} + \frac{\partial}{\partial z}\left(K_z\frac{\partial[BSi]}{\partial z}\right) + q_{si2n}m_{qp2}[P_2]^2 \\ &\quad + q_{si2n}\,(1-f_{seed})\left([R_{ice}] + r_{pond}\right)[IA]\frac{z_{ia}}{z_{oc}}\delta_{z,z_1} \\ &\quad + q_{si2n}\,(1-f_{lia})\,m_{lia}exp(b_{ia}[T]_{ia})[IA]\frac{z_{ia}}{z_{oc}}\delta_{z,z_1} \\ &\quad + q_{si2n}m_{qia}[IA]\frac{z_{ia}}{z_{oc}}\delta_{z,z0} \qquad \text{(A.52)}\end{aligned}$$

In each of Equations A.50, A.51, and A.52, the first term represents the unassimilated fraction of grazing that enter the detrital pool, the second term represents the source for detritus due to phytoplankton linear mortality, the third term represents the loss of detritus due to grazing, and the fourth term represents the remineralization of detrital materials. The rates of remineralization of small and large detritus and biogenic silica (R_{d1}, R_{d2}, R_{bsi}) depend on seawater temperature following the Q10 formulation:

$$R_{d1} = r_{d1}Q_{10b}^{([T]-10)/10} \qquad \text{(A.53)}$$

$$R_{d2} = r_{d2}Q_{10b}^{([T]-10)/10} \qquad \text{(A.54)}$$

$$R_{bsi} = r_{bsi}Q_{10b}^{([T]-10)/10} \qquad \text{(A.55)}$$

where r_{d1}, r_{d2}, and $_{bsi}$ represent the rate constants for remineralization, which are respectively set to 0.03 d^{-1} (this study), 0.3 d^{-1} (Lavoie et al., 2009), and 0.01

d^{-1} (Steiner et al., 2006).

The fifth terms in Equations A.50, A.51, and A.52 represent the loss due to sinking. It is assumed that detritus sink at a fixed rate; a rate of 1 m d^{-1} is given to small detritus, while a faster sinking rate of 50 m d^{-1} is prescribed for large detritus and biogenic silica. Both of these rates are taken from Lavoie et al. (2009). Detritus reaching the seafloor is accumulated in the deepest layer of the water column. The sixth terms in Equations A.50, A.51, and A.52 represent the vertical mixing of respective detrital materials.

The seventh terms in Equations A.50 and A.51 represent the sources for small and large detritus due to quadratic mortality of large phytoplankton. The last three terms in these equations represent the influxes of detrital materials from the ice skeletal layer due to flushing (the ninth terms), linear mortality (the tenth terms), and quadratic mortality (the eleventh terms) of ice algae. Note that the equation for biogenic silica is identical to the equation for large detritus except that the two state variables have different remineralization rates and that those terms expressed in nitrogen units are converted to silicon units by assuming a fixed intracellular nitrogen-to-silicon ratio of 1.7 mol N:mol Si (Mundy et al., 2014).

The equations for dissolved nutrients in the water column are defined as

$$\begin{aligned}\frac{\partial}{\partial t}[NO_3] =& -\left(\mu_{p1}[P1] + \mu_{p2}[P_2]\right) p_{no3} \frac{[NO_3]}{[NO_3] + [NH_4]} + \eta[NH_4] \\ & - \frac{D}{h_\nu}\left([NO_3] - [NO_3]_{ia}\right)\delta_{z,z_1} + \frac{\partial}{\partial z}\left(K_z \frac{\partial [NO_3]}{\partial z}\right) \qquad \text{(A.56)} \\ \frac{\partial}{\partial t}[NH_4] =& -\left(\mu_{p1}[P1] + \mu_{p2}[P_2]\right)\left(1 - p_{no3}\frac{[NO_3]}{[NO_3] + [NH_4]}\right) - \eta[NH_4] \\ & + M_{lz1}[Z1] + M_{lz2}[Z2] + R_{d1}[D1] + R_{d2}[D2] \\ & - \frac{D}{h_\nu}\left([NH_4] - [NH_4]_{ia}\right)\delta_{z,z_1} + \frac{\partial}{\partial z}\left(K_z \frac{\partial [NH_4]}{\partial z}\right) \qquad \text{(A.57)} \\ \frac{\partial}{\partial t}[Si] =& -q_{si2n}\mu_{p2}[P_2] + R_{bsi}[BSi] \\ & - \frac{D}{h_\nu}\left([Si] - [Si]_{ia}\right)\delta_{z,z_1} + \frac{\partial}{\partial z}\left(K_z \frac{\partial [Si]}{\partial z}\right) \qquad \text{(A.58)}\end{aligned}$$

where $[NO_3]$, $[NH_4]$, and $[Si]$ represent the concentrations of nitrate, ammonium, and silicate, respectively.

The first terms in Equations A.56 and A.57 represent the uptake by both small and large phytoplankton. The first term in Equation A.58 represents the uptake by large

phytoplankton only, assuming an insignificant silicon uptake by small phytoplankton. Similarly to the nitrogen uptake by ice algae, the relative preference index for nitrate uptake is formulated as a function of ammonium concentration following Denman (2003):

$$p_{no3} = \frac{v_n}{v_n + [NH_4]} \tag{A.59}$$

The second terms in Equations A.56 and A.57 represent the nitrification, which is a source for nitrate and a sink for ammonium. The rate of nitrification depends on temperature (Kawamiya et al., 1995) and is assumed to be photo-inhibited (Aumont et al., 2015):

$$\eta = \frac{r_{nit} \exp\left(b_{nit}[T]\right)}{1 + [PAR]} \tag{A.60}$$

where the rate constant (r_{nit}) and the temperature sensitivity coefficient (b_{nit}) for nitrification are set to 0.03 d^{-1} and 0.0693 $(°C)^{-1}$ following Kawamiya et al. (1995).

The third and the fourth terms in Equation A.57 respectively represent the sources for ammonium due to linear mortality of small and large zooplankton. The fifth and the six terms in the same equation represent the sources due to remineralization of small and large detritus, respectively.

The second term in Equation A.58 represents the source for silicate due to remineralization of biogenic silica. The second last terms in Equations A.56, A.57, and A.58 represent the diffusive exchange of nutrients between the uppermost layer of the water column and the ice skeletal layer. The last terms in these equations represent the vertical mixing of dissolved nutrients between the model layers in the water column.

Lastly, for each of the living organisms (IA, $P1$, $P2$, $Z1$, and $Z2$), all the sink terms in the equation are neglected (i.e., set to zero) when its biomass is below its initial concentration in order to maintain its overwintering level.

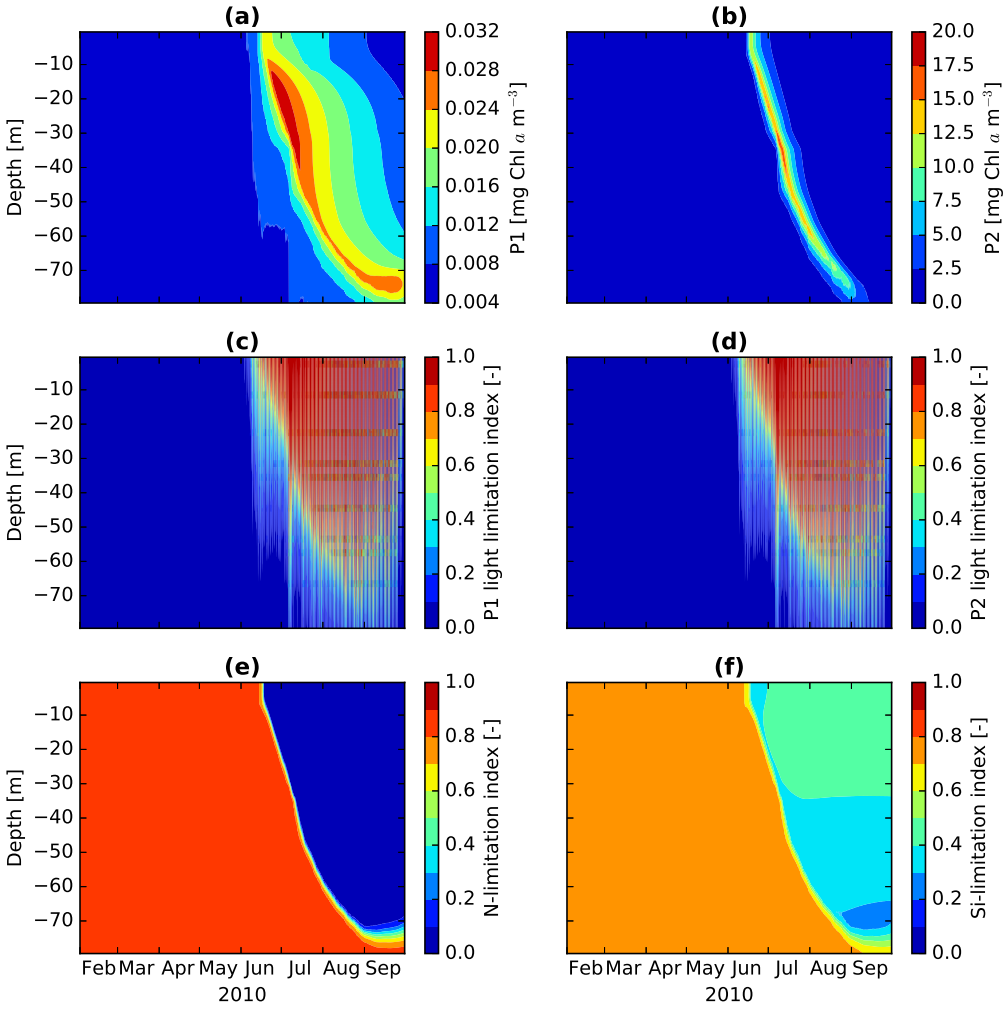

Figure A.1: P1, P2, and their light and nutrient limitations. Time series of simulated biomass of (a) P1 and (b) P2, light limitation index of (c) P1 and (d) P2, (e) nitrogen limitation index of P1 and P2, and (f) silicate limitation index of P2.

Table A.1: List of state variables in the coupled sea ice-ocean biogeochemical model.

Symbol	Description	Unit
$[IA]$	Ice algae in the bottom-ice skeletal layer	mmol N m^{-3}
$[NO_3]_{ia}$	Nitrate in the bottom-ice skeletal layer	mmol N m^{-3}
$[NH_4]_{ia}$	Ammonium in the bottom-ice skeletal layer	mmol N m^{-3}
$[Si]_{ia}$	Silicate in the bottom-ice skeletal layer	mmol Si m^{-3}
$[P1]$	Small phytoplankton in the water column	mmol N m^{-3}
$[P2]$	Large phytoplankton in the water column	mmol N m^{-3}
$[Z1]$	Small zooplankton in the water column	mmol N m^{-3}
$[Z2]$	Large zooplankton in the water column	mmol N m^{-3}
$[D1]$	Small detritus in the water column	mmol N m^{-3}
$[D2]$	Large detritus in the water column	mmol N m^{-3}
$[BSi]$	Biogenic silica in the water column	mmol Si m^{-3}
$[NO_3]$	Nitrate in the water column	mmol N m^{-3}
$[NH_4]$	Ammonium in the water column	mmol N m^{-3}
$[Si]$	Silicate in the water column	mmol Si m^{-3}

Table A.2: Parameters for the sea ice biogeochemical model.

Symbol	Description	Unit	Default value	Reference
α^{ia}/P_m^{ia}	Ratio of photosynthetic parameters (photosynthetic efficiency and maximum photosynthetic rate) for IA	(μmol photons m^{-2} s^{-1})$^{-1}$	0.44	Within the range of Lavoie et al. (2005)
b_{ia}	Temperature sensitivity coefficient for ice algal growth	(°C)$^{-1}$	0.0633	Lavoie et al. (2005)
C_{ice}	Critical ice growth/melt rate	m d^{-1}	0.015	Lavoie et al. (2005)
C_{io}	Drag coefficient at the ice-ocean interface	-	0.0054	Shirasawa and Ingram (1997)
D	Molecular diffusivity for nutrients at the ice-water interface	m^2 s^{-1}	0.47× 10^{-9}	Rebreanu et al. (2008)
f_{lia}	Fraction of ice algae linear mortality that goes to NH_4	-	0.3	This study
f_{seed}	Fraction of ice algae sloughing that contributes to P2 seeding	-	0.1	Lavoie et al. (2009)
k_n	Half-saturation constant for nitrogen uptake	mmol N m^{-3}	1	Lavoie et al. (2005)
k_s	Half-saturation constant for silicon uptake	mmol Si m^{-3}	4	Lavoie et al. (2005)
m_{lia}	Rate constant for ice algae linear mortality	d^{-1}	0.03	This study
m_{qia}	Rate constant of ice algae quadratic mortality	d^{-1} (mmol N m^{-3} d^{-1})$^{-1}$	0.00015	This study
μ_{ia}^{max}	Maximum specific ice algal growth rate	d^{-1}	0.85	Lavoie et al. (2005)
q_{si2n}	Intracellular silicon-to-nitrogen ratio	mol Si:mol N	1.7	Mundy et al. (2014)
r_{pond}	Melt pond drainage rate	m d^{-1}	0.0175	Taylor and Feltham (2004)
r_{nit}	Nitrification rate constant in sea ice	d^{-1}	0.01	This study
v_n	Scale factor for nitrogen preferance function	mmol N m^{-3}	0.2	Denman (2003)
ν	Kinematic viscosity of seawater	$m^2 s^{-1}$	1.85×10^{-6}	Lavoie et al. (2005)
z_{ia}	Thickness of the ice skeletal layer	m	0.03	This study
z_{oc}	Thickness of the ocean vertical grid	m	1	

Table A.3: Parameters for the ocean biogeochemical model.

Symbol	Description	Unit	Default value	Reference
a_1	Assimilated fraction of grazing by Z1	-	0.7	Lavoie et al. (2009)
a_2	Assimilated fraction of grazing by Z2	-	0.7	Lavoie et al. (2009)
α^{p1}/P_m^{p1}	Ratio of photosynthetic parameters (photosynthetic efficiency and maximum photosynthetic rate) for P1	(μmol photons m^{-2} s^{-1})$^{-1}$	0.07	This study
α^{p2}/P_m^{p2}	Ratio of photosynthetic parameters (photosynthetic efficiency and maximum photosynthetic rate) for P2	(μmol photons m^{-2} s^{-1})$^{-1}$	0.07	This study
b_{nit}	Temperature sensitivity coefficient for nitrification	$(°C)^{-1}$	0.0693	Kawamiya et al. (1995)
f_{d1}	Grazing preference on D1	-	0.5	Monahan and Denman (2004)
f_{d2}	Grazing preference on D2	-	0.5	Lavoie et al. (2009)
f_{z1}	Grazing preference on Z1	-	0.5	Monahan and Denman (2004)
γ_{z1}	Specific grazing rate of Z1	d^{-1}	1	This study
γ_{z2}	Specific grazing rate of Z2	d^{-1}	1	This study
k_{z1}	Half-saturation constant for Z1 grazing	mmol N m^{-3}	1	This study
k_{z2}	Half-saturation constant for Z2 grazing	mmol N m^{-3}	1	This study
m_{lp1}	Rate constant for P1 linear mortality	d^{-1}	0.03	This study
m_{lp2}	Rate constant for P2 linear mortality	d^{-1}	0.03	This study
m_{lz1}	Rate constant for Z1 linear mortality	d^{-1}	0.03	This study
m_{lz2}	Rate constant for Z2 linear mortality	d^{-1}	0.03	This study
m_{qp2}	Rate constant for P2 quadratic mortality	d^{-1} (mmol N m^{-3} d^{-1})$^{-1}$	0.05	This study
m_{qz2}	Rate constant for Z2 quadratic mortality	d^{-1} (mmol N m^{-3} d^{-1})$^{-1}$	0.1	This study
μ_{m1}^{max}	Maximum specific growth rate of P1	d^{-1}	0.5	Steiner et al. (2006)
μ_{m2}^{max}	Maximum specific growth rate of P2	d^{-1}	2.0	Steiner et al. (2006)
Q_{10p}	Q10 factor for phytoplankton	-	1.55	Suzuki and Takahashi (1995)
Q_{10z}	Q10 factor for zooplankton	-	2.14	Buitenhuis et al. (2006)
Q_{10b}	Q10 factor for bacteria	-	1.9	Aumont et al. (2015)
r_{d1}	Rate constant for D1 remineralization	d^{-1}	0.03	Steiner et al. (2006)
r_{d2}	Rate for D2 remineralization	d^{-1}	0.3	Lavoie et al. (2009)
r_{bsi}	Rate constant for BSi remineralization	d^{-1}	0.01	This study
r_{n0}	Nitrification rate at 0 °C in seawater	d^{-1}	0.03	Kawamiya et al. (1995)
w_{d1}	D1 sinking rate	m d^{-1}	1	This study
w_{d2}	D2 sinking rate	m d^{-1}	50	Lavoie et al. (2009)

A.2 Additional information for Chapter 3

A.2.1 Detailed model description

The set of differential equations describing the temporal evolution of DMSPp, DMSPd, and DMS concentrations in the bottom ice and water column is provided below. The list of variables and parameters involved in the model is provided in Table 3.1.

Sea-ice sulfur cycle

The meltwater equivalent concentration (nmol L^{-1}) of the particulate phase of DMSP in the bottom ice ($DMSPp$) is simulated diagnostically by assuming a fixed DMSPp-to-chlorophyll a intracellular ratio (nmol S:μg Chl a) for ice algae (q):

$$\frac{\partial}{\partial t}\left(DMSPp\right) = q\frac{\partial}{\partial t}\left(IA\right) \tag{A.61}$$

where IA is the ice algal biomass (μg Chl a L^{-1}). The intracellular ratio varies among algal species (Keller, 1989; Matrai and Keller, 1994) and also varies with various abiotic factors including temperature (Karsten et al., 1992; van Rijssel and Gieskes, 2002), salinity (Karsten et al., 1992), light (Karsten et al., 1992; Stefels and van Leeuwe, 1998; Sunda et al., 2002; Archer et al., 2009; Galindo et al., 2016) and nutrients (Stefels and van Leeuwe, 1998; Sunda et al., 2007; Archer et al., 2009). The reported values for q vary from 7.7 (Kirst et al., 1991) to about 20 (Uzuka, 2003; Stefels et al., 2012). Values of 9.4-9.5 have been reported for Resolute Passage (Galindo et al., 2014). In the standard run, we set q to 9.5 nmol S:μg Chl a.

The meltwater equivalent concentration (nmol L^{-1}) of the dissolved phase of DMSP in the bottom ice ($DMSPd$) is simulated prognostically:

$$\frac{\partial}{\partial t}\left(DMSPd\right) = F_{lysis} + F_{exudation} - F^{dmspd}_{consumption} - F_{free} - F^{dmspd}_{release} \tag{A.62}$$

where F denotes the production or removal rate (nmol L^{-1} d^{-1}) for each of the processes considered in the model (Fig. 3.1). The first two terms in Eq. (A.62) represent the production rates of bottom-ice DMSPd by cell lysis and exudation, respectively. Following Archer et al. (2004), these processes are parameterized to

increase under nutrient stress:

$$F_{lysis} = \frac{1}{L_{nut} + 0.1} k_{lysis} DMSPp \tag{A.63}$$

$$F_{exudation} = \left[f_{active} + (1 - f_{active}) (1 - L_{nut}) \right] \mu DMSPp \tag{A.64}$$

where L_{nut} represents the nutrient limitation index (-) for ice algal growth, k_{lysis} represents the rate constant (d^{-1}) for cell lysis, f_{active} represents the active exudation fraction (-), and μ represents the ice algal specific growth rate (d^{-1}). Both L_{nut} and μ are calculated by the ecosystem module. The two parameters involving cell lysis (k_{lysis}) and exudation (f_{active}) are generally poorly constrained in the sulfur cycle models because the measurements of production rates of DMSPd by cell lysis and exudation are very limited in seawater (Laroche et al., 1999). To our best knowledge, these rates have not been measured within sea ice. In the standard run, k_{lysis} and f_{active} are respectively set to 0.03 d^{-1} and 0.05, which are similar to the values used in previous ocean sulfur cycle models (Archer et al., 2004; Steiner and Denman, 2008).

The third term in Eq. (A.62) represents the removal rate of bottom-ice DMSPd by bacterial consumption. DMSPd is an important source of carbon and sulfur for bacteria in the marine environment, as the bacterial consumption of DMSPd can account for up to 15 % of their total carbon demand and almost all of their sulfur demand (Stefels et al., 2007). In the model, this removal process is parameterized as:

$$F_{consumption}^{dmspd} = k_{dmspd} DMSPd \tag{A.65}$$

where k_{dmspd} represents the rate constant (d^{-1}) for bacterial consumption of DMSPd. There are no reported values for k_{dmspd} in sea ice. In the standard run, k_{dmspd} is set to 1 d^{-1} based on the model calibration.

The fourth term in Eq. (A.62) (F_{free}) represents the removal rate of DMSPd by free DMSP-lyase present in the bottom ice. This process is parameterized as the product of a rate constant (k_{free} [d^{-1}]) and the concentration of bottom-ice DMSPd:

$$F_{free} = k_{free} DMSPd \tag{A.66}$$

In previous model studies, this process was considered as a minor removal pathway of DMSPd with k_{free} varying from 0.01 d^{-1} (Archer et al., 2004) to 0.04 d^{-1} (Steiner et al., 2006). In the standard run, k_{free} is set to 0.02 d^{-1}.

The fifth term in Eq. (A.62) ($F^{dmspd}_{release}$) represents the removal rate of DMSPd due to its release into the underlying water column. Various processes, including gravity drainage, flushing, brine expulsion, flooding, and basal melting, can account for vertical movement of tracers within the sea ice brine channel. Parameterizations of these processes are very complex (e.g. Vancoppenolle et al., 2007), although simpler approaches have also been taken to represent these processes in previous sea ice biogeochemical modelling studies (e.g., Tedesco and Vichi, 2014; Watanabe et al., 2015). By adopting a simpler approach similar to those previous studies, we parameterized the release resulting from two processes: 1) flushing due to drainage of snow meltwater accumulated in melt ponds and meltwater of surface and interior ice; and 2) sloughing due to basal melting. Specifically, the transfer velocity of flushing due to melt pond drainage is proportional to the area fraction (A_{mp}) and the drainage rate (r_{mp}) of melt ponds, while that of flushing of surface and interior ice meltwater and sloughing of basal ice is proportional to the rate of change (decrease) in sea ice thickness ($\min(0, \frac{dh_i}{dt})$). The removal rate due to the release is then calculated by multiplying the total (i.e. flushing and sloughing) transfer velocity by the concentration of bottom-ice DMSPd:

$$F^{dmspd}_{release} = \frac{1}{h_{bi}} \min\left(0, \frac{\rho_i}{\rho_{me}} \frac{dh_i}{dt} - A_{mp} r_{mp}\right) DMSPd \tag{A.67}$$

where h_{bi} represents the thickness of the bottom ice skeletal layer, which is set to 0.03 m. The ratio of sea ice to meltwater densities accounts for the volume difference between sea ice and meltwater, which are set respectively to 913 and 1000 kg m^{-3}. A_{mp} and $\frac{dh_i}{dt}$ are computed by the physical model (Flato and Brown, 1996; Abraham et al., 2015). A constant drainage rate of 0.0175 m d^{-1} is prescribed to r_{mp} following (Taylor and Feltham, 2004).

The meltwater equivalent concentration (nmol L^{-1}) of DMS in the bottom ice (DMS) is simulated prognostically:

$$\frac{\partial}{\partial t}(DMS) = F_{conversion} + F^{dms}_{free} - F^{dms}_{consumption} - F_{photolysis} - F^{dms}_{release} \tag{A.68}$$

The first term in Eq. (A.68) ($F_{conversion}$) represents the production rate of bottom-ice DMS by bacterial conversion of DMSPd to DMS. This process is one of the two major degradation pathways for DMSPd consumed by bacteria in open waters. The bacteria cleave DMSPd and yield DMS along with other products such as acrylate

and a proton (Stefels et al., 2007). The other major degradation pathway is known as demethylation/demethiolation (Kiene and Linn, 2000), which is accounted for in the model as part of the DMSPd removal rate by bacterial consumption. The rate of DMS production via bacterial DMSPd conversion is often scaled to the bacterial consumption rate of DMSPd, such that the former can be expressed as a fraction of the latter:

$$F_{conversion} = f_{yield} F^{dmspd}_{consumption} \tag{A.69}$$

where f_{yield} is known as the DMS yield fraction (-). Only one study has reported values for f_{yield} measured in the bottom ice, all less than 0.4 (Stefels et al., 2012). In the standard run, f_{yield} is set to 0.2.

The second term in Eq. (A.68) (F_{free}) represents the production rate of bottom-ice DMS via free DMSP-lyase which is equivalent to the fourth term in Eq. (A.62) and is defined in Eq. (A.66).

The third term in Eq. (A.68) ($F^{dms}_{consumption}$) represents the removal rate of bottom-ice DMS by bacterial consumption which is parameterized similarly to the bacterial consumption of bottom-ice DMSPd (Eq. (A.65)):

$$F^{dms}_{consumption} = k_{dms} DMS \tag{A.70}$$

where k_{dms} represents the rate constant (d^{-1}) for bacterial consumption of DMS. The only measurements of k_{dms} conducted for ice core samples showed a range from 0.1 to 0.5 d^{-1} for the bottom ice (J. Stefels, University of Groningen, personal communication). In the standard run, k_{dms} is set to 0.2 d^{-1}.

The fourth term in Eq. (A.68) ($F_{photolysis}$) represents the removal rate of bottom-ice DMS by photolysis, a photochemical process that converts DMS into its oxidation product, DMSO. The rate of photolysis is primarily determined by ambient light conditions, particularly in the ultraviolet (UV) wavelengths (Toole et al., 2004). However, we do not incorporate the UV dependence on the photlysis parameterization as the model does not have a representation for UV. Instead, we parameterize the light dependence of $F_{photolysis}$ using the photosynthetically active radiation similarly to Archer et al. (2004):

$$F_{photolysis} = k_{photolysis} \frac{PAR}{PAR + h_{photolysis}} DMS \tag{A.71}$$

where PAR represents the photosynthetically active radiation reaching the bottom ice (W m^{-2}), which is computed by the physical model. The parameters, $k_{photolysis}$ and $h_{photolysis}$ represent the rate constant (d^{-1}) and the half-saturation constant (W m^{-2}) for photolysis in the bottom ice. To the best of our knowledge, no studies have reported the values for photolysis rate constant in the bottom ice. In the standard run, $k_{photolysis}$ is set to 0.1 d^{-1} based on the measurements in the water column (discussed in Sec. A.2.1). We assume that photolysis is inhibited under low light conditions, and therefore set $h_{photolysis}$ to 1 W m^{-2}.

The last term in Eq. (A.68) ($F^{dms}_{release}$) represents the removal rate of bottom-ice DMS due to flushing and melting, which is parameterized in the same way as $F^{dmspd}_{release}$:

$$F^{dms}_{release} = \frac{1}{h_{bi}} \min\left(0, \frac{\rho_i}{\rho_{me}} \frac{dh_i}{dt} - A_{mp} r_{mp}\right) DMS \tag{A.72}$$

Ocean sulfur cycle

The concentration (nmol L^{-1}) of particulate DMSP in the water column ($DMSPp_{wc}$) is simulated diagnostically by assuming a fixed DMSPp-to-chlorophyll a intracellular ratio (nmol S:μg Chl a) for each phytoplankton group (q_{p1} and q_{p2}):

$$\frac{\partial}{\partial t}\left(DMSPp_{wc}\right) = q_{p1} \frac{\partial}{\partial t} P1 + q_{p2} \frac{\partial}{\partial t} P2 \tag{A.73}$$

where $P1$ and $P2$ represent the biomass of small and large phytoplankton (μg Chl a L^{-1}), respectively. Although the model does not specify the species group for $P1$, it is assumed that $P1$ produces more DMSP for a given amount of chlorophyll a than diatoms ($P2$). In the standard run, q_{p1} is set to 100 which is close to the intracellular ratios for non-diatom species groups reported in Stefels et al. (2007), and q_{p2} is set to 9.5 which is equivalent to the intracellular ratio for ice algae (q).

The concentration (nmol L^{-1}) of DMSPd in the water column ($DMSPd_{wc}$) is simulated prognostically:

$$\begin{aligned}\frac{\partial}{\partial t}\left(DMSPd_{wc}\right) = {} & F^{wc}_{lysis} + F^{wc}_{exudation} + F^{wc}_{sloppy} + F^{dmspd.wc}_{icesea} - F^{dmspd.wc}_{consumption} - F^{wc}_{free} \\ & + \frac{\partial}{\partial z}\left(K_z \frac{\partial}{\partial z}\left(DMSPd_{wc}\right)\right)\end{aligned} \tag{A.74}$$

where the last term represents the mixing rate of DMSPd between model layers, with K_z being the vertical eddy diffusivity (m^{2}s^{-1}) which is calculated by the ocean

physical model.

The first, second, fifth, and sixth terms in Eq. (A.74) (F^{wc}_{lysis}, $F^{wc}_{exudation}$, $F^{dmspd.wc}_{consumption}$, F^{wc}_{free}) are parameterized similarly to those in the sea-ice sulfur cycle (Eq. (A.62)):

$$F^{wc}_{lysis} = \frac{1}{L^{p1}_{nut} + 0.1} k^{p1}_{lysis} q_{p1} P1 + \frac{1}{L^{p2}_{nut} + 0.1} k^{p2}_{lysis} q_{p2} P2 \tag{A.75}$$

$$\begin{aligned} F^{wc}_{exudation} = &\left[f^{p1}_{active} + \left(1 - f^{p1}_{active}\right) \left(1 - L^{p1}_{nut}\right) \right] \mu_{p1} q_{p1} P1 \\ &+ \left[f^{p2}_{active} + \left(1 - f^{p2}_{active}\right) \left(1 - L^{p2}_{nut}\right) \right] \mu_{p2} q_{p2} P2 \end{aligned} \tag{A.76}$$

$$F^{dmspd.wc}_{consumption} = k^{wc}_{dmspd} DMSPd_{wc} \tag{A.77}$$

$$F^{wc}_{free} = k^{wc}_{free} DMSPd_{wc} \tag{A.78}$$

where the nutrient limitation indices (L^{p1}_{nut} and L^{p2}_{nut}) and the growth rates (μ_{p1} and μ_{p2}) of small and large phytoplankton, respectively, are calculated by the ocean ecosystem module. To our best knowledge, there are no reported values for the cell lysis rate constants (k^{p1}_{lysis} and k^{p2}_{lysis}) and the active exudation fractions (f^{p1}_{active} and f^{p2}_{active}) in ice-covered regions. In the standard run, k^{p1}_{lysis} and k^{p2}_{lysis} are set to 0.03 d^{-1}, and f^{p1}_{active} and f^{p2}_{active} are set to 0.05 for both small and large phytoplankton. k^{wc}_{dmspd} represents the bacterial DMSPd consumption rate constant in the water column. The reported values for k^{wc}_{dmspd} in Arctic surface water vary from 1.5 d^{-1} during autumn (Luce et al., 2011; Motard-Côté et al., 2012) to 4.1 d^{-1} during spring (Galindo et al., 2015). In the standard run, k^{wc}_{dmspd} is set to 5 d^{-1}) based on the model calibration. k^{wc}_{free} represents the rate constant for free DMSP-lyase in the water column, which is set to 0.02 d^{-1} in the standard run.

The third term in Eq. (A.74) represents the production rate of DMSPd in the water column by sloppy feeding:

$$F_{sloppy} = f^{z1}_{sloppy} q_{p1} R^{z1}_{p1} + f^{z2}_{sloppy} q_{p2} R^{z2}_{p2} \tag{A.79}$$

where f^{z1}_{sloppy} and f^{z2}_{sloppy} represent the fractions of sloppy feeding by small and large zooplankton. In the standard run, these fractions are set to 0.3 for both zooplankton groups, based on the findings that 20 to 70 % of grazed DMSPp is released into the ambient seawater as DMSPd (Stefels et al., 2007). R^{z1}_{p1} and R^{z2}_{p2} represent the loss rates (μg Chl a L^{-1} d^{-1}) of small and large phytoplankton due to grazing by small and large zooplankton, respectively, which are calculated by the ecosystem module.

The fourth term in Eq. (A.74) represents the rate of change in under-ice DMSPd

due to exchanges of DMSPd between the basal ice and underlying seawater and concentration (dilution) as a result of ice growth (melting), which can be written in the vertically discretized form as:

$$F_{icesea}^{dmspd.wc} = \frac{1}{h_{z_0}} \left(\frac{\rho_i}{\rho_{wc}} \frac{dH_i}{dt} - \frac{\rho_{me}}{\rho_{wc}} A_{mp} r_{mp} \right) \left(DMSPd_{wc} - \frac{\rho_{me}}{\rho_{wc}} DMSPd^* \right) \delta_{z,z_0} \tag{A.80}$$

where h_{z_0} is the thickness of the uppermost layer of the water column (set to 1 m) and ρ_{wc} is the density of seawater (calculated by the physical model). Again, the ratios of densities account for the volume differences in order to calculate the rate in seawater equivalent. $DMSPd^*$ represents the meltwater equivalent concentration of DMSPd taken up by the ice during ice growth, or released into the water column during melting. We make the assumption that, unlike salt, DMSPd taken up during ice growth is sufficiently small, such that $DMSPd^*$ can be set to zero. During the flushing and melting periods, $DMSPd^*$ is set to DMSPd in the bottom ice. The Kronecker's delta (δ_{z,z_0}) equals 1 at the uppermost layer of the water column (z_0), whereas it is 0 elsewhere.

The concentration (nmol L^{-1}) of DMS in the water column (DMS_{wc}) is simulated prognostically:

$$\begin{aligned} \frac{\partial}{\partial t} \left(DMS_{wc} \right) = {} & F_{conversion}^{wc} + F_{free}^{wc} + F_{icesea}^{dms.wc} - F_{consumption}^{dms.wc} - F_{photolysis}^{wc} \\ & - F_{seaair} + \frac{\partial}{\partial z} \left(K_z \frac{\partial}{\partial z} \left(DMS_{wc} \right) \right) \end{aligned} \tag{A.81}$$

where the last term represents the mixing of DMS between model layers, as described for the mixing rate of DMSPd.

The first, fourth, and fifth terms in Eq. (A.81) respectively represent the DMS production rate by bacterial conversion ($F_{conversion}^{wc}$), the DMS removal rates by bacterial consumption ($F_{consumption}^{dms.wc}$) and photolysis ($F_{photolysis}^{wc}$) in the water column, which are parameterized similarly to those in the bottom ice:

$$F_{conversion}^{wc} = f_{yield}^{wc} k_{dmspd}^{wc} DMSPd_{wc} \tag{A.82}$$

$$F_{consumption}^{dms.wc} = k_{dms}^{wc} DMS_{wc} \tag{A.83}$$

$$F_{photolysis}^{wc} = k_{photolysis}^{wc} \frac{PAR_{wc}}{PAR_{wc} + h_{photolysis}^{wc}} DMS_{wc} \tag{A.84}$$

where f^{wc}_{yield}, k^{wc}_{dms}, $k^{wc}_{photolysis}$, and $h^{wc}_{photolysis}$ respectively represent the DMS yield fraction (-), the bacterial DMS consumption rate constant (d^{-1}), and the rate constant (d^{-1}) and the half-saturation constant (W m^{-2}) for photolysis in the water column. The reported values for f^{wc}_{yield} are highly variable (0.05-1) in temperate water (Simó and Pedros-Alio, 1999) and moderately variable (0.04-0.3) in Arctic water (Luce et al., 2011; Motard-Côté et al., 2012). The only DMS yield fraction measurements available for the under-ice water column reported low values with relatively small range (0.02-0.1) as the measurements were conducted prior to the under-ice phytoplankton bloom (Galindo et al., 2015). In the standard run, f^{wc}_{yield} is set to 0.2. The reported values for k^{wc}_{dms} in Arctic surface water vary from 0.05 to 1.00 (mean of 0.17) d^{-1} for the Canadian High Arctic in October (Luce et al., 2011) and from 0.14 and 2.2 (mean of 0.9) d^{-1} for the Greenland Sea (Galí and Simó, 2010) in July. In the standard run, k^{wc}_{dms} is set to 0.2 d^{-1}. The reported range of $k^{wc}_{photolysis}$ measured in Arctic water during the summer varies from 0.01-0.11 d^{-1} for the Bering Sea (Deal et al., 2005) and the Canadian Arctic (Taalba et al., 2012) to 0.23-1.05 d^{-1} for the Greenland sea (Galí and Simó, 2010). In the standard run, $k^{wc}_{photolysis}$ is set to 0.1 d^{-1} and $h^{wc}_{photolysis}$ is set to 1 W m^{-2}.

The third term in Eq. (A.81) represents the rate of change in under-ice DMS due to exchanges of DMS between the ice and water column and concentration (dilution) during sea ice growth (melting), which is parameterized in the same way as $F^{dmspd.wc}_{icesea}$:

$$F^{dms.wc}_{icesea} = \frac{1}{h_{z_0}} \left(\frac{\rho_i}{\rho_{wc}} \frac{dH_i}{dt} - \frac{\rho_{me}}{\rho_{wc}} A_{mp} r_{mp} \right) \left(DMS_{wc} - \frac{\rho_{me}}{\rho_{wc}} DMS^* \right) \delta_{z,z_0} \qquad \text{(A.85)}$$

where DMS^* is neglected during ice growth, while it is set to DMS in the bottom ice during the flushing and melting periods.

Finally, the sixth term in Eq. (A.81) represents the removal rate (nmol L^{-1} d^{-1}) of DMS in the uppermost layer of the water column by the sea-to-air fluxes, which can be written in the vertically discretized form as:

$$F_{seaair} = f_{ow} \frac{k_{dms} DMS_{wc}}{h_{z_0}} \delta_{z,z_0} \qquad \text{(A.86)}$$

where f_{ow} represents the fraction (-) of open water to account for fluxes through a partially ice-covered surface. In the standard run, f_{ow} is set to 0 in the presence of sea ice, which is assumed to completely block the air-sea DMS fluxes. k_{dms} represents the gas transfer velocity (m s^{-1}) for DMS. Although previous flux measurements of DMS

based on the eddy covariance technique suggest that, under low to moderate winds, the gas transfer velocity can be reasonably predicted by assuming a linear wind-speed dependence (Huebert et al., 2010; Goddijn-Murphy et al., 2012; Bell et al., 2013, 2015), a recent study reconciling the eddy covariance technique with the dual tracer technique suggests that the linear wind-only-based parameterization will likely underestimate the gas transfer velocity under strong winds due to the enhancement of the bubble-mediated transfer (Goddijn-Murphy et al., 2015). In this study, the gas transfer velocity is parameterized based on Nightingale et al. (2000), which assumes a combination of linear and quadratic dependence on wind speed. Although this parameterization does not represent the bubble-mediated transfer, the gas transfer velocities predicted by this parameterization were, among other "wind speed only" parameterizations, closest to the prediction by the hybrid model of Goddijn-Murphy et al. (2015). The gas transfer velocity parameterization of Nightingale et al. (2000) was normalized to a Schmidt nubmer of 600 (k_{600}), and therefore, was corrected to a Schmidt number of DMS (Sc_{dms}) at a given temperature of ambient seawater (T_{z_0} in $^{\circ}C$) in the uppermost layer of the water column based on Saltzman et al. (1993):

$$k_{dms} = k_{600} \left(\frac{Sc}{600} \right)^{-1/2} \tag{A.87}$$

$$k_{600} = 0.333 U_{10} + 0.222 U_{10}^2 \tag{A.88}$$

$$Sc_{dms} = 2674 - 147.12 T_{z_0} + 3.726 T_{z_0}^2 - 0.038 T_{z_0}^3 \tag{A.89}$$

where U_{10} is the observed wind speed at 10 m (m s^{-1}).

A.2.2 Supplemantary material

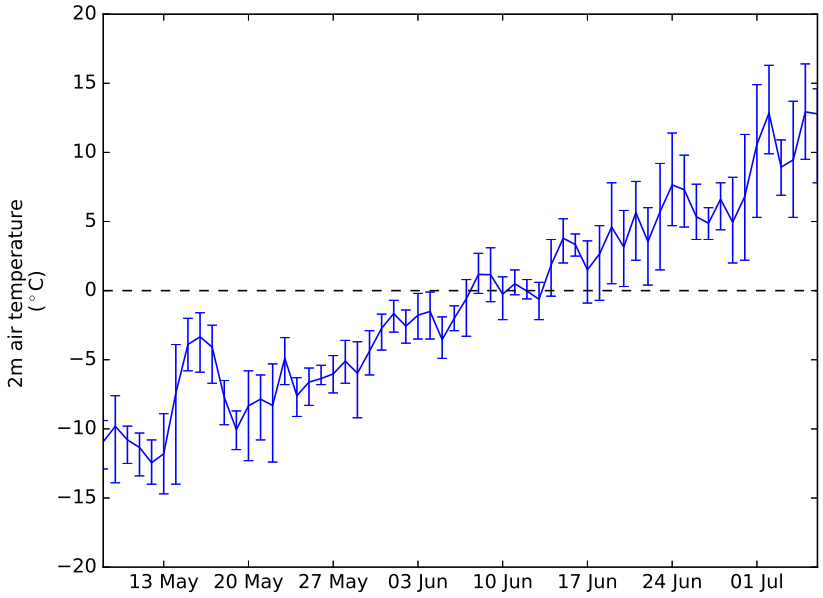

Figure A.2: Time series of daily mean surface 2-m air temperature observed at Resolute airport during 2010. The upper and lower vertical bars associated with the daily mean values represent the daily maximum and minimum values, respectively.

(a) Standard

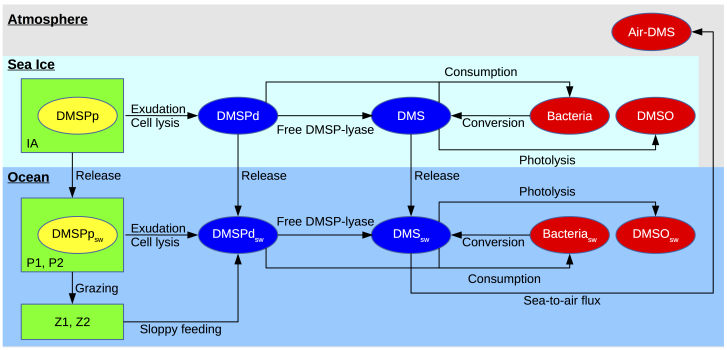

(b) NoIceSul

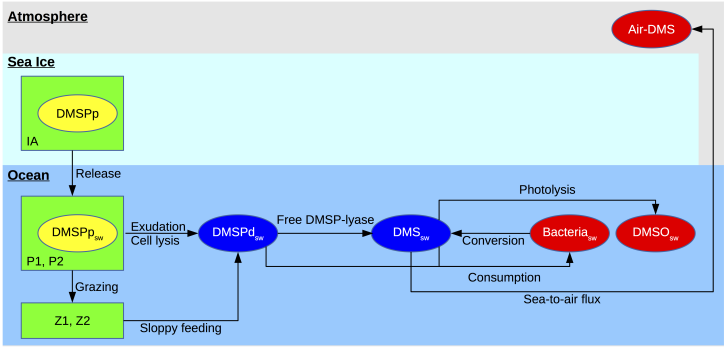

(c) NoIceBgc

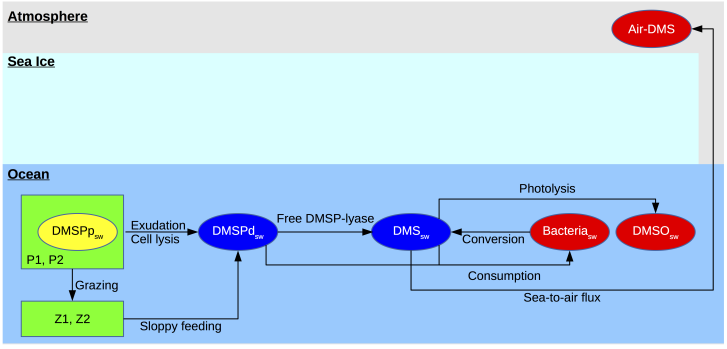

Figure A.3: Comparison of model schematic among (a) the standard run, (b) the NoIceSul run, and (c) the NoIceBgc run.

A.3 Additional information for Chapter 4

A.3.1 Implementation of ocean sulfur cycle and sea-ice biogeochemistry into the NEMO source code

Figure A.4 shows the structure of the NEMO v3.4 source code directory (NEMO), which includes the following subdirectories (submodels): OPA_SRC (OPA), LIM_SRC_2 (LIM2), and TOP_SRC (ocean biogeochemistry). The directory TOP_SRC contains two subdirectories: PISCES and MY_TRC. In this study, the directory PISCES contains the source code of CanOE, as CanOE has been developed using the code structure of the PISCES ocean biogeochemical model. The other directory, MY_TRC, consists of a list of generic modules that can be modified by end users to add their own biogeochemical models; we introduced an ocean sulfur cycle and sea-ice biogeochemistry into this interface. Furthermore, we modified a few modules in the directories LIM_SRC_2 and PISCES for the implementation of sea-ice biogeochemistry into the NEMO modelling system (Table A.4).

Numerically, the tendencies for the sea-ice biogeochemical state variables are computed at each time step as follows: first, the concentrations of all state variables from the previous time step are transferred from the module trcsms_my_trc.F90 to the module limtrp_2.F90 to compute the advective and diffusive tendencies. The updated concentrations are transferred back to the module trcsms_my_trc.F90 within which the biological and chemical sources and sinks as well as the ice-ocean fluxes of these state variables are computed.

In NEMO, user-specific modules built within MY_TRC are designed to be activated by defining the C preprocessor (CPP) key key_my_trc. As such, we assigned CPP keys for each component of the newly-developed modules, which can be activated as needed (Table A.5).

A.3.2 CanOE documentation

The following section is a draft of the CanOE documentation:

Christian, J.R., Denman, K.L., Lee, W.G., Riche, O.G.J., Steiner, N.S., and Swart, N. (in prep.): The Canadian Ocean Ecosystem Model (CanOE): a new ocean biogeochemistry model based on the NEMO modelling system.

The documentation is repeated here with permission of the lead author.

The Canadian Ocean Ecosystem Model (CanOE): a new ocean biogeochemistry model based on the NEMO modelling system

James R. Christian[1], Kenneth L. Denman[2], Warren G. Lee[3], Olivier G.J. Riche[2], Nadja Steiner[1], Neil Swart[3]

1 Fisheries and Oceans Canada, Canadian Centre for Climate Modelling and Analysis, Victoria, BC, Canada

2 School of Earth and Ocean Sciences, University of Victoria, Victoria, BC, Canada

3 Environment and Climate Change Canada, Canadian Centre for Climate Modelling and Analysis, Victoria, BC, Canada

Introduction

The Canadian Ocean Ecosystem Model (CanOE) is a new ocean biogeochemistry module developed for the Canadian Earth System Model (CanESM, cf. Arora et al., 2011). It differs from the earlier Canadian Model of Ocean Carbon (CMOC; Zahariev et al., 2008) in having multiple functional groups of phytoplankton and zooplankton, flexible elemental ratios, prognostic iron and oxygen cycles, and prognostic calcification and denitrification. The overall computational cost is greater by about a factor of three (19 tracers vs. 6). CanOE has been implemented within the NEMO ocean modelling system, and CMOC has also been adapted to run within NEMO, so that we have several different biogeochemistry models to compare under identical circulation.

Among the more unsatisfactory aspects of CMOC in CanESM1 and CanESM2 was the excessive accumulation of nitrate beneath the Eastern Boundary Currents. This is a common failing of coarse-resolution ocean models (Moore and Doney, 2007). In CMOC it is exacerbated by the denitrification parameterization, which spreads nitrate loss over the ocean basins so that total N is conserved within each vertical column (total N_2 fixation and total denitrification are equal at each grid point where N_2 fixation occurs). CanOE has prognostic denitrification, but like CMOC it uses a parameterization of inputs of 'new' fixed N as function of temperature, irradiance and nutrients rather than an explicit N_2-fixer functional group.

Another aspect of CMOC that is particularly unsatisfying is the parameterization of iron limitation as a static 'iron mask' based on the distribution of surface nitrate in the current climate. In order to implement a prognostic iron cycle with a minimum of additional tracers, CanOE has fixed C/N/Fe ratios in zooplankton and detritus and variable ratios only in phytoplankton. Detrital particulate iron, iron speciation, and the concentrations of the ligands that keep iron in solution are not explicitly represented. There are only three iron-based tracers: dissolved iron and small and large phytoplankton iron.

CanESM1 and CanESM2 also did not simulate dissolved oxygen. While it is straightforward to include oxygen (the biological sources and sinks are essentially those of DIC multiplied by -1 and solubility is well constrained), it was excluded due to limitations of processing capacity. The new NEMO version of CMOC reproduces exactly the original CanESM1/2 version in most respects, but also includes oxygen, which can be characterized as a 'downstream' tracer with no feedbacks to biology (e.g., effects on denitrification are neglected). Including oxygen further permits us to incorporate prognostic representations of processes like denitrification in CanOE, that were neglected in CMOC.

Model description

The NEMO modelling system is a publicly available archive of codes based on the OPA (Océan PArallelisé) ocean model (Madec and Imbard, 1996; Guilyardi and Madec, 1997). It comes with

two options for biogeochemistry: PISCES (Pelagic Interactions Scheme for Carbon and Ecosystem Studies) and LOBSTER (LODyC Ocean Biogeochemical System for Ecosystem and Resources). CanOE and the NEMO implementation of CMOC are built around the basic code structure of PISCES, using NEMO v3.4.1.

The biology, carbon chemistry, gas exchange and light attenuation have all been modified to various degrees; in a few cases PISCES parameterizations or a slightly modified version of these were adopted. CanOE uses PISCES three-band attenuation while NEMO-CMOC uses broadband (PAR) attenuation for consistency with the published version of CMOC. Carbon chemistry was modified to be consistent with the Best Practices Guide (Dickson et al., 2007). All calculations are done on the total scale and the recommended formulae for the equilibrium constants employed. The PISCES conventions for convergence of carbon chemistry calculations were retained, i.e., a greater number of iterations in the surface layer offers greater accuracy in calculating pCO_2 and gas exchange, while in subsurface layers the number of iterations is fixed at five (in subsurface layers the only function of the carbon chemistry is to calculate burial of calcite in the sediments). NEMO-CMOC uses the same carbon chemistry as CanOE but does not solve the carbon chemistry equations in the subsurface layers.

The biology model is a substantially new model based on the cellular regulation model of Geider et al. (1998). Each phytoplankton functional group has four state variables: carbon, nitrogen, iron and chlorophyll. Photosynthesis is decoupled from cell production and photosynthetic rate is a function of the cell's internal N and Fe quotas. Each functional group has a specified minimum

and maximum N quota and Fe quota, and nutrient uptake ceases when the maximal cell quota is reached. Chlorophyll synthesis is a function of nitrogen uptake and increases at low irradiance. Model parameters and their values are listed in Table 1.

2.1 Photosynthesis and phytoplankton growth

For simplicity and clarity, the equations are shown here for single phytopankton species, and do not differ structurally for small and large phytoplankton. Some parameter values differ for the two phytoplankton groups; all parameter values are listed in Table 1.

Temperature dependence of photosynthetic activity is expressed by the Arrhenius equation

$$T_f = \exp\left(-\frac{E_a}{R}\left(\frac{1}{T}-\frac{1}{T_{ref}}\right)\right) \quad (1)$$

where E_a is an enzyme activation energy that corresponds approximately to that of RuBisCo (cf. Raven and Geider 1988), R is the gas constant (8.314 J mol^{-1} K^{-1}), and temperature T and reference temperature T_{ref} are in Kelvin. Maximal rates of nutrient uptake are given by

$$V_{\max}{}^{X} = V_{ref}{}^{X} T_f \left(\frac{Q_{\max}{}^{X} - Q^{X}}{Q_{\max}{}^{X} - Q_{\min}{}^{X}}\right)^{0.05} \quad (2)$$

where $V_{max}{}^{X}$ is the maximal uptake rate in mg of nutrient X per mg of cell C, X can represent N or Fe, Q is the nutrient cell quota and Q_{min} and Q_{max} its minimum and maximum values, and $V_{ref}{}^{X}$ is a (specified) basal rate at T=T_{ref} and Q=Q_{min}. These maximum rates are then reduced according to the ambient nutrient concentration, i.e.

$$V^{N} = V_{\max}{}^{N}\left(L_{NH4} + (1 - L_{NH4})L_{NO3}\right) \tag{3a}$$

where $L_{NH4} = \dfrac{N_a}{K_{NH4} + N_a}$ and $L_{NO3} = \dfrac{N_i}{K_{NO3} + N_i}$, with N_i and N_a indicating nitrate and ammonium respectively, and

$$V^{Fe} = V_{\max}{}^{Fe}\left(\frac{Fe}{K_{Fe} + Fe}\right) \tag{3b}$$

The maximal carbon based growth rate is given by

$$P_{\max}{}^{C} = P_{ref}{}^{C} T_f \min\left\{\frac{Q^{N} - Q_{\min}{}^{N}}{Q_{\max}{}^{N} - Q_{\min}{}^{N}}, \frac{Q^{Fe} - Q_{\min}{}^{Fe}}{Q_{\max}{}^{Fe} - Q_{\min}{}^{Fe}}\right\} \tag{4}$$

where P^{C}_{ref} is the rate at the reference temperature T_{ref} under nutrient-replete conditions (Q=Q_{max}). The light-limited growth rate is then given by

$$P^{C}{}_{phot} = P^{C}{}_{\max}\left(1 - e^{-\alpha_{chl} E\theta / P^{C}{}_{\max}}\right) \tag{5}$$

where θ is the chlorophyll-to-carbon ratio. The rate of chlorophyll synthesis is

$$\rho_{chl} = \theta^{N}{}_{\max} \frac{P^{C}{}_{phot}}{E\alpha_{chl}\theta} \tag{6}$$

These rates are then used to define a set of state equations for phytoplankton carbon (C_p), nitrogen (N_p), iron (Fe_p), and chlorophyll (M).

$$\frac{dC_p}{dt} = \left(P^{C}{}_{phot} - \zeta V_N\right)C_p - \left(G + C_{XS}\right) - m_1 C_p - m_2 C_p{}^2 - k_{XU} C_{INTR} \quad (7)$$

where ζ is the respiratory cost of biosynthesis, G is the grazing rate (see Eq. 12), C_{XS} is the excess (above the ratio in grazer biomass) carbon in grazing losses, C_{INTR} is the concentration of intracellular carbohydrate carbon in excess of biosynthetic requirements, and k_{XU} is a rate coefficient for its exudation to the environment.

$$\frac{dN_p}{dt} = \frac{V^N}{Q_N} - \left(G + m_1 C_P + m_2 C_P{}^2\right)R_{NC} - N_{XS} \quad (8)$$

$$\frac{dFe_p}{dt} = \frac{V^{Fe}}{Q_{Fe}} - \left(G + m_1 C_P + m_2 C_P{}^2\right)R_{FeC} - Fe_{XS} \quad (9)$$

$$\frac{dM}{dt} = \frac{\rho_{chl} V^N}{\theta_C} M - \left(G + m_1 C_p + m_2 C_p{}^2\right)\theta_C - k_{dgr} M \quad (10)$$

where k_{dgr} is a rate coefficient for nonspecific losses of chlorophyll e.g., by photooxidation, in addition to losses to grazing and other processes that also affect C_p, N_p, and Fe_p. N_{XS} and Fe_{XS} are remineralization of "excess" (relative to grazer or detritus ratios) N or Fe and are defined below (Eq. 16).

2.2 Grazing and food web interactions

Grazing rate depends on the phytoplankton carbon concentration, which most closely represents the food concentration available to the grazer (Elser and Urabe 1999; Loladze et al. 2000). Zooplankton biomass is also in carbon units. State equations for small and large zooplankton are

$$\frac{dZ_s}{dt} = \lambda G_s - \left(R + G_Z + m_1 Z_s + m_2 Z_s^{\,2}\right) \tag{11a}$$

$$\frac{dZ_l}{dt} = \lambda G_l - \left(R + m_1 Z_l + m_2 Z_l^{\,2}\right) \tag{11b}$$

where

$$G_s = G_{so}\left(1 - e^{-a_s C_{ps}}\right) Z_s \tag{12a}$$

$$G_l = G_{lo}\left(1 - e^{-a_l \left(C_{pl} + Z_s\right)}\right) Z_l \tag{12b}$$

for small and large zooplankton respectively, G_Z is grazng of small zooplankton by large zooplankton, R is respiration, and m_1 and m_2 are nongrazing mortality rates. Large zooplankton grazing is divided into grazing on large phytoplankton and small zooplankton in proportion to the relative abundances of each

$$G_P = G_l \frac{P_l}{P_l + Z_s} \tag{13a}$$

$$G_Z = G_l \frac{Z_s}{P_l + Z_s} \tag{13b}$$

Zooplankton biomass loss to respiration is given by

$$R = \max\left\{r_z T_f Z - C_{XS}, 0\right\} \tag{14}$$

Respiration (R) is assumed to consume only carbon and not result in catabolism of existing biomass when "excess" carbon is available in the prey. In addition, conservation of mass must be maintained by recycling to the dissolved pool grazer consumption in excess of biosynthetic requirements when prey elemental ratios differ from the predator's. This is very straightforward in the case where the nutrient quota (relative to carbon) exceeds the grazer fixed ratio: the excess nutrient is remineralized to the dissolved inorganic pool. However, in the case where the nutrient quota is less than the grazer ratio, the grazer intake is reduced to what can be supported by the least abundant nutrient (relative to the grazer biomass ratio) and excess carbon is remineralized. For the case of two nutrients (in this case N and Fe) it is necessary to define

$$G' = G\min\left(\frac{N_P}{C_P}R_{CN}, \frac{Fe_P}{C_P}R_{CFe}, 1\right) \tag{15}$$

where G is equal to G_S (equation 12a) for small zooplankton and G_P (equation 13a) for large zooplankton, and R_{XY} indicates the fixed ratio of element X to element Y in grazer biomass. The 'excess' carbon available for respiration is

$$C_{XS} = G'\max\left(\frac{C_P}{N_P}R_{NC} - 1, \frac{C_P}{Fe_P}R_{FeC} - 1, 0\right) \tag{16a}$$

and the excess nutrients remineralized to their inorganic pools are

$$N_{XS} = G'\max\left(\frac{N_P}{C_P} - R_{NC}, 0\right) + G'\max\left(R_{NC}\left(\frac{N_P}{Fe_P}R_{FeN} - 1\right), 0\right) \tag{16b}$$

$$Fe_{XS} = G'\max\left(\frac{Fe_P}{C_P} - R_{FeC}, 0\right) + G'\max\left(R_{FeC}\left(\frac{Fe_P}{N_P}R_{NFe} - 1\right), 0\right) \tag{16c}$$

For three elements there are six (3!) possible cases: for nitrogen greater or less than $C_P R_{NC}$, iron may be either in excess relative to both C and N, deficient relative to both, or in excess relative to one but not the other. The second terms in equations 16b and 16c allow e.g. remineralization of Fe when it is it in excess relative to N but deficient relative to C, with the total intake determined by the element least abundant relative to the grazer biomass ratios. In all of these cases the second term in at least one of equations 16b and 16c is nonzero; one or both of the first terms are nonzero except when both N and Fe are deficient relative to carbon (Table 2).

2.3 Organic and inorganic pools

There are two pools of detritus with different sinking rates but the same fixed elemental ratios. Detrital C/N/Fe ratios are the same as zooplankton, so zooplankton mortality or grazing of small zooplankton by large zooplankton produce no 'excess'. Phytoplankton mortality and defecation by zooplankton grazing on phytoplankton produces excess nutrient or excess carbon that needs to be recycled into the inorganic pool in a similar fashion as outlined above for the assimilated fraction of grazing on phytoplankton.

The conservation equations for detrital C are

$$\frac{dD_s}{dt} = m_1\left(C_{ps} + Z_s\right) + m_2\left(C_{ps}^{\,2} + Z_s^{\,2}\right) - r_1 D_s T_g - w_s \frac{dD_s}{dz} \tag{17a}$$

$$\frac{dD_l}{dt} = m_1\left(C_{pl} + Z_l\right) + m_2\left(C_{pl}^{\,2} + Z_l^{\,2}\right) - r_2 D_l T_g - w_l \frac{dD_l}{dz} \tag{17b}$$

where T_g is an Arrhenius function for temperature dependence of remineralization and w is the sinking speed. The conservation equations for inorganic C, N, and Fe are

$$\frac{dC_i}{dt} = \left(\zeta V^N - P^C_{phot}\right)C_p + R + C_{XS} + \left(r_1 D_s + r_2 D_l\right)T_g \tag{18a}$$

$$\frac{dN_i}{dt} = -\frac{V^N}{Q^N} N_p \left(\frac{L_{NO3}}{L_{NO3} + L_{NH4}}\right) + N_{ox} - N_{dentr} \tag{18b}$$

$$\frac{dN_a}{dt} = -\frac{V^N}{Q^N} N_p \left(\frac{L_{NH4}}{L_{NO3} + L_{NH4}}\right) + \frac{R}{R_{CN}} + N_{XS} + \left(r_1 D_s + r_2 D_l\right)R_{NC}T_g - N_{ox} + N_{dnf} \tag{18c}$$

$$\frac{dFe}{dt} = \frac{V^{Fe}}{Q^{Fe}} Fe_p + \frac{R}{R_{CFe}} + Fe_{XS} + \left(r_1 D_s + r_2 D_l\right)R_{FeC}T_g \tag{18d}$$

where N_{ox} is microbial oxidation of ammonium to nitrate (nitrification) and N_{dnf} and N_{dentr} are sources and sinks associated with dinitrogen fixation and denitrification. The oxygen equation is essentially the inverse of equation 18a, with additional terms for oxidation and reduction of N, i.e.,

$$\frac{dO_2}{dt} = -\frac{dC_i}{dt} + 2\frac{V^N}{Q^N} N_p \left(\frac{L_{NO3}}{L_{NO3} + L_{NH4}}\right) - 2N_{ox} \tag{19}$$

Nitrification is given by

$$N_{ox} = k_{NH4ox} N_a \frac{1}{1 + E(z)} \tag{20}$$

where $E(z)$ is the layer mean irradiance at depth z. Dinitrogen fixation is parameterized as an external input of ammonium dependent on light, temperature and Fe availability, and inhibited by high ambient concentrations of inorganic N.

$$N_{dnf} = k_{dnf} T_{dnf} \left(1 - e^{-aE}\right) \left(\frac{Fe}{K_{Fe} + Fe}\right) \left(\frac{K_{NO3}}{K_{NO3} + N_i + N_a}\right) \quad (21)$$

Denitrification is parameterized as a fraction of total remineralization that increases as a linear function of oxygen concentration for concentrations less than a threshold concentration O_{mxd}

$$N_{frxn} = 1 - \frac{\min\left(O_2, O_{mxd}\right)}{O_{mxd}} \quad (22)$$

Remineralization is then divided among oxygen (1-N_{frxn}), nitrate (0.85N_{frxn}), and ammonium (0.15N_{frxn}) assuming an average annamox contribution of 30% (Babbin et al., 2014).

2.4 Calcification, calcite dissolution, and alkalinity

Calcification is represented in a fashion similar to PISCES, with a detrital $CaCO_3$ state variable but no explicit calcifier groups. Detrital $CaCO_3$ sinks in the same fashion as POC, with its own sinking rate that is independent of those for both large and small organic detritus. Calcite production is represented as a fixed fraction of POC production from small phytoplankton and small zooplankton mortality. Calcite dissolution occurs throughout the water column as a first order process (i.e., no dependence on temperature or saturation state). Approximately 80% of calcite produced is exported from the euphotic zone. Burial in the sediments is represented as a simple 'on/off' switch dependent on the calcite saturation state (zero when $\Omega_C<1$ and 1 when $\Omega_C \geq 1$).

For each mole of calcite production two moles of alkalinity equivalent are lost from the dissolved phase; the reverse occurs during calcite dissolution. There are additional sources and sinks for alkalinity associated with phytoplankton nutrient uptake, organic matter remineralization, nitrification, denitrification and dinitrogen fixation (Table 3; see also Wolf-Gladrow et al., 2007). The annamox reaction does not in itself contribute to alkalinity (Jetten at al., 2001); there is a sink associated with ammonium oxidation to nitrite that offsets the gain from dinitrogen fixation (the model does not distinguish between nitrite and nitrate). The sources and sinks offset each other such that there is no net gain or loss as long as the global fixed N pool is conserved. If dinitrogen fixation and denitrification are allowed to vary freely there will generally be a net gain or loss of fixed N and therefore of alkalinity.

References

Arora, V., J. Scinocca, G. Boer, J. Christian, K. Denman, G. Flato, V. Kharin, W. Lee, and W. Merryfield (2011), Carbon emission limits required to satisfy future representative concentration pathways of greenhouse gases, *Geophysical Research Letters*, *38*, doi:10.1029/2010GL046270

Babbin, A., R. Keil, A. Devol, and B. Ward (2014), Organic Matter Stoichiometry, Flux, and Oxygen Control Nitrogen Loss in the Ocean, *Science*, *344*, 406-408.

Christian, J. (2005), Biogeochemical cycling in the oligotrophic ocean: Redfield and non-Redfield models, *Limnology and Oceanography*, *50*, 646-657.

Christian, J., et al. (2010), The global carbon cycle in the Canadian Earth system model (CanESM1): Preindustrial control simulation, *Journal of Geophysical Research-Biogeosciences*, *115*, doi:10.1029/2008JG000920

Elser, J., and J. Urabe (1999), The stoichiometry of consumer-driven nutrient recycling: Theory, observations, and consequences, *Ecology*, *80*(3), 735-751.

Geider, R., H. MacIntyre, and T. Kana (1998), A dynamic regulatory model of phytoplanktonic acclimation to light, nutrients, and temperature, *Limnology and Oceanography*, *43*, 679-694.

Guilyardi, E., and G. Madec (1997), Performance of the OPA/ARPEGE-T21 global ocean-atmosphere coupled model, *Climate Dynamics*, *13*, 149-165.

Jetten, M., M. Wagner, J. Fuerst, M. van Loosdrecht, G. Kuenen, and M. Strous (2001), Microbiology and application of the anaerobic ammonium oxidation ('anammox') process, *Current Opinion in Biotechnology*, *12*, 283-288.

Loladze, I., Y. Kuang, and J. Elser (2000), Stoichiometry in producer-grazer systems: Linking energy flow with element cycling, *Bulletin of Mathematical Biology*, *62*, 1137-1162.

Madec, G., and M. Imbard (1996), A global ocean mesh to overcome the North Pole singularity, *Climate Dynamics*, *12*, 381-388.

Moore, J., and S. Doney (2007), Iron availability limits the ocean nitrogen inventory stabilizing feedbacks between marine denitrification and nitrogen fixation, *Global Biogeochemical Cycles*, *21*, doi:10.1029/2006GB002762.

Raven, J., and R. Geider (1988), Temperature and algal growth, *New Phytologist*, *110*, 441-461.

Wolf-Gladrow, D., R. Zeebe, C. Klaas, A. Kortzinger, and A. Dickson (2007), Total alkalinity: The explicit conservative expression and its application to biogeochemical processes, *Marine Chemistry*, *106*, 287-300.

Zahariev, K., J. Christian, and K. Denman (2008), Preindustrial, historical, and fertilization simulations using a global ocean carbon model with new parameterizations of iron limitation, calcification, and N_2 fixation, *Progress in Oceanography*, *77*, 56-82.

Table 1 – Ecosystem model parameters.

Symbol	Description	Unit	
T_{ref}	Reference temperature	K	298.15
E_a	Activation energy for phytoplankton Arrhenius function	kJ mol^{-1}	37.4
Q^N_{mins}	Small phytoplankton minimum N quota	g N g C^{-1}	0.04
Q^N_{maxs}	Small phytoplankton maximum N quota	g N g C^{-1}	0.172
Q^N_{minl}	Large phytoplankton minimum N quota	g N g C^{-1}	0.04
Q^N_{maxl}	Large phytoplankton maximum N quota	g N g C^{-1}	0.172
Q^{Fe}_{mins}	Small phytoplankton minimum Fe quota	µg Fe g C^{-1}	4.65
Q^{Fe}_{maxs}	Small phytoplankton maximum Fe quota	µg Fe g C^{-1}	93.08
Q^{Fe}_{minl}	Large phytoplankton minimum Fe quota	µg Fe g C^{-1}	4.65
Q^{Fe}_{maxl}	Large phytoplankton maximum Fe quota	µg Fe g C^{-1}	69.81
V^N_{ref}	Reference rate of N uptake	g N g C^{-1} d^{-1}	0.6
V^{Fe}_{ref}	Reference rate of Fe uptake	µg Fe g C^{-1} d^{-1}	79.28
P^C_{ref}	Reference rate of photosynthesis	g C g C^{-1} d^{-1}	3
k_{XU}	Rate coefficient for exhudation	d^{-1}	0.8
k_{dgr}	Rate coefficient for chlorophyll degradation	d^{-1}	0.02
ζ	Respiratory cost of biosynthesis	g C g N^{-1}	2
α_{chl}	Initial slope of P-E curve	(g C g CHL^{-1} h^{-1})	0.045
K_{NiS}	Half-saturation for small phytoplankton nitrate uptake	$mmol^{-1}$ m^3	0.1
K_{NaS}	Half-saturation for small phytoplankton ammonium uptake	$mmol^{-1}$ m^3	0.05
K_{FeS}	Half-saturation for small phytoplankton iron uptake	$nmol^{-1}$ m^3	100
K_{NiL}	Half-saturation for large phytoplankton nitrate uptake	$mmol^{-1}$ m^3	0.5
K_{NaL}	Half-saturation for large phytoplankton ammonium uptake	$mmol^{-1}$ m^3	0.05

K_{FeL}	Half-saturation for large phytoplankton iron uptake	$nmol^{-1}\ m^3$	200
m_{1S}	Small phytoplankton mortality rate (linear)	d^{-1}	0.05
m_{2L}	Small phytoplankton mortality coefficient (quadratic)	$mmol^{-1}\ C\ m^3\ d^{-1}$	
m_{1L}	Large phytoplankton mortality rate (linear)	d^{-1}	0.05
m_{2L}	Large phytoplankton mortality coefficient (quadratic)	$mmol^{-1}\ C\ m^3\ d^{-1}$	
a_L	Large zooplankton grazing parameter	$(mmol\ C\ m^{-3})^{-1}$	
G_{L0}	Large zooplankton maximum grazing rate	d^{-1}	
a_S	Small zooplankton grazing parameter	$(mmol\ C\ m^{-3})^{-1}$	
G_{S0}	Small zooplankton maximum grazing rate	d^{-1}	
λ	Assimilation efficiency	n.d.	0.8
r_z	Zooplankton specific respiration rate at T_{ref}	d^{-1}	0.05
r_{DS}	Small detritus remineralization rate at T_{ref}	d^{-1}	0.25
r_{D1}	Large detritus remineralization rate at T_{ref}	d^{-1}	0.25

Table 2 - Cases where the 'excess' terms are nonzero. These terms are always greater than or equal to zero, and always zero when the phytoplankton elemental ratio is equal to the grazer biomass ratio. A + indicates cases where a specific term is positive. N_1 and N_2 and Fe_1 and Fe_2 indicate the first and second terms in equations 15b and 15c. R_{NC} is the grazer N/C (Redfield) ratio.

	Fe in excess relative to both C and N					Fe in excess relative to C or N but not both					Fe deficient relative to both C and N				
	C	N_1	N_2	Fe_1	Fe_2	C	N_1	N_2	Fe_1	Fe_2	C	N_1	N_2	Fe_1	Fe_2
$N/C>R_{NC}$		+		+	+		+	+	+		+	+	+		
$N/C<R_{NC}$	+			+	+	+				+	+		+		

Table 3 - Alkalinity sources and sinks associated with nitrogen cycle processes in moles of alkalinity equivalent per mole of N. Positive value indicates alkalinity source.

Process	Alkalinity source/sink
Phytoplankton NH_4 uptake	-1
Phytoplankton NO_3 uptake	+1
Organic N remineralization	+1
N_2 fixation	+1
Nitrification (NH_4 oxidation to NO_3)	-2
Denitrification	+1
Annamox	0

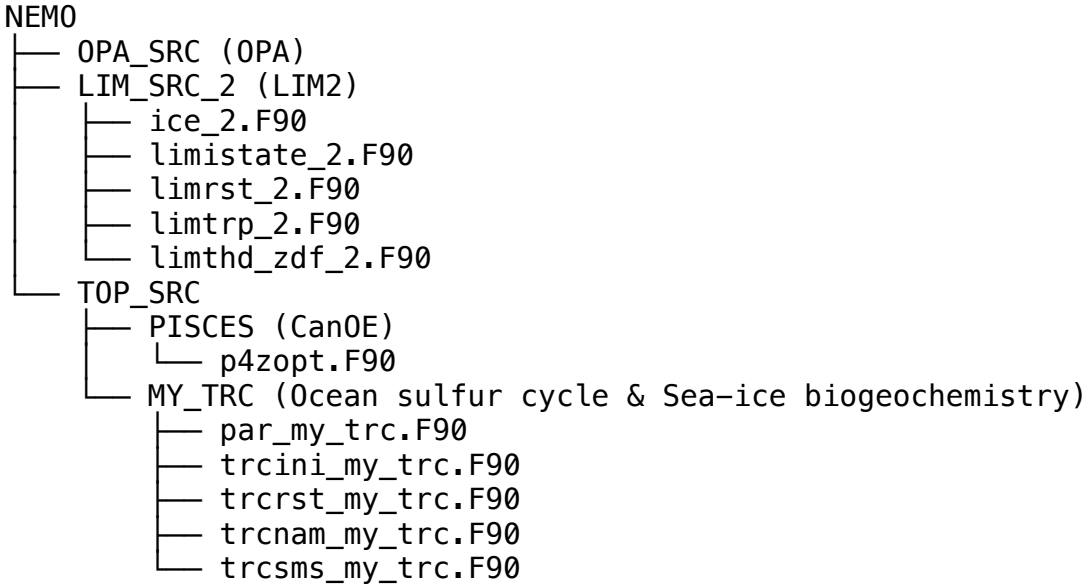

Figure A.4: File tree diagram of the OPA-LIM2-CanOE configuration of NEMO v3.4. The modules listed in the diagram (*.F90) have been modified in order to implement ocean sulfur cycle and sea-ice biogeochemistry into the present configuration.

Table A.4: A list of NEMO modules modified to add ocean sulfur cycle and sea-ice biogeochemistry.

Module	Description of the modification
ice_2.F90	Assign arrays for advective and diffusive tendencies of the sea-ice biogeochemical state variables.
limistate_2.F90	Initialize the arrays for the advective and diffusive tendencies.
limrst_2.F90	Restart the arrays for the advective and diffusive tendencies.
limtrp_2.F90	Compute the advective and diffusive tendencies as described in Section 4.3.3.
limthd_zdf_2.F90	Compute the light penetration parameterization through snow and sea ice as described in Section 4.3.1.
p4zopt.F90	Compute ice-algal shading and under-ice PAR as described in Section 4.3.2.
par_my_trc.F90	Define the number of state and diagnostic variables.
trcini_my_trc.F90	Initialize the state variables.
trcrst_my_trc.F90	Restart the state variables.
trcnam_my_trc.F90	Assign the arrays of the state and diagnostic variables.
trcsms_my_trc.F90	Compute the biological and chemical sources and sinks and ice-ocean fluxes.

Table A.5: A list of CPP keys created in the present study.

CPP key	Description
key_my_trc_ocedms	Activate ocean sulfur cycle.
key_my_trc_iceeco	Activate sea-ice ecosystem.
key_my_trc_icedms	Activate sea-ice sulfur cycle.

A.4 Additional information for Chapter 5

A.4.1 Surface and lateral boundary conditions

The model simulation was conducted by prescribing annually-varying surface and lateral boundary conditions. The surface boundary conditions are based on the Drakkar Forcing Set 5.2 (DFS; Dussin et al., 2016). Figure A.5 shows the interannual variability in the DFS dataset for the Arctic domain. Seawater temperature, salinity, and horizontal currents at the Pacific and Atlantic lateral open boundaries of the model domain were prescribed using the interannual monthly-mean fields based on the Ocean Reanalysis System 4 (ORAS4; Balmaseda et al., 2013). Figure A.6 shows the interannual variability in the ORAS4 dataset at the Pacific and Atlantic boundaries. River discharge of freshwater was prescribed based on the monthly-mean product of Dai and Trenberth (2002), which covers the period up to 2007. Due to the absence of the data product beyond 2007, the monthly-mean fields for 2007 were prescribed repeatedly beyond this year in the model simulation (Figure A.7b).

A.4.2 River runoff of biogeochemical state variables

The river runoff of nitrate, dissolved inorganic carbon (DIC), dissolved organic carbon (DOC) and nitrogen (DON), nitrate, and total alkalinity (TA) was prescribed by computing the product of the river discharge of freshwater (described above) and the river concentrations of these biogeochemical state variables. The river concentrations were prescribed based on various studies of the 6 major Arctic rivers (Mackenzie, Yukon, Kolyma, Lena, Yenisey, and Ob'; Table A.6). More specifically, the annual-mean river concentrations were prescribed at locations of river mouths of these rivers (Figure A.7d). The river concentrations of DON were prescribed by assuming DON-to-DIN (dissolved inorganic nitrogen) ratios (Holmes et al., 2012) where DIN is regarded as nitrate. For other locations, the river concentrations were set to zero, which results in the dilution of the seawater concentrations near these locations. More research is needed to prescribe the river concentrations for these little studied regions. The river concentrations of all other biogeochemical state variables were set to zero at all locations of river mouths including those of the 6 major Arctic rivers, which results in the dilution of the respective oceanic pools.

In the ocean, the river runoff was handled differently between the inorganic and organic matter. The runoff of the inorganic matter (DIC, nitrate, and TA) was set

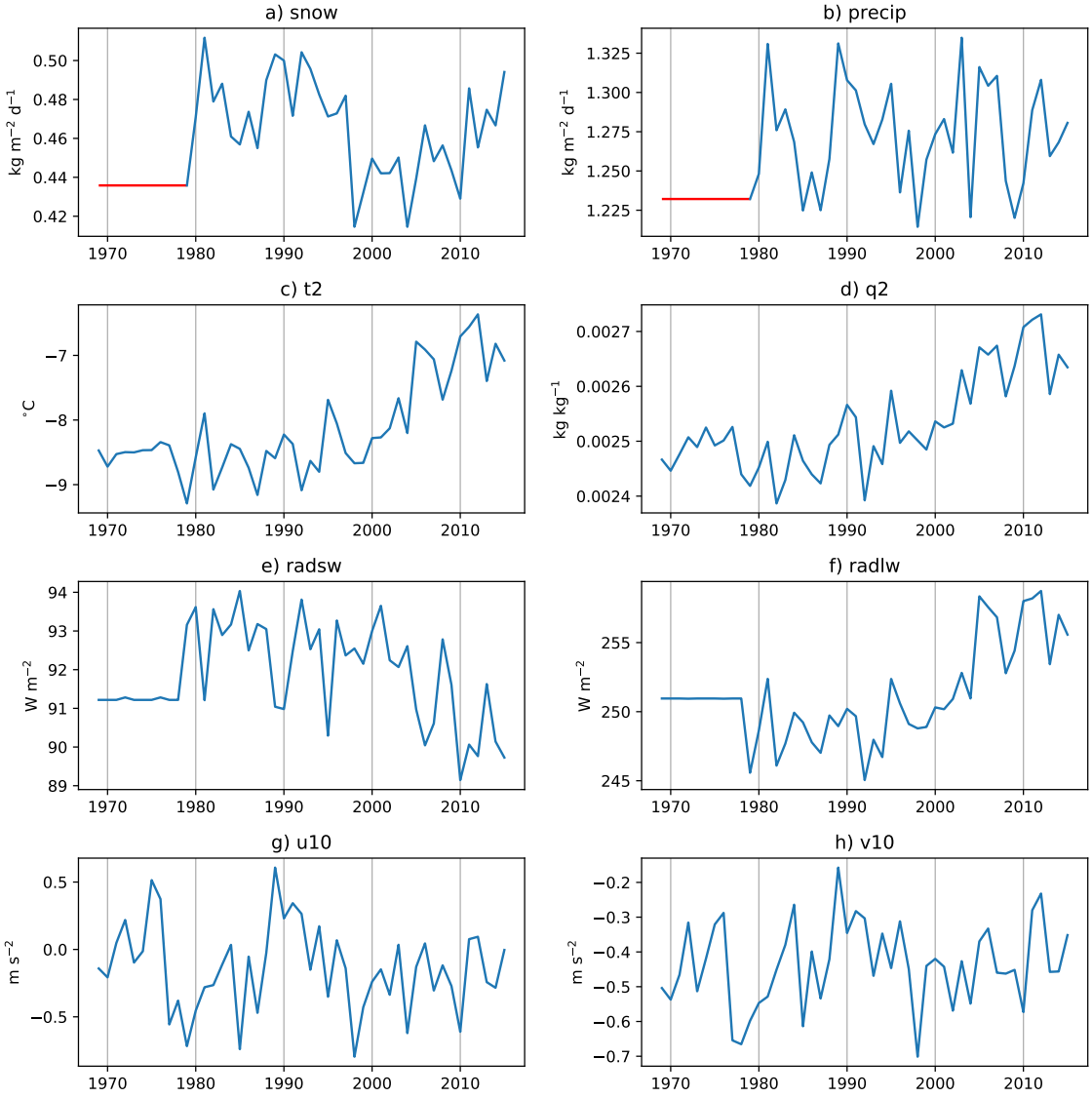

Figure A.5: Time series of annual mean a) snowfall, b) total precipitation (snowfall + rainfall), c) surface 2-m air temperature, d) surface 2-m specific humidity, e) incoming shortwave radiation, f) incoming longwave radiation, g) surface 10-m zonal wind, and h) surface 10-m meridional wind averaged over the region north of 60°N. Red lines denote the snowfall and total precipitation datasets prior to 1979 which were replaced by those of 1979 (see Chapter 4 for explanations).

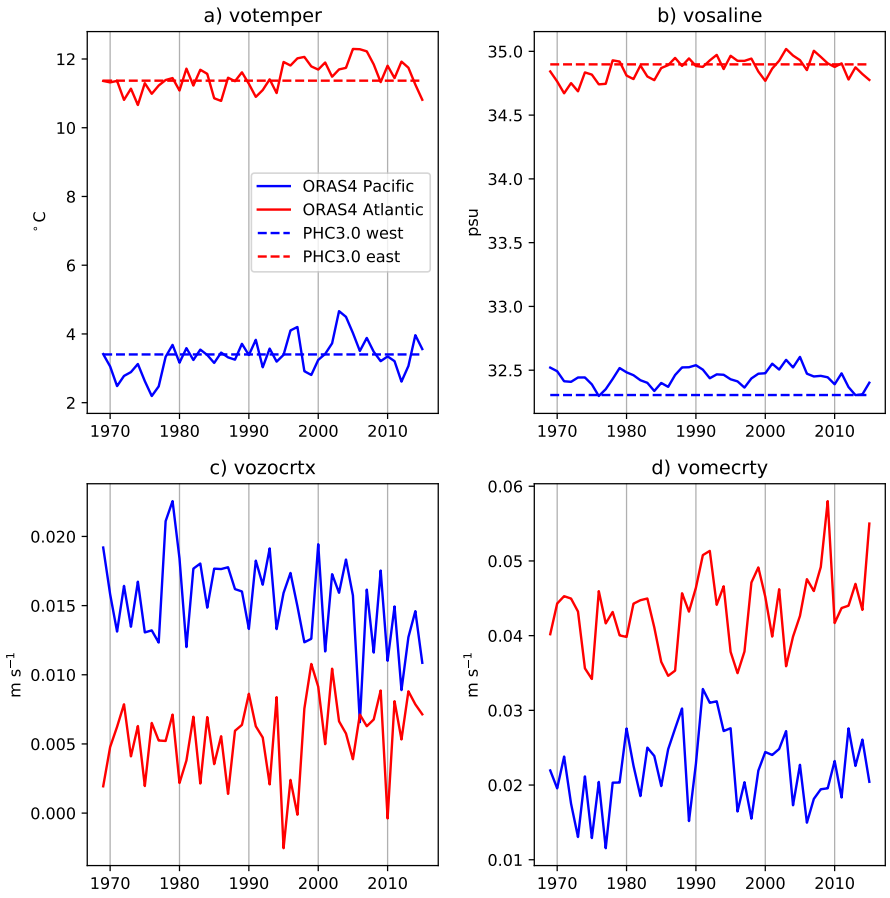

Figure A.6: Time series of a) temperature, b) salinity, c) zonal current, and d) meridional current in the uppermost layer of the water column averaged along the Pacific (blue) and Atlantic (red) lateral open boundaries. Dashed lines in panel a and b represent the mean SST and SSS based on PHC3.0, respectively.

Table A.6: Prescribed annual-mean concentrations of biogeochemical variables at the river mouths of the 6 major Arctic rivers in the model simulation.

Variable	Mackenzie	Yukon	Kolyma	Lena	Yenisey	Ob'	Reference
DIC (mmol C m^{-3})	1717	1792	642	817	908	1175	Tank et al. (2012)
DOC (mmol C m^{-3})	368	544	592	841	611	785	Cooper et al. (2008)
DON (mmol N m^{-3})	7.1	14.2	7.2	14.4	14.2	7.1	Holmes et al. (2012) and McClelland et al. (2012)
Nitrate (mmol N m^{-3})	7.1	7.1	3.6	3.6	7.1	7.1	McClelland et al. (2012)
TA (mmol C m^{-3})	1540	1707	449	788	845	1181	Cooper et al. (2008)

to directly feed into their respective oceanic pools. On the other hand, the runoff of the organic matter (DOC and DON) was set to feed into their respective inorganic (rather than organic) pools in the ocean. This treatment was necessary to prevent the implicit remineralization of DON originating from the rivers based on a fixed DOC:DON ratio prescribed in CanOE. Applying this ratio, which is representative of oceanic environments, is undesirable in this situation because the elemental ratios in the rivers differ from those of the ocean (e.g. Holmes et al., 2012).

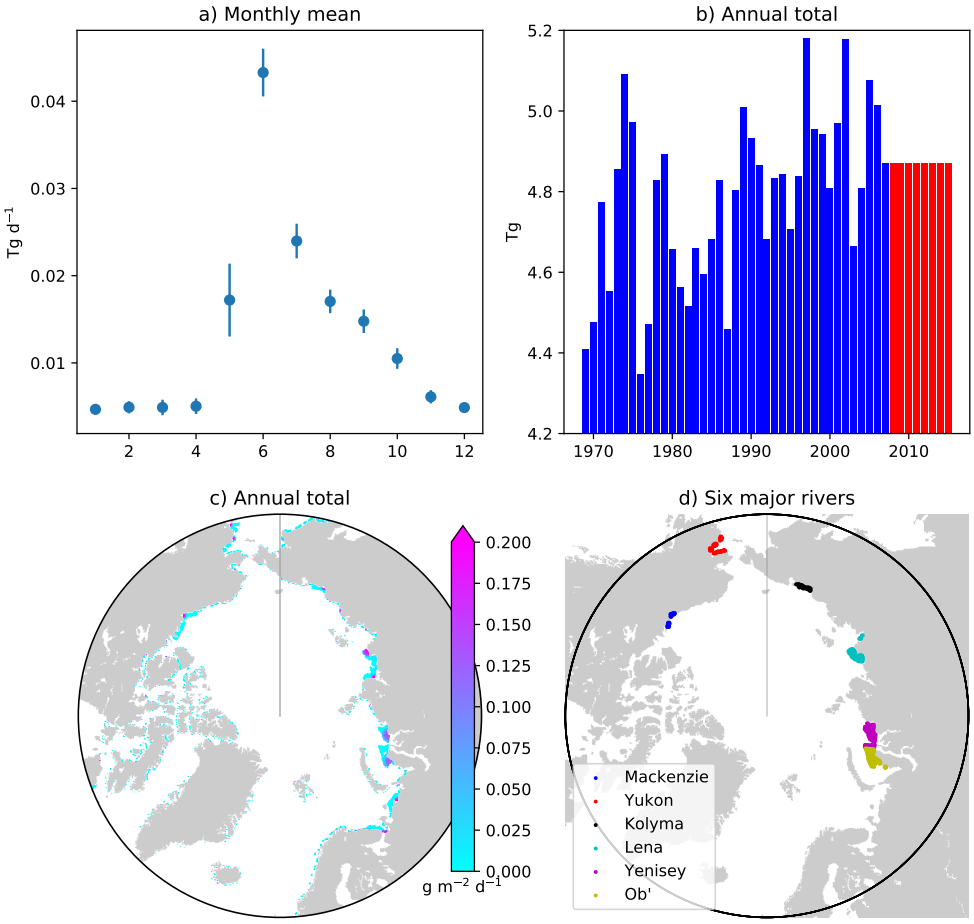

Figure A.7: a) Monthly-mean 1969-2015 climatology of river discharge rate of freshwater and b) the interannual time series of annual river discharge averaged over the region north of 60°N. Spatial maps of c) annual-mean climatology of river discharge rate of freshwater and d) locations of river mouths of the 6 major Arctic rivers in which the runoff of biogeochemical variables was prescribed.

Bibliography

Abraham, C., Steiner, N., Monahan, A., and Michel, C. (2015). Effects of subgrid-scale snow thickness variability on radiative transfer in sea ice. *Journal of Geophysical Research: Oceans*, 120(8):5597–5614.

Alcolombri, U., Ben-Dor, S., Feldmesser, E., Levin, Y., Tawfik, D. S., and Vardi, A. (2015). Identification of the algal dimethyl sulfide-releasing enzyme: A missing link in the marine sulfur cycle. *Science*, 348(6242):1466–1469.

Amante, C. and Eakins, B. W. (2009). *ETOPO1 1 arc-minute global relief model: procedures, data sources and analysis*. US Department of Commerce, National Oceanic and Atmospheric Administration, National Environmental Satellite, Data, and Information Service, National Geophysical Data Center, Marine Geology and Geophysics Division Colorado.

Andreae, M. O. and Crutzen, P. J. (1997). Atmospheric Aerosols: Biogeochemical Sources and Role in Atmospheric Chemistry. *Science*, 276(5315):1052–1058.

Archer, S., Cummings, D., Llewellyn, C., and Fishwick, J. (2009). Phytoplankton taxa, irradiance and nutrient availability determine the seasonal cycle of DMSP in temperate shelf seas. *Marine Ecology Progress Series*, 394:111–124.

Archer, S. D., Gilbert, F. J., Allen, J. I., Blackford, J., and Nightingale, P. D. (2004). Modelling of the seasonal patterns of dimethylsulphide production and fate during 1989 at a site in the North Sea. *Canadian Journal of Fisheries and Aquatic Sciences*, 61(5):765–787.

Ardyna, M., Babin, M., Gosselin, M., Devred, E., Bélanger, S., Matsuoka, A., and Tremblay, J.-É. (2013). Parameterization of vertical chlorophyll in the Arctic Ocean: impact of the subsurface chlorophyll maximum on regional, seasonal, and annual primary production estimates. *Biogeosciences*, 10(6):4383–4404.

Arora, V. K., Scinocca, J. F., Boer, G. J., Christian, J. R., Denman, K. L., Flato, G. M., Kharin, V. V., Lee, W. G., and Merryfield, W. J. (2011). Carbon emission limits required to satisfy future representative concentration pathways of greenhouse gases. *Geophysical Research Letters*, 38(5):L05805.

Arrigo, K. R. (2014). Sea Ice Ecosystems. *Annual Review of Marine Science*, 6(1):439–467.

Arrigo, K. R. and Dijken, G. L. v. (2011). Secular trends in Arctic Ocean net primary production. *Journal of Geophysical Research: Oceans*, 116(C9).

Arrigo, K. R. and Sullivan, C. W. (1994). A high resolution bio-optical model of microalgal growth: Tests using sea-ice algal community time-series data. *Limnology and Oceanography*, 39(3):609–631.

Arrigo, K. R., Sullivan, C. W., and Kremer, J. N. (1991). A bio-optical model of Antarctic sea ice. *Journal of Geophysical Research: Oceans*, 96(C6):10581–10592.

Arrigo, K. R. and van Dijken, G. L. (2015). Continued increases in Arctic Ocean primary production. *Progress in Oceanography*, 136:60–70.

Asher, E. C., Dacey, J. W. H., Mills, M. M., Arrigo, K. R., and Tortell, P. D. (2011). High concentrations and turnover rates of DMS, DMSP and DMSO in Antarctic sea ice. *Geophysical Research Letters*, 38(23):L23609.

Assmy, P., Ehn, J. K., FernÃ¡ndez-MÃ©ndez, M., Hop, H., Katlein, C., Sundfjord, A., Bluhm, K., Daase, M., Engel, A., Fransson, A., Granskog, M. A., Hudson, S. R., Kristiansen, S., Nicolaus, M., Peeken, I., Renner, A. H. H., Spreen, G., Tatarek, A., and Wiktor, J. (2013). Floating Ice-Algal Aggregates below Melting Arctic Sea Ice. *PLoS ONE*, 8(10):e76599.

Aumack, C. F. and Juhl, A. R. (2015). Light and nutrient effects on the settling characteristics of the sea ice diatom Nitzschia frigida. *Limnology and Oceanography*, 60(3):765–776.

Aumont, O., Ethé, C., Tagliabue, A., Bopp, L., and Gehlen, M. (2015). PISCES-v2: an ocean biogeochemical model for carbon and ecosystem studies. *Geoscientific Model Development*, 8(8):2465–2513.

Aumont, O., Maier-Reimer, E., Blain, S., and Monfray, P. (2003). An ecosystem model of the global ocean including Fe, Si, P colimitations. *Global Biogeochemical Cycles*, 17(2):1060.

Balmaseda, M. A., Mogensen, K., and Weaver, A. T. (2013). Evaluation of the ECMWF ocean reanalysis system ORAS4. *Quarterly Journal of the Royal Meteorological Society*, 139(674):1132–1161.

Barber, D. G., Hop, H., Mundy, C. J., Else, B., Dmitrenko, I. A., Tremblay, J.-E., Ehn, J. K., Assmy, P., Daase, M., Candlish, L. M., and Rysgaard, S. (2015). Selected physical, biological and biogeochemical implications of a rapidly changing Arctic Marginal Ice Zone. *Progress in Oceanography*, 139:122–150.

Bates, T. S., Lamb, B. K., Guenther, A., Dignon, J., and Stoiber, R. E. (1992). Sulfur emissions to the atmosphere from natural sourees. *Journal of Atmospheric Chemistry*, 14:315–337.

Bell, T. G., De Bruyn, W., Marandino, C. A., Miller, S. D., Law, C. S., Smith, M. J., and Saltzman, E. S. (2015). Dimethylsulfide gas transfer coefficients from algal blooms in the Southern Ocean. *Atmos. Chem. Phys.*, 15(4):1783–1794.

Bell, T. G., De Bruyn, W., Miller, S. D., Ward, B., Christensen, K., and Saltzman, E. S. (2013). Air–sea dimethylsulfide (DMS) gas transfer in the North Atlantic: evidence for limited interfacial gas exchange at high wind speed. *Atmospheric Chemistry and Physics*, 13(21):11073–11087.

Bouillon, R.-C., Lee, P. A., de Mora, S. J., Levasseur, M., and Lovejoy, C. (2002). Vernal distribution of dimethylsulphide, dimethylsulphoniopropionate, and dimethylsulphoxide in the North Water in 1998. *Deep Sea Research Part II: Topical Studies in Oceanography*, 49:5171–5189.

Bouillon, S., Maqueda, M. A. M., Legat, V., and Fichefet, T. (2009). An elastic–viscous–plastic sea ice model formulated on Arakawa B and C grids. *Ocean Modelling*, 27(3):174–184.

Brown, K. A., Miller, L. A., Mundy, C. J., Papakyriakou, T., Francois, R., Gosselin, M., Carnat, G., Swystun, K., and Tortell, P. D. (2015a). Inorganic carbon system dynamics in landfast Arctic sea ice during the early-melt period: Spring Sea Ice

Inorganic Carbon System. *Journal of Geophysical Research: Oceans*, 120(5):3542–3566.

Brown, Z. W., Lowry, K. E., Palmer, M. A., van Dijken, G. L., Mills, M. M., Pickart, R. S., and Arrigo, K. R. (2015b). Characterizing the subsurface chlorophyll a maximum in the Chukchi Sea and Canada Basin. *Deep Sea Research Part II: Topical Studies in Oceanography*, 118:88–104.

Bruggeman, J. and Bolding, K. (2014). A general framework for aquatic biogeochemical models. *Environmental Modelling & Software*, 61:249–265.

Buitenhuis, E., Le Quéré, C., Aumont, O., Beaugrand, G., Bunker, A., Hirst, A., Ikeda, T., O'Brien, T., Piontkovski, S., and Straile, D. (2006). Biogeochemical fluxes through mesozooplankton. *Global Biogeochemical Cycles*, 20(2):GB2003.

Burchard, H., Bolding, K., Kühn, W., Meister, A., Neumann, T., and Umlauf, L. (2006). Description of a flexible and extendable physical–biogeochemical model system for the water column. *Journal of Marine Systems*, 61:180–211.

Burchard, H., Bolding, K., and Villarreal, M. R. (1999). *GOTM, a general ocean turbulence model: Theory, implementation and test cases*. Space Applications Institute.

Carmack, E. and McLaughlin, F. (2011). Towards recognition of physical and geochemical change in Subarctic and Arctic Seas. *Progress in Oceanography*, 90:90–104.

Carmack, E. C., McLaughlin, F. A., Vagle, S., Melling, H., and Williams, W. J. (2010). Structures and property distributions in the three oceans surrounding Canada in 2007: A basis for a long-term ocean climate monitoring strategy. *Atmosphere-Ocean*, 48(4):211–224.

Carnat, G., Brabant, F., Dumont, I., Vancoppenolle, M., Ackley, S. F., Fritsen, C., Delille, B., and Tison, J.-L. (2016). Influence of short-term synoptic events and snow depth on DMS, DMSP, and DMSO dynamics in Antarctic spring sea ice. *Elem Sci Anth*, 4(135).

Castellani, G., Losch, M., Lange, B. A., and Flores, H. (2017). Modeling Arctic sea-ice algae: Physical drivers of spatial distribution and algae phenology. *Journal of Geophysical Research: Oceans*, 122(9):7466–7487.

Chang, R. Y.-W., Leck, C., Graus, M., Müller, M., Paatero, J., Burkhart, J. F., Stohl, A., Orr, L. H., Hayden, K., Li, S.-M., Hansel, A., Tjernström, M., Leaitch, W. R., and Abbatt, J. P. D. (2011a). Aerosol composition and sources in the central Arctic Ocean during ASCOS. *Atmospheric Chemistry and Physics*, 11(20):10619–10636.

Chang, R. Y.-W., Sjostedt, S. J., Pierce, J. R., Papakyriakou, T. N., Scarratt, M. G., Michaud, S., Levasseur, M., Leaitch, W. R., and Abbatt, J. P. D. (2011b). Relating atmospheric and oceanic DMS levels to particle nucleation events in the Canadian Arctic. *Journal of Geophysical Research*, 116:D00S03.

Charlson, R. J., Lovelock, J. E., Andreae, M. O., and Warren, S. G. (1987). Oceanic phytoplankton, atmospheric sulphur, cloud albedo and climate. *Nature*, 326(6114):655–661.

Cooper, L. W., McClelland, J. W., Holmes, R. M., Raymond, P. A., Gibson, J. J., Guay, C. K., and Peterson, B. J. (2008). Flow-weighted values of runoff tracers (δ ^{18} O, DOC, Ba, alkalinity) from the six largest Arctic rivers. *Geophysical Research Letters*, 35(18).

Cota, G. F., Prinsenberg, S. J., Bennett, E. B., Loder, J. W., Lewis, M. R., Anning, J. L., Watson, N. H. F., and Harris, L. R. (1987). Nutrient fluxes during extended blooms of Arctic ice algae. *Journal of Geophysical Research: Oceans*, 92(C2):1951–1962.

Crank, J. and Nicolson, P. (1996). A practical method for numerical evaluation of solutions of partial differential equations of the heat-conduction type. *Advances in Computational Mathematics*, 6(1):207–226.

Croft, B., Martin, R. V., Leaitch, W. R., Tunved, P., Breider, T. J., D'Andrea, S. D., and Pierce, J. R. (2016). Processes controlling the annual cycle of Arctic aerosol number and size distributions. *Atmospheric Chemistry and Physics*, 16(6):3665–3682.

Dai, A. and Trenberth, K. E. (2002). Estimates of Freshwater Discharge from Continents: Latitudinal and Seasonal Variations. *Journal of Hydrometeorology*, 3(6):660–687.

Damm, E., Nomura, D., Martin, A., Dieckmann, G., and Meiners, K. (2016). DMSP and DMS cycling within Antarctic sea ice during the winter–spring transition. *Deep Sea Research Part II: Topical Studies in Oceanography*, 131:150–159.

Deal, C., Jin, M., Elliott, S., Hunke, E., Maltrud, M., and Jeffery, N. (2011). Large-scale modeling of primary production and ice algal biomass within arctic sea ice in 1992. *Journal of Geophysical Research*, 116(C7):C07004.

Deal, C. J., Kieber, D. J., Toole, D. A., Stamnes, K., Jiang, S., and Uzuka, N. (2005). Dimethylsulfide photolysis rates and apparent quantum yields in Bering Sea seawater. *Continental Shelf Research*, 25(15):1825–1835.

Dee, D. P., Uppala, S. M., Simmons, A. J., Berrisford, P., Poli, P., Kobayashi, S., Andrae, U., Balmaseda, M. A., Balsamo, G., Bauer, P., Bechtold, P., Beljaars, A. C. M., van de Berg, L., Bidlot, J., Bormann, N., Delsol, C., Dragani, R., Fuentes, M., Geer, A. J., Haimberger, L., Healy, S. B., Hersbach, H., Hólm, E. V., Isaksen, L., Kållberg, P., Köhler, M., Matricardi, M., McNally, A. P., Monge-Sanz, B. M., Morcrette, J.-J., Park, B.-K., Peubey, C., de Rosnay, P., Tavolato, C., Thépaut, J.-N., and Vitart, F. (2011). The ERA-Interim reanalysis: configuration and performance of the data assimilation system. *Quarterly Journal of the Royal Meteorological Society*, 137(656):553–597.

Denman, K. L. (2003). Modelling planktonic ecosystems: parameterizing complexity. *Progress in Oceanography*, 57(3–4):429–452.

Dirkson, A., Merryfield, W. J., and Monahan, A. (2016). Impacts of Sea Ice Thickness Initialization on Seasonal Arctic Sea Ice Predictions. *Journal of Climate*, 30(3):1001–1017.

Dukhovskoy, D. S., Myers, P. G., Platov, G., Timmermans, M.-L., Curry, B., Proshutinsky, A., Bamber, J. L., Chassignet, E., Hu, X., Lee, C. M., and Somavilla, R. (2016). Greenland freshwater pathways in the sub-Arctic Seas from model experiments with passive tracers. *Journal of Geophysical Research: Oceans*, 121(1):877–907.

Dupont, F. (2012). Impact of sea-ice biology on overall primary production in a biophysical model of the pan-Arctic Ocean. *Journal of Geophysical Research: Oceans*, 117(C8):C00D17.

Dupont, F., Higginson, S., Bourdallé-Badie, R., Lu, Y., Roy, F., Smith, G. C., Lemieux, J.-F., Garric, G., and Davidson, F. (2015). A high-resolution ocean and sea-ice modelling system for the Arctic and North Atlantic oceans. *Geosci. Model Dev.*, 8(5):1577–1594.

Dussin, R., Barnier, B., Brodeau, L., and Molines, J. M. (2016). The making of the Drakkar Forcing Set DFS5. *DRAKKAR/MyOcean Rep. 01–04*, 16.

Elliott, S., Deal, C., Humphries, G., Hunke, E., Jeffery, N., Jin, M., Levasseur, M., and Stefels, J. (2012). Pan-Arctic simulation of coupled nutrient-sulfur cycling due to sea ice biology: Preliminary results. *Journal of Geophysical Research*, 117(G1):G01016.

Else, B. G. T., Papakyriakou, T. N., Galley, R. J., Mucci, A., Gosselin, M., Miller, L. A., Shadwick, E. H., and Thomas, H. (2012). Annual cycles of pCO2sw in the southeastern Beaufort Sea: New understandings of air-sea CO2 exchange in arctic polynya regions. *Journal of Geophysical Research: Oceans*, 117(C9):C00G13.

Eppley, R. W. (1972). Temperature and phytoplankton growth in the sea. *Fish. Bull*, 70(4):1063–1085.

Fichefet, T. and Maqueda, M. A. M. (1997). Sensitivity of a global sea ice model to the treatment of ice thermodynamics and dynamics. *Journal of Geophysical Research: Oceans*, 102(C6):12609–12646.

Flato, G. M. and Brown, R. D. (1996). Variability and climate sensitivity of landfast Arctic sea ice. *Journal of Geophysical Research: Oceans*, 101(C11):25767–25777.

Frey, K. E., Perovich, D. K., and Light, B. (2011). The spatial distribution of solar radiation under a melting Arctic sea ice cover. *Geophysical Research Letters*, 38(22):L22501.

Friedrichs, M. A. M., Dusenberry, J. A., Anderson, L. A., Armstrong, R. A., Chai, F., Christian, J. R., Doney, S. C., Dunne, J., Fujii, M., Hood, R., McGillicuddy, D. J., Moore, J. K., Schartau, M., Spitz, Y. H., and Wiggert, J. D. (2007). Assessment of skill and portability in regional marine biogeochemical models: Role of multiple planktonic groups. *Journal of Geophysical Research: Oceans*, 112(C8):C08001.

Fripiat, F., Sigman, D. M., Fawcett, S. E., Rafter, P. A., Weigand, M. A., and Tison, J.-L. (2014). New insights into sea ice nitrogen biogeochemical dynamics from the nitrogen isotopes. *Global Biogeochemical Cycles*, 28(2):115–130.

Gabric, A., Murray, N., Stone, L., and Kohl, M. (1993). Modelling the production of dimethylsulfide during a phytoplankton bloom. *Journal of Geophysical Research: Oceans (1978–2012)*, 98(C12):22805–22816.

Gabric, A. J., Matrai, P. A., and Vernet, M. (1999). Modelling the production and cycling of dimethylsulphide during the vernal bloom in the Barents Sea. *Tellus B: Chemical and Physical Meteorology*, 51(5):919–937.

Gabric, A. J., Qu, B., Matrai, P., and Hirst, A. C. (2005). The simulated response of dimethylsulfide production in the Arctic Ocean to global warming. *Tellus B*, 57(5):391–403.

Gale, M. (2014). *On the biophysical factors that control under-ice phytoplankton bloom onset in the Central Canadian Archipelago*. PhD thesis, University of Manitoba.

Galí, M., Devred, E., Levasseur, M., Royer, S.-J., and Babin, M. (2015). A remote sensing algorithm for planktonic dimethylsulfoniopropionate (DMSP) and an analysis of global patterns. *Remote Sensing of Environment*, 171:171–184.

Galí, M., Levasseur, M., Devred, E., Simó, R., and Babin, M. (2018). Sea-surface dimethylsulfide (DMS) concentration from satellite data at global and regional scales. *Biogeosciences*, 15(11):3497–3519.

Galí, M. and Simó, R. (2010). Occurrence and cycling of dimethylated sulfur compounds in the Arctic during summer receding of the ice edge. *Marine Chemistry*, 122:105–117.

Galí, M. and Simó, R. (2015). A meta-analysis of oceanic DMS and DMSP cycling processes: Disentangling the summer paradox. *Global Biogeochemical Cycles*, 29(4):496–515.

Galindo, V., Levasseur, M., Mundy, C., Gosselin, M., Tremblay, J.-E., Scarratt, M., Gratton, Y., Papakiriakou, T., Poulin, M., and Lizotte, M. (2014). Biological and physical processes influencing sea ice, under-ice algae, and dimethylsulfoniopropionate during spring in the Canadian Arctic Archipelago. *Journal of Geophysical Research: Oceans*, 119(6):3746–3766.

Galindo, V., Levasseur, M., Mundy, C. J., Gosselin, M., Scarratt, M., Papakyriakou, T., Stefels, J., Gale, M. A., Tremblay, J.-É., and Lizotte, M. (2016). Contrasted sensitivity of DMSP production to high light exposure in two Arctic under-ice blooms. *Journal of Experimental Marine Biology and Ecology*, 475:38–48.

Galindo, V., Levasseur, M., Scarratt, M., Mundy, C., Gosselin, M., Kiene, R., Gourdal, M., and Lizotte, M. (2015). Under-ice microbial dimethylsulfoniopropionate metabolism during the melt period in the Canadian Arctic Archipelago. *Marine Ecology Progress Series*, 524:39–53.

Garcia, H. E., Locarnini, R. A., Boyer, T. P., Antonov, J. I., Baranova, O. K., Zweng, M. M., Reagan, J. R., and Johnson, D. R. (2014). World Ocean Atlas 2013, Volume 3: Dissolved Oxygen, Apparent Oxygen Utilization, and Oxygen Saturation. S. Levitus, Ed., A. Mishonov Technical Ed.; NOAA Atlas NESDIS 75, 27 pp.

Garrison, D. L., Ackley, S. F., and Buck, K. R. (1983). A physical mechanism for establishing algal populations in frazil ice. *Nature*, 306(5941):363–365.

Geilfus, N.-X., Galley, R. J., Crabeck, O., Papakyriakou, T., Landy, J., Tison, J.-L., and Rysgaard, S. (2015). Inorganic carbon dynamics of melt-pond-covered first-year sea ice in the Canadian Arctic. *Biogeosciences*, 12(6):2047–2061.

Ghahremaninezhad, R., Norman, A.-L., Abbatt, J. P. D., Levasseur, M., and Thomas, J. L. (2016). Biogenic, anthropogenic and sea salt sulfate size-segregated aerosols in the Arctic summer. *Atmos. Chem. Phys.*, 16(8):5191–5202.

Goddijn-Murphy, L., Woolf, D. K., Callaghan, A. H., Nightingale, P. D., and Shutler, J. D. (2015). A reconciliation of empirical and mechanistic models of the air-sea gas transfer velocity. *Journal of Geophysical Research: Oceans*, 121:818–835.

Goddijn-Murphy, L., Woolf, D. K., and Marandino, C. (2012). Space-based retrievals of air-sea gas transfer velocities using altimeters: Calibration for dimethyl sulfide. *Journal of Geophysical Research: Oceans*, 117(C8):C08028.

Goosse, H. and Fichefet, T. (1999). Importance of ice-ocean interactions for the global ocean circulation: A model study. *Journal of Geophysical Research: Oceans*, 104(C10):23337–23355.

Gosselin, M., Legendre, L., Therriault, J.-C., and Demers, S. (1990). Light and nutrient limitation of sea-ice microalgae (Hudson Bay, Canadian Arctic). *Journal of Phycology*, 26(2):220–232.

Gosselin, M., Levasseur, M., Wheeler, P. A., Horner, R. A., and Booth, B. C. (1997). New measurements of phytoplankton and ice algal production in the Arctic Ocean. *Deep Sea Research Part II: Topical Studies in Oceanography*, 44(8):1623–1644.

Gourdal, M., Lizotte, M., Massé, G., Gosselin, M., Poulin, M., Scarratt, M., Charette, J., and Levasseur, M. (2018). Dimethyl sulfide dynamics in first-year sea ice melt ponds in the Canadian Arctic Archipelago. *Biogeosciences*, 15(10):3169–3188.

Grenfell, T. C. and Maykut, G. A. (1977). The optical properties of ice and snow in the Arctic Basin. *Journal of Glaciology*, 18:445–463.

Harrison, W. G., Cota, G. F., and Smith, R. E. H. (1990). Nitrogen utilization in ice algal communities of Barrow Strait, Northwest Territories, Canada. *Marine Ecology Progress Series*, 67:275–283.

Hayashida, H., Steiner, N., Monahan, A., Galindo, V., Lizotte, M., and Levasseur, M. (2017). Implications of sea-ice biogeochemistry for oceanic production and emissions of dimethyl sulfide in the Arctic. *Biogeosciences*, 14(12):3129–3155.

Hill, V. J., Matrai, P. A., Olson, E., Suttles, S., Steele, M., Codispoti, L., and Zimmerman, R. C. (2013). Synthesis of integrated primary production in the Arctic Ocean: II. In situ and remotely sensed estimates. *Progress in Oceanography*, 110:107–125.

Holmes, R. M., McClelland, J. W., Peterson, B. J., Tank, S. E., Bulygina, E., Eglinton, T. I., Gordeev, V. V., Gurtovaya, T. Y., Raymond, P. A., Repeta, D. J., Staples, R., Striegl, R. G., Zhulidov, A. V., and Zimov, S. A. (2012). Seasonal and Annual Fluxes of Nutrients and Organic Matter from Large Rivers to the Arctic Ocean and Surrounding Seas. *Estuaries and Coasts*, 35(2):369–382.

Hu, X. and Myers, P. G. (2013). A Lagrangian view of Pacific water inflow pathways in the Arctic Ocean during model spin-up. *Ocean Modelling*, 71:66–80.

Hu, X. and Myers, P. G. (2014). Changes to the Canadian Arctic Archipelago Sea Ice and Freshwater Fluxes in the Twenty-First Century under the Intergovernmental Panel on Climate Change A1b Climate Scenario. *Atmosphere-Ocean*, 52(4):331–350.

Huebert, B. J., Blomquist, B. W., Yang, M. X., Archer, S. D., Nightingale, P. D., Yelland, M. J., Stephens, J., Pascal, R. W., and Moat, B. I. (2010). Linearity of DMS transfer coefficient with both friction velocity and wind speed in the moderate wind speed range. *Geophysical Research Letters*, 37(1):L01605.

Irish, V. E., Elizondo, P., Chen, J., Chou, C., Charette, J., Lizotte, M., Ladino, L. A., Wilson, T. W., Gosselin, M., Murray, B. J., Polishchuk, E., Abbatt, J. P. D., Miller, L. A., and Bertram, A. K. (2017). Ice-nucleating particles in Canadian Arctic sea-surface microlayer and bulk seawater. *Atmospheric Chemistry and Physics*, 17(17):10583–10595.

Jakobsson, M. (2002). Hypsometry and volume of the Arctic Ocean and its constituent seas. *Geochemistry, Geophysics, Geosystems*, 3(5):1–18.

Jakobsson, M., Grantz, A., Kristoffersen, Y., and Macnab, M. (2003). Bathymetry and Physiography of the Arctic Ocean and Its Constituent Seas. In *Arctic Ocean Organic Carbon Cycle: Present and Past*. Springer, New York, NY, USA.

Jarníková, T., Dacey, J., Lizotte, M., Levasseur, M., and Tortell, P. (2018). The distribution of methylated sulfur compounds, DMS and DMSP, in Canadian subarctic and Arctic marine waters during summer 2015. *Biogeosciences*, 15(8):2449–2465.

Jin, M., Deal, C., Lee, S. H., Elliott, S., Hunke, E., Maltrud, M., and Jeffery, N. (2012). Investigation of Arctic sea ice and ocean primary production for the period 1992–2007 using a 3-D global ice–ocean ecosystem model. *Deep Sea Research Part II: Topical Studies in Oceanography*, 81–84:28–35.

Jin, M., Deal, C., Maslowski, W., Matrai, P., Roberts, A., Osinski, R., Lee, Y. J., Frants, M., Elliott, S., Jeffery, N., Hunke, E., and Wang, S. (2018). Effects of Model Resolution and Ocean Mixing on Forced Ice-Ocean Physical and Biogeochemical Simulations Using Global and Regional System Models. *Journal of Geophysical Research: Oceans*, 123(1):358–377.

Jin, M., Deal, C., Wang, J., Alexander, V., Gradinger, R., Saitoh, S.-i., Iida, T., Wan, Z., and Stabeno, P. (2007). Ice-associated phytoplankton blooms in the southeastern Bering Sea. *Geophysical Research Letters*, 34(6):L06612.

Jin, M., Deal, C. J., Wang, J., Shin, K.-H., Tanaka, N., Whitledge, T. E., Lee, S. H., and Gradinger, R. R. (2006). Controls of the landfast ice–ocean ecosystem offshore Barrow, Alaska. *Annals of Glaciology*, 44(1):63–72.

Jin, M., Popova, E. E., Zhang, J., Ji, R., Pendleton, D., Varpe, Ø., Yool, A., and Lee, Y. J. (2015). Ecosystem model intercomparison of under-ice and total primary production in the Arctic Ocean. *Journal of Geophysical Research: Oceans*, 121(1):934–948.

Jodwalis, C. M., Benner, R. L., and Eslinger, D. L. (2000). Modeling of dimethyl sulfide ocean mixing, biological production, and sea-to-air flux for high latitudes. *Journal of Geophysical Research: Atmospheres*, 105(D11):14387–14399.

Karsten, U., Kirst, G. O., and Wiencke, C. (1992). Dimethylsulphoniopropionate (DMSP) accumulation in green macroalgae from polar to temperate regions: interactive effects of light versus salinity and light versus temperature. *Polar Biology*, 12(6-7):603–607.

Kawamiya, M., Kishi, M. J., Yamanaka, Y., and Suginohara, N. (1995). An ecological-physical coupled model applied to Station Papa. *Journal of Oceanography*, 51(6):635–664.

Keller, M. D. (1989). Dimethyl sulfide production and marine phytoplankton: the importance of species composition and cell size. *Biological Oceanography*, 6(5-6):375–382.

Kettle, A. J. and Andreae, M. O. (2000). Flux of dimethylsulfide from the oceans: A comparison of updated data sets and flux models. *Journal of Geophysical Research: Atmospheres*, 105(D22):26793–26808.

Kettle, A. J., Andreae, M. O., Amouroux, D., Andreae, T. W., Bates, T. S., Berresheim, H., Bingemer, H., Boniforti, R., Curran, M. a. J., DiTullio, G. R., Helas, G., Jones, G. B., Keller, M. D., Kiene, R. P., Leck, C., Levasseur, M., Malin, G., Maspero, M., Matrai, P., McTaggart, A. R., Mihalopoulos, N., Nguyen, B. C., Novo, A., Putaud, J. P., Rapsomanikis, S., Roberts, G., Schebeske, G., Sharma, S., Simó, R., Staubes, R., Turner, S., and Uher, G. (1999). A global database of sea surface dimethylsulfide (DMS) measurements and a procedure to predict sea surface DMS as a function of latitude, longitude, and month. *Global Biogeochemical Cycles*, 13(2):399–444.

Kiene, R. P. and Linn, L. J. (2000). The fate of dissolved dimethylsulfoniopropionate (DMSP) in seawater: tracer studies using 35 S-DMSP. *Geochimica et Cosmochimica Acta*, 64(16):2797–2810.

Kirst, G. O., Thiel, C., Wolff, H., Nothnagel, J., Wanzek, M., and Ulmke, R. (1991). Dimethylsulfoniopropionate (DMSP) in icealgae and its possible biological role. *Marine Chemistry*, 35:381–388.

Kirst, G. O. and Wiencke, C. (1995). Ecophysiology of polar algae. *Journal of Phycology*, 31(2):181–199.

Krembs, C., Eicken, H., and Deming, J. W. (2011). Exopolymer alteration of physical properties of sea ice and implications for ice habitability and biogeochemistry in a warmer Arctic. *Proceedings of the National Academy of Sciences*, 108(9):3653–3658.

Lana, A., Bell, T. G., Simó, R., Vallina, S. M., Ballabrera-Poy, J., Kettle, A. J., Dachs, J., Bopp, L., Saltzman, E. S., Stefels, J., Johnson, J. E., and Liss, P. S. (2011). An updated climatology of surface dimethlysulfide concentrations and emission fluxes in the global ocean. *Global Biogeochemical Cycles*, 25(1):GB1004.

Laroche, D., Vézina, A. F., Levasseur, M., Gosselin, M., Stefels, J., Keller, M. D., Matrai, P. A., and Kwint, R. L. J. (1999). DMSP synthesis and exudation in phytoplankton: a modeling approach. *Marine Ecology Progress Series*, 180:37–49.

Lauvset, S. K., Key, R. M., Olsen, A., van Heuven, S., Velo, A., Lin, X., Schirnick, C., Kozyr, A., Tanhua, T., Hoppema, M., Jutterström, S., Steinfeldt, R., Jeansson, E., Ishii, M., Perez, F. F., Suzuki, T., and Watelet, S. (2016). A new global interior ocean mapped climatology: the $1^\circ \times 1^\circ$ GLODAP version 2. *Earth System Science Data*, 8:325–340.

Lavoie, D., Denman, K., and Michel, C. (2005). Modeling ice algal growth and decline in a seasonally ice-covered region of the Arctic (Resolute Passage, Canadian Archipelago). *Journal of Geophysical Research*, 110(C11):C11009.

Lavoie, D., Macdonald, R. W., and Denman, K. L. (2009). Primary productivity and export fluxes on the Canadian shelf of the Beaufort Sea: A modelling study. *Journal of Marine Systems*, 75(1–2):17–32.

Leaitch, W. R., Sharma, S., Huang, L., Toom-Sauntry, D., Chivulescu, A., Macdonald, A. M., von Salzen, K., Pierce, J. R., Bertram, A. K., Schroder, J. C., Shantz, N. C., Chang, R. Y.-W., and Norman, A.-L. (2013). Dimethyl sulfide control of the clean summertime Arctic aerosol and cloud. *Elementa: Science of the Anthropocene*, 1(17).

Leck, C. and Persson, C. (1996). The central Arctic Ocean as a source of dimethyl sulfide Seasonal variability in relation to biological activity. *Tellus B*, 48(2):156–177.

Lefèvre, M., Vézina, A., Levasseur, M., and Dacey, J. W. (2002). A model of dimethylsulfide dynamics for the subtropical North Atlantic. *Deep Sea Research Part I: Oceanographic Research Papers*, 49(12):2221–2239.

Legendre, L., Ackley, S. F., Dieckmann, G. S., Gulliksen, B., Horner, R., Hoshiai, T., Melnikov, I. A., Reeburgh, W. S., Spindler, M., and Sullivan, C. W. (1992). Ecology of sea ice biota. *Polar Biology*, 12:429–444.

Leu, E., Mundy, C. J., Assmy, P., Campbell, K., Gabrielsen, T. M., Gosselin, M., Juul-Pedersen, T., and Gradinger, R. (2015). Arctic spring awakening – Steering principles behind the phenology of vernal ice algal blooms. *Progress in Oceanography*, 139:151–170.

Levasseur, M. (2013). Impact of Arctic meltdown on the microbial cycling of sulphur. *Nature Geoscience*, 6(9):691–700.

Levasseur, M., Gosselin, M., and Michaud, S. (1994). A new source of dimethylsulfide (DMS) for the Arctic atmosphere: Ice diatoms. *Marine Biology*, 121(2):381–387.

Light, B., Grenfell, T. C., and Perovich, D. K. (2008). Transmission and absorption of solar radiation by Arctic sea ice during the melt season. *Journal of Geophysical Research*, 113:C03023.

Lindsay, R. and Schweiger, A. (2015). Arctic sea ice thickness loss determined using subsurface, aircraft, and satellite observations. *The Cryosphere*, 9(1):269–283.

Lindsay, R. W. and Rothrock, D. A. (1995). Arctic sea ice leads from advanced very high resolution radiometer images. *Journal of Geophysical Research: Oceans*, 100(C3):4533–4544.

Loose, B., McGillis, W. R., Perovich, D., Zappa, C. J., and Schlosser, P. (2014). A parameter model of gas exchange for the seasonal sea ice zone. *Ocean Science*, 10(1):17–28.

Loose, B., McGillis, W. R., Schlosser, P., Perovich, D., and Takahashi, T. (2009). Effects of freezing, growth, and ice cover on gas transport processes in laboratory seawater experiments. *Geophysical Research Letters*, 36(5):L05603.

Loose, B., Miller, L., Elliot, S., and Papakyriakou, T. (2011). Sea ice biogeochemistry and material transport across the frozen interface. *Oceanography*, 24(3):202–218.

Lovelock, J. E., Maggs, R. J., and Rasmussen, R. A. (1972). Atmospheric Dimethyl Sulphide and the Natural Sulphur Cycle. *Nature*, 237(5356):452–453.

Luce, M., Levasseur, M., Scarratt, M. G., Michaud, S., Royer, S.-J., Kiene, R., Lovejoy, C., Gosselin, M., Poulin, M., Gratton, Y., and Lizotte, M. (2011). Distribution and microbial metabolism of dimethylsulfoniopropionate and dimethylsulfide during the 2007 Arctic ice minimum. *Journal of Geophysical Research*, 116(C9):C00G06.

Madec, G. (2008). NEMO ocean engine. Technical Report 27, Institut Pierre Simon Laplace (ISPL).

Matrai, P. A. and Keller, M. D. (1994). Total organic sulfur and dimethylsulfoniopropionate in marine phytoplankton: intracellular variations. *Marine Biology*, 119(1):61–68.

Maykut, G. A. and Untersteiner, N. (1971). Some results from a time-dependent thermodynamic model of sea ice. *Journal of Geophysical Research*, 76(6):1550–1575.

McClelland, J. W., Holmes, R. M., Dunton, K. H., and Macdonald, R. W. (2012). The Arctic Ocean Estuary. *Estuaries and Coasts*, 35(2):353–368.

McDonald, S., Koulis, T., Ehn, J., Campbell, K., Gosselin, M., and Mundy, C. (2015). A functional regression model for predicting optical depth and estimating attenuation coefficients in sea-ice covers near Resolute Passage, Canada. *Annals of Glaciology*, 56(69):147–154.

McLaughlin, F. A. and Carmack, E. C. (2010). Deepening of the nutricline and chlorophyll maximum in the Canada Basin interior, 2003–2009. *Geophysical Research Letters*, 37(24):L24602.

Michel, C., Ingram, R. G., and Harris, L. R. (2006). Variability in oceanographic and ecological processes in the Canadian Arctic Archipelago. *Progress in Oceanography*, 71(2–4):379–401.

Michel, C., Legendre, L., Ingram, R. G., Gosselin, M., and Levasseur, M. (1996). Carbon budget of sea-ice algae in spring: Evidence of a significant transfer to zooplankton grazers. *Journal of Geophysical Research: Oceans*, 101(C8):18345–18360.

Michel, C., Legendre, L., Therriault, J.-C., Demers, S., and Vandevelde, T. (1993). Springtime coupling between ice algal and phytoplankton assemblages in south-eastern Hudson Bay, Canadian Arctic. *Polar Biology*, 13(7):441–449.

Miller, L. A., Fripiat, F., Else, B. G., Bowman, J. S., Brown, K. A., Collins, R. E., Ewert, M., Fransson, A., Gosselin, M., Lannuzel, D., Meiners, K. M., Michel, C., Nishioka, J., Nomura, D., Papadimitriou, S., Russell, L. M., Sørensen, L. L., Thomas, D. N., Tison, J.-L., van Leeuwe, M. A., Vancoppenolle, M., Wolff, E. W., and Zhou, J. (2015). Methods for biogeochemical studies of sea ice: The state of the art, caveats, and recommendations. *Elementa: Science of the Anthropocene*, 3(38).

Monahan, A. H. and Denman, K. L. (2004). Impacts of atmospheric variability on a coupled upper-ocean/ecosystem model of the subarctic Northeast Pacific. *Global Biogeochemical Cycles*, 18(2):GB2010.

Monod, J. (1949). The growth of bacterial cultures. *Annual Review of Microbiology*, 3(1):371–394.

Moreau, S., Vancoppenolle, M., Zhou, J., Tison, J.-L., Delille, B., and Goosse, H. (2014). Modelling argon dynamics in first-year sea ice. *Ocean Modelling*, 73:1–18.

Morel, A. (1988). Optical modeling of the upper ocean in relation to its biogenous matter content (case I waters). *Journal of Geophysical Research: Oceans*, 93(C9):10749–10768.

Mortenson, E., Hayashida, H., Steiner, N., Monahan, A., Blais, M., Gale, M. A., Galindo, V., Gosselin, M., Hu, X., Lavoie, D., and Mundy, C. J. (2017). A model-based analysis of physical and biological controls on ice algal and pelagic primary production in Resolute Passage. *Elem Sci Anth*, 5(39).

Motard-Côté, J., Levasseur, M., Scarratt, M. G., Michaud, S., Gratton, Y., Rivkin, R. B., Keats, K., Gosselin, M., Tremblay, J.-É., Kiene, R. P., and Lovejoy, C. (2012). Distribution and metabolism of dimethylsulfoniopropionate (DMSP) and phylogenetic affiliation of DMSP-assimilating bacteria in northern Baffin Bay/Lancaster Sound. *Journal of Geophysical Research: Oceans*, 117(C9):C00G11.

Mundy, C., Gosselin, M., Ehn, J., Gratton, Y., Rossnagel, A., Barber, D. G., Martin, J., Tremblay, J.-É., Palmer, M., Arrigo, K. R., Darnis, G., Fortier, L., Else, B., and Papakyriakou, T. (2009). Contribution of under-ice primary production to an ice-edge upwelling phytoplankton bloom in the Canadian Beaufort Sea. *Geophysical Research Letters*, 36(17):L17601.

Mundy, C., Gosselin, M., Gratton, Y., Brown, K., Galindo, V., Campbell, K., Levasseur, M., Barber, D., Papakyriakou, T., and Bélanger, S. (2014). Role of environmental factors on phytoplankton bloom initiation under landfast sea ice in Resolute Passage, Canada. *Marine Ecology Progress Series*, 497:39–49.

Mungall, E. L., Croft, B., Lizotte, M., Thomas, J. L., Murphy, J. G., Levasseur, M., Martin, R. V., Wentzell, J. J. B., Liggio, J., and Abbatt, J. P. D. (2016). Dimethyl sulfide in the summertime Arctic atmosphere: measurements and source sensitivity simulations. *Atmos. Chem. Phys.*, 16(11):6665–6680.

Niemi, A., Michel, C., Hille, K., and Poulin, M. (2011). Protist assemblages in winter sea ice: setting the stage for the spring ice algal bloom. *Polar Biology*, 34(12):1803–1817.

Nightingale, P. D., Malin, G., Law, C. S., Watson, A. J., Liss, P. S., Liddicoat, M. I., Boutin, J., and Upstill-Goddard, R. C. (2000). In situ evaluation of air-sea gas exchange parameterizations using novel conservative and volatile tracers. *Global Biogeochemical Cycles*, 14(1):373–387.

Niki, T., Kunugi, M., and Otsuki, A. (2000). DMSP-lyase activity in five marine phytoplankton species: its potential importance in DMS production. *Marine Biology*, 136(5):759–764.

Nomura, D., Koga, S., Kasamatsu, N., Shinagawa, H., Simizu, D., Wada, M., and Fukuchi, M. (2012). Direct measurements of DMS flux from Antarctic fast sea ice to the atmosphere by a chamber technique. *Journal of Geophysical Research: Oceans*, 117(C4):C04011.

Nöthig, E.-M., Bracher, A., Engel, A., Metfies, K., Niehoff, B., Peeken, I., Bauerfeind, E., Cherkasheva, A., Gäbler-Schwarz, S., Hardge, K., Kilias, E., Kraft, A., Kidane, Y. M., Lalande, C., Piontek, J., Thomisch, K., and Wurst, M. (2015). Summertime plankton ecology in Fram Strait—a compilation of long- and short-term observations. *Polar Research*, 34(1):23349.

Onodera, J., Watanabe, E., Harada, N., and Honda, M. C. (2015). Diatom flux reflects water-mass conditions on the southern Northwind Abyssal Plain, Arctic Ocean. *Biogeosciences*, 12(5):1373–1385.

Orellana, M. V., Matrai, P. A., Leck, C., Rauschenberg, C. D., Lee, A. M., and Coz, E. (2011). Marine microgels as a source of cloud condensation nuclei in the high Arctic. *Proceedings of the National Academy of Sciences*, 108(33):13612–13617.

Pabi, S., van Dijken, G. L., and Arrigo, K. R. (2008). Primary production in the Arctic Ocean, 1998–2006. *Journal of Geophysical Research: Oceans*, 113(C8):C08005.

Palmer, M. A., Saenz, B. T., and Arrigo, K. R. (2014). Impacts of sea ice retreat, thinning, and melt-pond proliferation on the summer phytoplankton bloom in the Chukchi Sea, Arctic Ocean. *Deep Sea Research Part II: Topical Studies in Oceanography*, 105:85–104.

Pandis, S. N., Russell, L. M., and Seinfeld, J. H. (1994). The relationship between DMS flux and CCN concentration in remote marine regions. *Journal of Geophysical Research*, 99(D8):16945.

Papakyriakou, T. and Miller, L. (2011). Springtime CO2 exchange over seasonal sea ice in the Canadian Arctic Archipelago. *Annals of Glaciology*, 52(57):215–224.

Park, K.-T., Jang, S., Lee, K., Yoon, Y. J., Kim, M.-S., Park, K., Cho, H.-J., Kang, J.-H., Udisti, R., Lee, B.-Y., and Shin, K.-H. (2017). Observational evidence for the formation of DMS-derived aerosols during Arctic phytoplankton blooms. *Atmospheric Chemistry and Physics*, 17(15):9665–9675.

Perovich, D. K., Grenfell, T. C., Light, B., and Hobbs, P. V. (2002). Seasonal evolution of the albedo of multiyear Arctic sea ice. *Journal of Geophysical Research: Oceans*, 107(C10):8044.

Pogson, L., Tremblay, B., Lavoie, D., Michel, C., and Vancoppenolle, M. (2011). Development and validation of a one-dimensional snow-ice algae model against observations in Resolute Passage, Canadian Arctic Archipelago. *Journal of Geophysical Research*, 116(C4):C04010.

Popova, E. E., Yool, A., Coward, A. C., Dupont, F., Deal, C., Elliott, S., Hunke, E., Jin, M., Steele, M., and Zhang, J. (2012). What controls primary production in the Arctic Ocean? Results from an intercomparison of five general circulation models with biogeochemistry. *Journal of Geophysical Research: Oceans*, 117(C8):C00D12.

Prather, M. J. (1986). Numerical advection by conservation of second-order moments. *Journal of Geophysical Research: Atmospheres*, 91(D6):6671–6681.

Qu, B. and Gabric, A. J. (2010). Using genetic algorithms to calibrate a dimethylsulfide production model in the Arctic ocean. *Chinese Journal of Oceanology and Limnology*, 28(3):573–582.

Qu, B., Gabric, A. J., Zeng, M., and Lu, Z. (2016). Dimethylsulfide model calibration in the Barents Sea using a genetic algorithm and neural network. *Environmental Chemistry*, 13(2):413–424.

Quinn, P. K. and Bates, T. S. (2011). The case against climate regulation via oceanic phytoplankton sulphur emissions. *Nature*, 480(7375):51–56.

Rampal, P., Bouillon, S., Bergh, J., and Ólason, E. (2016). Arctic sea-ice diffusion from observed and simulated Lagrangian trajectories. *The Cryosphere*, 10(4):1513–1527.

Rampal, P., Weiss, J., and Marsan, D. (2009). Positive trend in the mean speed and deformation rate of Arctic sea ice, 1979–2007. *Journal of Geophysical Research: Oceans*, 114(C5).

Rebreanu, L., Vanderborght, J.-P., and Chou, L. (2008). The diffusion coefficient of dissolved silica revisited. *Marine Chemistry*, 112(3–4):230–233.

Redfield, A. C., Ketchum, B., and Richards, F. (1963). The influence of organisms on the composition of sea-water. In *The composition of sea-water: comparative and descriptive oceanography*, volume 2 of *The sea, ideas and observations on progress in the study of the seas*, pages 26–77. Interscience Pub, New York.

Rempillo, O., Seguin, A. M., Norman, A.-L., Scarratt, M., Michaud, S., Chang, R., Sjostedt, S., Abbatt, J., Else, B., Papakyriakou, T., Sharma, S., Grasby, S., and Levasseur, M. (2011). Dimethyl sulfide air-sea fluxes and biogenic sulfur as a source of new aerosols in the Arctic fall. *Journal of Geophysical Research: Atmospheres*, 116(D17):D00S04.

Riedel, A., Michel, C., and Gosselin, M. (2006). Seasonal study of sea-ice exopolymeric substances on the Mackenzie shelf: implications for transport of sea-ice bacteria and algae. *Aquatic Microbial Ecology*, 45:195–206.

Różańska, M., Poulin, M., and Gosselin, M. (2008). Protist entrapment in newly formed sea ice in the Coastal Arctic Ocean. *Journal of Marine Systems*, 74(3-4):887–901.

Russell, L. M., Pandis, S. N., and Seinfeld, J. H. (1994). Aerosol production and growth in the marine boundary layer. *Journal of Geophysical Research*, 99(D10):20989–21003.

Sakshaug, E. (2004). Primary and Secondary Production in the Arctic Seas. In Stein, R. and MacDonald, R. W., editors, *The Organic Carbon Cycle in the Arctic Ocean*, pages 57–81. Springer Berlin Heidelberg.

Saltzman, E. S., King, D. B., Holmen, K., and Leck, C. (1993). Experimental determination of the diffusion coefficient of dimethylsulfide in water. *Journal of Geophysical Research: Oceans*, 98(C9):16481–16486.

Schweiger, A., Lindsay, R., Zhang, J., Steele, M., Stern, H., and Kwok, R. (2011). Uncertainty in modeled Arctic sea ice volume. *Journal of Geophysical Research: Oceans*, 116(C8):C00D06.

Sharma, S., Barrie, L. A., Plummer, D., McConnell, J. C., Brickell, P. C., Levasseur, M., Gosselin, M., and Bates, T. S. (1999). Flux estimation of oceanic dimethyl sulfide around North America. *Journal of Geophysical Research: Atmospheres*, 104(D17):21327–21342.

Sharma, S., Chan, E., Ishizawa, M., Toom-Sauntry, D., Gong, S. L., Li, S. M., Tarasick, D. W., Leaitch, W. R., Norman, A., Quinn, P. K., Bates, T. S., Levasseur, M., Barrie, L. A., and Maenhaut, W. (2012). Influence of transport and ocean ice extent on biogenic aerosol sulfur in the Arctic atmosphere. *Journal of Geophysical Research: Atmospheres*, 117(D12):D12209.

Shaw, G. E. (1983). Bio-controlled thermostasis involving the sulfur cycle. *Climatic Change*, 5(3):297–303.

Shirasawa, K. and Ingram, R. G. (1997). Currents and turbulent fluxes under the first-year sea ice in Resolute Passage, Northwest Territories, Canada. *Journal of Marine Systems*, 11(1–2):21–32.

Sibert, V., Zakardjian, B., Saucier, F., Gosselin, M., Starr, M., and Senneville, S. (2010). Spatial and temporal variability of ice algal production in a 3d ice-ocean model of the Hudson Bay, Hudson Strait and Foxe Basin system: Modelling ice algal production in the Hudson Bay system. *Polar Research*, 29(3):353–378.

Simó, R. (2001). Production of atmospheric sulfur by oceanic plankton: biogeochemical, ecological and evolutionary links. *Trends in Ecology & Evolution*, 16(6):287–294.

Simó, R. and Pedros-Alio, C. (1999). Short-term variability in the open ocean cycle of dimethylsulfide. *Global Biogeochemical Cycles*, 13(4):1173–1181.

Six, K. D., Kloster, S., Ilyina, T., Archer, S. D., Zhang, K., and Maier-Reimer, E. (2013). Global warming amplified by reduced sulphur fluxes as a result of ocean acidification. *Nature Climate Change*, 3(11):975–978.

Smith, R. E., Harrison, W. G., Harris, L. R., and Herman, A. W. (1990). Vertical fine structure of particulate matter and nutrients in sea ice of the high Arctic. *Canadian Journal of Fisheries and Aquatic Sciences*, 47(7):1348–1355.

Smith, R. E. H. (1988). Abundance and production of ice algae in Resolute Passage, Canadian Arctic. *Mar. Ecol. Prog. Ser.*, 48:251–263.

Soltwedel, T., Bauerfeind, E., Bergmann, M., Bracher, A., Budaeva, N., Busch, K., Cherkasheva, A., Fahl, K., Grzelak, K., Hasemann, C., Jacob, M., Kraft, A., Lalande, C., Metfies, K., Nöthig, E.-M., Meyer, K., Quéric, N.-V., Schewe,

I., Włodarska-Kowalczuk, M., and Klages, M. (2016). Natural variability or anthropogenically-induced variation? Insights from 15 years of multidisciplinary observations at the arctic marine LTER site HAUSGARTEN. *Ecological Indicators*, 65:89–102.

Stefels, J. (2000). Physiological aspects of the production and conversion of DMSP in marine algae and higher plants. *Journal of Sea Research*, 43(3–4):183–197.

Stefels, J., Carnat, G., Dacey, J. W. H., Goossens, T., Elzenga, J. T. M., and Tison, J.-L. (2012). The analysis of dimethylsulfide and dimethylsulfoniopropionate in sea ice: Dry-crushing and melting using stable isotope additions. *Marine Chemistry*, 128–129:34–43.

Stefels, J., Steinke, M., Turner, S., Malin, G., and Belviso, S. (2007). Environmental constraints on the production and removal of the climatically active gas dimethylsulphide (DMS) and implications for ecosystem modelling. *Biogeochemistry*, 83(1-3):245–275.

Stefels, J. and van Leeuwe, M. A. (1998). Effects of Iron and Light Stress on the Biochemical Composition of Antarctic Phaeocystis Sp. (prymnesiophyceae). I. Intracellular Dmsp Concentrations. *Journal of Phycology*, 34(3):486–495.

Steiner, N., Deal, C., Lannuzel, D., Lavoie, D., Massonnet, F., Miller, L. A., Moreau, S., Popova, E., Stefels, J., and Tedesco, L. (2016). What sea-ice biogeochemical modellers need from observers. *Elementa: Science of the Anthropocene*, 4(84).

Steiner, N. and Denman, K. (2008). Parameter sensitivities in a 1-D model for DMS and sulphur cycling in the upper ocean. *Deep Sea Research Part I: Oceanographic Research Papers*, 55(7):847–865.

Steiner, N., Denman, K., McFarlane, N., and Solheim, L. (2006). Simulating the coupling between atmosphere–ocean processes and the planktonic ecosystem during SERIES. *Deep Sea Research Part II: Topical Studies in Oceanography*, 53(20-22):2434–2454.

Steiner, N. S., Lee, W. G., and Christian, J. R. (2013). Enhanced gas fluxes in small sea ice leads and cracks: Effects on CO 2 exchange and ocean acidification. *Journal of Geophysical Research: Oceans*, 118(3):1195–1205.

Steiner, N. S., Sou, T., Deal, C., Jackson, J. M., Jin, M., Popova, E., Williams, W., and Yool, A. (2015). The Future of the Subsurface Chlorophyll-a Maximum in the Canada Basin - A Model Intercomparison. *Journal of Geophysical Research: Oceans*, 120(1):387–409.

Stroeve, J. C., Kattsov, V., Barrett, A., Serreze, M., Pavlova, T., Holland, M., and Meier, W. N. (2012a). Trends in Arctic sea ice extent from CMIP5, CMIP3 and observations. *Geophysical Research Letters*, 39(16):L16502.

Stroeve, J. C., Serreze, M. C., Holland, M. M., Kay, J. E., Malanik, J., and Barrett, A. P. (2012b). The Arctic's rapidly shrinking sea ice cover: a research synthesis. *Climatic Change*, 110(3-4):1005–1027.

Sunda, W., Kieber, D. J., Kiene, R. P., and Huntsman, S. (2002). An antioxidant function for DMSP and DMS in marine algae. *Nature*, 418(6895):317–320.

Sunda, W. G., Hardison, R., Kiene, R. P., Bucciarelli, E., and Harada, H. (2007). The effect of nitrogen limitation on cellular DMSP and DMS release in marine phytoplankton: climate feedback implications. *Aquatic Sciences*, 69(3):341–351.

Suzuki, Y. and Takahashi, M. (1995). Growth Responses of Several Diatom Species Isolated from Various Environments to Temperature. *Journal of Phycology*, 31(6):880–888.

Taalba, A., Xie, H., Scarratt, M. G., Bélanger, S., and Levasseur, M. (2012). Photo-oxidation of Dimethylsulfide (DMS) in the Western Canadian Arctic. *AGU Fall Meeting Abstracts*, 10:6793– 6806.

Tank, S. E., Raymond, P. A., Striegl, R. G., McClelland, J. W., Holmes, R. M., Fiske, G. J., and Peterson, B. J. (2012). A land-to-ocean perspective on the magnitude, source and implication of DIC flux from major Arctic rivers to the Arctic Ocean. *Global Biogeochemical Cycles*, 26(4):GB4018.

Taylor, P. D. and Feltham, D. L. (2004). A model of melt pond evolution on sea ice. *Journal of Geophysical Research: Oceans*, 109(C12):C12007.

Tedesco, L., Miettunen, E., An, B. W., Happala, J., and Kaartokallio, H. (2017). Long-term mesoscale variability of modelled sea-ice primary production in the northern Baltic Sea. *Elem Sci Anth*, 5(29).

Tedesco, L. and Vichi, M. (2014). Sea Ice Biogeochemistry: A Guide for Modellers. *PLoS ONE*, 9(2):e89217.

Tedesco, L., Vichi, M., and Thomas, D. N. (2012). Process studies on the ecological coupling between sea ice algae and phytoplankton. *Ecological Modelling*, 226:120–138.

Tesdal, J.-E., Christian, J. R., Monahan, A. H., and von Salzen, K. (2016a). Evaluation of diverse approaches for estimating sea-surface DMS concentration and air–sea exchange at global scale. *Environmental Chemistry*, 13(2):390–412.

Tesdal, J.-E., Christian, J. R., Monahan, A. H., and von Salzen, K. (2016b). Sensitivity of modelled sulfate aerosol and its radiative effect on climate to ocean DMS concentration and air–sea flux. *Atmospheric Chemistry and Physics*, 16(17):10847–10864.

Thorndike, A. S. (1986). Diffusion of sea ice. *Journal of Geophysical Research: Oceans*, 91(C6):7691–7696.

Tison, J.-L., Brabant, F., Dumont, I., and Stefels, J. (2010). High-resolution dimethyl sulfide and dimethylsulfoniopropionate time series profiles in decaying summer first-year sea ice at Ice Station Polarstern, western Weddell Sea, Antarctica. *Journal of Geophysical Research: Biogeosciences*, 115(G4):G04044.

Tjernström, M., Leck, C., Birch, C. E., Bottenheim, J. W., Brooks, B. J., Brooks, I. M., Bäcklin, L., Chang, R. Y.-W., de Leeuw, G., Di Liberto, L., de la Rosa, S., Granath, E., Graus, M., Hansel, A., Heintzenberg, J., Held, A., Hind, A., Johnston, P., Knulst, J., Martin, M., Matrai, P. A., Mauritsen, T., Müller, M., Norris, S. J., Orellana, M. V., Orsini, D. A., Paatero, J., Persson, P. O. G., Gao, Q., Rauschenberg, C., Ristovski, Z., Sedlar, J., Shupe, M. D., Sierau, B., Sirevaag, A., Sjogren, S., Stetzer, O., Swietlicki, E., Szczodrak, M., Vaattovaara, P., Wahlberg, N., Westberg, M., and Wheeler, C. R. (2014). The Arctic Summer Cloud Ocean Study (ASCOS): overview and experimental design. *Atmos. Chem. Phys.*, 14(6):2823–2869.

Toole, D. A., Kieber, D. J., Kiene, R. P., White, E. M., Bisgrove, J., del Valle, D. A., and Slezak, D. (2004). High dimethylsulfide photolysis rates in nitrate-rich Antarctic waters. *Geophysical Research Letters*, 31(11):L11307.

Tremblay, J.-É., Simpson, K., Martin, J., Miller, L., Gratton, Y., Barber, D., and Price, N. M. (2008). Vertical stability and the annual dynamics of nutrients and chlorophyll fluorescence in the coastal, southeast Beaufort Sea. *Journal of Geophysical Research: Oceans*, 113(C7):C07S90.

Trevena, A. J., Jones, G. B., Wright, S. W., and van den Enden, R. L. (2000). Profiles of DMSP, algal pigments, nutrients and salinity in pack ice from eastern Antarctica. *Journal of Sea Research*, 43(3–4):265–273.

Trevena, A. J., Jones, G. B., Wright, S. W., and van den Enden, R. L. (2003). Profiles of dimethylsulphoniopropionate (DMSP), algal pigments, nutrients, and salinity in the fast ice of Prydz Bay, Antarctica. *Journal of Geophysical Research: Oceans*, 108(C5):3145.

Uppala, S. M., KÅllberg, P. W., Simmons, A. J., Andrae, U., Bechtold, V. D. C., Fiorino, M., Gibson, J. K., Haseler, J., Hernandez, A., Kelly, G. A., Li, X., Onogi, K., Saarinen, S., Sokka, N., Allan, R. P., Andersson, E., Arpe, K., Balmaseda, M. A., Beljaars, A. C. M., Berg, L. V. D., Bidlot, J., Bormann, N., Caires, S., Chevallier, F., Dethof, A., Dragosavac, M., Fisher, M., Fuentes, M., Hagemann, S., Hólm, E., Hoskins, B. J., Isaksen, L., Janssen, P. a. E. M., Jenne, R., Mcnally, A. P., Mahfouf, J.-F., Morcrette, J.-J., Rayner, N. A., Saunders, R. W., Simon, P., Sterl, A., Trenberth, K. E., Untch, A., Vasiljevic, D., Viterbo, P., and Woollen, J. (2005). The ERA-40 re-analysis. *Quarterly Journal of the Royal Meteorological Society*, 131(612):2961–3012.

Uzuka, N. (2003). A time series observation of DMSP production in the fast ice zone near Barrow (extended abstract). *Tohoku Geophysical Journal*, 36:439–442.

van Rijssel, M. and Gieskes, W. W. C. (2002). Temperature, light, and the dimethylsulfoniopropionate (DMSP) content of Emiliania huxleyi (Prymnesiophyceae). *Journal of Sea Research*, 48(1):17–27.

Vancoppenolle, M., Bitz, C. M., and Fichefet, T. (2007). Summer landfast sea ice desalination at Point Barrow, Alaska: Modeling and observations. *Journal of Geophysical Research*, 112(C4):C04022.

Vancoppenolle, M., Bouillon, S., Fichefet, T., Goosse, H., Lecomte, O., Maqueda, M. A. M., and Madec, G. (2012). The Louvain-la-Neuve sea ice model. Technical report, Université catholique de Louvain.

Vancoppenolle, M., Fichefet, T., Goosse, H., Bouillon, S., Madec, G., and Maqueda, M. A. M. (2009). Simulating the mass balance and salinity of Arctic and Antarctic sea ice. 1. Model description and validation. *Ocean Modelling*, 27(1–2):33–53.

Vancoppenolle, M., Goosse, H., de Montety, A., Fichefet, T., Tremblay, B., and Tison, J.-L. (2010). Modeling brine and nutrient dynamics in Antarctic sea ice: The case of dissolved silica. *Journal of Geophysical Research*, 115(C2):C02005.

Vancoppenolle, M., Meiners, K. M., Michel, C., Bopp, L., Brabant, F., Carnat, G., Delille, B., Lannuzel, D., Madec, G., Moreau, S., Tison, J.-L., and van der Merwe, P. (2013). Role of sea ice in global biogeochemical cycles: emerging views and challenges. *Quaternary Science Reviews*, 79:207–230.

Vancoppenolle, M. and Tedesco, L. (2016). Numerical models of sea ice biogeochemistry. In *Sea Ice*, pages 492–515. Wiley-Blackwell, 3 edition.

Vaughan, D., Comiso, J., Allison, I., Carrasco, J., Kaser, G., Kwok, R., Mote, P., Murray, T., Paul, F., Ren, J., Rignot, E., Solomina, O., Steffen, K., and Zhang, T. (2013). Observations: Cryosphere. In Stocker, T., Qin, D., Plattner, G.-K., Tignor, M., Allen, S., Boschung, J., Nauels, A., Xia, Y., Bex, V., and Midgley, P., editors, *Climate Change 2013: The Physical Science Basis. Contribution of Working Group I to the Fifth Assessment Report of the Intergovernmental Panel on Climate Change*, pages 317–382. Cambridge University Press, Cambridge, United Kingdom and New York, NY, USA.

Vogt, M., Vallina, S. M., Buitenhuis, E. T., Bopp, L., and Quéré, C. L. (2010). Simulating dimethylsulphide seasonality with the Dynamic Green Ocean Model PlankTOM5. *Journal of Geophysical Research: Oceans*, 115(C6).

von Glasow, R. and Crutzen, P. J. (2004). Model study of multiphase DMS oxidation with a focus on halogens. *Atmospheric Chemistry and Physics*, 4(3):589–608.

Wang, S., Maltrud, M., Elliott, S., Cameron-Smith, P., and Jonko, A. (2018). Influence of dimethyl sulfide on the carbon cycle and biological production. *Biogeochemistry*, 138(1):49–68.

Warren, S. G., Rigor, I. G., Untersteiner, N., Radionov, V. F., Bryazgin, N. N., Aleksandrov, Y. I., and Colony, R. (1999). Snow Depth on Arctic Sea Ice. *Journal of Climate*, 12(6):1814–1829.

Watanabe, E. (2013). Linkages among halocline variability, shelf-basin interaction, and wind regimes in the Beaufort Sea demonstrated in pan-Arctic Ocean modeling framework. *Ocean Modelling*, 71:43–53.

Watanabe, E., Onodera, J., Harada, N., Aita, M. N., Ishida, A., and Kishi, M. J. (2015). Wind-driven interannual variability of sea ice algal production in the western Arctic Chukchi Borderland. *Biogeosciences*, 12(20):6147–6168.

Willis, M. D., Burkart, J., Thomas, J. L., Köllner, F., Schneider, J., Bozem, H., Hoor, P. M., Aliabadi, A. A., Schulz, H., Herber, A. B., Leaitch, W. R., and Abbatt, J. P. D. (2016). Growth of nucleation mode particles in the summertime Arctic: a case study. *Atmospheric Chemistry and Physics*, 16(12):7663–7679.

Windnagel, A., Brandt, M., Fetterer, F., and Meier, W. (2017). Sea Ice Index Version 3 Analysis. NSIDC Special Report 19.

Winter, A., Henderiks, J., Beaufort, L., Rickaby, R. E. M., and Brown, C. W. (2014). Poleward expansion of the coccolithophore Emiliania huxleyi. *Journal of Plankton Research*, 36(2):316–325.

Wolf-Gladrow, D. A., Zeebe, R. E., Klaas, C., Körtzinger, A., and Dickson, A. G. (2007). Total alkalinity: The explicit conservative expression and its application to biogeochemical processes. *Marine Chemistry*, 106(1):287–300.

Zahariev, K., Christian, J. R., and Denman, K. L. (2008). Preindustrial, historical, and fertilization simulations using a global ocean carbon model with new parameterizations of iron limitation, calcification, and N2 fixation. *Progress in Oceanography*, 77(1):56–82.

Zeebe, R. E., Eicken, H., Robinson, D. H., Wolf-Gladrow, D., and Dieckmann, G. S. (1996). Modeling the heating and melting of sea ice through light absorption by microalgae. *Journal of Geophysical Research: Oceans*, 101(C1):1163–1181.

Zemmelink, H. J., Dacey, J. W. H., Houghton, L., Hintsa, E. J., and Liss, P. S. (2008). Dimethylsulfide emissions over the multi-year ice of the western Weddell Sea. *Geophysical Research Letters*, 35(6):L06603.

Zhang, J. and Rothrock, D. A. (2003). Modeling Global Sea Ice with a Thickness and Enthalpy Distribution Model in Generalized Curvilinear Coordinates. *Monthly Weather Review*, 131(5):845–861.

Zhang, J., Spitz, Y. H., Steele, M., Ashjian, C., Campbell, R., Berline, L., and Matrai, P. (2010). Modeling the impact of declining sea ice on the Arctic marine planktonic ecosystem. *Journal of Geophysical Research: Oceans*, 115(C10):C10015.

Zhou, J., Delille, B., Eicken, H., Vancoppenolle, M., Brabant, F., Carnat, G., Geilfus, N.-X., Papakyriakou, T., Heinesch, B., and Tison, J.-L. (2013). Physical and biogeochemical properties in landfast sea ice (Barrow, Alaska): Insights on brine and gas dynamics across seasons. *Journal of Geophysical Research: Oceans*, 118(6):3172–3189.